Nickel and cobalt oxide nanoparticles embedded into polypyrrole films as efficient electrocatalytic material for water oxidation

Catalina Andrea Astudillo Neira

THÈSE

Pour obtenir le grade de

DOCTEUR DE L'UNIVERSITE GRENOBLE ALPES

Spécialité : **Chimie inorganique et bioinorganique**

Arrêté ministériel : 25 mai 2016

Présentée par

Catalina Andrea ASTUDILLO NEIRA

Thèse dirigée par **Marie-Noëlle COLLONB, DR CNRS, UGA,** et co-encadrée par **Jérôme FORTAGE, CR CNRS, UGA**

préparée au sein du **Département de Chimie Moléculaire (DCM)** dans **l'École Doctorale Chimie et Sciences du Vivant (EDCSV)**

Nickel and cobalt oxide nanoparticles embedded in polypyrrole films as effective electrocatalytic materials for the oxidation of water

Thèse soutenue publiquement le **07 octobre 2020**, devant le jury composé de :

Mme. Christine MOUSTY
Directrice de Recherche CNRS, Université Clermont Auvergne, Rapportrice

M. Christophe BUCHER
Directeur de Recherche CNRS, Ecole Normale Supérieure de Lyon, Rapporteur et Président

M. Bruno FABRE
Directeur de Recherche CNRS, Université de Renne 1, Examinateur

Mme. Marie-Noëlle COLLOMB
Directrice de Recherche CNRS, Université Grenoble Alpes, Directrice de thèse

M. Jérôme FORTAGE
Chargé de Recherche CNRS, Université Grenoble Alpes, Membre invité

Acknowledgements

I would like to thank Serge Cosnier (CNRS Research Director and Director of the «Département de Chimie Moleculaire» (DCM)), and Fabrice Thomas (UGA Professor and Director of the group «Chimie Inorganique Rédox» (CIRE)), to allow me to do my thesis studies in DCM laboratory and CIRE group, and I am especially grateful to BecasChile (ANID, former Conicyt) "Programa de formación de capital humano avanzado", from the Chilean Government for all the economic support they gave me, letting me to successfully finish my PhD studies with their scholarship.

I would like to thank the members of the Jury of my defense: Christine Mousty (CNRS Research Director), Bruno Fabre (CNRS Researcher Director), and especially to Christophe Bucher (CNRS Research Director), who attended as president of the jury with such a short notice and during a pandemic season. I also thank Karine Gorgy (UGA Assistant Professor) and Lionel Dubois (CEA Researcher) for accepting to be members of my *Comité de Suivi Individuel* jury during the years prior the defense, for the support and advise to carry on over the years. I would like to thank my PhD supervisors, Marie-Noëlle Collomb (CNRS Research Director) and Jérôme Fortage (CNRS Researcher), for accepting me as a PhD student in your group. I would like to thank Veronika Anastasoiae (PhD student) as I enjoyed the time we shared in the Electrochemistry lab and our collaboration in science; to Baptiste Agnely (Lycée student) as he was the best student I could have; to Baptiste Dautreppe (PhD student) as we shared our thesis subjects so closely; Selim Sirach (UGA Assistant Engineer) for the synthesis of the pyrrole ammonium and for supervise me in the synthesis laboratory during my first year; and Florian Molton (CNRS Engineer) for teaching me how to weld electrodes and especially for his kindness and understanding. Thanks to Chantal Gondran (UGA Assistant Professor) for her kind help and patience in the EIS analyses. Thanks as well to Benoit Chovelon (Biologist and Doctor in CHU Grenoble) and Dominique André (Technician in CHU Grenoble) for the ICPMS analyses, Jean-Luc Puteaux (CNRS Research Director) and Christine Lancelon-Pin (CNRS Engineer) for SEM and TEM analyses, Frédéric Charlot (INP-UGA Research Engineer) for the SEM-EDX analyses, and Dmitry Aldakov (CNRS Researcher) for the XPS analyses.

I would like to express my deepest appreciation to foreign office members (room 311) and surroundings for putting up with my random singing: particularly to Lianke Wang, the one I consider my very first friend in the office, and to Daniela Morales who brought me here and show me to move through Grenoble the first days. A special appreciation lines to my work-wifey Suzanne «Suzanita» Adam (*from* the States!), the best *virgo* friend I could ever dream having: her dear support, affection and English-teaching moments were of huge value to my daily routine. Thanks as well to Marcello Gennari for his unexpected friendship and support, and the encouragement to live my real life (e.g., to unplug myself from the *online* world). Thanks to Emiliano Martínez, the final months of the PhD would have been tougher without our Coca-Cola meetings: our friendship and understanding turn out to be possible even if some said the contrary. Thanks to Eder «el bello» Tomás, Javier Gutiérrez, Romain Sanahuges for their kindness and discussions in the coffee room and hallways.

Finally, to my *latin-grenoblois* best friends outside the lab: Yina Betancourt, José Sayriputac, and Nicolás Cuadrado, for all your love and support that stayed with me over these difficult years until the day of my defense, *gracias a la vida por tenerlos*. Lastly, thanks to Camila Rivera, my long-lasting friend with whom I started studying chemistry and get our degrees within a two-month gap, worked at the same pharmaceutical lab, and won the same scholarship

in the same year: I would like to thank her friendship and her quick support when I needed it during the tough pandemic days.

Last but not least, I want to thank my family. To my father Hernán, who took his family into an adventure in Germany in the 90s: while he did his PhD in Physics, he did not know that he was encouraging me to try my best to be as awesome as he was. To my mother Mariela, the woman who was born to be the best mom someone could have. To my twin sister and soulmate Natalia, you are my sun(flower)shine.

Abbreviations list

HER: Hydrogen evolution reaction
OER: Oxygen evolution reaction
PEM: Proton exchange membrane
SOE: Solid oxide electrolyzer
SHE: Standard hydrogen electrode
PCET: Proton coupled electron transfer
NHE: Normal hydrogen electrode
RHE: Reversible hydrogen electrode
SCE: Saturated calomel electrode
TOF: Turnover frequency
FTO: Fluorine tin oxide
ITO: Indium tin oxide
NF: Nickel foam
PPN^+: Poly(pyrrole-alkyl ammonium)
Bi: Borate
Pi: Phosphate
LDH: Layer double hydroxide
η: Overpotential
CV: Cyclic voltammogram
CA: Chronoamperometry
CPE: Controlled-potential electrolysis
ICP-MS: Inductively coupled plasma mass spectroscopy
ICP-AES: Inductively coupled plasma atomic emission spectroscopy
AFM: Atomic force microscopy
XPS: X-ray photoelectron spectroscopy
SEM: Scanning electron microscopy
EDX: Energy dispersive X-ray microscopy
TEM: Transmission electron microscopy
SAED: Selected area electron diffraction
EIS: Electrochemical impedance spectroscopy
XRD: X-ray diffraction
XAS: X-ray absorption spectroscopy
XAFS: X-ray absorption fine structure
EXAFS: Extended X-ray absorption fine structure
XANES: X-ray absorption near edge structure
HERFD: High energy resolution fluorescence detection
SERS: Surface enhanced Raman spectroscopy
EELS: Electron energy loss spectrometry
GIXRD: Grazing incidence X-ray diffraction

Résumé de la thèse en français

Nos technologies les plus avancées dépendent de combustibles carbonés tels que le pétrole, le charbon et le gaz naturel. Les combustibles fossiles devraient être complètement épuisés dans un avenir proche et ne seront donc pas suffisants pour répondre à nos grands besoins énergétiques. L'exploitation excessive pour maintenir le progrès technologique a provoqué l'épuisement des ressources naturelles, le dégagement de gaz dangereux, la production de déchets et le changement climatique. En outre, le concept de "Journée du dépassement de la Terre" est apparu comme un exemple et marque la date à laquelle la demande de l'humanité en ressources et services écologiques pour une année donnée dépasse ce que la Terre peut régénérer. Depuis sa première utilisation en 2006 jusqu'à aujourd'hui, cette journée est passée d'octobre à août. Dans ce contexte, l'hydrogène moléculaire (H_2) est un bon candidat pour apporter une solution aux problèmes environnementaux liés à l'énergie. Il est considéré comme un vecteur d'énergie intéressant et peut être stocké pour une utilisation ultérieure dans des piles à combustible. Néanmoins, la principale source de production d'hydrogène provient toujours essentiellement des combustibles fossiles via un processus industriel, le vaporeformage du méthane, qui présente un faible coût et un rendement élevé d'environ 70 à 80 %. Cependant, ce procédé utilisant des combustibles fossiles libère du CO_2, un gaz à effet de serre. Une alternative plus propre pour obtenir de l'hydrogène consiste à utiliser l'eau comme source d'hydrogène et à recourir à des sources d'électricité renouvelables telles que le solaire ou l'éolien pour sa production. La dissociation de l'eau en hydrogène (réaction de dégagement d'hydrogène (HER)), et en oxygène (réaction de dégagement d'oxygène (OER)), peut être réalisée par l'intermédiaire d'électrolyseurs.

Depuis plusieurs décennies, les technologies pour l'électrolyse de l'eau ont évolué, et trois types d'électrolyseurs ont vu le jour : les électrolyseurs alcalins, les électrolyseurs PEM à membrane échangeuse de protons (PEM pour Proton Exchange Membrane) et les électrolyseurs à oxyde solide (SOEC pour Solid Oxide Electrolysis Cell). Le plus fiable de ces électrolyseurs est l'électrolyseur alcalin, et il est largement utilisé pour des applications industrielles à grande échelle depuis le début du 20ème siècle. Cependant, la faible densité de courant et la faible pression de fonctionnement ont un impact négatif sur la taille du système et les coûts de production d'hydrogène. Par conséquent, les électrolyseurs alcalins ont subi différents changements, parmi lesquels le matériau des électrodes qui est passé de l'acier inoxydable au nickel. Le matériau de l'électrode doit présenter une bonne résistance à la corrosion, une conductivité élevée et un faible prix. L'objectif actuel est de concevoir des électrocatalyseurs hautement actifs qui tiennent compte de ces paramètres, afin d'améliorer les performances catalytiques pour la demi-réaction d'oxydation de l'eau (OER) à l'anode et la demi-réaction de réduction de l'eau (HER) à la cathode. Ce travail de thèse se concentrera sur l'élaboration de matériau pour l'anode, car la cinétique lente de l'OER représente la limitation de cette technologie.

Même si de nombreuses avancées ont été réalisées pour améliorer les performances des anodes, de nombreux problèmes doivent encore être résolus pour obtenir des anodes efficaces, stables et peu coûteuses afin de rendre la production d'hydrogène à partir d'électrolyseurs compétitive par rapport au vaporeformage :

(i) La morphologie du matériau catalytique doit être contrôlée afin d'augmenter la surface électroactive des anodes tout en minimisant la quantité de catalyseurs présents à la surface de l'électrode, ce qui diminuera leur coût sans pour autant réduire leur efficacité.

(ii) Les anodes doivent fonctionner efficacement dans des conditions de pH doux, proches de pH 7, afin d'augmenter la durée de vie des électrolyseurs en évitant le problème de corrosion lié à l'électrolyte acide ou alcalin, et donc les coûts de maintenance élevés.

(iii) La stabilité globale des anodes doit être améliorée par le développement de matériaux catalytiques innovants résistant au phénomène de corrosion (qui pourrait également être minimisé par l'utilisation d'un électrolyte neutre ou légèrement basique).

Mon travail de doctorat vise à aborder toutes ces questions en développant des matériaux nanocomposites composés de particules d'oxyde métallique de nickel, de nickel-fer et de cobalt (NiO_x, $NiFeO_x$ et CoO_x) dispersées dans une matrice de polypyrrole. En effet, depuis le début des années 1980, les oxydes de métaux de transition de la première rangée, tels que l'oxyde de nickel (NiO_x), l'oxyde mixte de nickel et de fer ($NiFeO_x$) et l'oxyde de cobalt (CoOx), se sont révélés très prometteurs comme catalyseurs de l'oxydation de l'eau, en raison de leur abondance relativement élevée sur la croûte terrestre, de leur faible surtension pour l'OER et de leur résistance à la corrosion, ce qui leur confère une grande stabilité en conditions opérationnelles. En outre, les exemples de matériaux nanocomposites combinant des nanoparticules d'oxyde métallique comme catalyseurs de l'OER dans un film polymère sont encore rares, bien qu'ils soient très prometteurs pour contrôler la formation et la taille des particules en vue d'améliorer la surface électrochimiquement active et donc les performances électrocatalytiques.

Le chapitre I est consacré à une description détaillée des études les plus pertinentes de la littérature concernant les oxydes de nickel, de nickel-fer et cobalt pour l'oxydation de l'eau. Bien que ces oxydes puissent être préparés par beaucoup de méthodes chimiques et physiques, nous allons nous concentrer sur la méthode électrochimique pour laquelle les oxydes métalliques sont électrodéposés sur une surface d'électrode, méthode directement en rapport avec les travaux présentés dans ce manuscrit.

Chapitre I. Nickel, nickel-iron and cobalt oxide-based anodes for electrocatalytic water oxidation: a bibliographic study

Actuellement, la réaction de dissociation de l'eau effectuée avec un électrolyseur alcalin pour produire de l'hydrogène est toujours considérée comme l'une des meilleures alternatives aux combustibles fossiles, car l'hydrogène peut produire de l'électricité dans une pile à combustible avec un rendement de conversion relativement bon (environ 50 %) tout en ne libérant que de l'eau comme sous-produit. Cependant, le point faible de la dissociation de l'eau, qui empêcherait son utilisation à plus grande échelle, est la demi-réaction oxydante (OER), en raison de sa barrière énergétique élevée qui doit être contournée, ainsi que de sa cinétique lente à la surface des électrodes et de la grande surtension anodique. Le nickel a été présent comme matériau d'électrode dès les premières conceptions d'électrolyseurs alcalins, et dans les années 80, les études relatives à d'autres oxydes à base de métaux de transition ont connu une évolution considérable. Cependant, le nickel et le cobalt demeurent les éléments favoris pour la synthèse de matériaux pour l'OER, en raison de la grande efficacité des oxydes correspondants comme catalyseurs de cette réaction. Parmi les nombreuses méthodes de synthèse pour l'obtention de

ces oxydes, dont certaines comportent de multiples étapes telles que la précipitation solvothermique ou chimique suivie de procédés qui déposent le matériau sur l'électrode (spin coating, dropcasting, procédé sol-gel, etc.), le dépôt électrochimique est la méthode la plus simple et la plus propre pour la préparation des anodes à base d'oxydes métalliques pour l'OER.

Les travaux de Nocera sur les oxydes de nickel et de cobalt au début des années 2000 peuvent être considérés comme une étape importante. En effet, ce groupe a montré que la présence d'un électrolyte acceptant les protons, comme le phosphate ou le borate, est un paramètre essentiel pour réaliser efficacement le dépôt du catalyseur d'oxyde métallique (cobalt ou nickel) à partir d'un simple sel métallique dans des conditions neutres (pH 7,0) ou proche de la neutralité (pH 9,2). De nombreuses études ont également permis de mieux comprendre la structure chimique des films catalytiques, ainsi que leur éventuel mécanisme pour l'OER, et ont fait état de leur forte activité dans ces milieux neutres ou faiblement basiques. Depuis les travaux de Nocera, divers précurseurs d'oxydes métalliques ont été explorés. Par exemple, le groupe de Spiccia a utilisé des complexes de nickel avec des ligands amine pour déposer des films d'oxyde de nickel, tandis que le groupe de Du a utilisé des cobaloximes pour obtenir un film d'oxyde de cobalt très actif. Néanmoins, il y a encore des lacunes dans la connaissance de ces catalyseurs d'OER largement étudiés. En particulier, l'oxyde de nickel est connu comme étant très actif pour l'OER mais il a été rapporté par Corrigan que cette forte activité pourrait être due à l'impureté de fer présente dans l'électrolyte KOH, qui est insérée dans le film d'oxyde de nickel même à des concentrations aussi faibles que 1 %, et augmente ainsi son activité électrocatalytique. Il a été suggéré que cette augmentation d'activité due à la présence de Fe dans le NiO_x pourrait être due à une augmentation de la conductivité du film, bien que le groupe de Boettcher ait suggéré que d'autres paramètres soient susceptibles d'être impliqués. Le rôle réel du fer dans le catalyseur à base d'oxyde de nickel est toujours en débat et le fait de comprendre la dépendance du fer dans les oxydes $NiFeO_x$ à l'égard de son activité pour l'OER permettra de concevoir de nouveaux électrocatalyseurs efficaces et stables à base d'oxydes métalliques mixtes pour l'oxydation de l'eau.

Chapitre II. Elaboration of porous ITO electrodes to improve the adsorption of nickel oxide-polypyrrole nanocomposite material for electrocatalytic water oxidation

Introduction et résumé des travaux antérieurs réalisés dans le groupe. Comme mentionné plus haut, parmi les nombreux électrocatalyseurs qui sont apparus pour activer la réaction d'oxydation de l'eau, les oxydes de nickel et de cobalt des métaux de transition sont parmi les plus efficaces à base de métaux non nobles. Par ailleurs, depuis des décennies, les nanoparticules de métal et d'oxyde de métal insérées dans une matrice polymère ont fait l'objet d'une attention considérable : les nanoparticules confèrent les propriétés catalytiques au nanocomposite polymère, tandis que le polymère contrôle leur formation en termes de taille, de forme, d'emplacement, etc. C'est donc le polymère qui régit en partie les propriétés catalytiques du nanocomposite qui en résulte.

Le polypyrrole est un polymère qui a été largement étudié pour la modification de surfaces d'électrodes en raison de sa polymérisation aisée, de sa conductivité élevée, de sa stabilité chimique et de sa biocompatibilité. De plus, les propriétés d'échange d'anions de la forme

oxydée du polypyrrole ont été beaucoup utilisées pour immobiliser des espèces catalytiques à la surface d'électrodes. Cependant, l'incorporation d'un catalyseur métallique dans un film de polypyrrole en utilisant ces propriétés d'échange d'anions présente certains inconvénients ; le polypyrrole ayant une capacité d'échange limitée à une charge négative pour trois cycles pyrrole. Ses propriétés d'échange d'anions peuvent être considérablement améliorées en ajoutant des substituants ioniques au squelette du polypyrrole, par exemple en utilisant un monomère pyrrole substitué par un groupe alkyl ammonium. Le dérivé alkylammonium pyrrole (3-pyrrole-1-yl-propyl)-triethylammonium tetrafluoroborate, **PN**$^+$, que nous avons utilisé dans ce travail de thèse (Schéma 1), a été synthétisé et étudié pour la première fois par notre groupe en 1989.

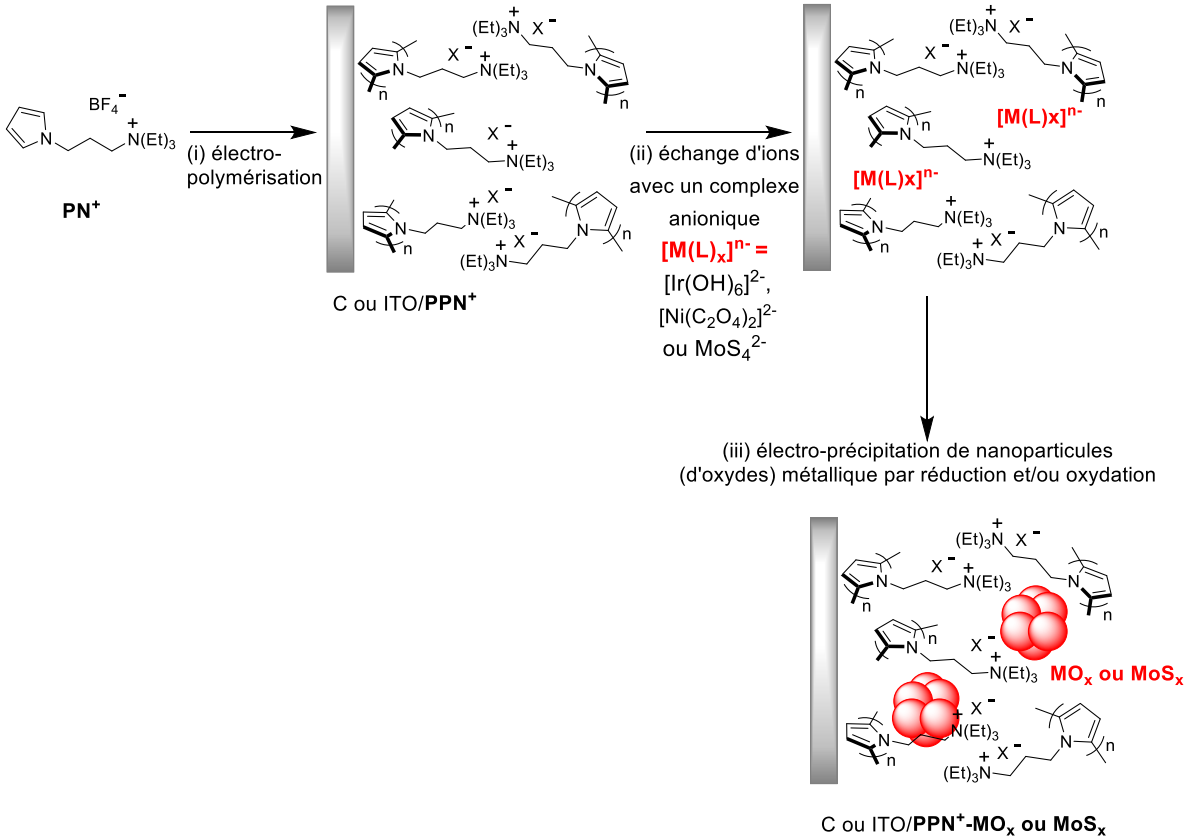

Schéma 1. Stratégie générale pour l'électrosynthèse des films nanocomposite de **PPN**$^+$**-MO$_x$** (M = Ir ou Ni) ou **PPN**$^+$**-MoS$_x$** à la surface d'électrodes: (i) électropolymérisation du monomère pyrrole PN$^+$ dans CH_3CN; (ii) incorporation de $[M(L)_x]^{n-}$ dans **PPN**$^+$ par trempage dans une solution aqueuse, (iii) electro-precipitation de nanoparticules (d'oxyde) de métaux dans le film de **PPN**$^+$ dans une solution aqueuse par réduction et/ou oxidation.

Les films de polypyrrole électropolymérisés de **PN**$^+$ (nommés **PPN**$^+$) se sont avérés avoir un comportement d'échange d'anions amélioré par rapport au polypyrrole non susbtitué. Ce polymère a permis l'incorporation efficace de complexes métalliques, d'anions organiques et inorganiques, à partir de milieux organiques et aqueux, ainsi que l'étude des électrodes modifiées résultantes dans ces deux milieux. En effet, suivant cette approche, notre groupe a récemment élaboré des matériaux nanocomposites de poly(pyrrole-alkyl ammonium)-nanoparticules de métal ou d'oxyde de métal (**IrO$_x$**, **NiO$_x$** et **MoS$_x$**) pour les réactions OER et HER. Ces nanomatériaux ont été facilement électrodéposés à la surface d'une électrode par une

simple procédure électrochimique (Schéma 1). La première étape consiste en (i) l'électropolymérisation du monomère **PN^+** à la surface de l'électrode, suivie par (ii) l'incorporation d'un complexe métallique anionique par échange d'ions dans la matrice **PPN^+** chargée positivement et enfin par (iii) l'électro-précipitation de nanoparticules *in situ* soit par réduction soit par oxydation. Des matériaux nanocomposites à base d'oxyde d'iridium (**PPN^+-IrO_x**) ont d'abord été obtenus par oxydation d'espèces anioniques $[Ir(OH)_6]^{2-}$. Ces anodes se révèlent beaucoup plus efficaces pour l'oxydation électrocatalytique de l'eau, plus stables et plus économiques en termes de quantité de catalyseur que les anodes en **IrO_x** pur déposées directement sous forme de films minces à la surface de l'électrode. Cette méthode d'électrosynthèse a été étendue avec succès au développement de matériaux sans métaux nobles tels que le sulfure de molybdène (**MoS_x**) pour la production de H_2 (HER) puis ensuite les oxydes de Ni (**NiO_x**) pour l'OER. Les nanoparticules de NiO_x ont été obtenues par incorporation du complexe anionique d'oxalate de Ni(II), $[Ni^{II}(oxalate)]^{2-}$, dans le **PPN^+** suivie de sa réduction en **Ni^0** puis de l'oxydation de **Ni^0** en **NiO_x**. En plus de la matrice polymère chargée positivement qui permet d'incorporer le précurseur de l'anion métallique, le polymère permet la formation de particules d'oxyde métallique de taille nanométrique, ainsi que leur protection en évitant leur libération dans la solution lors des expériences d'électrocatalyses. Les caractérisations par microscopie électronique à transmission (TEM) et microscopie à force atomique (AFM) du **PPN^+-IrO_x** et du **PPN^+-NiO_x** ont confirmé la grande nanostructuration du matériau, les particules de petite taille (2 nm pour IrO_x et 21 nm et NiO_x) étant bien dispersées dans le film **PPN^+** du polymère. En ce qui concerne le nanocomposite **PPN^+-NiO_x**, la nature des nanoparticules de nickel a été déterminée comme étant β-Ni^{III}(O)(OH) par titration coulométrique et la quantité de nickel déposée à la surface de l'électrode a été estimée par spectroscopie de masse à plasma inductif (ICPMS). En raison de la petite taille des nanoparticules de **NiO_x** et de la grande nanostructuration du nanocomposite **PPN^+-NiO_x**, ce matériau déposé sur une électrode de carbone vitreux (noté C, diamètre 3 mm) affiche des performances électrocatalytiques très élevées pour l'OER avec une forte activité massique (1,12 A mg^{-1}) et une valeur de TOF de 0,17 s^{-1} à pH 9,2 à une surtension de 0,61 V. Ces performances placent l'électrode C/**PPN^+-NiO_x** parmi les anodes les plus actives à base d'oxyde de nickel déjà publiées pour l'oxydation de l'eau et non dopées avec du fer (voir Chapitre I). En outre, les électrodes **PPN^+-NiO_x** préparées dans ces travaux antérieurs (Thèse de Daniela Morales Montecinos, Université Grenoble Alpes, 2018, doi:2018GREAV012), se sont révélées plus efficaces que le film d'oxyde de nickel électrogénéré directement sur une surface d'électrode sans polymère (nommée C/**NiO_x**) par le même procédé électrochimique, ce qui met en évidence le rôle bénéfique de la matrice de polypyrrole. Néanmoins, la stabilité des électrodes C/**PPN^+-NiO_x** et C/**NiO_x** pendant l'électrolyse à +1,2 V *vs* Ag/AgCl à pH 9,2 ne dépasse pas 3 heures. Cette perte d'activité est due au détachement progressif du film polymère de la surface de l'électrode, causé par le fort dégagement de bulles d'oxygène au cours de l'électrolyse, mais elle n'est pas due à la dégradation du matériau C/**PPN^+-NiO_x**. L'électrogénération du film nanocomposite sur un autre substrat d'électrode comme une électrode en verre recouverte d'une couche d'oxyde d'indium et d'étain (ITO) est un défi car le film de **PPN^+-NiO_x** peut se détacher encore plus facilement de la surface de l'électrode de carbone que lors de l'insertion du nickel ou de l'électrocatalyse. Dans cette optique, Zhang et coll. ont introduit en 2015 une nouvelle méthode facile et peu coûteuse pour modifier les couches sur le substrat d'ITO par

nanostructuration, selon une procédure électrochimique. L'électrodéposition de différents métaux (Au, Ag, Pt, Cu...) sur ces électrodes d'ITO nanostructurées augmente considérablement la stabilité mécanique des matériaux déposés.

Dans ce contexte, l'objectif des travaux décrits dans ce Chapitre II était de mettre au point une procédure pour modifier la surface de l'ITO en s'inspirant des travaux décrits par Zhang, afin d'augmenter la physisorption du nanocomposite **PPN^+-NiO_x** sur la surface de l'électrode ITO et d'empêcher le détachement du film au cours des expériences d'électrocatalyse. Ainsi, l'objectif était de démontrer pleinement la plus grande stabilité des matériaux nanocomposites **PPN^+-NiO_x** par rapport aux films de **NiO_x** simplement électrodéposés sur la surface d'une électrode.

Résumé des travaux. La méthode mise au point pour l'introduction de la porosité sur la surface d'ITO requière deux étapes. La première, électrochimique, consiste à réduire une fine couche d'oxyde d'indium et d'étain de la surface de la plaque d'ITO en appliquant un potentiel cathodique de -1,15 V *vs* Ag/AgCl dans une solution de tampon phosphate dégazée (0,1 M, pH 7,0) pour une charge de 20 mC (environ 70 secondes sont nécessaires pour une électrode ITO de surface de 0,4 cm^2). Dans une deuxième étape, la couche réduite d'In-Sn est décapée par trempage de l'électrode dans de l'eau régale (acide chlorhydrique et acide nitrique dans un rapport de 3:1) pendant 1 seconde, et le processus se termine par le rinçage immédiat et abondant de l'électrode d'ITO poreuse (ITO_{por}) avec de l'eau pour éliminer l'excès d'acide. Cette procédure a été optimisée pour assurer autant que possible la reproductibilité du processus, sans compromettre considérablement la conductivité de la plaque d'ITO (30 Ohms, Solens). Une réduction plus longue a conduit à des électrodes ITO non conductrices, probablement en raison du fait que tout le matériau conducteur a été réduit. Pour les mêmes raisons, le temps de trempage dans l'acide, initialement fixé à 2 secondes dans la procédure de Zhang, a été réduit à 1 seconde.

La nanostructuration de ces électrodes est bien visible grâce aux images obtenues par microscopie électronique à balayage (MEB ou SEM) et AFM de l'ITO_{por} comparée à une ITO sans traitement préalable. L'indice de rugosité de l'ITO_{por} a diminué de 4,0 nm à 2,35 nm par rapport à l'ITO non nanostructurée. De plus, la conductivité de l'électrode résultante est conservée après le traitement et l'électro-polymérisation du pyrrole ammonium ainsi que les étapes électrochimiques suivantes pour électro-générer les particules de **NiO_x** à l'intérieur du film **PPN^+**, celles-ci n'étant pas affectées par le pré-traitement de l'électrode. De plus, nous n'avons pas observé de désorption du film de **PPN^+** lors de ces étapes, ce qui a souvent été le cas lors de l'utilisation de simples électrodes ITO non nanostructurées.

Les films de nanocomposite **PPN^+-NiO_x** ont été électrogénérés à la surface des électrodes ITO_{por} (surface 0,4 cm^2) en plusieurs étapes. La 1ère consiste à électropolymériser les films de **PPN^+** à un potentiel imposé de 1.1 V *vs* $Ag/AgNO_3$ dans CH_3CN. La charge anodique de 22,4 mC utilisée correspond à une charge par unité de surface à 56 mC cm^{-2}, équivalente à celle utilisée pour les électrodes de carbone de diamètre 3 mm (4 mC pour une surface de 0.07 cm^2). La surface de recouvrement de l'électrode en unités ammonium (Γ_{N+} = 9,36 (± 0,46) × 10^{-8} mol cm^{-2}) a été calculée par intégration de la vague réversible du polypyrrole. Les nanoparticules de **Ni^0** sont ensuite électroprécipitées dans le film de **PPN^+** à -1,4 V *vs* Ag/AgCl

(charge cathodique 22,4 mC) après trempage préalable de l'électrode ITO_{por}/**PPN^+** pendant 1 heure dans une solution aqueuse de tampon borate (0,1 M) à pH 6 contenant le complexe anionique $[Ni(C_2O_4)_2]^{2-}$ généré *in-situ*. La quantité de nickel (Γ_{Ni}) des électrodes ITO_{por}/**PPN^+-Ni^0**, estimée à 5,76 (± 1,48) × 10^{-8} mol cm^{-2} par ICPMS, correspond à un rendement de dépôt de 19,8 %. Par comparaison, le rendement de dépôt est limité à 11,4 % pour des électrodes de C (Γ_{Ni} = 3,32 (± 0,19) × 10^{-8} mol cm^{-2}). L'électrooxidation de **Ni^0** en **NiO_x** est ensuite réalisée par 50 cycles successifs entre 0 et 1,2 V *vs* Ag/AgCl après transfert de l'électrode ITO_{por}/**PPN^+-Ni^0** dans une solution de borate (0.1 M) à pH 9,2. La formation de **NiO_x** est facilement observée par l'apparition progressive du système rédox $Ni^{II}(OH)_2/Ni^{III}(O)(OH)$ caractéristique de cet oxyde. Le polypyrrole étant suroxydé dès le 1er balayage, il devient non conducteur. A ce stade le polymère n'agit donc plus que comme matrice, la conduction du matériau nanocomposite **PPN^+-NiO_x** étant assurée par les nanoparticules de **NiO_x**.

Si la réponse électrochimique des électrodes ITO_{por}/**PPN^+-NiO_x** associée aux mesures d'ICPMS et d'EDX confirment bien la présence de nickel, les images obtenues par SEM et AFM, ne permettent pas d'observer les particules de **NiO_x**, ces dernières étant localisées à l'intérieur du polymère.

La procédure de nanostructuration d'électrodes ITO a permis d'éviter le détachement des films polymères en introduisant de la porosité à la surface de l'électrode avec une grande stabilité mécanique. Lorsque le nanocomposite **PPN^+-NiO_x** est déposé sur de telles surfaces d'électrodes, sa physisorption est considérablement améliorée. En effet, ce traitement permet à notre anode ITO_{por}/**PPN^+-NiO_x** efficace pour l'OER de rester opérationnelle pendant une semaine lors d'une électrolyse à 1,2 V *vs* Ag/AgCl, tant que la solution tampon de borate (0.1 M) à pH 9,2 est renouvelée pour éviter la baisse du pH, même dans des conditions de forte agitation ainsi que la formation de grosses bulles d'O_2. Ces résultats confirment également sans ambiguïté que les électrodes à base de nanocomposites **PPN^+-NiO_x** sont plus stables et plus robustes pour l'OER que les électrodes à base de **NiO_x**, grâce au rôle bénéfique de la matrice polypyrrole qui empêche la corrosion et la libération de nanoparticules de **NiO_x** en solution.

Cette méthode de nanostructuration d'ITO très reproductible et peu coûteuse, inspirée des travaux de Zhang, qui utilise la réduction électrochimique dans un tampon de phosphate neutre et la redissolution en milieu acide, résout l'un des problèmes les plus importants concernant l'utilisation des électrodes ITO modifiées dans les applications pratiques: la mauvaise adhérence des films sur la surface de ces électrodes.

Chapitre III. Cobalt oxide-polypyrrole nanocomposite as efficient and stable electrode material for electrocatalytic water oxidation

Introduction. L'oxyde de cobalt (**CoO_x**) a été intensivement étudié par de nombreux groupes dans des conditions alcalines. Identifié à l'origine comme un électrocatalyseur pour l'oxydation de l'eau à pH 14 en 1950 par El Wakkad et Hickling, cet oxyde a suscité un regain d'intérêt en 2008, grâce aux travaux de Nocera et de ses collaborateurs qui ont démontré que des couches minces de cet oxyde métallique relativement abondant sur terre, déposées par électrolyse dans un tampon de phosphate (pH 7) ou de borate (pH 9,2) accepteur de protons, sont également des électrocatalyseurs très actifs pour l'OER dans des conditions neutres ou quasi neutres.

Dans ce contexte, nous avons étendu l'élaboration de nanocomposite **PPN$^+$-MO$_x$** à l'oxyde de cobalt. Ce travail a été initié lors de la thèse de Daniela Morales (Université Grenoble Alpes, 2018, doi:2018GREAV012) qui a optimisé les conditions d'incorporation du complexe d'oxalate de cobalt dans le nanocomposite, et obtenu des images AFM et TEM du nanocomposite **PPN$^+$-CoO$_x$** déposé sur l'ITO.

Résumé des travaux. L'électrodéposition du matériau nanocomposite **PPN$^+$-CoO$_x$** a été réalisée sur des électrodes de carbone vitreux (diamètre 3 mm, surface de 0,071 cm^2) pour les études d'électrochimie analytique et sur des ITO poreuses (ITO$_{por}$, surface 0,4 cm^2) pour les études de microscopie et de spectroscopie ainsi que pour les expériences électrocatalytiques. Des procédures d'électrodéposition similaires à celles présentées dans le chapitre précédent ont été employées. La concentration du complexe $[Co(C_2O_4)_2]^{2-}$ a cependant été multipliée par 4 par rapport à celle de $[Ni(C_2O_4)_2]^{2-}$ afin de faciliter l'incorporation du cobalt. De plus, à la différence des nanoparticules métallique de nickel (**Ni^0**), les nanoparticules de cobalt métallique (**Co^0**) présentes dans le composite sont partiellement oxydées en oxyde de cobalt **CoO** sous simple exposition à l'air, puis entièrement oxydées en **CoO$_x$** par seulement 5 balayages successifs entre 0 et 1,2 V *vs* Ag/AgCl dans un tampon de borate (0,1 M) à pH 9,2. A titre de comparaison, des films de **CoO$_x$** ont également été déposés sur des électrodes de C et ITO$_{por}$ sans dépôt préalable de film de **PPN$^+$**.

Des mesures d'ICPMS montrent que la quantité de cobalt (Γ_{Co}) déposée dans les électrodes de C/**PPN$^+$** et de C sans **PPN$^+$** a été estimée à 2,27 (± 0,45) × 10^{-8} et 5,07 (± 0,33) × 10^{-8} mol cm^{-2}, respectivement, ce qui correspond à des rendements de déposition de 7,8 et 17,4%. Donc, pour la même quantité de charge (4 mC), la quantité de **Co^0** déposée pour C/**PPN$^+$** est 2,23 plus faible que celle déposée sur des électrodes de C nues. Pour les électrodes ITO$_{por}$, la quantité de cobalt est 1,8 fois plus importante dans le nanocomposite que dans l'ITO$_{por}$ nue avec des valeurs Γ_{Co} de 3,24 (± 0,72) × 10^{-8} mol cm^{-2} et 1,93 (± 0,10) × 10^{-8} mol cm^{-2}, pour l'ITO$_{por}$/**PPN$^+$** et l'ITO$_{por}$ respectivement correspondant à des rendements de 11,2 et 6,6 % pour la même charge de 22,4 mC. Le taux d'incorporation du Co dans **PPN$^+$** est donc de 38% pour C/**PPN$^+$** et de 70% pour ITO$_{por}$/**PPN$^+$**.

Les matériaux ont été caractérisé par diverses techniques électrochimiques (voltampérométrie cyclique, spectroscopie d'impédance électrochimique (ESI), chronoampérométrie, courbe de Tafel) et microscopiques (SEM-EDX et XPS). La nature de l'oxyde de cobalt a été identifiée par XPS comme étant un mélange de Co_3O_4/CoOOH. Les mesures ESI ont mis en évidence la grande nanostructuration du nanocomposite **PPN$^+$-CoO$_x$** confirmant ce qui avait été observé précédemment par des études de TEM avec la présence de petites nanoparticules de CoO_x d'environ 30 nm bien dispersées dans le film de polypyrrole et non agrégées. Le matériau nanocomposite présente une activité massique très élevée de 3,01 A mg^{-1} et des valeurs de TOF de 0,46 s^{-1} pour l'OER pour une surtension de 0,61 V à pH 9,2, et une pente de Tafel de 65 mV dec^{-1}. Ces performances surpassent la plupart des anodes à base d'oxyde de cobalt précédemment décrites fonctionnant dans une solution tampon de borate (0,1 M) à pH 9,2, mais aussi l'oxyde de cobalt électrogénéré sur une surface d'électrode nue par le même procédé électrochimique.

De plus, lorsque le matériau **PPN^+-CoO_x** est électrodéposé sur des électrodes d'ITO nanostructurées, sa physisorption est considérablement améliorée et, par conséquent, son activité catalytique est stable au-delà de 24 heures d'électrocatalyse à 1,2 V dans une solution de tampon borate (0.1 M) à pH 9,2. Ces résultats, comme dans les cas des films de nanocomposites **PPN^+- MO_x** élaborés avec l'iridium ou le nickel, confirme le rôle bénéfique de la matrice de polypyrrole chargée positivement dans la préparation de petites particules d'oxyde métallique et dans l'obtention d'une anode très stable et active pour l'oxydation de l'eau.

L'élaboration de tels matériaux nanocomposite polypyrrole-oxyde métallique pourrait facilement être étendue à la préparation d'oxydes métalliques mixtes tels que **$NiFeO_x$** ou **$CoFeO_x$**, qui sont les catalyseurs d'OER les plus efficaces dans des conditions alcalines ou légèrement basiques. Ces travaux feront l'objet du chapitre IV, avec le développement de matériaux d'électrode nanocomposites **PPN^+-$NiFeO_x$**.

Chapitre IV. Iron doping of Nickel Oxide-Polypyrrole Nanocomposite Material to Improve the Electrocatalytic Performance of Water Oxidation

Introduction. L'oxyde mixte de nickel-fer (**$NiFeO_x$**), qui n'est composé que d'éléments abondants sur terre, est considéré comme l'un des meilleurs électrocatalyseurs pour l'oxydation de l'eau et une alternative prometteuse aux catalyseurs à base de métaux rares comme l'oxyde de ruthénium et d'iridium, du fait qu'il présente des densités de courant catalytique élevées à faible surtension avec une grande stabilité dans un électrolyte alcalin. Depuis les travaux pionniers de Tichenor en 1952, de nombreux groupes ont étudié l'effet positif du fer inséré dans des films d'oxyde de nickel sur leur activité électrocatalytique d'oxydation de l'eau, même si le rôle réel du fer dans la catalyse est encore un sujet de débat. Globalement, deux théories s'affrontent. La première est basée sur le fait que l'oxyde de fer est le centre catalytique de l'oxydation de l'eau, l'oxyde de nickel ne servant que de matrice électroniquement conductrice pour l'oxyde de fer, qui a une faible conductivité. La seconde préconise que l'espèce active pour l'oxydation de l'eau est l'espèce Ni(IV)=O (présente dans la phase γ-NiOOH) dont la formation est favorisée par la présence d'un acide de Lewis fort tel que Fe^{3+}, et qui présente par résonance un fort caractère radicalaire oxyle (*i.e.* Ni(III)-O•). Ce dernier a été identifié comme étant impliqué dans la formation de la liaison O-O *via* un mécanisme PCET conduisant à l'intermédiaire hydroperoxyde responsable de la libération d'oxygène. Au regard de la littérature, l'électrocatalyseur **$NiFeO_x$** a été obtenu sous diverses morphologies et nanostructures par différentes méthodes synthétiques telles que le dépôt solvothermique, la co-précipitation et l'électrodéposition.

Afin d'améliorer encore les performances d'oxydation de l'eau des anodes utilisant le nanocomposite **PPN^+-NiO_x** décrit dans le Chapitre II, nous avons étendu notre approche à l'élaboration d'un matériau nanocomposite d'oxyde mixte de nickel/fer dispersé dans un film de poly(pyrrole-alkyl ammonium), **PPN^+-$NiFeO_x$**. Parmi les différentes méthodes possibles pour introduire du fer, nous avons choisi l'électrodéposition à partir de solutions aqueuses contenant un mélange de complexes anioniques d'oxalate de nickel et de citrate de fer à différentes concentrations. En outre, contrairement aux travaux décrits dans les chapitres précédents, où les oxydes de nickel ou de cobalt sont incorporés dans le polymère cationique

en deux étapes électrochimiques successives, génération des nanoparticules de $\mathbf{M^0}$ par réduction puis oxydation en $\mathbf{MO_x}$, nous avons testé une méthode plus simple qui consiste à oxyder directement les complexes anioniques de nickel et de fer imprégnés dans le film de $\mathbf{PPN^+}$ pour générer les nanoparticules de $\mathbf{NiFeO_x}$. Cette stratégie a été inspirée des travaux des groupes de Boettcher, Nocera et Halaoui qui ont montré que l'électrodéposition de $\mathbf{NiFeO_x}$ sur des électrodes à partir de sels de nickel et de fer est possible et efficace grâce à un procédé potentiostatique anodique dans un tampon borate à pH 9,2. A des fin de comparaison, nous avons tout d'abord préparé des matériaux nanocomposites $\mathbf{PPN^+\text{-}NiO_x}$ par cette méthode potentiostatique anodique plus simple à partir d'une solution contenant uniquement de l'oxalate de nickel.

Résumé des travaux. L'ensemble des études ont été réalisées sur électrodes de carbone vitreux (diamètre 3 mm). Les matériaux nanocomposites $\mathbf{PPN^+\text{-}NiO_x}$ ont été préparé par une procédure qui ne nécessite plus que deux étapes électrochimiques: (i) electropolymérisation du $\mathbf{PPN^+}$ sur électrode de carbone dans l'acétonitrile, (ii) incorporation des complexes anioniques d'oxalate de nickel (1 mM) dans $\mathbf{PPN^+}$ à partir d'une solution aqueuse avec un tampon de borate (0,1 M) à pH 9,2, puis (iii) electrogénération des particules de $\mathbf{NiO_x}$ dans le film polymère en appliquant un potentiel de 1,0 V *vs* Ag/AgCl dans ce même électrolyte. La présence de traces de fer dans l'électrolyte conduit à une incorporation involontaire de fer non négligeable dans les particules d'oxyde de nickel. En effet, les quantités de Ni et Fe (Γ_{Ni} et Γ_{Fe}) incorporées dans les électrodes de C/$\mathbf{PPN^+}$ estimées par ICPMS à 1,13 (± 0,29) × 10^{-7} et 3,55 (± 1,00) × 10^{-8} mol cm^{-2}, respectivement, correspondent à environ 25 % molaire de Fe par rapport au Ni. Cependant les marges d'erreur de 26 et 28 % sont importantes entre les différentes électrodes. Etudiées par voltammétrie cyclique dans le tampon borate (0.1 M) à pH 9,2, ces électrodes C/$\mathbf{PPN^+\text{-}Ni(Fe)O_x}$, présentent des densités de courant catalytique de l'ordre de 2.80 mA cm^{-2} à un potentiel de 1,2 V *vs* Ag/AgCl (*i.e.* à une surtension de 0,71 V). L'activité catalytique de ces électrodes a pu être nettement améliorée par un processus d'anodisation consistant à appliquer un potentiel de 0,95 V *vs* Ag/AgCl pendant 45 minutes dans un tampon borate à 1,0 M. Le courant catalytique augmente significativement pour atteindre 16,3 et 6,96 mA cm^{-2} à des surtensions de 0,71 et 0,61 V dans le tampon de borate 1,0 M. L'amélioration des performances des électrodes C/$\mathbf{PPN^+\text{-}Ni(Fe)O_x}$ a été attribuée à l'incorporation supplémentaire de fer au cours de l'anodisation, le pourcentage de Fe dans $\mathbf{NiO_x}$ ayant augmenté jusqu'à 51 %. Cependant on note encore une grande disparité des mesures entre les différentes électrodes qui tend à montrer que cette méthode d'incorporation du fer est non contrôlée et non reproductible (Γ_{Ni} = 4,03 (± 0,73) × 10^{-8} et Γ_{Fe} = 2,90 (± 1,97) × 10^{-8} mol cm^{-2}).

Dans un deuxième temps, des matériaux nanocomposites C/$\mathbf{PPN^+\text{-}NiFeO_x}$ ont été préparés selon la même procédure mais à partir d'une solution de tampon borate (0,1 M) à pH 9,2 contenant un mélange de complexes anioniques d'oxalate de nickel (1 mM) et de citrate de fer à deux concentrations différentes (0,4 et 0,8 mM). Avec 0.8 mM de citrate de fer, l'incorporation de fer est tout à fait reproductible avec environ 54 % molaire de Fe par rapport au Ni et des valeurs de Γ_{Ni} et Γ_{Fe} de 3,07 (± 0,18) × 10^{-8} et 3,74 (± 0,75) × 10^{-8} mol cm^{-2}, respectivement. Les marges d'erreur de 6 et 13 % respectivement, sont en effet beaucoup plus faibles que précédemment. L'étude par voltammétrie cyclique révèle que les électrodes C/$\mathbf{PPN^+\text{-}NiFeO_x}$ présentent des performances électrocatalytiques très élevées pour l'OER dans un tampon borate

à 1,0 M (pH 9,2), parmi les meilleures de la littérature, avec un courant catalytique qui atteint 22,6 et 14,6 mA cm^{-2} à des surtensions de 0,71 et 0,61 V, une faible surtension de 0,44 V à 1 mA cm^{-2}, ainsi que de très fortes valeurs d'activité massique et de TOF de 7,7 A mg^{-1} et 1,17 s^{-1} respectivement à la surtension de 0,61 V. En définitive, l'activité catalytique de C/**PPN^+-$NiFeO_x$**, avec une incorporation intentionnelle de fer dans NiO_x, se révèle être supérieure à celles de C/**PPN^+-Ni(Fe)O_x**, sans ajout volontaire de fer, qu'elles soient anodisées ou non. De plus, l'introduction de fer dans les particules d'oxyde de nickel semble se faire de façon beaucoup plus contrôlée et reproductible, lorsque l'électrogénération de particules de **$NiFeO_x$** dans le film de **PPN^+** est réalisée avec un mélange de citrate de fer et d'oxalate de nickel.

Cette étude préliminaire a révélé des performances très prometteuses du matériau nanocomposite **PPN^+-$NiFeO_x$** vis-à-vis de l'oxydation électrocatalytique de l'eau et des caractérisations supplémentaires doivent être effectuées pour confirmer et rationaliser ces performances élevées. Tout d'abord, un plus grand nombre d'électrodes doit être préparé afin d'estimer avec précision la reproductibilité de la procédure entièrement électrochimique en termes de comportement rédox, d'activité catalytique pour l'OER et de quantités relatives de nickel et de fer incorporées dans le film polymère. Il est à noter que la mesure des quantités de nickel et de fer déposées sur l'électrode, après leur dissolution dans l'acide nitrique, sera plus précise en utilisant la spectroscopie d'émission atomique avec un plasma à couplage inductif (ICP-AES) au lieu de l'ICP-MS, en raison de sa limite de détection beaucoup plus basse (µg L^{-1} pour l'ICP-AES contre mg L^{-1} pour l'ICP-MS). Ensuite, le matériau nanocomposite **PPN^+-$NiFeO_x$** pourra être caractérisé par SEM et AFM pour observer la morphologie et la nanostructuration du film, par TEM et XAS pour estimer la taille des particules de **$NiFeO_x$** dans le **PPN^+**, par SEM-EDX, XPS et XANES pour déterminer la composition et les états d'oxydation de l'oxyde métallique mixte, et par TEM-SAED et EXAFS pour évaluer la nature et la cristallinité des particules de **$NiFeO_x$**. Par ailleurs, le comportement redox et l'activité électrocatalytique du C/**PPN^+-$NiFeO_x$** doivent être étudiés plus en détails par spectroscopie d'impédance électrochimique pour évaluer sa conductivité et sa capacitance, cette dernière étant corrélée à sa nanostructuration, et par des courbes de Tafel pour obtenir certaines informations mécanistiques telles que l'étape cinétiquement déterminante au travers de la pente de Tafel. De plus, de longues électrolyses à potentiel ou à courant imposé devront être réalisées avec les électrodes C/**PPN^+-$NiFeO_x$** afin de démontrer la stabilité du matériau nanocomposite dans des conditions électrocatalytiques.

Ce travail ouvre la voie à une nouvelle génération d'anodes nanocomposites composées d'oxydes métalliques mixtes bien dispersés dans des polymères organiques, et très actifs pour l'oxydation électrocatalytique de l'eau. Ce type de matériau nanocomposite, rarement exploré dans la littérature pour développer des anodes d'oxydation de l'eau, pourrait être étendu à la mise en œuvre d'anodes contenant d'autres catalyseurs multimétalliques efficaces tels que **$CoFeO_x$**, **$NiCoFeO_x$** et **$MnCaO_x$**, ce dernier pouvant mimer le centre naturel de dégagement du dioxygène (OEC) trouvé dans le photosystème II des plantes vertes.

Table of Contents

General introduction

Our most advanced technologies depend on harmful carbon-based fuels such as oil, coal, and natural gas. Fossil fuels are expected to be completely depleted in the near future and therefore will not be sufficient to meet our great energy requirements. The excessive exploitation to maintain the technologic progress has caused natural resources exhaustion, hazardous gasses, waste generation and climate change. Additionally, the concept of Earth Overshoot Day has appeared as an exemplifier and marks the date when humanity's demand for ecological resources and services in a given year exceeds what Earth can regenerate, since its first use in 2006 to present, this day has moved from October to August. By this means, molecular hydrogen (H_2) is a good candidate to provide a solution to the energy related environmental problems. It is considered as an attractive energy carrier and can be stored for later use in fuel cells, to produce electricity with water as the only by-product. Nevertheless, the main source of hydrogen production still comes essentially from fossil fuels *via* an industrial process (e.g., steam reforming process) which presents a low cost and a high efficiency of about 70-80 %. However, this process that uses fossil fuels, also releases CO_2, a well-known greenhouse gas. A cleaner alternative to obtain hydrogen is using water as the hydrogen source and to use renewable electricity source such as solar or wind for its production. The water splitting reaction consists in dissociation of water into hydrogen, the hydrogen evolution reaction (HER), and oxygen, the oxygen evolution reaction (OER), and it can be achieved through electrolyzers.

For several decades, water splitting technology has evolved, and three electrolyzers have emerged: alkaline water electrolyzers, proton exchange membrane (PEM) electrolyzers and solid oxide electrolyzers (SOE). The most reliable among these electrolyzers is the alkaline water electrolyzers as it is widely used for large-scale industrial applications since the beginning of the 20th century. However, low current density and operating pressure negatively impact the system size and hydrogen production costs. Consequently, and up to this date, alkaline water electrolyzer went through many and different changes; for example, the electrode material moved from stainless steel and lead to nickel. The electrode material must hold good corrosion resistance, high conductivity, and low price. The current goal is to design highly active electrocatalysts that comprises these parameters, to enhance the catalytic performance of both oxidative (OER) and reductive (HER) sides of the water-splitting reaction. This work will focus on the anodes since its sluggish kinetics represents the bottleneck of this technology.

Even though there were many advances to improve the performance of anodes, many issues still have to be addressed to obtain efficient, stable, and low-cost anodes in view to render hydrogen production from electrolyzers cost competitive with steam reforming:

(i) The morphology of the catalytic material has to be controlled in order to increase the electroactive surface area of anodes while minimizing the amount of catalysts present at the surface of the electrode, which will diminish their cost without dwarfing their efficiency.
(ii) Anodes have to operate efficiently under mild pH condition, close to pH 7, to increase the lifetime of electrolyzers by avoiding the corrosion issue related to acid or alkaline electrolyte, and thus high maintenance costs.
(iii) The global stability of anodes has to be improved though the development of innovative catalytic materials resistant to the corrosion phenomenon (that also could be minimized with the use of a neutral or mildly basic electrolyte; see above).

My PhD work aims to address all these issues by developing nanocomposite materials composed of metal oxide particles of nickel (NiO_x), nickel-iron ($NiFeO_x$) and cobalt (CoO_x) well dispersed into a polypyrrole matrix. Since the early 1980s, the transition metal oxides from the first row, such as the nickel oxide (NiO_x), mixed nickel/iron oxide ($NiFeO_x$) and cobalt oxide (CoO_x) have shown great promise as catalysts for water oxidation, because of their relatively high abundance on the earth's crust, their low OER overpotential and their corrosion resistance, which gives them a high stability in operational requirements. In addition, examples of nanocomposite materials combining metal oxide nanoparticles as OER catalysts within a polymer film are still rare, although they are very promising to control the formation and the size of metal particles in view to enhance the electrochemically active surface area and thus the electrocatalytic performances.

In Chapter I, we present a bibliographic study on the development of representative anodes for electro-induced OER, giving details of anodes based on the oxides of nickel, the nickel-iron alloy, and cobalt; in order to trace a logical guideline in which the thesis will be directed. Although such oxides can be prepared by many chemical and physical methods, we will focus on the electrochemical synthesis pathway, in which the metal oxides are electrodeposited on an electrode surface.

Chapter II is devoted to the elaboration and characterization of the nano-structuration performed on the surface of the indium tin oxide (ITO) electrodes in view to enhance the

physisorption of our previously reported poly(pyrrole-alkyl ammonium)-nickel oxide nanocomposite (PPN^+-NiO_x) and prevent the film desorption under OER electrocatalytic experiments. Thus, the objective was to fully demonstrate the greater stability of PPN^+-NiO_x nanocomposite materials compared to NiO_x films simply electrodeposited at the surface of a naked electrode. The method used for the nanostructuration of ITO surfaces and the characterization of the resulting porous electrodes are first described. Then the elaboration and characterization by SEM-EDX and AFM spectroscopies of the poly(pyrrole-alkylammonium)-nickel oxide nanocomposite materials on these porous ITO electrodes will be detailed. Finally the electrocatalytic performances and stability of the resulting electrodes for OER at pH 9.2 in borate buffer is investigated under a long electrolysis.

Subsequent, Chapter III extends the elaboration of nanocomposites anodes for OER to cobalt oxides. The electrodeposition of poly(pyrrole-alkyl ammonium)-cobalt oxide (PPN^+-CoO_x) nanocomposite onto glassy carbon as well as on porous ITO electrodes, using similar procedures to those introduced in the previous chapter is described. The material has been then characterized by various electrochemical and microscopy techniques (SEM-EDX and XPS). The electrocatalytic performances of our anodes for OER at pH 9.2 in borate buffer is then compared to other reported cobalt oxide electrocatalysts of literature under similar catalytic conditions and with that of CoO_x films directly deposited on a naked electrode by the same electrochemical procedure.

Finally, in Chapter IV are described the results concerning a new mixed-metal nanocomposite material, using a slightly different pathway than the previous two chapters. Herein is described the simultaneous electro-decomposition of nickel and iron complexes precursors, in which is confirmed that the intentional addition of iron further enhances the OER performance and the synergetic association between nickel and iron, rather than being present as an impurity.

CHAPTER I

Nickel, nickel-iron and cobalt oxide-based anodes for electrocatalytic water oxidation: a bibliographic study

Index

I – Water-splitting for hydrogen production

The water-splitting reaction into hydrogen and oxygen (Equation 1) can be achieved by electrolysis through a two-electrodes cell.

$$H_2O \rightarrow H_2(g) + \frac{1}{2} O_2(g) \qquad (1)$$

The water reduction into hydrogen (the hydrogen evolving reaction (HER)) occurs at the cathode while on the anode takes place the water oxidation into oxygen (oxygen evolving reaction (OER)). Although HER involves only a transfer of two protons and two electrons, OER is a four electron-proton coupled reaction with a high energetic barrier and sluggish kinetics, making the OER the bottleneck of the water-splitting reaction. Therefore, many efforts have been made for improving OER by extensively studying various catalysts for overcome this high energetic barrier (see next section).

HER and OER are usually performed either on highly acidic (Equation 2-4) or alkaline (Equations 5-7) conditions to minimize the accompanying energy loss. The catalysts have evolved over the years from stainless steel and lead to precious metals such as Pt for HER and Ir and Ru for OER.[1] However, the use of precious metals increases investment costs and therefore are unable to pursue a large-scaled hydrogen production.

In aqueous acidic solution (pH 0):

OER $2\ H_2O\ (l) \rightarrow O_2\ (g) + 4\ H^+ + 4e^- \quad E^0 = -1.23\ V\ vs\ SHE$ (2)

HER $4\ H^+ + 4e^- \rightarrow 2\ H_2\ (g) \qquad E^0 = 0.0\ V\ vs\ SHE$ (3)

$$2H_2O\ (l) \rightarrow O_2\ (g) + 2H_2\ (g) \quad E^0 = -1.23\ V\ vs\ SHE \qquad (4)$$

In aqueous basic solution (pH 14):

OER $4\ OH^- \rightarrow O_2\ (g) + 2\ H_2O\ (l) + 4e^- \quad E^0 = -0.40\ V\ vs\ SHE$ (5)

HER $4\ H_2O + 4e^- \rightarrow 2H_2\ (g) + 4\ OH^- \qquad E^0 = -0.83\ V\ vs\ SHE$ (6)

$$2H_2O\ (l) \rightarrow O_2\ (g) + 2H_2\ (g) \quad E^0 = -1.23\ V\ vs\ SHE \qquad (7)$$

The technology of water electrolyzers has been applied for the past two hundred years. For instance, by 1902 there were already 400 working industrial alkaline water electrolyzers, and by the 1960s the proton exchange membrane (PEM) electrolyzers and solid oxide electrolyzers (SOE) were implemented.[2] SOE is the most efficient among the electrolyzers, although it is still under development since one of its main problems is the corrosion; and even though PEM is more efficient than alkaline electrolyzer, and corrosion plays no role here, its cost is too high compared with alkaline electrolyzers systems. Alkaline water electrolyzer have the lowest capital cost and have the lowest efficiency thus the electrical energy cost is too high.[3] Nevertheless, alkaline water electrolyzers are the most reliable, safe with a longer lifetime and suitable to a large-scale hydrogen production since it has been exposed to improvements over the time. Indeed, the Golden Age of this mature technology range between the years 1920 and 1970, as there was a huge demand of hydrogen to produce ammonia fertilizers. For such alkaline electrolyzers, the electrode material evolved from stainless steel and lead to nickel, since it tolerates better the strong alkaline conditions. On last years, reduction of the operating costs concerning the electricity consumption and investment costs was achieved by minimizing the space between the electrodes, replacing asbestos by exchange inorganic membranes, designing high-temperature electrolyzers, to name a few.

In Figure 1, the schematic representation of alkaline and PEM water electrolyzers is given, and we will further highlight the reason why the first example is more suitable for a large-scale hydrogen production. Alkaline water electrolyzer consists of two electrodes separated by a membrane, which is immersed in a liquid electrolyte. The operating range of temperature of this electrolyzer goes from 65 to 100 °C and a maximum allowable current density is about 0.4 A cm^{-2}, leading to efficient operation range of 47-82 %. The purity of the obtained hydrogen can reach up to 99.7 to 99.9 %vol. In contrast, in the case of PEM electrolyzers, the liquid is replaced by a polymeric membrane with a crossed-linked structure functionalized with strongly acidic groups of sulfonic acid. The main drawback of this electrolyzer is the electrode's material, made from precious metals such as platinum and iridium, which increases greatly its investment costs. Furthermore, such electrolyzers have shorter lifetimes than the alkaline water electrolyzers (5 years *vs* 10 years).[4] Thus, PEM electrolyzers are less suitable for large-scale hydrogen production although their efficiency can achieve 74 % along, [5] with a higher current density of 2 A cm^{-2} and a purity of the produced H_2 can reach up to 99.999 %vol.

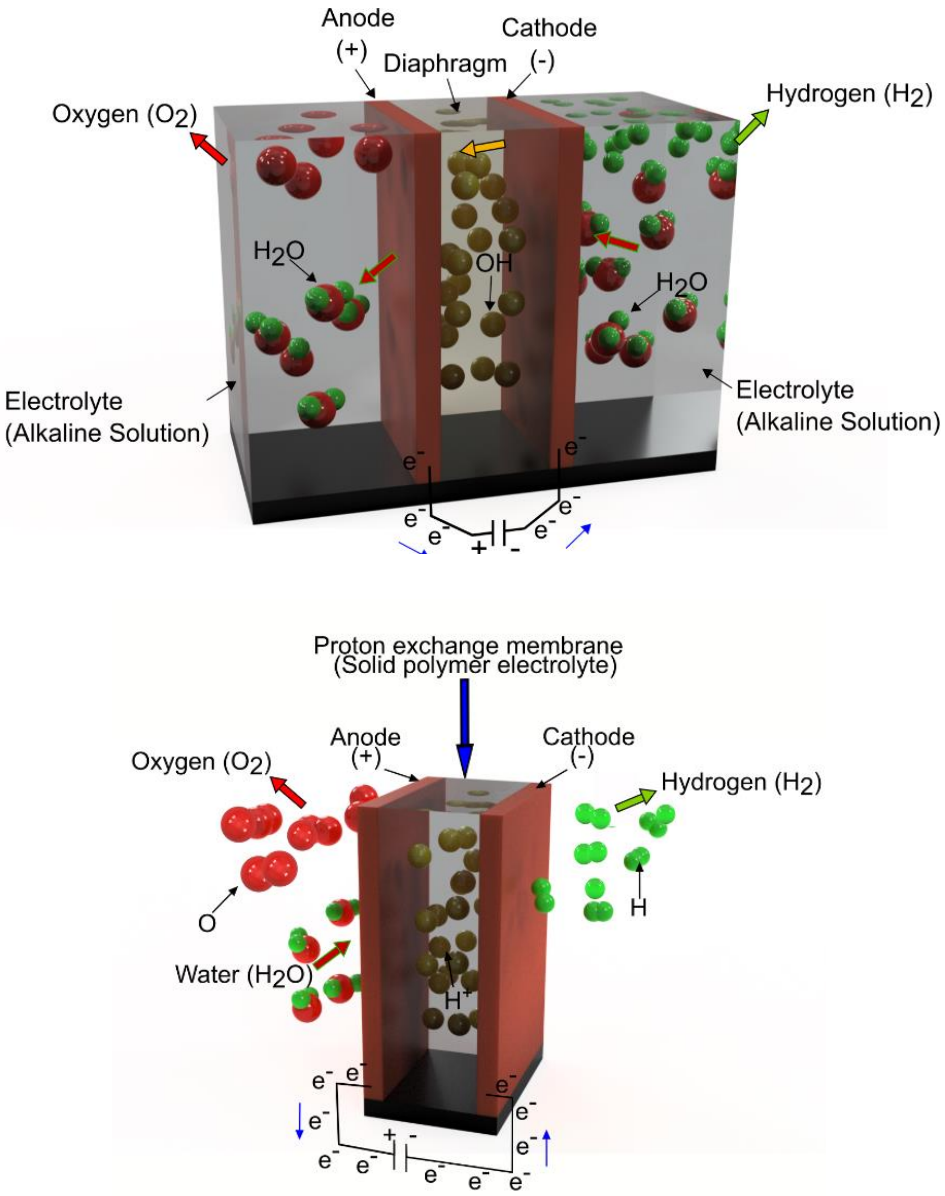

Figure 1: Alkaline water electrolyzer (top) and proton exchange membrane (PEM) electrolyzer (down).

II – OER electrocatalysts

The focus on the research has been drawn to substitute precious metal such as RuO_2 and IrO_2 to cheaper and abundant metals, which are able to function under highly oxidizing conditions, such as oxides from transition metals of Mn, Fe, Co and Ni. These oxides have been investigated in various forms: perovskite (ABO_3, A = alkaline- and/or rare-earth metals, B = transition metals), spinel ($A'B'_2O_4$, A' = alkaline-earth and/or transition metals, B' = group 13 elements and/or transition metals) and the layer structure type-family ($M(OH)_2$, MOOH and $LiMO_2$, M = transition metal). Non-oxides metals such as chalcogenides, pnictogenides and carbides (so-called as metal X-ide, where X refers to counter anions from groups 4-6, for

example C, N, P, S, Se and Te) have emerged as new interesting type of OER catalysts,[6] although it is still not clear whether the metal X-ide is the real catalyst or the catalytic behavior starts after it reaches an oxidized form, then the metal X-ide may be referred just as a pre-catalyst.

Many reviews have listed the numerous studies of OER catalysts that have been developed over several years; Roger and Symes focused on the first row transition metal cobalt, nickel, manganese, copper and iron catalysts produced by electrodeposition,[7] Gong and Dai listed catalysts such as alloys and oxides layered double hydroxides of nickel-iron, as well as NiFe containing another elements,[8] the group of Spiccia reviewed a long list of molecular catalysts based on complexes of manganese, iron, cobalt, copper and polyoxometallates, followed by metal oxides of manganese, cobalt, nickel.[9] More recently, the group of Sun revised the recent progress of the nickel-based oxides and oxy-hydroxides electrocatalysts.[10] In order to be able to objectively compare all these electrocatalysts for the OER and HER, the group of Jaramillo in 2015 established a protocol for organized them by activity and stability using standard methods under identical conditions (Figure 2).[11] This study of activity, short-term stability and electrochemically surface area comprises 18 catalysts for HER and 26 catalysts for OER deposited onto glassy carbon substrate, under harsh alkaline (1 M NaOH) or acidic (1 M H_2SO_4) environments to give a quick preliminary evaluation of the catalyst performance.

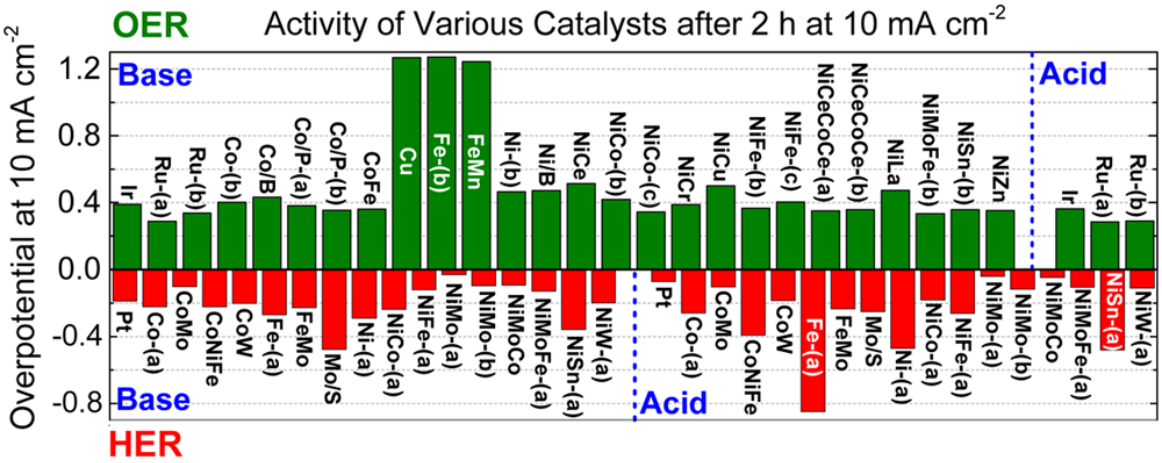

Figure 2: Various metal-based catalysts for both OER (26) and HER (18) reactions arranged by their overpotential at 10 mA cm^{-2} after two hour activity (reproduced from ref[11] with the permission from the American Chemical Society, Copyright 2015).

The catalysts were pictographically arranged based on the overpotential they presented at 10 mA cm^{-2} after two hours of catalytic activity. Although most of the earth abundant metal OER catalysts investigated showed overpotentials (η) between 0.3 and 0.5 V under alkaline

conditions, the study emphasizes the NiMoFe catalyst with the lowest overpotential of the study below 0.35 V even after 2h of electrolysis, which is comparable to the benchmark catalysts for OER, the iridium and ruthenium oxides. Catalysts with metal oxides and mixed metal oxides such as Co/P, CoFe, NiCo, NiFe, NiFeCoFe, NiSn and NiZn exhibit low overpotentials between 0.35 and 0.39 V, the list finishes with Co, NiCo and NiCr with overpotentials in the range of 0.40 and 0.45 V. Long-term stability of 24h for 12 of the set OER catalyst was also performed in the study, showing a great stability for Co, CoFe, NiCo, NiFe, NiMoFe, NiZn and Ru. Finally, the study highlights the lack of novel OER catalysts that sustain catalytic activity over time under acidic conditions. In summary and from a general point of view, a desirable electrocatalyst for OER has to present a low overpotential at 10 mA cm^{-2} (an overpotential below 0.4 V is desirable), with a stability that can last over 10 hours.[12] Additionally, Suen et al. have listed kinetic parameters such as Tafel slope, which provides valuable and detailed information concerning the mechanism of the reaction, especially for elucidating the rate-determining step: a smaller Tafel slope number implies good electrocatalytic kinetics.[13] Moreover, parameters of the catalyst performance have been identify by McCrory et al. such as mass activity in which current normalized per unit mass of catalysts.[1] Finally, electrocatalyst should ideally display high values of mass activity, turnover frequency (TOF) and faradaic yield which are about 1.0 A mg^{-1} and 1.0 s^{-1} and close to 100 % respectively, as well as a low Tafel slope below 60 mV dec^{-1}. Considering these figures of merit, the metal oxides containing nickel, cobalt, or a mixture of both metals along with iron are the most studied catalysts for OER due to their great electrocatalytic performance and their great stability under alkaline or weakly alkaline solution.

In the next section of this chapter, we will give a detailed description of the most relevant studies of these efficient OER catalysts reported in literature based on oxides of nickel, nickel/iron and cobalt which are directly in correlation with the nanocomposite materials developed in my PhD work presented in the Chapters II, III and IV.

III – Nickel oxide-based catalysts for OER

Among all materials mention above, nickel oxides and hydroxides have been widely studied as a material for OER, due to their promising performance and cost-effectiveness. $Ni(OH)_2$ can be prepared by many chemical or physical method: sol-gel processes, hydrothermal synthesis, chemical precipitation, vacuum evaporation, mechanical grinding,

sputtering, electrodeposition, etc. Depending on the method used and the experimental parameters, the obtained metal oxide can take different nanostructures such as hollow spheres, nanoplates, nanosheets, nanoneedles, nanorods and nanoparticles, making possible to control the physical and chemical properties of the surface of the metal oxide film. In this chapter we will focus on the electrochemical synthesis pathway (galvanostatic or potentiostatic), in which a nickel oxide film is electrodeposited on a conductive surface, such as glassy carbon or Fluorine doped Tin Oxide (FTO) electrode, by applying either an anodic or cathodic potential from an aqueous solution that contains a suitable nickel salt (usually nickel nitrate or nickel sulfate) or a nickel complex.

For electrodeposited nickel oxides, Bode diagram[14] is commonly accepted for the mechanisms of the charge and discharge of nickel oxide (Figure 3). Fundamentally, Bode diagram states that freshly prepared α-$Ni(OH)_2$ (Ni oxidation state 2.0 – 2.2), with an inter crystallographic plans distance of 8 Å, can be oxidized into γ-NiOOH (Ni oxidation state 3.5 - 3.7) in a more organized phase with an inter-planer distance of 7 Å.[15] These two phases can be transformed into a more crystalline β-$Ni(OH)_2$ form (Ni oxidation state 2.0 – 2.2) by aging process in an alkaline solution (treatment in 6 M KOH at 70-80 °C) or continuous charging/discharging process. Thus, this latter phase undergoes the loss of water molecules between the crystallographic planes leading to smaller inter-planer distance of 4.6 Å. The β-$Ni(OH)_2$ form can be oxidized into β-NiOOH (Ni oxidation state 3.0) by the same continuous

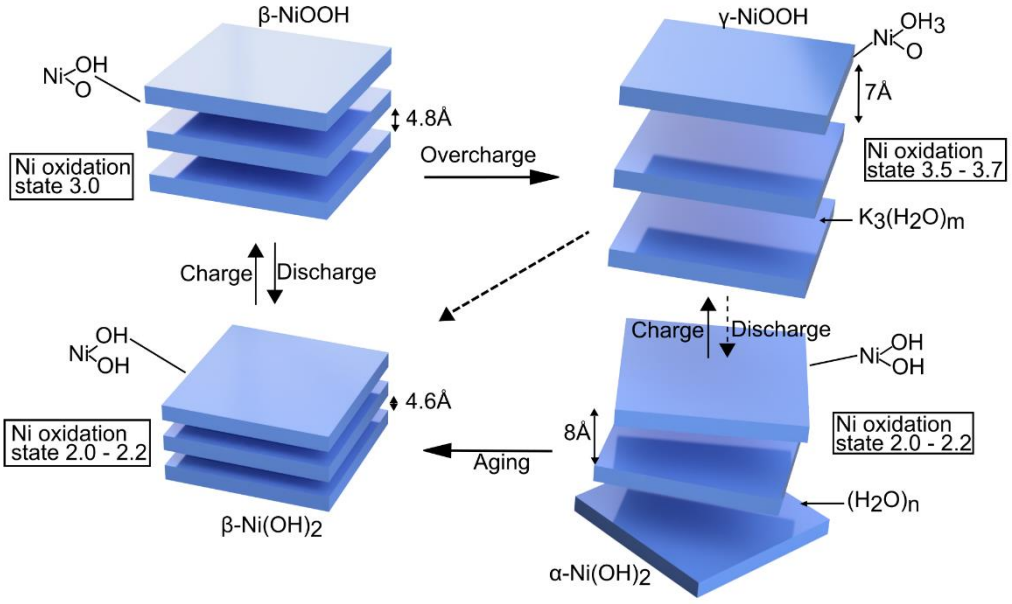

Figure 3: Bode's schematic representation for the cycle of Ni^{II} to $Ni^{III/IV}$ redox transition in nickel hydroxide layers (adapted from ref[15]).

charging/discharging process ascribed for α/γ transformation. The transformation from the oxidized form β- to γ-NiOOH take place by overcharging, in which all the active material has been transformed into charge state and the charge current is directed towards gas production from the electrolyte in the cell.[16] The large increase of the inter-planer distance (from 4.8 to 7 Å) caused by the overcharging outlines the damage caused by the process.

Lyons and coworkers[17] were able to show the different wave shapes of the cycling voltamograms, resulted in films prepared at different sweep rates. The films were deposited by sweeping 30 times with scan rates of 10, 20 or 50 mV s^{-1} for nickel oxide deposited onto an Au electrode from a 1.0 M NaOH solution (Figure 4). As it can be seen in Figure 4, the timescale for deposition can affect the nature of the nickel oxide film. They labeled the α/γ-Ni(II/III) and β/β-Ni(II/III) redox transitions (described Bode's diagram, Figure 3), and attributed an effect of dehydration on doublets shown on the cyclic voltammograms (CVs) of the set of β/β. Furthermore, it was proven that the chemical nature of the support also plays an important role on the clear visualization of the redox transitions of the nickel oxide on the CV. Nickel oxide deposited under the same parameters on Au, C and Pt displays different electrocatalytic activities, being Au the clearest with the greater catalytic activity, apparently because of its better electronegativity.

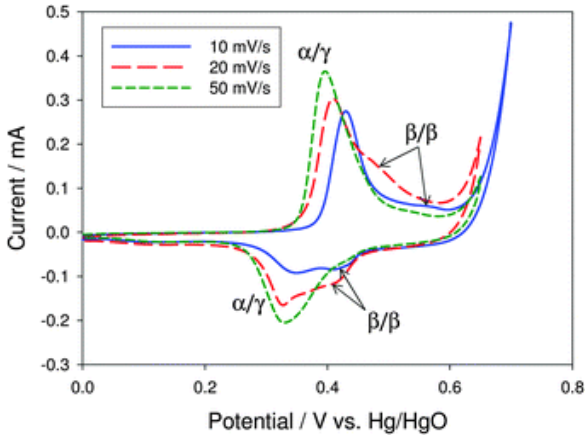

Figure 4: Cyclic voltammograms recorded in 1.0 M NaOH at 40 mV s^{-1} for an Au electrode modified with nickel hydroxide films deposited using 30 growth cycles performed at a sweep rate of 10, 20 and 50 mV s^{-1} (reproduced from ref[17] with the permission from the Royal Society of Chemistry, Copyright 2013).

Nocera and workers[18] confirmed the growth of a surface-deposited material on a glassy carbon electrode. The film was deposited by cycling in a 0.1 M potassium borate (K-Bi) buffered solution in mild alkaline conditions (pH 9.2), which contained 1 mM of nickel nitrate as Ni^{2+} source. This growth process was evidenced by the appearance of a broad cathodic signal

in the return scan from the catalytic wave at 0.87 V *vs* NHE (Normal Hydrogen Electrode), attributed to the reduction of deposited material (Figure 5). Subsequently, a sharp anodic peak appears at 1.02 V, while the catalytic wave experiences a positive shift during cycling at a scan rate of 50 mV s^{-1}. The amplitude of the anodic and cathodic peaks increases when the number of scans keep progressing. After 20 scans, the estimated thickness of the deposited material corresponds to 10-12 layers and each monolayer has a surface density of 5 Ni atoms/ 25 Å, by integration of the charge of the anodic peak. In addition, this behavior was not observed when $NaNO_3$ electrolyte was used instead of borate salt, since the signal of the nickel solution is indistinguishable from the background of the glassy carbon. This suggests that a proton-accepting electrolyte such as borate is needed for performing this facile electrodeposition and catalysis. As the CV features are very similar of those of nickel oxide thin films, a study on the pH dependence was performed by plotting the potentials of anodic and cathodic peaks ($E_{p,a}$) in function of the pH, using catalysts films deposited by 13-15 CV scans on glassy carbon electrodes. The slope obtained suggested that the Ni-Bi system undergoes a loss of 1 e^- accompanied by a transfer of ~1.5 H^+ instead of the 1 e^- and 1 H^+ redox couple assigned for the anodic pre-feature centered at ~0.65-1.25 V for Ni oxides (-96 mV pH $unit^{-1}$, instead of the -59 mV pH $unit^{-1}$ expected for 1 e^-/1 H^+ process). To test the morphology and composition of the Ni-Bi material, Ni-Bi films with a thickness of 3-4 µm were electrodeposited on indium tin oxide (ITO) electrodes by a bulk electrolysis at 1.3 V *vs* NHE with a charge of 10 C cm^{-2}. Scanning electron microscopy (SEM) on the film exposed a smooth and amorphous surface, while elemental analysis of the film dried in air revealed a $Ni^{III}O(OH)_{2/3}(H_2BO_3)_{1/3}$•1.5 H_2O formula. These characterizations confirm that the film is composed by nickel oxy(hydroxide) and borate anions. The current density for OER was then analyzed from films electrodeposited with a charge of 300 mC cm^{-2} in which it was necessary to perform a preconditioning electrolysis step by an applied current density of 1.4 mA cm^{-2} for 12 hours. The Tafel plot was performed with current

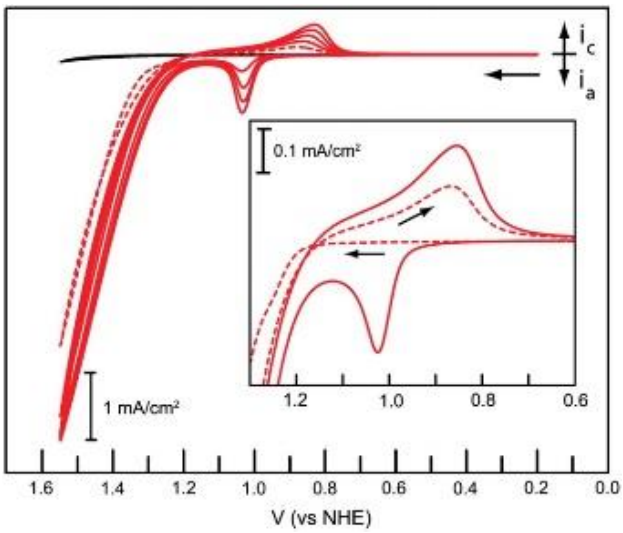

Figure 5: Successive cyclic voltammetry scans recorded at glassy carbon in 0.1 M Bi electrolyte (pH 9.2) in presence (red) or absence (black) of 1 mM Ni^{2+} (scan rate 50 mV s^{-1}). Inset: first (dashed line) and second (solid line) CV scans (reproduced from ref[18] with the permission from the National Academy of Sciences, Copyright 2012).

densities between 1 mA cm^{-2} to 7 µA cm^{-2} and gave a slope of ~59 mV dec^{-1}, which is consistent with typical Tafel slopes obtained with nickel oxides (40-80 mV dec^{-1}). No preconditioning lead to films with slopes than can reach up to 120 mV dec^{-1}, making the preconditioning step essential for obtaining reproducible and active Ni-Bi films. This study highlighted the stability of very thin films of Ni-Bi under cathodic bias (up to 100 CV cycles below the catalytic wave) and opened the possibility to use this catalyst film for oxygen reduction.

Further studies were performed on this OER catalyst with slightly different conditions, aiming to obtain thinner and more uniform films.[19] These films were obtained by electrodeposition under controlled potential electrolysis (CPE) at 1.15 V *vs* NHE with a charge of 1 mC cm^{-2}, from a solution of 0.1 M K-Bi (pH 9.2) containing 0.4 mM $NiNO_3$. As mention above, an anodization treatment (pre-conditioning) was necessary to activate the nickel centers and to obtain active nickel oxide films. Anodization of the electrodeposited nickel oxide films was performed by applying a potential of 1.1 V *vs* NHE in 1.0 M K-Bi (pH 9.2) from a few minutes to 4 hours, resulting in an improvement of the catalytic activity that can reach up to almost three orders of magnitude. The use of a more concentrated buffer solution (1.0 M KBi) in this step is required as anodization using 0.1 M KBi resulted in a very gradual increase in the current density over time, with no observed plateau in the activity after 3 h. This dependence could be explained by an intercalation of potassium ions between the NiO_2 sheets in the Ni-Bi films during the formation of γ-NiOOH from the alkali cation-free β-NiOOH throughout anodization (see Figure 3). From X-ray absorption near edge structure (XANES), the Nocera's group obtained similarities in the spectra of γ-NiOOH and anodized Ni-Bi films poised at 1.0 V *vs* NHE, while fully reduced Ni-Bi film maintained at a potential of 0.4 V matches with the spectra of $Ni(OH)_2$ with an oxidation state of +2. This trend could confirm a significant Ni^{IV} content with a mean of oxidation state of nickel centers of +3.6 in the anodized films, which is consistent with the results obtained by coulometric studies. From extended X-ray absorption fine structure (EXAFS) data, the authors proposed that the anodized nickel films

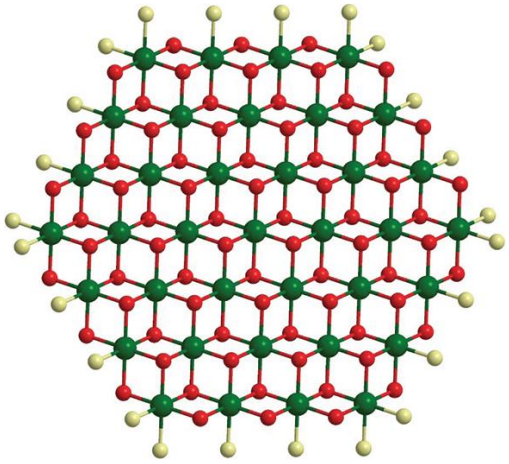

Figure 6: Simplified hexagonal cluster model of Ni-Bi with an average size of between 2 and 3 nm. Ni ions are shown in green, bridging oxo/hydroxo ligands are shown in red, and nonbridging oxygen ligands, which may include water, hydroxide, or borate, are shown in pale green (reproduced from ref[19] with the permission from the American Chemical Society, Copyright 2012).

exhibit structural features of γ-NiOOH, where Ni^{IV} atoms are coordinated by bis-oxo/hydroxo bridging ligands within layers of octahedral edge-sharing NiO_6 with a domain of *ca.* 2 nm (Figure 6).

Yoshida et al[20] focused on further characterizations on Nocera's Ni-Bi electrocatalyst by O K-edge X-ray absorption fine structure (XAFS). In this study, this electrocatalyst forms a μ-oxo/hydroxo nickel centers organized into higher order domains of edge-sharing NiO_6 octahedral with β-NiOOH structure at higher potential. The formation of this NiO_6 octahedral can be monitored by the direct observation of the oxygen species in Ni-Bi thin film, like the one of β-NiOOH, which corresponds to the peak at 528.7 eV. As shown in the Figure 7, the authors remark that the appearance of the peak at potentials above 0.6 V *vs* Ag/AgCl, followed by its persistence when the potential decreases, indicates that the generated NiO_6 octahedral was not easily reduced to Ni^{2+} species.

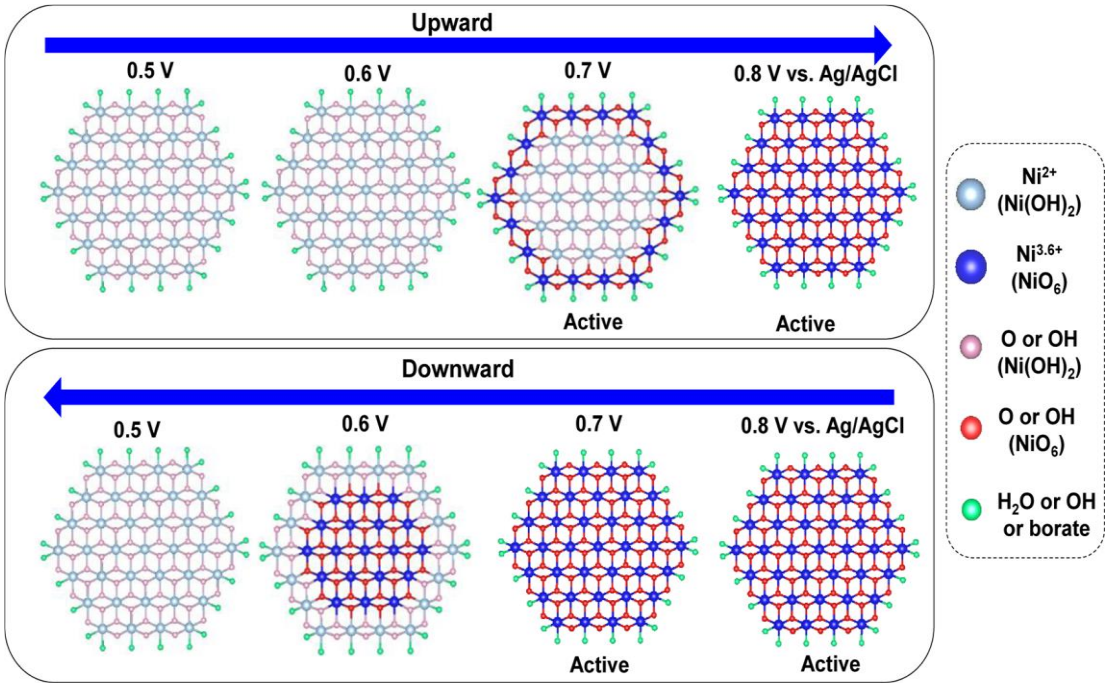

Figure 7: Schematic model for nickel nanocluster in the Ni-Bi electrocatalyst during OER catalysis in KBi aqueous solution with the electrode potential swept upward and downward (reproduced from ref[20] with the permission from the American Chemical Society, Copyright 2012).

However, no changes were observed in the catalytic current for OER during the upward and downward scans. These observations implicate that the interior of the NiO_6 cluster does not act as an OER catalytic site.

Another nickel source for nickel oxide electrodeposition proposed by the group of Spiccia,[21] that has been extensively studied is Ni(II)-amine complexes. The $[Ni(en)_3]^{2+}$ complex (en = 1,2-diaminoethane) was compared with other nickel amine complexes such as $[Ni(NH_3)_6]^{2+}$ and with $[Ni(OH_2)_6]^{2+}$. The electrodeposition on glassy carbon electrodes was performed by constant potential electrolysis (CPE) at +1.1 V *vs* Ag/AgCl, from 0.1 M sodium borate (NaBi) buffer solutions at pH 9.2 containing 1 mM of the nickel complex (Figure 8(a)). The best catalytic activity was obtained with nickel oxide films obtained from $[Ni(en)_3]^{2+}$, denoted NiO_x-en, which generated a current density that increased up to 1.8 mA cm^{-2}, when applying a potential of +1.1 V for 2 hours. The NiO_x-NH_3 and NiO_x-aqua films, generated from $[Ni(NH_3)_6]^{2+}$ and $[Ni(OH_2)_6]^{2+}$ respectively, only reached a current of 1.2 mA cm^{-2} under the same conditions. In addition, scanning electron microscopy (SEM) images revealed that NiO_x-en films were more homogeneous (Figure 8(b)), and by capacitance measurements it was determined that they have a higher electroactive surface. Finally, X-ray absorption spectroscopy analysis (XAS) also revealed that NiO_x-en films correspond to a γ-NiOOH phase.

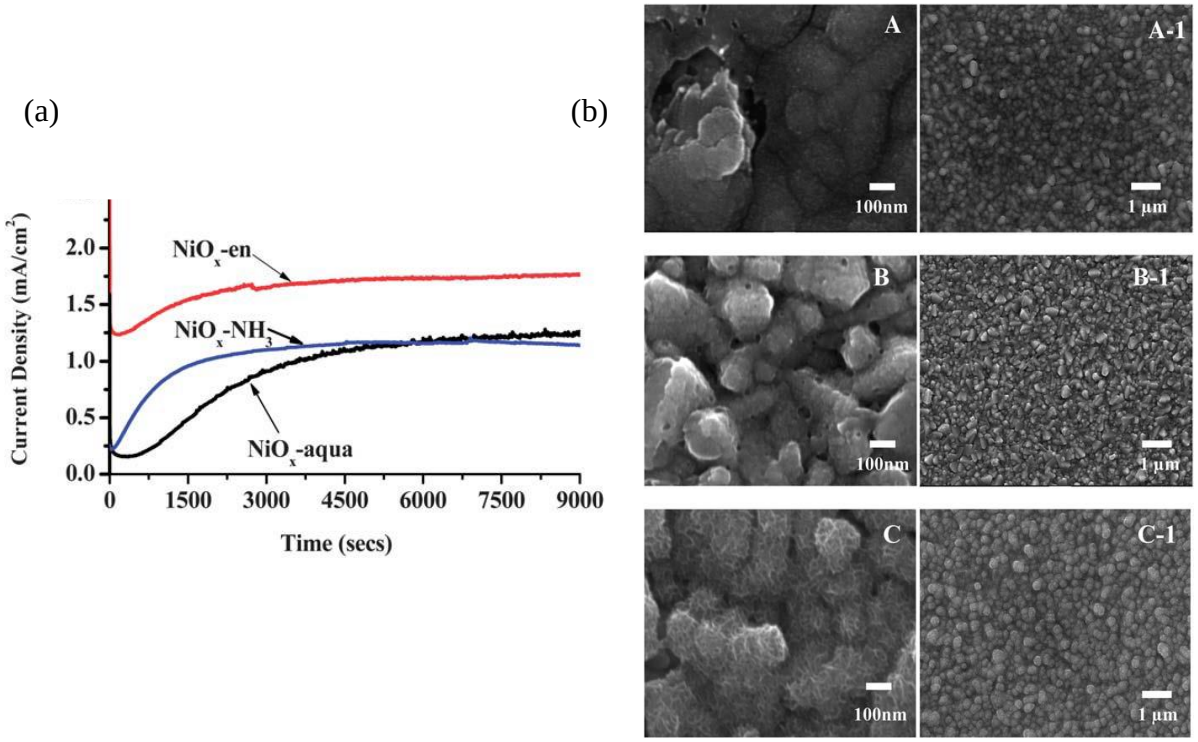

Figure 8: (a) current density trace for NiO_x-en (red), NiO_x-NH_3 (blue) and NiO_x-aqua (black) films deposited on FTO conducting glass; (b) high (left) and low (right) magnification SEM images of NiO_x-aqua (A, A-1), NiO_x-NH_3 (B, B-1) and NiO_x-en (C, C-1) films deposited on FTO electrode (reproduced from ref[21] with the permission from the Royal Society of Chemistry, Copyright 2013).

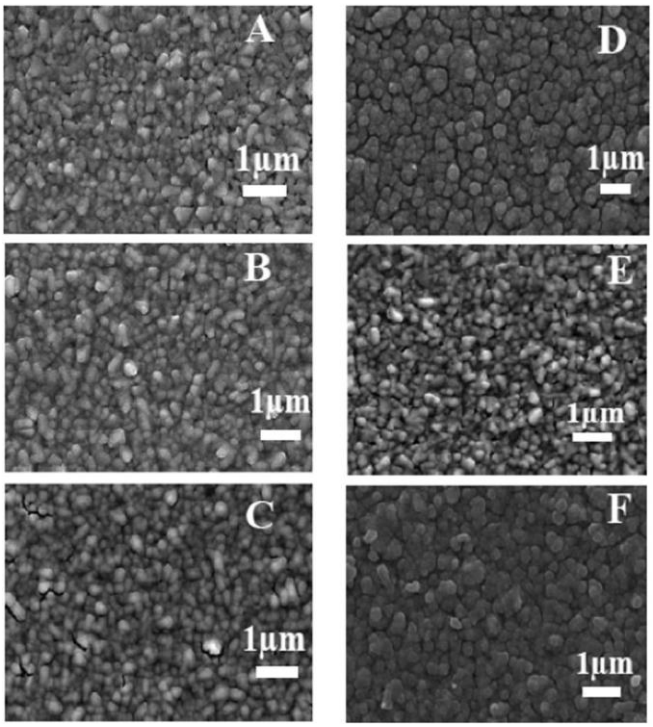

Figure 9: SEM images of freshly prepared tacn-Bi (A), cyclen-Bi (B), SWtacn-Bi (C), SWtacn-OH (D), films; (E) and (F) show the SWtacn-Bi and SWtacn-OH films after 30 minutes of CPE testing in 0.60M NaBi buffer (reproduced from ref[22], with the permission from the Royal Society of Chemistry, Copyright 2013).

Considering that the complex precursor $[Ni(en)_3]^{2+}$ gave very homogeneous and well-adherent NiO_x films compared to $[Ni(OH_2)_6]^{2+}$, three macrocyclic nickel(II) amine complexes, namely, $[Ni(tacn)_2]^{2+}$, $[Ni(tacn)(OH_2)_3]^{2+}$ and $[Ni(cyclen)(OH_2)_3]^{2+}$ (where tacn = 1,4,7-triazacyclononane and cyclen = 1,4,8,11-tetraazacyclotetradecane) were also tested by the group of Spiccia for the electrodeposition of NiO_x films from borate buffer at pH 9.2 and NaOH buffer at pH 12.9.[22] The authors showed that this type of precursors offer an advantage in solubility and stability allowing to work under a wider operational conditions. NiO_x films were electrodeposited from these macrocyclic Ni(II) amine complexes (*i.e.* through their electro-induced decomposition on glassy carbon and FTO electrodes by applying a constant potential of +1.1 V *vs* Ag/AgCl in the case of NaBi buffer and +0.75 V vs Ag/AgCl for NaOH solution. According to SEM images (Figure 9), all complexes gave very homogeneous films with well-defined grain boundaries, even after 30 min of water oxidation electrocatalysis. The NiO_x film electrodeposited from $[Ni(tacn)_2]^{2+}$ in a NaBi buffer (denoted SWtacn-Bi), was also characterized by Raman spectroscopy. The Raman spectrum showed two strong peaks at 481 and 558 cm^{-1} characteristics to the γ-

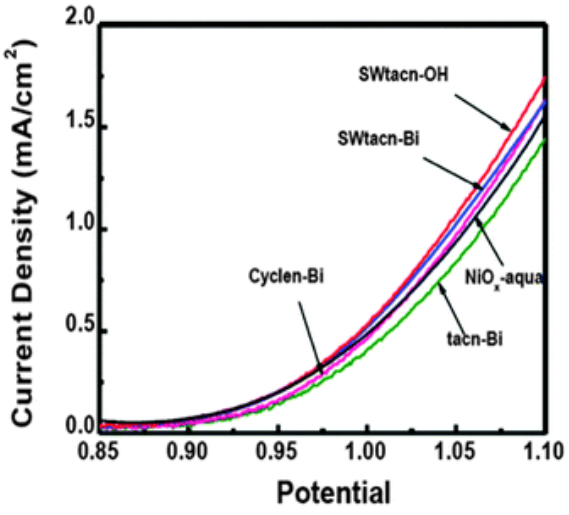

Figure 10: Linear scan voltammograms for nickel oxide films derived from each macrocyclic nickel(II) complex and $[Ni(OH_2)_6]^{2+}$ recorded in NaBi buffer at a scan rate of 1 mV s^{-1} (reproduced from ref[22], with the permission from the Royal Society of Chemistry, Copyright 2013).

NiOOH phase. Despite the fact that no bands were found in the IR spectrum to suggest the incorporation of borate in the films, the role of this buffer may be to promote the movement of protons and anions species in response to changes in nickel oxidation state and proton release through water oxidation. The activity of these films was similar, and it was suggested that all films are equally efficient catalysts for water oxidation by comparing their linear scan voltammetry (Figure 10) and Tafel slope in NaBi buffer (100-110 mV dec^{-1}). However, in this study, it is not known if the OER boost is inherent to the nickel material or due to an external factor such as iron doping (see below).

IV– Nickel-iron oxide-based catalysts for OER

The groups of Tichenor[23] in the 50s, Troilus[24] et al in the 60s, Radniecka[25] and Corrigan[26] et al. in the 80s were the first to report the beneficial effect of the intentional or involuntary introduction of iron within nickel oxide films (as low as 1 ppm) on their OER activity, particularly with thin metal oxide films. Since these pioneer works, many groups have been interested in developing mixed nickel/iron oxides ($NiFeO_x$), due to their high activity at low overpotentials under alkaline conditions. Indeed, $NiFeO_x$ oxides are currently considered among the best OER electrocatalysts of literature, with an activity comparable to the benchmark noble metal-based catalysts RuO_2 and IrO_2. Several synthetic methods have been explored in literature to prepare $NiFeO_x$-based anodes, such as solvothermal deposition, co-precipitation and electrodeposition, to obtain various nanostructured morphologies like nanoparticles, nanosheets, nanocages, nanoplates, nanotubes and nanorods.[8,27–30] This section will essentially focus on the $NiFeO_x$ material synthesis by electrodeposition, which remains among the easiest method to prepare OER anodes of metal oxides.

The group of Boettcher reinvestigated the effect of iron within NiO_x on the OER electrocatalytic activity, especially in KOH electrolyte which naturally contains iron. To that end, they developed an easy way to purify the KOH electrolyte by simply adding highly pure $Ni(OH)_2$ powder, which readily absorbs Fe impurities and, therefore, they were able to study properly the authentic OER catalytic activity of a nickel film free of iron (Figure 11).[31] They compared the electrochemical behavior of cathodically deposited (-0.1 mA cm^{-2} for 120 s) $Ni(OH)_2$/NiOOH films in KOH electrolyte without purification: the ratio of Ni/Fe measured by X-ray photoelectron spectroscopy (XPS) was 95:5 with an enhanced OER activity only after 5 CV cycles. In addition, a rotating disk electrode coated with a pure NiO_x and dipped in a KOH

solution during 12 min with a rotation of 1500 rpm and without applying a potential, exhibits a Ni/Fe ratio of 98:2 and catalytic activity. In the case of the $Ni(OH)_2$/NiOOH films deposited and tested in the pure KOH electrolyte, there is no enhanced OER activity (>400 mV) and no addition of Fe was observed after 300 CV cycles. By this way, for films which contained co-deposited iron, $FeCl_4$ was added in different concentrations to the purged solution nickel that was held in a concentration of 0.1 M.

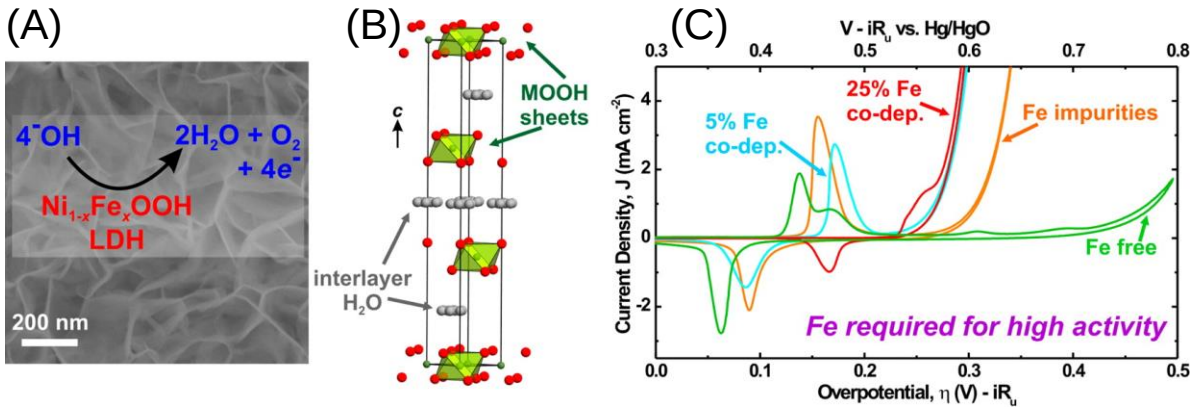

Figure 11: (A) SEM image of $Ni_{0.75}Fe_{0.25}(OH)_2$ films as-deposited in a 1 M KOH electrolyte. (B) Crystal structure of NiFe-LDH (fougèrite-like) viewed roughly along the [110] direction; Red = OH, blue = Ni^{2+}, green = Ni^{2+}/Fe^{3+}, gray = water. (C) Cyclic voltammograms of NiO_x films deposited on Au/Ti electrode with various amounts of iron and recorded in a pure 1 M KOH electrolyte (scan rate of 10 mv s^{-1}). Potentials are given *versus* Hg/HgO, which can be converted to the Ag/AgCl reference by adding 0.097 V (reproduced from ref[31], with the permission from the American Chemical Society, Copyright 2014).

These results confirm that, in previous reported studies, the relatively high OER activity of NiO_x catalysts is most likely due to an unintentional contamination with Fe impurities from the electrolyte. Additionally, by gazing induced X-ray diffraction (GIXRD), patterns of β-$Ni(OH)_2$ arrangement were observed in the case of a Fe-free $Ni(OH)_2$ film after aging in KOH over 24h. In the case of the film elaborated by co-precipitation with Fe, $Ni_{0.75}Fe_{0.25}(OH)_2$, the film converts into layered doubled-hydroxide conformation (NiFe-LDH) through the process of aging. This type of organization is characterized by an increase in intersheet spacing compared with β-$Ni(OH)_2$, that could facilitate $^-OH/O_2$ transport throughout the film. Although, it is expected to observe a change in the electrochemical behavior with different ratios of Ni:Fe, between 5% and 25% in Fe content, the OER activity of the film is not affected. Therefore, the catalytic activity is inherent to the mixed Ni-Fe oxyhydroxide sheet and not to the structural defects within the $Ni_{0.75}Fe_{0.25}(OH)_2$. In addition, if all films showed an increased crystallinity upon aging, only those exposed to iron exhibit an increased OER activity, demonstrating that

β-NiOOH is not intrinsically more OER active than γ-NiOOH as previously thought, but β-NiOOH is more active because of the presence of Fe impurities.

Another aspect that the authors investigated was the effect on the electric conductivity that the film experienced when Fe is introduced. As Corrigan hypothesized, an increase of conductivity might explain the enhanced activity of $Ni_{1-x}Fe_xOOH$ relative to NiOOH. While the conductivity of all reduced films was measured to be low, independently of the Fe quantities, the conductivity of oxidized films increased more than 30-fold with iron co-precipitation. However, this is not sufficient to explain the enhanced activity when Fe is introduced. Finally, the authors measured the electrocatalytic activity of the $NiFeO_x$ film (in term of turnover frequency, TOF) in function of its thickness on Au and glassy carbon electrodes. In principle, partial exchange transfer between iron and $Ni^{3+/4}$ that has been proposed by Corrigan.[26] If the iron exerts a similar electron-withdrawing effect on Ni as does the gold substrate, the group of Boettcher assumed that the thickness-dependence of the OER TOF for NiOOH on Au would be diminish after iron in incorporated. They showed that the TOF values remain almost constant with the increase of thickness. This result is consistent with the hypothesis of Corrigan[26] which suggests that throughout $NiFeO_x$ films, Fe^{III} undergoes a partial-charge-transfer activation effect on Ni, similar to that observed for noble-metal electrode surfaces.

To further investigate the Fe impurities present on different reported nickel oxide films, the group of Boettcher analyzed the Fe content of Nocera's Ni-borate (NiB_i) OER catalyst operating at pH 9.2[32], in which anodic conditioning in KOH electrolyte was required to reach the film's most active form[18]. Indeed, as we discussed above, the unintentional Fe incorporation also may play an important role in the high activity of the Ni-Bi system. On a gold-coated glass-slide electrode, a film of Ni oxy(hydroxide) was electrodeposited by applying a potential of 0.909 V *vs* SCE until 10 mC was passed from a borate buffer at pH 9.2 containing 0.4 mM $Ni(NO_3)_2$, followed by anodic conditioning (2, 5, 15, 30, 120 min at 0.856 V vs SCE) in 0.5 M potassium borate (KB_i) electrolyte at pH 9.2 with different Fe traces (approximately 0, 0.1 and 1 ppm). As expected, the OER activity increased in function of the quantity of Fe impurities present in the electrolyte as well as the conditioning time. For example, after 2 h of conditioning in the lowest purity electrolyte, the Fe content throughout the film reached 14 % relative to the nickel amount measured by XPS. When iron is co-deposited with nickel from a solution containing $Ni(NO_3)_2$: $FeCl_3$ at a ratio 9:1, the iron content reached 21 % and the conditioning time is reduced from 2 h to 30 min. Furthermore, the intrinsic activity of the different catalysts

was determined by the comparison of the turnover frequencies (TOFs) and Tafel slopes. The activity of Ni-Bi films remained constant regardless the anodic conditioning in presence of a Fe-free electrolyte (TOFs ~ 0.025 s^{-1}) and increased dramatically once the Fe is co-deposited (TOFs ~1.4 s^{-1}). Additionally, Tafel slope of an unconditioned co-deposited Ni-Fe film had a similar catalytic activity as the conditioned Ni-Bi (56 and 46 mV dec^{-1}, respectively), suggesting a similar OER mechanism involving iron, in contrast of the Fe-free Ni-Bi film (73 mV dec^{-1}).

While the role of Fe in the NiOOH film is yet not understood and it was thought that the enhanced electric conductivity of the Ni-film promoted by the Fe was responsible of the increase of OER activity, another factors are likely to be involved in the increase of OER activity. Currently, the discussion is focused on whether the active site is Fe^{4+}, Fe^{3+} or Ni^{4+}. By this means, a recent report involving the Fe impurities in the electrolyte was published by Song and coworkers.[33] A nickel foam (NF) was used as the support and the incorporation of Fe ions was performed by 100 CV cycles (between 1.21 to 1.54 V vs RHE) in a 1 M commercial KOH solution which contains 0.18 mg L^{-1} of Fe measure by Inductively couple plasma mass spectrometry (ICP-MS)). This simple procedure increased the modest activity of the NF by loading it with 4.3 µg cm^{-2} of Fe. The amount of iron increased to 14.3 µg cm^{-2} by immersing the NF into 10 wt % of hydrochloric acid for 30 min (denoted as NF-AC) to obtain a rougher surface before cycling in the 1M KOH electrolyte. To further enhance the Fe content, the NF-AC was dipped in a 0.01 M $FeCl_3$ solution for 15 min (denoted as NF-AC-FD). The average TOF calculated for NF-AC-NiO_x-Fe in 10 electrodes (4.4 - 14.1 µg/cm^{-2}) was of 0.78 s^{-1} at η = 270 mV; while characterization by Raman spectroscopy revealed signals that corresponds to those of γ-NiOOH under OER conditions. However, no Fe signals were observed by this technique. Operando XAS data revealed nanoclusters of γ-FeOOH covalently linked to γ-NiOOH *via* bridging oxygen atoms. According to DFT calculations, the group suggested that the structure may allow a mechanism in which iron acts as the oxygen evolving center and a nearby terrace O site on the γ-NiOOH support oxide as a hydrogen acceptor.

Louie and Bell gave a detailed study of the structure and electroactivity of electrodeposited thin Ni-Fe films on Au substrate using *in-situ* Raman spectroscopy.[34] Films were deposited at a constant current density of 50 µA cm^{-2} during 1125 s in alkaline electrolytes. Ni-Fe films containing 40% of Fe present the highest catalytic current densities which are 2 and 3 orders of magnitude higher than that of individually deposited Ni and Fe films (Figure 12(a)). The CV of Ni films showed a progressive decrease of the oxidation peak

intensity of the electrochemical redox process $Ni(OH)_2/NiOOH$ with the increase of Fe content (at 41 % Fe, the oxidation peak is no longer visible), along with the anodic shift of this redox process, consistent with previous reports.

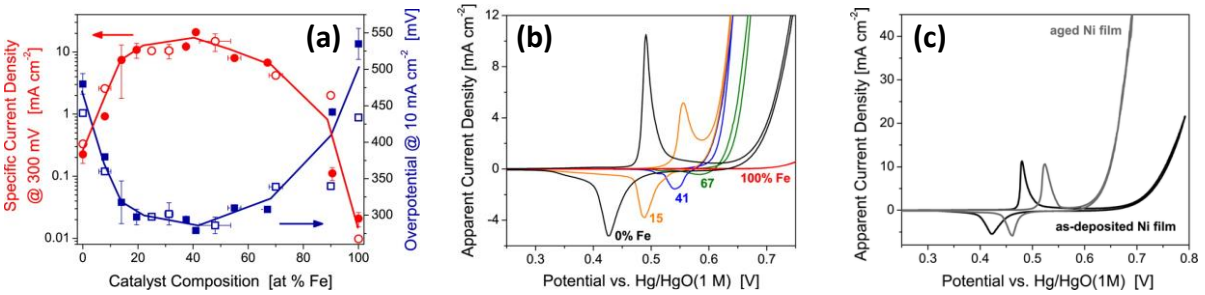

Figure 12: (a) OER activity of Ni-Fe films in 0.1 M KOH at 300 mV overpotential and 10 mA cm^{-2} current density, in function of Fe content. Filled and open marks correspond to measures recorded at rotating and stationary gold working electrode for which electrodeposited films are 70 and 25 nm thick, respectively. Cyclic voltammograms (b) of NiO_x (black), $NiFeO_x$ (15% Fe: orange; 41% Fe: blue; 67% Fe: green) and FeO_x (red) films, and (c) as-deposited (black) and aged NiO_x films (grey) on Au electrode in 0.1 M KOH at 10 mV s^{-1} and 2400 rpm (reproduced from ref[34], with the permission from the American Chemical Society, Copyright 2013).

In the same way, aging Ni films in 0.1 KOH electrolyte over 24 h also causes a drastic increase of its OER activity (20 times more) and a positive shift of the $Ni(OH)_2/NiO(OH)$ process (Figure 12(c)), in contrast to what is reported, the authors do not attribute this increase by Fe poisoning from the electrolyte, since the concentration of the freshly deposited and aged films are comparable and close to the detection limit for elemental analysis. Characterizations by *in-situ* Raman spectroscopy of Ni and Ni-Fe films under OER conditions have shown that the two bands attributed to Ni–O vibrations for NiOOH (~ 480 and 560 cm^{-1}) are inverted in their relative intensity. The implication of this alteration on the Raman spectra is attributed to change of phase of the Ni film from γ-NiOOH to β-NiOOH when Fe is present in the film, even at a content as low as 20 %, along with evidence that the films display some degree of disorder, especially those that exhibit high OER activities. Finally, the authors demonstrated that mixed Ni-Fe films (containing up to 95% of Fe) and Ni aged films present the same Tafel slope (40 mV dec^{-1}) and reaction order of one in OH^-, which means that both catalysts share a common rate-limiting step within the OER mechanism.

Bell and coworkers carried on their investigation on mixed NiFe oxide analyzing its structure by *in-situ* XAS using high energy resolution fluorescence detection (HERFD). Thinner films were used (deposition at constant current density of 50 µA cm^{-2} for 20 s) to avoid the formation of metallic byproducts of Ni and Fe that were detected on thicker films.[35] The authors succeeded in identifying the OER active site in $Ni_{1-x}Fe_xOOH$, as the Fe center, instead

of a Ni center, which is most commonly supposed. HERFD-XAS allowed studying the local electronic environment of nickel and iron centers in the mixed oxide. They showed that the increase of potential applied on $Ni_{1-x}Fe_xOOH$ induces changes in the oxidation state and in metal-to-oxygen bond distance. Gonzalez-Flores and coworkers[36] observed a similar behavior with their NiFe-based OER catalyst. The latter was cathodically electrodeposited on carbon paper by applying a constant current of -250 mA cm^{-2} from a nickel and iron containing acidic buffered solution (9 mM $NiSO_4$, 9 mM $FeSO_4$, 9 mM $(NH_4)_2SO_4$ at pH 2.5). After conditioning the films at 1.50 V *vs* RHE for 20 minutes, *in situ* XANES and EXAFS characterizations were performed. A redox transition of Ni^{2+} to Ni^{3+} was confirmed when the applied potential increases from 1.23 to 1.5 V *vs* RHE. Moreover, a mixture of phases α-$Ni(OH)_2$/γ-NiOOH were found in a ratio of 1:1 at 1.23 V *vs* RHE, and the predominant phase was γ-NiOOH at 1.5 V *vs* RHE on the NiFe film. In the case of iron, applying the same conditions, small changes may suggest changes in the Fe^{3+} coordination environment rather than a change of oxidation state from Fe^{3+} to Fe^{4+}. Time-resolved X-ray data excludes that changes in the Fe ligand environment occur before or after Ni redox reaction but indicates that these occur simultaneously.

Most groups have used a conditioning process to enhance the OER activity of the NiFe films. Despite the different conditions of the electrodeposition, the catalysts seem to share similarities after conditioning. Following this notion, the group of Smith[37] characterized two Ni-based oxygen evolution catalysts: nickel iron borate (Ni(Fe)-Bi) and nickel iron oxyhydroxide (Ni(Fe)OOH). The electrodeposition of these catalysts on FTO was carried out by both potentiostatic (1.7 V vs RHE, for a period time that ensured 20 monolayers of coverage) and galvanostatic way (10 µA for Ni(Fe)-Bi and -10 µA for Ni(Fe)OOH), from a 0.5 mM aqueous solution of $Ni(NO_3)_2$•$6H_2O$ in 0.5 M KBi at pH 9.2 for Ni(Fe)-Bi, and a 5 mM aqueous solution of $Ni(ClO_4)_2$•$6H_2O$ in 0.1 M KCl for Ni(Fe)OOH. The group focused on the nickel acknowledging the presence of iron impurities, as was extensively studied in the previous reports mentioned above, but they do not give further details such as the Fe content. Characterizations by Surface Enhanced Raman (SER) spectroscopy and XAS, evidenced a chemically similarity for both catalysts studied. Furthermore, XPS experiments have shown that the small differences observed between these two catalysts disappear after the electrochemical conditioning process. There is a strong pH-dependency in this study that suggests that the "active oxygen" is formed *via* deprotonation of the nickel oxy-hydroxide to produce a negatively charge nickel oxide ($NiOO^-$). Taking this work in consideration, Nocera and co-worker concluded that iron doping influences the nickel on its valency, acting like a

Lewis acid.[38] The maximal mixed-valence resting state of $Ni^{3.6+}$ was achieved by only doping the NiBi film with 4% of Fe content, further percentage of iron do not increased the nickel valency. The authors also observed by a cross-sectional elemental analysis that in thicker films (~1 µm) the distribution of the iron on the NiBi film was more homogeneous by a co-deposition than anodized NiBi films in reagent KOH with traces of iron, in which the predominant distribution of iron was in the outermost ~100 nm of the catalyst film. This homogeneity may offer an insight upon the apparently high OER activity in the co-deposited films. Electron energy loss spectrometry (EELS) measurements on $Ni^{II}O$, $Ni^{II}(OH)_2$, $LiNi^{III}O_2$ and γ-$Ni^{III/IV}OOH$ revealed a pronounced increase of the pre-edge feature peak centered at 530 eV, related with the covalency of M-O bonds, with the increasing oxidation state of nickel. The authors explained that increasing Ni^{4+} population with iron incorporation is beneficial to the catalytic OER activity, because it leads to a greater Ni-O valency, and thus a greater oxyl character (formal oxidation state of Ni(IV)-oxo possesses a significant Ni(III)-$O^{\bullet}$), which can lead in increased OER activity.

The group of Halaoui[39] investigated the effect of co-precipitation of Fe with Ni in NiFe-Bi films on borate buffer. Films were electrodeposited at 0.953 V *vs* Ag/AgCl from 0.1 M KBi solution (pH 9.2) which contained 0.4 mM $Ni(NO_3)_2$, doping with $Fe(NO_3)_3$ at different Ni:Fe ratios (9:1; 6:4; 4:6), followed by a conditioning step at 0.903 V *vs* Ag/AgCl for ~3 h in 1.0 M KBi solution (pH 9.2). As it was reported by Bell,[34] the film deposited from a solution that contained 40% of iron gave the highest OER catalytic current. However, the study only gives estimations of the iron doping throughout the film since it integrates the well-known $Ni(OH)_2$/NiOOH wave, but no further analysis was made. Figure 13 shows the first scan of the as-deposited $Ni_{0.6}Fe_{0.4}$-Bi film, an intermediate CV cycle and the CV cycle of the film after the conditioning step which displays a current density of 3.5 mA

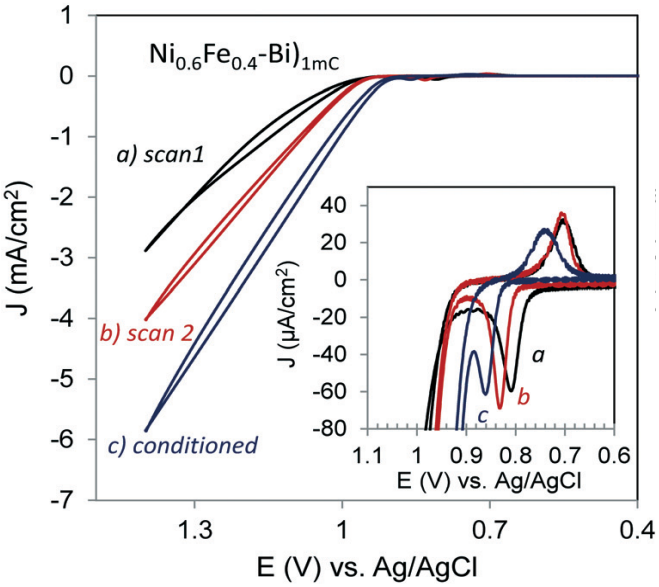

Figure 13: First scan (a), an intermediate scan (b), and a CV after conditioning by applying an anodic bias of 0.903 V for approximately 3h, acquiered for $Ni_{0.6}Fe_{0.4}$-$Bi)_{1mC}$ in1.0 M KBi at pH 9.2 (c) (reproduced from ref[39], with the permission from the Royal Society of Chemistry, Copyright 2017).

cm^{-2} at 1.2 V in 1.0 KBi buffer at pH 9.2 and an estimated Tafel slope of 37 ± 1 mV dec^{-1}. Another interesting aspect of this article is the use of Al^{3+}, which is a Lewis acid comparable to iron in terms of size and charge, to assess the hypothesis presented by Nocera previously.[38] The doping of each ion was simply achived by performing 10 CV scans on fresh NiBi films at a scan rate of 100 mV s^{-1} in a solution of 1.0 M KBi after addition of 0.16 mM of Al^{3+} or Fe^{3+}. Adding iron ions to the electrolyte solution caused a fast increase in the OER activity, while adding aluminum ions poisoned the OER catalysis.

In addition to studies aimed at understanding the high electrocatalytic activity of the mixed oxide of nickel and iron, some groups have explored various electrosynthetic pathways to prepare this mixed oxide, in order to obtain materials with different morphologies, which can strongly influence their catalytic performance. For example, Shao and co-workers[40] developed

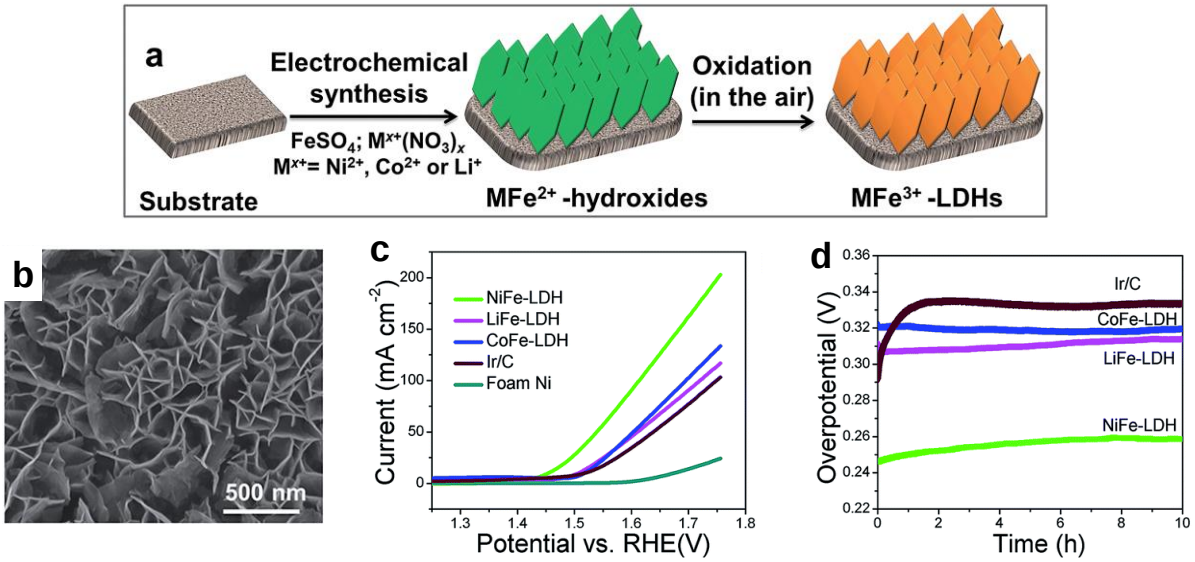

Figure 14: a) Scheme of the preparation of MFe-LDH (M = Ni, Co, Li) nanoplatelets arrays on conducting substrates. b) SEM images of NiFe-LDH deposited on Ni foam. c) LSV curves and d) chronopotentiometric experiments during 10 h at 10 mA cm^{-2} of MFe-LDH (M = Ni, Co, Li) nanoplatelets arrays and commercial Ir/C deposited on Ni foam in 1 M KOH solution (adapted from ref[40], with the permission from the Royal Society of Chemistry, Copyright 2015).

a new and rapid electrochemical synthesis route for the fabrication of Fe containing layered double hydroxide of Ni, Co and Li (denoted MFe-LDHs, M = Ni, Co and Li) which does not involve a conditioning step, and which exhibits high electrocatalytic performance for water oxidation (Figure 14a). Ultra-thin MFe-LDHs nanoplatelets were directly electrodeposited on conducting electrode (Ni foam or glassy carbon) by reducing $FeSO_4$ and $Ni(NO_3)_2$ (either $Co(NO_3)_2$ or $LiNO_3$) *via* potentiostatic experiment at -1.0 V *vs* SCE during less than 300 s. The electrodeposited nanoplatelets (with high catalyst loading of 1 mg cm^{-2}) were positioned

perpendicular to the electrode surface with size of 200-300 nm of lateral length and of 8-12 nm thickness (Figure 14b).

The NiFe-LDH nanoplatelet arrays deposited on Ni foam appeared to be very promising for OER in alkaline solution (1.0 KOH), presenting a low overpotential of 0.224 V at current density of 10 mA cm^{-2} with high durability over 10 h, which is 0.064, 0.053 and 0.065 V less than CoFe-LDH, LiFe-LDH and commercial Ir/C, respectively (Figure 14c, d). At an overpotential of 0.3 V, NiFe-LDH presents a current density of 44.3 mA cm^{-2}, which is ~3.1, 2.6 and 3.6 times greater than those of CoFe-LDH, LiFe-LDH and commercial Ir/C, respectively. NiFe-LDH displays a smaller Tafel slope of 52.8 mV dec^{-1} in comparison with 92.0, 104.0, 145.0 mV dec^{-1} for CoFe-LDH, LiFe-LDH and commercial Ir/C, respectively. The highest TOF value in the series at an overpotential of 0.3 V was also obtained with NiFe-LDH (0.013 s^{-1}) compared to those of CoFe-LDH, LiFe-LDH and commercial Ir/C (*i.e.* 0.0075, 0.0054 and 0.0036 s^{-1}, respectively). The MFe-LDH nanoplatelet arrays present thus high electrocatalytic performance towards OER and are also efficient catalysts for several oxidation reactions of other fuel molecules as hydrazine, methanol, and ethanol, presenting a satisfactory catalytic activity and high stability. The electrochemical preparation of MFe-LDHs is rapid, effective at large-scale production and shows high potential for water splitting, fuel cells and other clean energies.

More recently, the group of Cao[41] improved the electrochemical process firstly introduced by Shao for the preparation of ultrathin NiFe hydroxide films with high OER activity, by using a stepwise electrodeposition of porous nanoribbon of nickel and iron oxide (denoted NiFe-SW). The stepwise strategy consists in (i) Ni film deposition on glassy carbon electrode by a cathodic electrolysis (-0.8 V *vs* NHE) of an aqueous $Ni(NO_3)_2$ solution, (ii) followed by the incorporation of Fe ions *via* one cycle voltammetry sweeping between 0.2 and 1.35 V vs NHE of a degassed acetate buffer solution containing $FeSO_4$ (Figure 15). The authors clearly showed that the NiFe-SW electrode presents higher OER performance in comparison with that of bare NiO_x electrode (Ni) or a mixed $NiFeO_x$ electrode prepared through an electroinduced co-precipitation of Ni and Fe salts (NiFe-CP). NiFe-SW requires a very low overpotential of 0.4 V to reach a catalytic current of 10 mA cm^{-2} in 1.0 M KOH electrolyte and it displays a very high catalytic current of 210 mA cm^{-2} at an overpotential of 0.329 V on a simple glassy carbon electrode (not on metal foam or carbon sponge featuring very large specific surface area and high non-faradaic background currents). NiFe-SW displays extremely high TOF value for OER of 8.7 s^{-1} at an overpotential of 0.329 V, higher than 0.4 s^{-1}

(corresponding to 9 mA cm^{-2}) for NiFe-CP and surpassing the most efficient heterogeneous OER catalysts of literature that typically exhibit TOF values inferior to 1 s^{-1} under similar overpotentials. Besides, when deposited on ITO electrode, NiFe-SW film shows high stability in long-term galvanostatic electrolysis over 24 h, while maintaining a potential of ca. 1.6 V vs RHE at applied current density of 10 mA cm^{-2} (Figure 15d). From ICPMS analysis, it was established that NiFe-SW and NiFe-CP electrodes on glassy carbon possess closer values of catalyst loading respectively of 62.6 nmol cm^{-2} and 73.7 nmol cm^{-2}, with similar NiFe composition of 82:18 and 87:13, respectively. Consequently, the large difference in catalytic activity between NiFe-SW NiFe-CP could not be due to the difference in catalyst content. The highest OER performance of NiFe-SW can be first ascribed to its peculiar morphology observed by SEM which consisted of interconnected nanoribbons with porous structures, confering a great number of accessible catalytic sites at the electrode surface and a low resistance to the mass transport related to water substrate (*i.e.* reactants as hydroxide anions) and O_2 release (Figure 15e). By contrast, NiFe-CP presents a weakly porous morphology composed of isolated

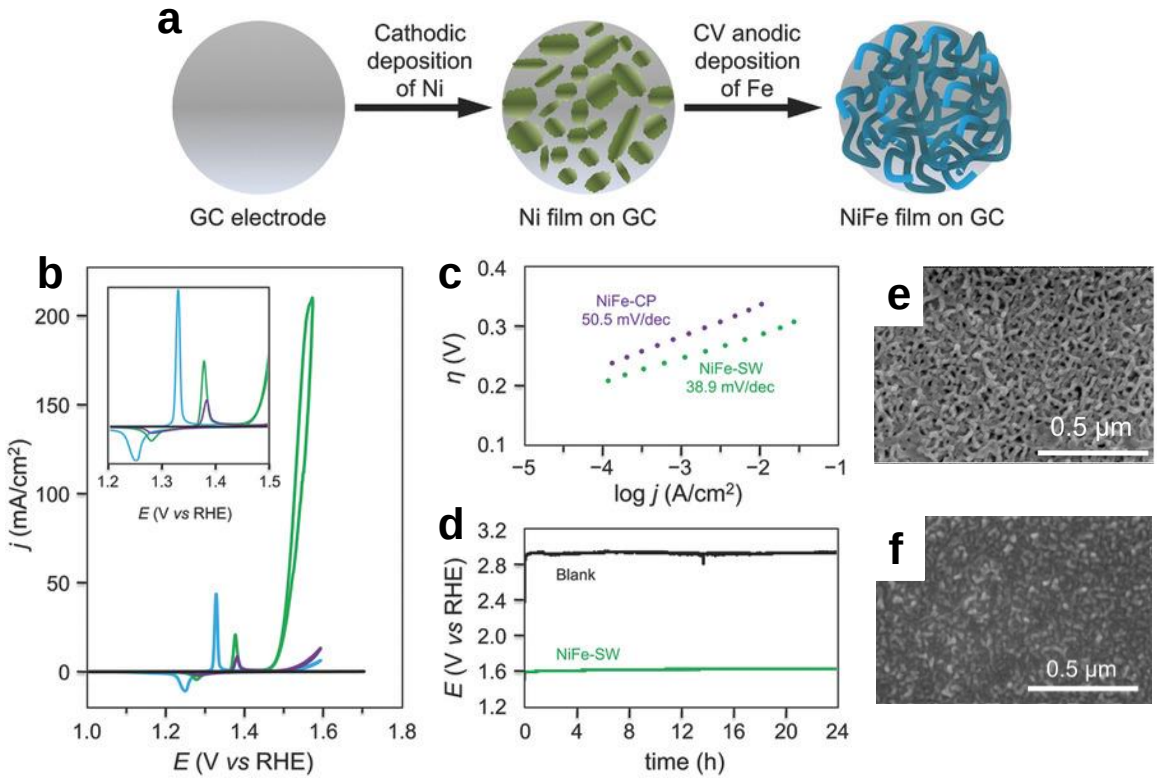

Figure 15: a) Representation of the stepwise electrodeposition of NiFe-SW on glassy carbon (GC) electrode. b) Cyclic voltammograms of NiFe-SW (green), NiFe-CP (purple) and Ni-based film (blue) on GC electrodes and blank GC electrode (black) in 1M KOH electrolyte. c) Tafel plots of NiFe-SW (green) and NiFe-CP (purple). d) Chronopotentiometry plots of NiFe-SW on ITO electrode (green) and blank ITO electrode (black). SEM images of e) NiFe-SW and f) NiFe-CP on GC (adapted from ref[41], with the permission from Wiley, Copyright 2017).

nanoparticles limiting the accessibility of reacting substances. The greater electrocatalytically active surface area of NiFe-SW compared to that NiFe-CP were also confirmed by the measure of their double-layer capacitance revealing a higher value for NiFe-SW (20.6 µF) than that of NiFe-CP (13.6 µF). The second reason of the highest catalytic activity of NiFe-SW is the depth insertion of Fe^{III} into $Ni^{II}(OH)_2$ structure, as supported by XPS and Raman analyses, that promote the high oxidation state of Ni in favor of high OER performance. The highly efficient catalytic activity, the simple and low energy consumption of the NiFe-SW film preparation makes them a good alternative for application on solar-driven water splitting.

V – Cobalt oxide-based catalysts for OER

Cobalt oxide has been also extensively studied for the OER catalysis. In 1950, El Wakkad and Hickling[42] were the first to identify the OER electrocatalytic activity of the cobalt oxide and at the end of 70s and at the beginning of 80s the groups of Shafirovich,[43] Burke,[44] Bockris,[45,46] Noufi[47] and Tseung,[48,49] , to name a few, have studied in detail the electrocatalytic activity of this oxide in alkaline conditions (pH 14). However, only few studies on the subject were reported in the decade of the 90s until the work of Nocera[50] which reported in 2008 a material based on cobalt oxide-phosphate (CoPi) enable to work in near neutral conditions (pH 9.2), which renewed the interest of the cobalt oxide as an active OER material.

In 2002, the group of Casella[51] acknowledged that cobalt oxide films could be deposited on a conductive electrode *via* electro-decomposition of a cobalt complex. They obtained a good chemical stability and a high catalytic activity for the electrooxidation of carbohydrates and

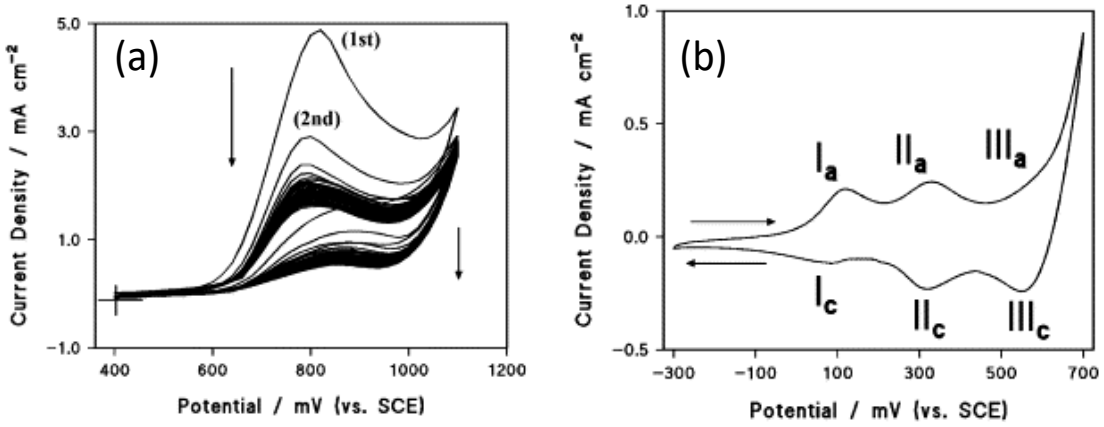

Figure 16: (a) Consecutive cyclic voltammograms of cobalt oxide film growth on glassy carbon electrode in a 30 mM NaOH electrolyte in presence of 30 mM sodium citrate and 3 mM $CoCl_2$ (scan rate 50 mV s^{-1}). (b) Cyclic voltammogram (30^{th} cycle) of cobalt oxide film on glassy carbon electrode in a 30 mM NaOH electrolyte (scan rate 50 mV s^{-1}) (reproduced from ref[51].

other molecules, when they worked in presence of moderately alkaline media. Therefore, they were encouraged to work under this condition for OER. The deposition of the cobalt oxide film on glassy carbon was conducted *via* electro-decomposition of a cobalt(II)-citrate complex from an electrolyte solution of 30 mM NaOH (pH 12.5) containing 30 mM sodium citrate as a complexing agent and 3-6 mM of $CoCl_2$ salt, by performing either several consecutive cycles between 0.4 and 1.1 V *vs* SCE, or by potentiostatic experiment at *ca.* 0.5 V *vs* SCE. Concerning the growth of the cobalt oxide film, as shown in Figure 16(a), it involves different and simultaneous electrochemical process. Initially, the oxidation of the Co(II)-citrate complex occurs with the formation of the insoluble oxide species Co^{III} and Co^{IV} that deposit on the surface of the electrode. In the first stages, the monolayer induce a drastic increase of the OER anodic currents, but then decreasing with the increasing number of cycles, which can be explained by the competing adsorption reaction of citrate ions rather than the hydroxide species on the cobalt active sites. Characterization by CV of the cobalt films in moderate alkaline solution shows an electrochemical complexity since many oxidation states and cobalt species are involved (Figure 16(b)). For instance, the hydrous Co(II) film gradually converts to Co(III)-containing species (Co_3O_4, Co_2O_3, CoOOH) simultaneously present. Thus, in the three set of peaks of Figure 16b, IIa/IIc and IIIa/IIIc redox couple were assigned to the Co_3O_4/CoOOH (0.3 V vs SCE) and CoOOH/CoO_2 (0.55 V) redox processes respectively while Ia/Ic redox couple was attributed to $Co(OH)_2$/Co_3O_4 (0.08 V). This study gives an insight regarding the electrochemical behavior of cobalt oxide films in alkaline conditions.

In 2008, Nocera[50] confirmed a dark coating on an ITO electrode by a cobalt oxide film, which was deposited *in situ* by bulk electrolysis at 1.29 V *vs* NHE from a 0.1 M phosphate (Pi) neutral solution containing 0.5 mM of Co^{2+} (Figures 17(A-B)). The nature of counter anions such as nitrate, sulfate or triflate, or whether the buffer contained potassium or sodium, is irrelevant in the deposition.

After 8 h of electrolysis, the current density reached a plateau of about 1 mA cm^{-2} (Figure 17(B)). SEM characterizations shows micro-sized particles joined into a thin film (Figure 17(C)), whereas the maximum activity was reached at about 2 µm thickness. EDX and elemental analysis on the film described a composition of 31.1 % Co, 7.70 % P and 7.71% K in the resulting film, while XPS signals confirms the presence of phosphate and Co^{2+} or Co^{3+} bonded to oxygen atoms. This electrodeposited cobalt oxide cleanly oxidizes water to oxygen in the neutral KPi solution, in view of the quantitative Faradaic yield and the ^{13}P NMR studies demonstrating that the electrolyte is not decomposed under electrocatalytic conditions.

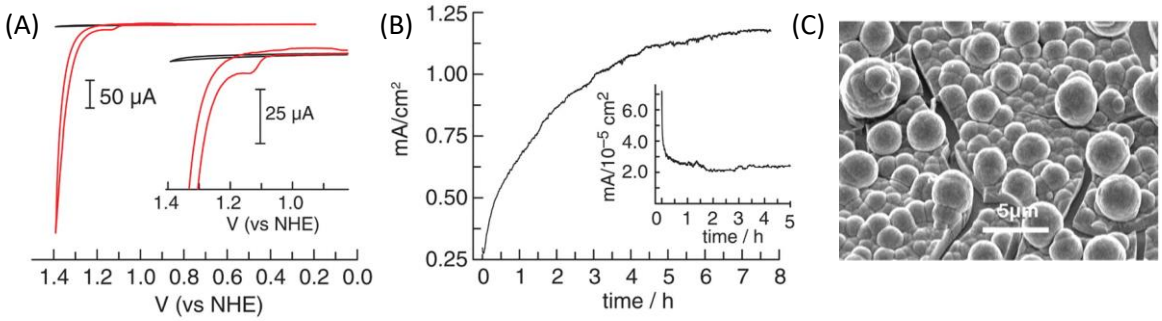

Figure 17: (A) CVs recorded at glassy carbon electrode (0.071 cm^2) in aqueous 0.1 M Pi electrolyte (pH 7) with (red trace) and without (black trace) 0.5 mM Co^{2+} (scan rate 50 mV s^{-1}). (B) Chronoamperometry recorded at ITO electrode (1.5 cm^2) at 1.29 V *vs* NHE in 0.1 M Pi electrolyte (pH 7) with 0.5 mM Co^{2+}. Inset: Chronoamperometry without cobalt salt. (C) SEM images of the Co-Pi catalyst electrodeposited on ITO (30 C cm^{-2}) in 0.1 M Pi electrolyte (pH 7) with 0.5 mM Co^{2+} (reproduced from ref[50] with the permission from the American Association for the Advancement of Science, Copyright 2008).

The group of Nocera also reported the effect of a high surface area of cobalt oxide electrodeposited from different electrolyte solutions: potassium phosphate (pH 7.0, KPi), methyl phosphonate (pH 8.5, MePi) and borate (pH 9.2, Bi).[52] Firstly, the group studied the activity of the materials in function of the film thickness of cobalt oxide deposited on Fluorine-doped Tin Oxide (FTO) electrode from borate, denoted Co-Bi (0.5 mM Co^{2+}, 0.1 M KPi at pH 7.0, 0.72 V vs Ag/AgCl). Thus, they measured the different film thickness in the range of ~15-400 nm when charge limits varied from 12 to 384 mC cm^{-2}. Additionally, the different thickness were compared with their Tafel slope in 0.1 M borate buffer, showing a linear increase in the activity with the film thickness, indicating a high porosity that allows oxygen not be confined to the outermost layer of the film. In order to increase the number of electrochemical active cobalt sites, the growth of cobalt oxide films on nickel foam (NF) presenting a higher OER activity was accomplished by applying 1.1 V *vs* Ag/AgCl in a deposition bath which contained 10 mM of $Co(NO_3)_2 \cdot 6H_2O$ dissolved in 0.1 M methylphosphonate (MePi). This electrolyte was chosen for the electrodeposition since it allows a better solubility of the cobalt salt, further studies were performed in Pi and Bi electrolytes, obtaining a current density of 100 mA cm^{-2} and overpotentials of 442 and 363 mV, respectively. Furthermore, in borate buffer, the material was able to successfully maintain the overpotential for nearly 65 h of activity. Additional SEM characterization images showed a thick forest-like film when applied a charge of 100 mC cm^{-2}.

The group of Nocera also showed that a proton-accepting buffer is needed to deposit such films (Figure 18).[53] They obtained a dark green film when deposited by controlled

potential electrolysis (CPE) at 1.3 V *vs* NHE from a deposition bath that contains either 1 mM Co^{2+} in MePi or 0.5 mM Co^{2+} in Bi. The catalytic current of these films at 1.3 V can reached up to 1.5 mA cm^{-2} (in 2 h) in MePi and 2.3 mA cm^{-2} (in 10 minutes) in Bi. No formation of cobalt film is observed when poor proton-accepting electrolytes are used, such as SO_4^{2-}, NO_3^- and ClO_4^-, confirming that a proton-accepting electrolyte is required for the electrodeposition of cobalt oxide. SEM images revealed spherical nodules with a diameter of 1-5 µm when 40 C cm^{-2} was used for a film of 3 µm thick in MePi, while in Bi electrolyte these particles appear early in the deposition stages (2 C cm^{-2}) which aggregate upon prolonged electrolysis. Powder X-ray diffraction of these both films showed an amorphous nature rather than a crystalline one. Similar Tafel slopes were obtained in each electrolyte environment, implying that all catalysts generated in the different electrolytes are equally active for the water oxidation catalysis. The faradaic efficiency measured in MePi and Bi was determined to be 98 ± 5 % and 104 ± 5 %, respectively.

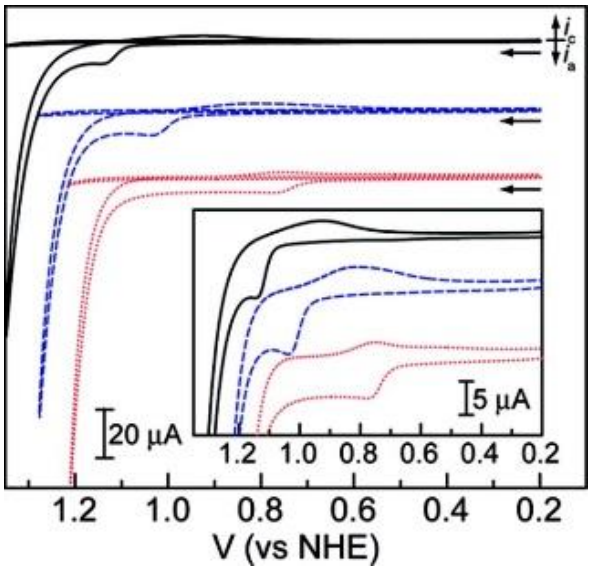

Figure 18: CVs recorded at glassy carbon electrode (scan rate 50 mV s^{-1}) of aqueous 0.5 mM Co^{2+} in 0.1 M Pi (pH 7, black), 0.1 M MePi (pH 8, blue) and 0.1 M Bi electrolytes (pH 9.2, red); background traces in each electrolyte are CVs without cobalt salt. Inset: expanded current scale of CVs in presence of Co^{2+} (reproduced from ref[53], with the permission from the American Chemical Society, Copyright 2009).

Cobaloximes are popular H_2 evolution molecular catalysts and in 2013 the group of Du used them for electrodeposition of cobalt oxide films on FTO electrode to catalyze OER.[54] Four different cobaloximes (**1**-**4**) at 1 mM were used for the electrodeposition of cobalt oxide films (denoted CoO_x-**1**, CoO_x-**2**, CoO_x-**3** and CoO_x-**4**) *via* bulk electrolysis on FTO in 0.1 M borate buffer (pH 9.2) at two different potentials, +1.5 V and +1.1 V *vs* Ag/AgCl during 7 hours (Figure 19(A)). The four CoO_x films exhibited a catalytic current above 1.5 and 2.0 mA cm^{-2} with a bulk electrolysis at 1.1 and 1.5 V, respectively. The CoO_x film obtained from the cobaloxime **1** (CoO_x-**1**) presented the highest activity with 5.5 mA cm^{-2} after 7 h of electrodeposition. The high performance of CoO_x-**1** was attributed to the nano-sized particles (~100-200 nm) observed by SEM (Figure 19(B)). Whereas the other precursors with lower catalytic currents provided darker films on FTO, indicating thicker films and/or bigger particles,

microscopic characterizations confirmed clusters aggregation with irregular shapes at microsized scales (~1 µm). The change of morphology was followed as a measure of stability of the CoO_x-**1** films in which the bulk electrolysis did not undergo any modification on its size, dispersity, or homogeneity after 7 h at an applied potential of +1.1 V *vs* Ag/AgCl.

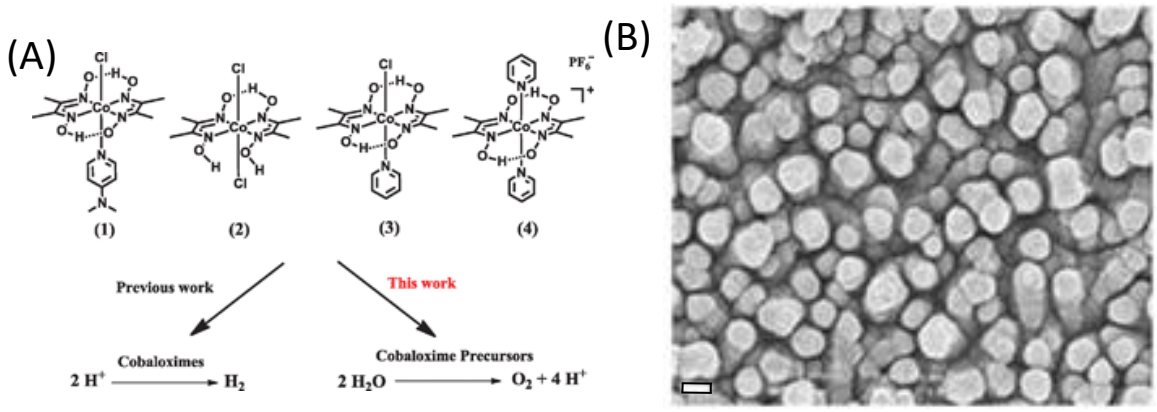

Figure 19: (A) Molecular structures of cobaloximes **1-4** used by the group of Du. (B) SEM image of CoOx-**1** film electrodeposited on FTO after 7 h of electrolysis at 1.5 V *vs* Ag/AgCl in 0.1 M borate buffer at pH 9.2 containing 1 mM of cobaloxime **1**; scale bar 200 nm (reproduced from ref[54] with the permission from the Royal Society of Chemistry, Copyright 2013).

Complementary elemental analysis by XPS support the presence of Co(II) or Co(III). The oxygen evolution was measured with a fluorescence-based oxygen sensor and Faradaic efficiency of the CoO_x-**1** catalyst at 1.1 V and estimated to be around 80 %. CoO_x-**1** displayed a Tafel slope of ~66 mV dec^{-1}, which is usually obtained for CoO_x at pH 9.2. In addition, a comparison with a Co-Bi film deposited under similar conditions but with just a simple Co^{2+} salt in borate buffer reveals that the mass activity of Co-Bi (1.1 mA cm^{-2} mg^{-1}) is 17 times weaker than those of CoO_x-**1** (19 mA cm^{-2} mg^{-1}). This demonstrated the relevance of the approach to synthesize nanostructured cobalt oxide catalysts with high OER performance from molecular cobaloximes.

In the same vein, the group of Du also studied six cobalt-salen complexes (derivates from *N*,*N*′-bis(salicylidene)ethylenediamine) as precursors of cobalt oxide films (Figure 20(A)).[55] Cobalt oxides films (denoted as **films 1-6** prepared from the corresponding cobalt salen complexes **1-6**) were electrodeposited on FTO from 0.1 M KBi (pH 9.2) containing X mM of cobalt salen at 1.2 V *vs* Ag/AgCl during 11 h (60 nmol cm^{-2}). Among all the complexes and films prepared from commercial Co_3O_4 and Co^{2+} as control experiments, **film 4** stands out as the most active water catalyst film with a current density of ~1.4 mA cm^{-2} during a bulk electrolysis at 1.1 V *vs* Ag/AgCl. SEM images of all films (**1-6**) showed the formation of heterogeneous nanomaterials on FTO (Figure 20(B)), suggesting that the structure of the

different complexes plays a significant role on the activity of the film. Lower activities were obtained from very bulky complexes (four ter-butyl groups on precursors **1**, **3** and **5**), in contrast of the precursors with better planarity structures (**2**, **4** and **6**). This is probably due to a better contact between the complex molecules and the FTO surface. EDX and XRD confirmed the presence of cobalt, which resulted from the decomposition of the cobalt-salen complexes, with a probably amorphous structure since the XRD patterns of the FTO and the film were practically the same.

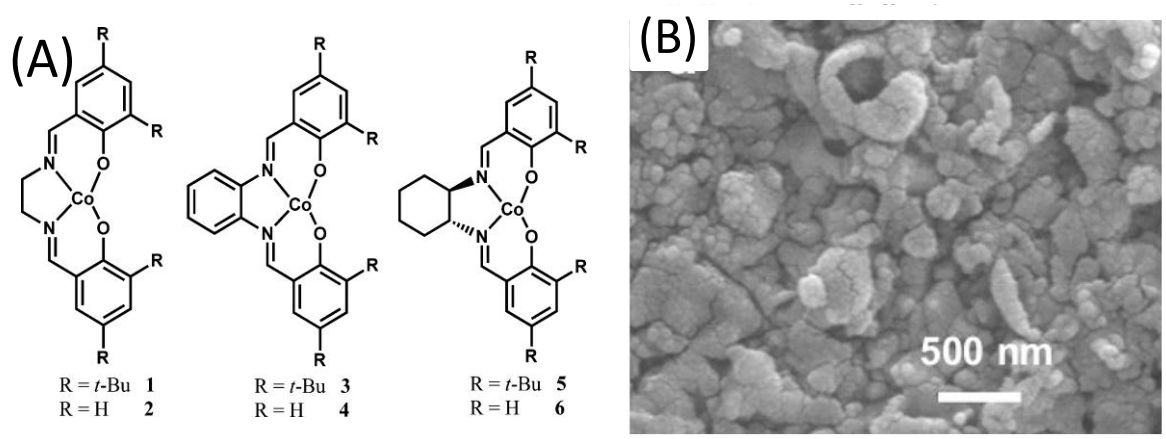

Figure 20: (A) Structures of the cobalt salen complexes **1-6** as precursors of CoOx films **1-6**. (B) SEM image of the film **4** on FTO (reproduced from ref[55], with the permission from the American Chemical Society, Copyright 2015)

In conclusion, **film 4** presented the optimal performance within the cobalt-salen complexes studied with a required overpotential of ~350 mV for a current density of 0.1 mA cm^{-2} for water oxidation, as well as a low Tafel slope of ~62 mV dec^{-1} and a Faradaic efficiency of about 93 %. According to the authors, the use of salen complex is an appealing method to prepare active CoO_x catalysts for water oxidation.

The group of Spiccia studied the inexpensive aminopolycarboxylate cobalt complexes as another cobalt precursors for the synthesis of CoO_x films (Figure 21).[56] The electrodeposition on FTO was conducted by controlled potential electrolysis (CPE) at 1.4 V *vs* Ag/AgCl, through a solution of each cobalt complex (1 M) in a 0.1 M borate buffer at pH 9.2. To easily compare the electrodeposition of the different complexes, CPE was stopped when the OER catalytic current reached a plateau. This asymptotic behavior was observed after 4, 10, 60 and 120 minutes of CPE for $[Co(OH_2)_6]^{2+}$, $[Co(IDA)_2]^{2-}$, $[Co(NTA)(OH_2)_2]^{-}$ and $[Co(EDTA)]^{2-}$, respectively. SEM images revealed that the deposition did not fully coat the surface of the FTO

and that the particles size of CoO_x range between 100-250 nm, which are comparable with the CoO_x nanoparticles reported previously by Du.[55] EDX and ICP-MS studies confirmed that the amount of deposited Co decreases according to the increase of the denticity of the ligands in the precursor (0.06 ± 0.01 µmol cm^{-2} from $[Co(OH_2)_6]^{2+}$, 0.04 ± 0.01 µmol cm^{-2} from $[Co(IDA)_2]^{2-}$, 0.0019 ± 0.008 µmol cm^{-2} from $[Co(NTA)(OH_2)_2]^-$, and no Co deposition from $[Co(EDTA)]^{2-}$). Concerning the nature of the CoO_x films, it resembles an oxy-hydroxide CoO(OH) phase regardless of the precursors used, according to XAS and XANES studies. CVs of the deposited films in 0.60 M Bi buffer at pH 9.2, in presence of 0.23 M Na_2SO_4 to increase the ionic strength of the solution, are shown in Figure 21. As displayed in the figure's inset in the range of 500-800 mV *vs* Ag/AgCl, the oxidative process of Co^{III} to Co^{IV} occurs within the film. In addition, differences in the magnitudes of this redox process are correlated to the amount of deposited cobalt, which is consistent with the results obtained by ICP-MS. Finally, thin films formed by these inexpensive complex precursors were highly transparent and highly catalytically active, with a Tafel slope of 61±3 mV dec^{-1}, which made these materials suitable for direct coupling to light-harvesting materials.

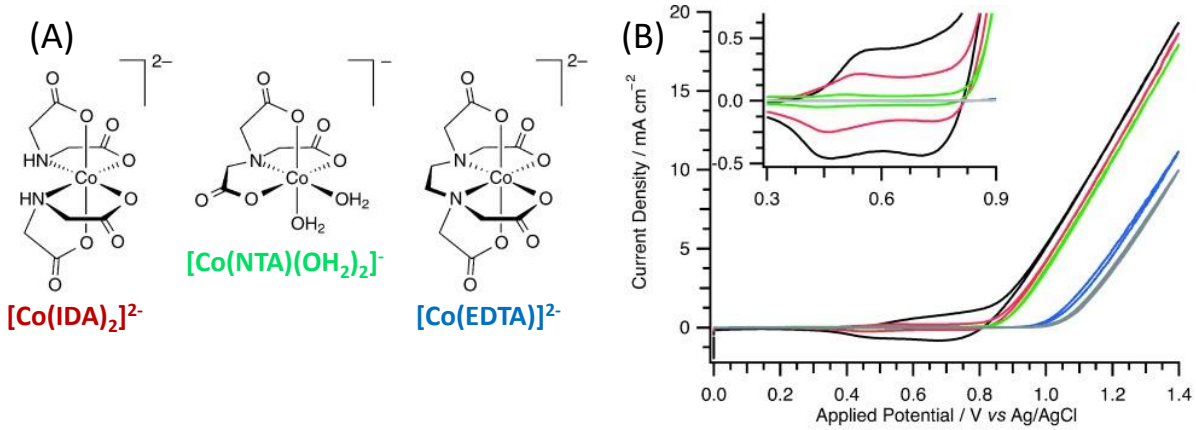

Figure 21: (A) Structures of the **$[Co(IDA)_2]^{2-}$**, **$[Co(NTA)(OH_2)_2]^-$** and **$[Co(EDTA)]^{2-}$** precursors for CoO_x films for water oxidation. (B) CVs of CoO_x derivated from **$[Co(OH_2)_6]^{2+}$** (black), **$[Co(IDA)_2]^{2-}$** (red), **$[Co(NTA)(OH_2)_2]^-$** (green) and **$[Co(EDTA)]^{2-}$** (blue) precursors on FTO recorded at 20 mV s^{-1} in 0.60 M Bi with 0.23 M Na_2SO_4, pH 9.2, stirring at 650 rpm and at 35 °C. The grey trace corresponds to the CV of the FTO blank without CoO_x film.

VI – Conclusions

Nowadays, water splitting reaction performed with an alkaline electrolyzer to produce hydrogen is still considered as one of the best energetic alternatives to fossil fuels available, since hydrogen can produce electricity in a fuel cell with a relatively good conversion efficiency (ca. 50 %) while only releasing water as byproduct. However, the weak point of water splitting reaction, that would prevent its use on a larger scale, is its oxidative half reaction (OER), due to its high energetic barrier that has to be overcome, along with the slow electrode kinetics and large anodic overpotential. Nickel has been present in the early designs of the alkaline electrolyzers as electrode's material, and in the 80s the studies of other oxides based on transition metals experience an obvious increase. However, nickel and cobalt are the preferred elements for synthetize materials for OER, due to the great activity towards this reaction that they can achieve in their many forms (oxyhydroxides, perovskite, spinel, layer double hydroxide). Regardless of the numerous synthetic methods for obtaining the OER catalyst, in which some have multiple steps such as solvothermal or chemical precipitation followed by processes that deposited the material onto electrode (spin coating, dropcasting, sol-gel process, etc), electrochemical deposition is the simplest and cleanest method for the preparation of metal oxide-based anodes for OER.

The works of Nocera on this subject in the early 2000 can be seen as a milestone, since their findings concerning a proton-accepting electrolyte, such as phosphate or borate, as an essential parameter to effectively achieve the deposition of the metal oxide catalyst from a metal salt. Many studies came after providing insights of the chemical structure of the catalyst films, along with their possible OER mechanism and reported their high activities in neutral (pH 7.0) and near neutral conditions (pH 9.2). Since the work of Nocera, various metal oxide precursors have been explored. For example, the group of Spiccia used nickel complexes with ligands of amine to deposit nickel oxide films, while the group of Du used cobaloximes to obtain a highly active cobalt oxide film. Nevertheless, there are still gaps in the research concerning these widely studied OER catalysts. In particular, nickel oxide is known as very active for OER, but it has been reported by Corrigan that this high activity may be due to the iron impurity present in the KOH electrolyte, which is inserted into the nickel oxide film even at concentrations as low as 1 %, and thus increases its OER electrocatalytic activity. At the moment, this increase of activity due to the presence of Fe into NiO_x was assumed to be caused by an increase in the film conductivity, although the group of Boettcher suggested that other parameters are likely to be involved. These authors detected that the usual conditioning step used firstly by Nocera to

"activate" the nickel oxide film, is not likely to increase the oxidation state of nickel until +3.6, but it is a process that adds impurity of iron in the film, and therefore increases the activity of the film. The groups of Boettcher and Bell also suggested that FeO_x is the active site towards OER within $NiFeO_x$, NiO_x playing the role of a conductive matrix for FeO_x that is intrinsically poorly conductive. Other groups suggested that iron acts as lewis acid and activates NiO_x for OER catalysis. The real role of iron inside nickel oxide catalyst is still under debate and deciphering the iron dependence of $NiFeO_x$ on its OER activity will allow designing new efficient and stable electrocatalysts based on mixed metal oxides for water oxidation.

References

1. McCrory, C. C. L., Jung, S., Peters, J. C., & Jaramillo, T. F. Benchmarking heterogeneous electrocatalysts for the oxygen evolution reaction. *J. Am. Chem. Soc.* **135**, 16977–16987 (2013).
2. Santos, D. M. F., Sequeira, C. A. C., & Figueiredo, J. L. Hydrogen production by alkaline water electrolysis. *Quim. Nova* **36**, 1176–1193 (2013).
3. El-Shafie, M., Kambara, S., & Hayakawa, Y. Hydrogen Production Technologies Overview. *J. Power Energy Eng.* **07**, 107–154 (2019).
4. Marini, S., Salvi, P., Nelli, P., Pesenti, R., Villa, M., Berrettoni, M., Zangari, G., & Kiros, Y. Advanced alkaline water electrolysis. *Electrochim. Acta* **82**, 384–391 (2012).
5. Sanchis, P. & Ieee, M. Water Electrolysis : Current Status and Future Trends. **100**, (2012).
6. Wygant, B. R., Kawashima, K., & Mullins, C. B. Catalyst or Precatalyst? the Effect of Oxidation on Transition Metal Carbide, Pnictide, and Chalcogenide Oxygen Evolution Catalysts. *ACS Energy Lett.* **3**, 2956–2966 (2018).
7. Roger, I. & Symes, M. D. First row transition metal catalysts for solar-driven water oxidation produced by electrodeposition. 6724–6741 (2016) doi:10.1039/c5ta09423b.
8. Gong, M. & Dai, H. A mini review of NiFe-based materials as highly active oxygen evolution reaction electrocatalysts. **8**, 23–39 (2015).
9. Singh, A. & Spiccia, L. Water oxidation catalysts based on abundant 1st row transition metals. *Coord. Chem. Rev.* **257**, 2607 (2013).
10. Chen, Y., Rui, K., Zhu, J., Dou, S. X., & Sun, W. Recent Progress on Nickel-Based Oxide/(Oxy)Hydroxide Electrocatalysts for the Oxygen Evolution Reaction. *Chem. - A Eur. J.* **25**, 703–713 (2019).
11. McCrory, C. C. L., Jung, S., Ferrer, I. M., Chatman, S. M., Peters, J. C., & Jaramillo, T. F. Benchmarking Hydrogen Evolving Reaction and Oxygen Evolving Reaction Electrocatalysts for Solar Water Splitting Devices. *J. Am. Chem. Soc.* **137**, 4347–4357 (2015).
12. Weber, M. F. & Dignam, M. J. Splitting Water With Semiconducting Photoelectrodes: Efficiency Considerations. *Adv. Hydrog. Energy* **3**, 957–968 (1984).
13. Suen, N. T., Hung, S. F., Quan, Q., Zhang, N., Xu, Y. J., & Chen, H. M. Electrocatalysis for the oxygen evolution reaction: Recent development and future perspectives. *Chem. Soc. Rev.* **46**, 337–365 (2017).
14. Bode, H., Dehmelt, K & Witte, J. Zur kenntnis der nickelhydroxideelektrode-I. Uber das nickel (II)-hydroxidhydrat. *Electrochim. Acta* **11**, 1079–1084 (1966).
15. Wehrens-Dijksma, M. & Notten, P. H. L. Electrochemical Quartz Microbalance characterization of Ni(OH)2-based thin film electrodes. *Electrochim. Acta* **51**, 3609–3621 (2006).
16. Performance, E. Sealed Lead Cells and Batteries. *Recharg. Batter. Appl. Handb.* 153–235 (1998)
17. Doyle, R. L., Godwin, I. J., Brandon, M. P., & Lyons, M. E. G. Redox and electrochemical water splitting catalytic properties of hydrated metal oxide modified electrodes. *Phys. Chem. Chem. Phys.* **15**, 13737 (2013).

18. Dincă, M., Surendranath, Y., & Nocera, D. G. Nickel-borate oxygen-evolving catalyst that functions under benign conditions. *Proc. Natl. Acad. Sci. U. S. A.* **107**, 10337–10341 (2010).
19. Bediako, D. K., Lassalle-Kaiser, B., Surendranath, Y., Yano, J., Yachandra, V. K., & Nocera, D. G. Structure-activity correlations in a nickel-borate oxygen evolution catalyst. *J. Am. Chem. Soc.* **134**, 6801–6809 (2012).
20. Yoshida, M., Mitsutomi, Y., Mineo, T., Nagasaka, M., Yuzawa, H., Kosugi, N., & Kondoh, H. Direct Observation of Active Nickel Oxide Cluster in Nickel-Borate Electrocatalyst for Water Oxidation by in Situ O K-Edge X-ray Absorption Spectroscopy. *J. Phys. Chem. C* **119**, 19279–19286 (2015).
21. Singh, A., Chang, S. L. Y., Hocking, R. K., Bach, U., & Spiccia, L. Highly active nickel oxide water oxidation catalysts deposited from molecular complexes. *Energy Environ. Sci.* **6**, 579–586 (2013).
22. Singh, A., Chang, S. L. Y., Hocking, R. K., Bach, U., & Spiccia, L. Anodic deposition of NiOx water oxidation catalysts from macrocyclic nickel(ii) complexes. *Catal. Sci. Technol.* **3**, 1725–1732 (2013).
23. Tichenor, R. L. Nickel Oxides-Relation Between Electrochemical and Foreign Ion Content. *Ind. Eng. Chem.* **44**, 973–977 (1952).
24. Troilius, G. & Alfelt, G. The migration of iron in alkaline nickel cadmium cells with pocket electrodes. *In Power Sources; Elsevier* 337−347 (1967).
25. Młynarek, G., Paszkiewicz, M., & Radniecka, A. The effect of ferric ions on the behaviour of a nickelous hydroxide electrode. *J. Appl. Electrochem.* **14**, 145–149 (1984).
26. Corrigan, D. A. The Catalysis of the Oxygen Evolution Reaction by Iron Impurities in Thin Film Nickel Oxide Electrodes. *J. Electrochem. Soc.* **134**, 377 (1987).
27. Han, L., Dong, S., & Wang, E. Transition-Metal (Co, Ni, and Fe)-Based Electrocatalysts for the Water Oxidation Reaction. *Adv. Mater.* **28**, 9266–9291 (2016).
28. Tang, C., Wang, H. F., Zhu, X. L., Li, B. Q., & Zhang, Q. Advances in Hybrid Electrocatalysts for Oxygen Evolution Reactions: Rational Integration of NiFe Layered Double Hydroxides and Nanocarbon. *Part. Part. Syst. Charact.* **33**, 473–486 (2016).
29. Hunter, B. M., Winkler, J. R., & Gray, H. B. Iron is the active site in nickel/iron water oxidation electrocatalysts. *Molecules* **23**, (2018).
30. Feng, C., Faheem, M. B., Fu, J., Xiao, Y., Li, C., & Li, Y. Fe-Based Electrocatalysts for Oxygen Evolution Reaction: Progress and Perspectives. *ACS Catal.* **10**, 4019–4047 (2020).
31. Trotochaud, L., Young, S. L., Ranney, J. K., & Boettcher, S. W. Nickel-Iron oxyhydroxide oxygen-evolution electrocatalysts: The role of intentional and incidental iron incorporation. *J. Am. Chem. Soc.* **136**, 6744–6753 (2014).
32. Smith, A. M., Trotochaud, L., Burke, M. S., & Boettcher, S. W. Contributions to activity enhancement via Fe incorporation in Ni-(oxy)hydroxide/borate catalysts for near-neutral pH oxygen evolution. *Chem. Commun.* **51**, 5261–5263 (2015).
33. Song, F., Busch, M. M., Lassalle-Kaiser, B., Hsu, C. S., Petkucheva, E., Bensimon, M., Chen, H. M., Corminboeuf, C., & Hu, X. An Unconventional Iron Nickel Catalyst for the Oxygen Evolution Reaction. *ACS Cent. Sci.* **5**, 558–568 (2019).
34. Louie, M. W. & Bell, A. T. An investigation of thin-film Ni-Fe oxide catalysts for the electrochemical evolution of oxygen. *J. Am. Chem. Soc.* **135**, 12329–12337 (2013).

35. Friebel, D., Louie, M. W., Bajdich, M., Sanwald, K. E., Cai, Y., Wise, A. M., Cheng, M. J., Sokaras, D., Weng, T. C., Alonso-Mori, R., Davis, R. C., Bargar, J. R., Nørskov, J. K., Nilsson, A., & Bell, A. T. Identification of highly active Fe sites in (Ni,Fe)OOH for electrocatalytic water splitting. *J. Am. Chem. Soc.* **137**, 1305–1313 (2015).

36. González-Flores, D., Klingan, K., Chernev, P., Loos, S., Mohammadi, M. R., Pasquini, C., Kubella, P., Zaharieva, I., Smith, R. D. L., & Dau, H. Nickel-iron catalysts for electrochemical water oxidation-redox synergism investigated by: In situ X-ray spectroscopy with millisecond time resolution. *Sustain. Energy Fuels* **2**, 1986–1994 (2018).

37. Trzešniewski, B. J., Diaz-Morales, O., Vermaas, D. A., Longo, A., Bras, W., Koper, M. T. M., & Smith, W. A. In Situ Observation of Active Oxygen Species in Fe-Containing Ni-Based Oxygen Evolution Catalysts: The Effect of pH on Electrochemical Activity. *J. Am. Chem. Soc.* **137**, 15112–15121 (2015).

38. Li, N., Bediako, D. K., Hadt, R. G., Hayes, D., Kempa, T. J., Von Cube, F., Bell, D. C., Chen, L. X., & Nocera, D. G. Influence of iron doping on tetravalent nickel content in catalytic oxygen evolving films. *Proc. Natl. Acad. Sci. U. S. A.* **114**, 1486–1491 (2017).

39. Fayad, R., Dhainy, J., Ghandour, H., & Halaoui, L. Electrochemical study of the promoting effect of Fe on oxygen evolution at thin 'NiFe-Bi' films and the inhibiting effect of Al in borate electrolyte. *Catal. Sci. Technol.* **7**, 3876–3891 (2017).

40. Li, Z., Shao, M., An, H., Wang, Z., Xu, S., Wei, M., Evans, D. G., & Duan, X. Fast electrosynthesis of Fe-containing layered double hydroxide arrays toward highly efficient electrocatalytic oxidation reactions. *Chem. Sci.* **6**, 6624–6631 (2015).

41. Zhang, W., Wu, Y., Qi, J., Chen, M., & Cao, R. A Thin NiFe Hydroxide Film Formed by Stepwise Electrodeposition Strategy with Significantly Improved Catalytic Water Oxidation Efficiency. *Adv. Energy Mater.* **7**, (2017).

42. El Wakkad, S. E. S. & Hickling, A. The anodic behaviour of metals. Part VI.—Cobalt. *Trans. Faraday Soc.* **46**, 820–824 (1950).

43. Shafirovich, V. Y. & Strelets, V. V. Catalytic-oxidation of water by cobalt complexes. *Nouv. J. Chim.* **2**, 199–201 (1978).

44. Burke, L. D., Lyons, M. E., & Murphy, O. J. Formation of hydrous oxide films on cobalt under potential cycling conditions. *J. Electroanal. Chem.* **132**, 247–261 (1982).

45. Bockris, J. O. The Electrocatalysis of Oxygen Evolution on Perovskites. *J. Electrochem. Soc.* **131**, 290 (1984).

46. Otagawat, T. Oxygen Evolution on Perovskites. *Electrochemistry* **79**, 2960–2971 (1983).

47. Chen, Y.-W. D. Electrodeposition of Nickel and Cobalt Oxides onto Platinum and Graphite Electrodes for Alkaline Water Electrolysis. *J. Electrochem. Soc.* **131**, 1447 (1984).

48. Rasiyah, P. The Role of the Lower Metal Oxide/Higher Metal Oxide Couple in Oxygen Evolution Reactions. *J. Electrochem. Soc.* **131**, 803 (1984).

49. Rasiyah, P. A Mechanistic Study of Oxygen Evolution on Li-Doped Co[sub 3]O[sub 4]. *J. Electrochem. Soc.* **130**, 365 (1983).

50. Kanan, M. W. & Nocera, D. G. In situ formation of an oxygen-evolving catalyst in neutral water containing phosphate and Co2+. *Science (80-.).* **321**, 1072–1075 (2008).

51. Casella, I. G. & Gatta, M. Study of the electrochemical deposition and properties of cobalt oxide species in citrate alkaline solutions. *J. Electroanal. Chem.* **534**, 31–38 (2002).

52. Esswein, A. J., Surendranath, Y., Reece, S. Y., & Nocera, D. G. Highly active cobalt phosphate and borate based oxygen evolving catalysts operating in neutral and natural waters. *Energy Environ. Sci.* **4**, 499–504 (2011).

53. Surendranath, Y., Dincă, M., & Nocera, D. G. Electrolyte-dependent electrosynthesis and activity of cobalt-based water oxidation catalysts. *J. Am. Chem. Soc.* **131**, 2615–2620 (2009).

54. Han, A., Wu, H., Sun, Z., Jia, H., & Du, P. Facile deposition of nanostructured cobalt oxide catalysts from molecular cobaloximes for efficient water oxidation. *Phys. Chem. Chem. Phys.* **15**, 12534–12538 (2013).

55. Chen, H., Sun, Z., Liu, X., Han, A., & Du, P. Cobalt-Salen Complexes as Catalyst Precursors for Electrocatalytic Water Oxidation at Low Overpotential. *J. Phys. Chem. C* **119**, 8998–9004 (2015).

56. Bonke, S. A., Wiechen, M., Hocking, R. K., Fang, X. Y., Lupton, D. W., Macfarlane, D. R., & Spiccia, L. Electrosynthesis of Highly Transparent Cobalt Oxide Water Oxidation Catalyst Films from Cobalt Aminopolycarboxylate Complexes. *ChemSusChem* **8**, 1394–1403 (2015).

CHAPTER II

Elaboration of porous ITO electrodes to improve the adsorption of nickel oxide-polypyrrole nanocomposite material for electrocatalytic water oxidation

Part of the work presented in this chapter has been published in the following article:

Nickel oxide–polypyrrole nanocomposite electrode materials for electrocatalytic water oxidation. *Catal. Sci. Technol.* **2018,** *8* (16), 4030-4043, Morales, D. V.; Astudillo, C. N.; Lattach, Y.; Urbano, B. F.; Pereira, E.; Rivas, B. L.; Arnaud, J.; Putaux, J.-L.; Sirach, S.; Cobo, S.; Moutet, J.-C.; Collomb, M.-N.; Fortage, J.

Index

I – Introduction

As we saw in the previous chapter of this manuscript, an attractive approach to produce molecular hydrogen to replace fossil fuels is to perform water splitting reaction *via* an electrochemical way. Nevertheless, the oxidative half-reaction, the water oxidation into oxygen (oxygen evolving reaction (OER)), remains a difficult reaction since it displays high activation barrier and large anodic overpotential. Numerous electrocatalysts have emerged to assess this problem, including the transition metals nickel and cobalt oxides.[1] For decades, metal and metal oxides nanoparticles inserted within a polymer matrix have received considerable attention; the nanoparticles impart the catalytic properties to the polymer nanocomposite, while the polymer controls their formation (size, shape, location), therefore, regulates the catalytic properties of the nanocomposite.[2] Polypyrrole has been an extensively studied polymer for the modification of electrode surfaces because of its easy polymerization, high conductivity, chemical stability, and biocompatibility.[3–5] Moreover, the anion-exchange properties of the oxidized form of polypyrrole have been largely used to immobilize catalytic species on electrode surfaces. However, obtaining metal catalyst-containing polypyrrole applying this anion-exchange properties has some drawbacks, polypyrrole acting only as an anion-exchange material, with an exchange capacity restricted to one negative charge per three pyrrole rings. The anion-exchange properties can be improved dramatically by linking ionic substituents to the polypyrrole skeleton, employing a monomer such as pyrrole substituted by an alkyl ammonium group. The pyrrole alkylammonium derivative depicted in Scheme 1, (3-pyrrole-1-yl-propyl)-triethylammonium tetrafluoroborate, denoted as **PN**$^+$), was firstly synthetized and studied by our group in 1989.[6] Electropolymerized polypyrrole films of **PN**$^+$ (denoted **PPN**$^+$) have proven to have an enhanced and potential-independent anion-exchange behaviour, as compared to the regular polypyrrole. It allowed the effective extraction and binding of metal complexes, organic and inorganic anions, from organic and aqueous media as well as the study of the resulting modified electrodes in organic and aqueous electrolytes.[7–10] Indeed, with this approach, our group has recently elaborated nanocomposite materials of poly(pyrrole-alkyl ammonium)/nanoparticles of metal or metal oxide (**IrO_x**, **NiO_x** and **MoS_x**) for both the OER and HER.[10,11] Such nanomaterials were easily electrodeposited at the surface of an electrode by a simple "all electrochemical" procedure (Scheme 1).

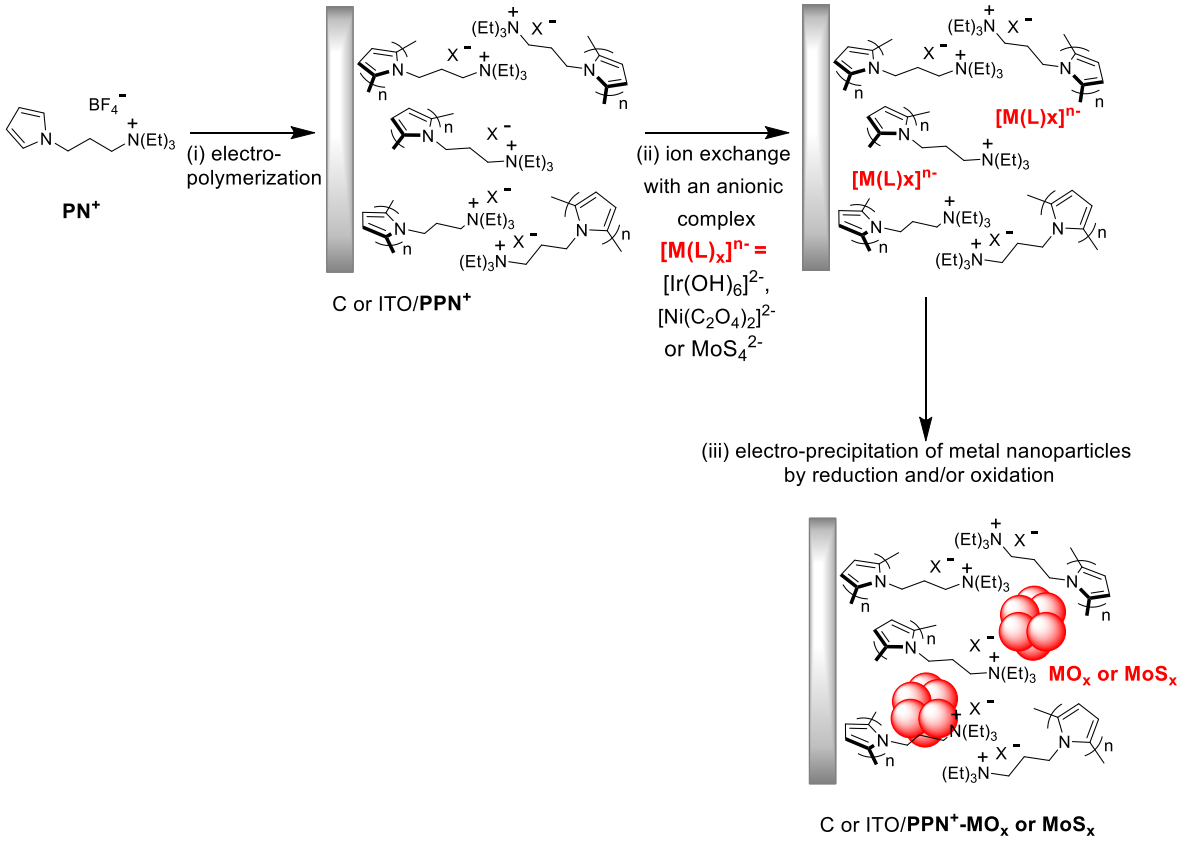

Scheme 1: General strategy for the electrosynthesis of **PPN$^+$-MO$_x$** (M = Ir or Ni) or **PPN$^+$-MoS$_x$** nanocomposite film at the surface of electrodes: (i) oxidative electropolymerization of the pyrrole monomer **PN$^+$** in CH_3CN; (ii) incorporation of $[M(L)_x]^{n-}$ into **PPN$^+$** upon soaking in an aqueous solution; (iii) electro-precipitation of metal (oxides) nanoparticles within the **PPN$^+$** film in an aqueous solution by reduction and/or oxidation.

The first step consists in the (i) electropolymerization of the **PN$^+$** monomer on the electrode surface, followed by the(ii) incorporation of an anionic metal complex by ion exchange in the positively charged **PPN$^+$** matrix and finally the (iii) electro-precipitation of nanoparticles *in situ* either by reduction or oxidation (Scheme 1). Nanocomposite materials based on iridium oxide (denoted **PPN$^+$-IrO$_x$**) were first obtained by oxidation of anionic species $[Ir(OH)_6]^{2-}$.[10] These anodes prove to be much more effective for electrocatalytic water oxidation, more stable and more economical in terms of amount of catalyst than pure **IrO$_x$** anodes directly deposited as thin films on the surface of the electrode. The method of electrosynthesis has been further extended with success to the development of materials without noble metals such as molybdenum sulfide (**MoS$_x$**) for the production of H_2 (HER) and then Ni oxides (**NiO$_x$**) for OER.[11,12] **MoS$_x$** was generated by simple incorporation and reduction of MoS_4^{2-} in **PPN$^+$** while **NiO$_x$** nanoparticles were obtained by incorporation of the anionic oxalate complex of Ni(II), $[Ni^{II}(oxalate)_2]^{2-}$, in **PPN$^+$** and then reduction to **Ni^0** followed by oxidation of **Ni^0** into **NiO$_x$**.[11] In addition to the positively charged polymer matrix that allows to entrap the metal anion

precursor, the polymer ensures the nano-sized particles of the metal oxide and, furthermore, provides them protection by avoiding their release into the solution, while performing the electrocatalytic experiments. Characterizations by transmission electron microscopy (TEM) and atomic force microscopy (AFM) of **PPN$^+$-IrO$_x$** and **PPN$^+$-NiO$_x$** confirmed the great nanostructuration of the material with small particles (2 nm for **IrO$_x$** and 21 nm and **NiO$_x$**) well dispersed into the polymer PPN$^+$ film.[10,11]

Regarding the **PPN$^+$-NiO$_x$** nanocomposite, the nature of the nickel nanoparticles was determined to be β-Ni^{III}(O)(OH) by coulometric titrations (Figure 1). In addition, the amount of nickel deposited at the electrode surface was estimated by inductively coupled plasma mass spectroscopy (ICP-MS).

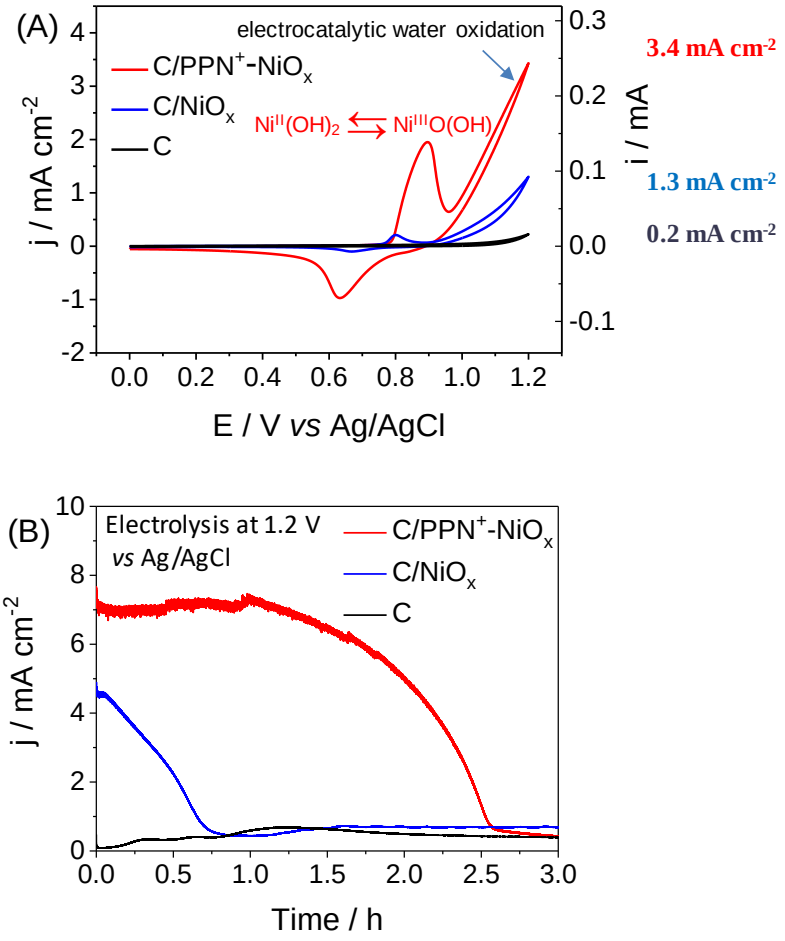

Figure 1: (A) Cyclic voltammograms (CVs) of C/**PPN$^+$-NiO$_x$** (red) (Γ_{N^+} = 1.1 x 10^{-7} mol cm^{-2}, Γ_{Ni} = 3.3 x10^{-8} mol cm^{-2}) and C/**NiO$_x$** (blue) (Γ_{Ni} = 1.2 x 10^{-8} mol cm^{-2}) electrodes (in black, the electroactivity of a naked C electrode of 3 mm diameter) in an aqueous 0.1 M borate buffer solution (pH 9.2), scan rate 50 mV s^{-1}. (B) Chronoamperograms recorded at C/**PPN$^+$-NiO$_x$** (red) and C/**NiO$_x$** (blue) (C electrode of 3 mm diameter) in a stirred 0.1 M aqueous borate buffer solution (pH 9.2), at constant potential of +1.2 V *vs* Ag/AgCl (adapted from ref,[11] with permission from the Royal Society of Chemistry, Copyright 2018)

Owing to the small size of the **NiO_x** nanoparticles and the great nanostructuration of the **PPN^+-NiO_x** nanocomposite, this material deposited on a glassy carbon electrode displays a very high electrocatalytic OER performances with strong mass activity and TOF values at pH 9.2 calculated to be 1.12 A mg^{-1} and 0.17 s^{-1} for an overpotential of 0.61 V.[1] These performances place the C/**PPN^+-NiO_x** electrode among the most active anodes based on nickel oxide already reported for the OER and undoped with iron ions (see Chapter I). In addition, the PPN^+-NiO_x electrodes prepared in this previous work appeared to be more efficient than the nickel oxide film electrogenerated directly on a naked electrode surface (denoted C/NiO_x) by the same electrochemical procedure, highlighting the beneficial role of the polypyrrole matrix (Figure 1(A)). Nevertheless, the stability of C/**PPN^+-NiO_x** and C/**NiO_x** electrodes during the electrolysis at pH 9.2 does not exceed 3 hours at an applied potential of +1.2 V *vs* Ag/AgCl. Indeed, after 1 h of electrolysis, the current density of the C/**PPN^+-NiO_x** electrode starts to drastically decreases (Figure 1(B)). This loss in activity is due to the progressive detachment of the polymer film from the electrode surface caused by the oxygen bubbling in the course of the electrolysis but it is not caused by the degradation of the C/**PPN^+-NiO_x** material. The electrogeneration of the nanocomposite film onto a different electrode substrate as indium tin oxide (ITO) electrode to perform some structural characterization of the film was also challenging since it can detach even more easily from the glass surface than from the C electrode surface, especially in aqueous solution. In this line, Zhang and coworkers introduced in 2015 a new, facile, and cheap method to modify layers on the ITO substrate by nanostructuration, following an electrochemical procedure.[13] The electrodeposition of different metal (Au, Ag, Pt, Cu…) onto such nanostructured ITO electrodes considerably increases the mechanical stability of the deposited materials. In this context, the objective of the work described in this chapter was to develop a procedure to modify the surface of the ITO based on the work described by Zhang, in view to increase the physisorption of the metal oxide-poly(pyrrole-alkyl ammonium) nanocomposite on the ITO electrode surface by preventing the film detachment during electrolyses. Thus, the aim was to fully demonstrate the greater stability of the nanocomposite materials compared to simple **NiO_x** films deposited on an electrode surface.

In this chapter, we will first describe the method used for the nanostructuration of ITO surfaces and the characterization of the resulting porous electrodes. Then the elaboration and characterization by SEM-EDX and AFM spectroscopies of the poly(pyrrole-alkylammonium)-

nickel oxide nanocomposite materials on these porous ITO electrodes will be presented. Finally the electrocatalytic performances of the resulting electrodes for OER is discussed.

II – Results

II.1. Elaboration and characterization of the nanostructured Indium Tin Oxide (ITO) electrodes

II.1.1. Elaboration of the nanostructured ITO plates by electrochemical reduction and acidic pre-treatment to introduce nanostructuration

The physisorption of the metal oxide-poly(pyrrole-alkyl ammonium) nanocomposite on the electrode was insufficient to retain the polymeric film onto its surface during analysis especially in water, neither through a long electrolysis under basic mild aqueous solutions. To successfully achieve experiments with the nanocomposite material on this type of electrode, it is necessary to modify its surface. Different strategies have been already used to modify the ITO electrode's surface with various functional molecules, including drop-casting, the Langmuir-Blodgett technique, electrostatic adsorption, covalent bonding, vapor deposition as well as electrodeposition.[14–16] In particular, we focused on the different approach reported recently by Zhang et al[13], in which porosity is introduced on the ITO electrode by a pre-treatment using a simple two-step procedure. The first step involves the reduction of a thin layer of indium and tin oxide on the surface of the ITO plate: this step was achieved by applying a cathodic potential at -1.15 V vs Ag/AgCl in a degassed neutral buffer phosphate solution (0.1 M, pH 7.0), in a time range that varied between 60 and 200 seconds (no information upon dimensions of the ITO surface was given in this article). In a second step, the reduced In-Sn layer was stripped through soaking the electrode in aqua regia (hydrochloric acid and nitric acid in a ratio of 3:1) for 2 seconds, and the process was finished by rinsing the porous ITO electrode with abundant water to remove the excess of acid. We adapted this procedure to ensure as much as possible the reproducibility of the process, without compromising considerably the conductivity of the ITO plate. Indeed, the conditions of reduction and stripping were changed as the reported process was too harsh for the ITO plates that we have in hand (30 Ohms purchased from Solens). The reduction time of 60-200 seconds at -1.15 V *vs* Ag/AgCl in phosphate buffer of step 1 (Scheme 2) was replaced to a limit of 20 mC of reduction charge passed through the plate (ITO surface of 0.4 cm^2). About 70 seconds is required to pass this amount of charge which is in the range of time used by Zhang et al., but this method is more reproducible for the preparation of porous ITO electrodes. This limit of 20 mC was initially established empirically as it was noticeable to provide the best activity when the nanocomposite

was electrodeposited on its surface. Further reduction lead to electrochemically non-conducting ITO electrodes, probably due to the fact that all the conductive material was reduced, causing a great irreversible damage. In addition, the acid treatment in step 2 was reduced from 2 to 1 second, to avoid the excessive exposure to harsh conditions and minimize as much as possible the damage in the conductivity of the electrode.

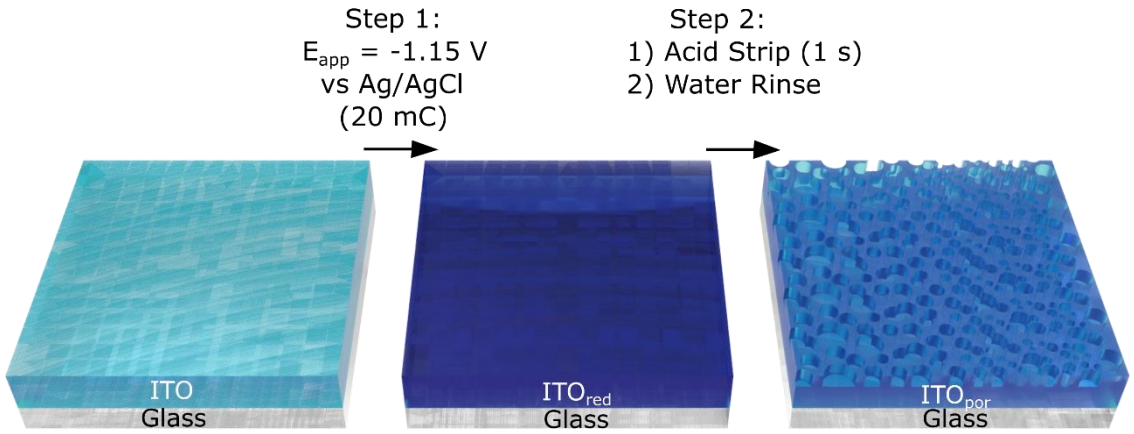

Scheme 2: Schematic illustration of the pre-treatment method used to introduce nanostructuration on the ITO plates, based on reference.[13]

II.1.2. Characterization of the nanostructured ITO plates by SEM-EDX and AFM spectroscopies

To follow the evolution of the ITO plates before and after nanostructuration, scanning electron microscopy (SEM) images were recorded. The comparison of the surface of simple ITO plates and ITO plates that underwent the pre-treatment procedure and are referred as "porous ITO" (denoted as ITO_{por}) are shown in Figure 2. The cross-section and the surface image of the untreated simple ITO (Figure 2(A-B)) display a flat and highly uniform surface at a macro and microscale, which contains only a few noticeable crystal defects. Images of the ITO plate with the reduced In-Sn layer were not taken in consideration since no obvious change in the topography was observed in the in-between step of the process in the published report.[13] Nevertheless, when the In–Sn layer that was stripped with aqua regia to generate the ITO_{por} electrodes (Figure 2(C-D)), a bumpy and uniformly nanosized porous surface was observed.[13] The report of Zhang et al. assumes that the crystal defects act as the anchoring sites for the growth of the electrodeposited materials, with a subsequent high mechanical stability. It is also presumed that only the crystal nuclei that grows and fills the defects on the surface is stable enough to not drop into the solution during the initial deposition phase, resulting in a *zip-like*

material/electrode interface with countless toeholds to stabilize the material deposited on ITO_{por}, unlike the untreated flat ITO electrode.

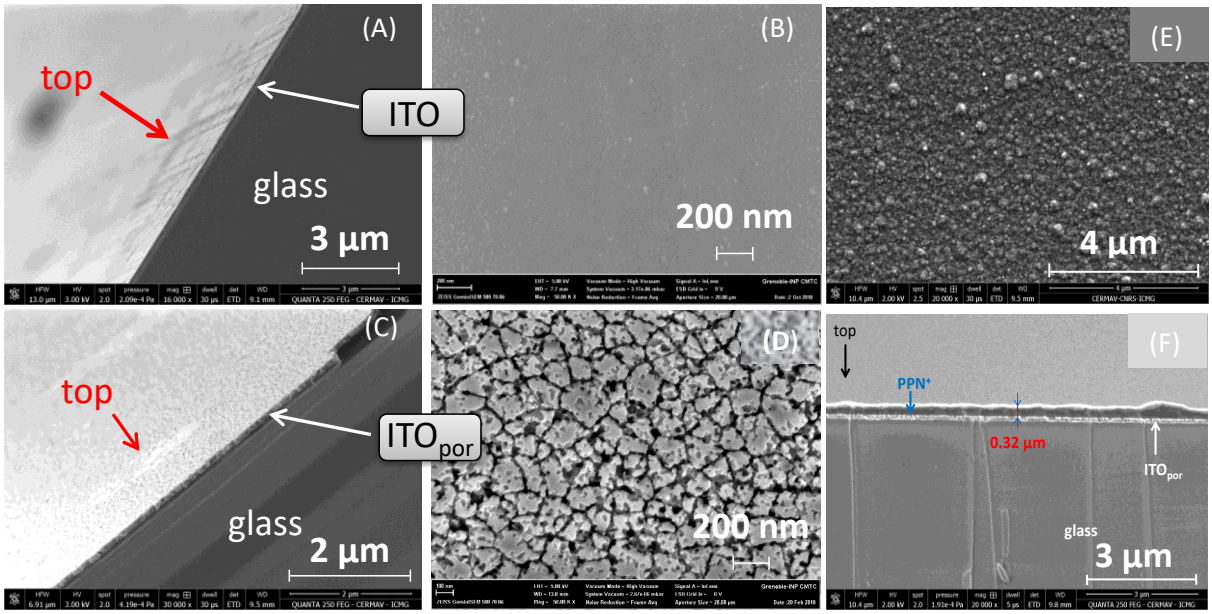

Figure 2: SEM images of cross-section and top view of the surface of simple ITO plate (A-B) and the nanostructured ITO plate, ITO_{por} (C-D). SEM images of the top view (E) and the cross section (F) of ITO_{por}/**PPN**$^{+}$.

Complementary studies by SEM coupled with EDX detector on the nanostructured ITO_{por} plates confirmed that the film of indium tin oxide is present (Figure 3). However, as tin acts only as a dopant in the ITO electrode, it is thought that the signal of this element is below the detection limit of the instrument, and therefore, not visible.

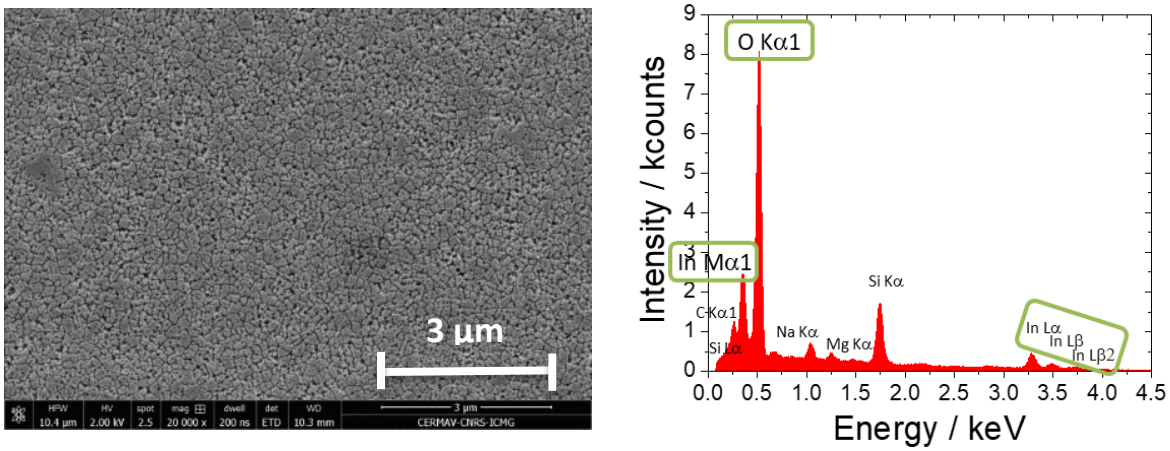

Figure 3: SEM images (left) and EDX spectrum (right) of ITO_{por}.

Studies by atomic force microscopy (AFM) on ITO and ITO_{por} showed similar results as SEM. The flat and uniform untreated ITO plate (not shown) displayed a root-mean square (r. m. s.) roughness of 1.1 nm. By contrast, for the porous ITO nanostructurated by our method of reduction and stripping of the metallic In-Sn layer at the surface, the roughness number increased from 1.1 nm to 2.35 nm (Figure 4). This quantifies what was observed by SEM images.

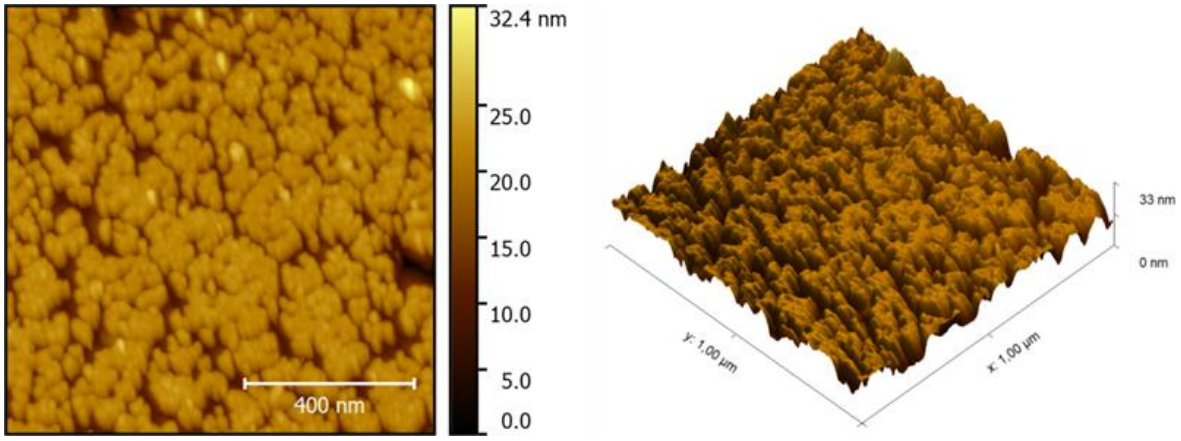

Figure 4: AFM images in tapping mode (left) and in 3D profile (right) of the porous ITO.

The effectiveness on the nanostructuration procedure of the ITO plates observed *via* the adhesion of the poly(pyrrole-alkyl ammonium) polymer will be discussed on the next section.

II.2. Electrosynthesis and characterization of the poly(pyrrole-alkylammonium)-nickel oxide nanocomposite electrode materials on the porous ITO

For the electro-deposition of the poly(pyrrole-alkylammonium)-nickel oxide nanocomposite electrode material at the surface of ITO_{por} electrodes, we used the four-step procedure depicted in Scheme 3, which was previouly used for films deposition on glassy carbon (diameter of 3 mm) or regular ITO electrodes. The electropolymerization of **PPN^+** from a concentrated solution of the pyrrole-alkylammonium PN^+ monomer (4 mM) in CH_3CN is the first step of the process. This step is performed in a dry glove box.

Scheme 3 : Formation of PPN^+ by oxidative electro-polymerization of monomer $\mathbf{PN^+}$ (4 mM) at E_{app} = +1.1 V vs Ag/$AgNO_3$ in CH_3CN, 0.1 M $[Bu_4N]ClO_4$; (ii) incorporation of $[Ni(C_2O_4)_2]^{2-}$ into PPN^+ upon soaking during 1h in an aqueous solution (pH 6) of 1 mM $NiSO_4$, 5 mM $Na_2C_2O_4$, 0.1 M Na_2SO_4 and 0.1 M H_3BO_3; (iii) electro-precipitation of $\mathbf{Ni^0}$ within $\mathbf{PPN^+}$ at E_{app} = -1.4 V vs Ag/AgCl in the previously mentioned aqueous solution of nickel oxalate; (iv) electrooxidation of $\mathbf{Ni^0}$ to $\mathbf{NiO_x}$ by repeated cyclic voltammetry scans between 0 and +1.2 V *vs* Ag/AgCl in an aqueous solution (pH 9.2) of 0.1 M H_3BO_3 and 0.05 M NaOH.

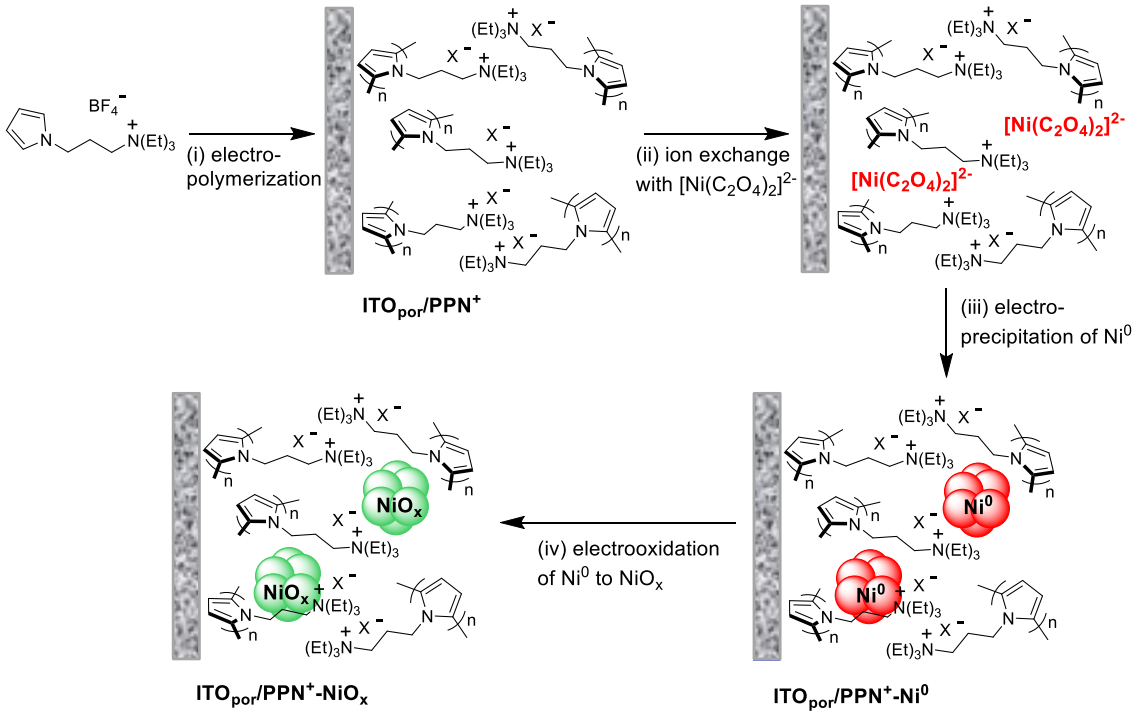

II.2.1. Elaboration of the ITO_{por}/PPN^+-NiO_x

The electrochemical behaviour of the monomer $\mathbf{PN^+}$ was firstly studied to establish the best electrodeposition parameters, employing a three-electrode system. The cyclic voltammogram at a glassy carbon working electrode (C, diameter 3 mm) of a solution of PN^+ (4 mM) in acetonitrile solution containing 0.1 M tetrabutylammonium perchlorate ($[Bu_4N]ClO_4$), exhibits an intense irreversible peak at about 0.95 V, corresponding to the oxidation of the pyrrole units into polypyrrole (Figure 5(A)). The formation of the polypyrrole film on the electrode surface can be achieved by successive cycles ranging between -0.2 V and 1.1 V as shown in Figure 5(A). The progressive growth of the polypyrrole film is evidenced by the increase in current density of a reversible wave located at about +0.3 V typical of the electroactivity of the polypyrrole. If scans are limited to lower anodic potentials, this behaviour was not observed, and no polymeric growth is detected (not shown).

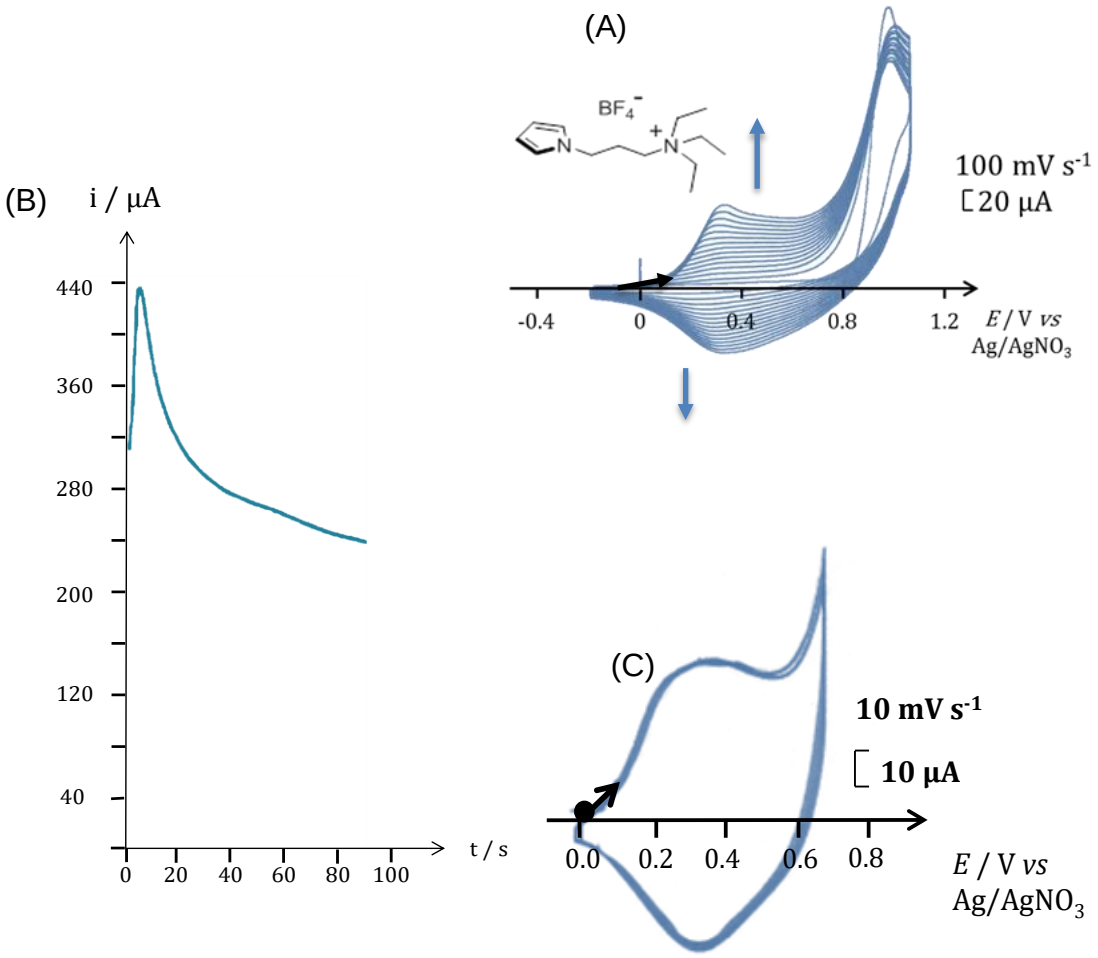

Figure 5: (A) Oxidative electropolymerization of a 4 mM solution of the monomer $\mathbf{PN^+}$ (inset) in CH_3CN + 0.1 M $[Bu_4N]ClO_4$ by 15 successive scans between -0.2 and +1.1 V *vs* $Ag/AgNO_3$ on a glassy carbon electrode (3 mm in diameter) ; scan rate 100 mV s^{-1}. (B) Chronoamperogram of the electrodeposition of the $\mathbf{PPN^+}$ film on a ITO_{por} electrode (0.4 cm^2) at an applied potential of 1.1 V (charge passed 22.4 mC) from a 4 mM of the monomer $\mathbf{PN^+}$ in CH_3CN + 0.1 M $[Bu_4N]ClO_4$. (C) Cyclic voltammograms (3 successive scans) of the $ITO_{por}/\mathbf{PPN^+}$ modified electrode after transfer in CH_3CN + 0.1 M $[Bu_4N]ClO_4$, scan rate 10 mV s^{-1}.

Films of $\mathbf{PPN^+}$ can be also deposited at an applied potential of +1.1 V, *i.e.* a potential corresponding to the edge of the irreversible oxidation wave of the pyrrole monomer. We used this procedure to electrodeposit films of $\mathbf{PPN^+}$ on the surface of ITO_{por} electrodes (0.4 cm^2), and the anodic charge passed for polymerization was fixed at 22.4 mC. This charge corresponds to 56 mC cm^{-2}, the same charge by surface unit having been used for regular C electrode (4 mC for a surface of 0.071 cm^2) in view to ensure a good comparison with the previous work. For the ITO_{por}, the deposition time of the $\mathbf{PPN^+}$ polymer for 22.4 mC at +1.1 V usually takes about two minutes (Figure 5(B)). The amount of the polymer electrodeposited on the ITO_{por} (0.40 cm^2), corresponding to the surface coverage in ammonium units Γ_{N+} (mol cm^{-2}), *i.e.* the quantity of pyrrole units, was measured electrochemically through the integration of the

polypyrrole reversible wave between 0.0 V to +0.6 V *vs* $Ag/AgNO_3$ at a low scan rate (10 mV s^{-1}) after transfer of the modified electrode in a CH_3CN +0.1 M $[Bu_4N]ClO_4$ solution free of $\mathbf{PN^+}$ (Figure 5(C)). Γ_{N+} of 9.36 (± 0.46) × 10^{-8} mol cm^{-2} was calculated for an average of ten ITO_{por} electrodes with a of 22.4 mC of charge under polymerization at +1.1 V.

The anion-exchange behavior of the poly(pyrrole-alkylammonium) film was previously evaluated by electrochemical measurements in aqueous and organic media, using anions such as ferricyanide ($[Fe(CN)_6]^{3-}$), and is known to efficiently extract anions from their containing solvents by incorporating them into the polymeric matrix[6], even with compounds as bulky as porphyrin.[9] Thus, the anion-exchange properties of this cationic polymeric film was used to incorporate the anionic nickel oxalate complex, $[Ni(C_2O_4)_2]^{2-}$, by soaking the $ITO_{por}/\mathbf{PPN^+}$ electrode for 1 hour in an aqueous borate buffer (0.1 M) solution at pH 6 (Scheme 3 (ii)), which contained the $[Ni(C_2O_4)_2]^{2-}$ complex *in situ* generated by mixing 1 mM of nickel sulfate ($NiSO_4$) and 5 mM of sodium oxalate ($Na_2C_2O_4$). According to previous studies under such conditions, the dianionic $[Ni(C_2O_4)_2]^{2-}$ complex is the largely predominant species present in solution compared to $Ni(C_2O_4)$ and $[Ni(C_2O_4)_3]^{4-}$.[17]

The electro-precipitation of the metallic particles ($\mathbf{Ni^0}$) was performed as previously reported,[11] by applying a potential of E_{appl} = -1.4 V *vs* Ag/AgCl in the nickel oxalate solution under argon atmosphere (Scheme 3, (iii)), since the reduction of Ni^{2+} into $\mathbf{Ni^0}$ at the surface of the electrode is observed to occur below -0.9 V *vs* Ag/AgCl[17] under the same conditions. In terms of comparison, a film of Ni^0 electrode was electrodeposited on a nude porous ITO following the same conditions, but without the soaking process. The deposition times on the $ITO_{por}/\mathbf{PPN^+}$ for 22.4 mC (56 mC cm^{-2}) is almost 140 seconds, while for the nude ITO_{por} it is less than 50 s for the same amount of charge (Figure 6). The explanation can be found in the inherent resistivity to the mass and electrons of the polypyrrole derivative film which does not exist in the case of the ITO_{por} alone. The Ni loading (Γ_{Ni}) on the $ITO_{por}/\mathbf{PPN^+}$ and ITO_{por} electrodes was estimated to 5.76 (± 1.48) × 10^{-8} mol cm^{-2} and 1.09 (± 0.41) × 10^{-8} mol cm^{-2} by ICP-MS measurements, corresponding to deposition yields of 19.8 and 3.8%, respectively. Thus, for the same quantity of charge (22.4 mC), the amount of Ni^0 deposited on the $ITO_{por}/\mathbf{PPN^+}$ film is 5.2 times larger than that deposited on the naked ITO_{por} electrode. For regular carbon electrodes, with a charge of 4 mC passed for nickel deposition, Γ_{Ni} of 3.32 (±0.19) x 10^{-8} mol cm^{-2} for $C/\mathbf{PPN^+}$ and 1.19 (±0.03) x 10^{-8} mol cm^{-2} for naked C electrode were obtained, corresponding to deposition yields of 11.4% and 4.1%, respectively[13].

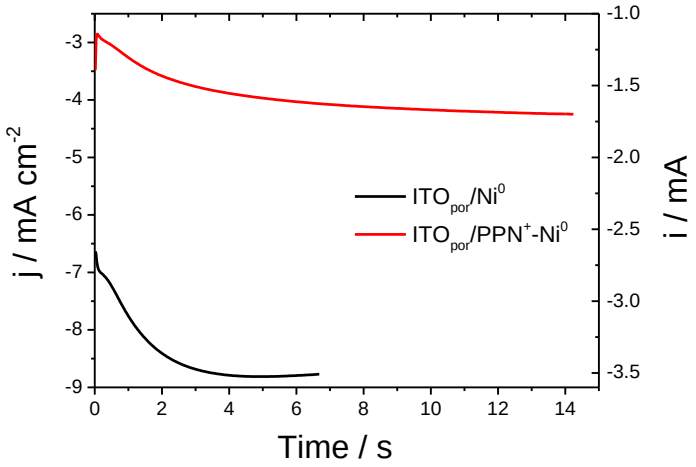

Figure 6: Nickel deposition (E_{appl} = -1.4 V, $Q_{deposition}$= 22.5mC) on ITO_{por} /**PPN$^+$** (Γ_{N^+} = 9.36 (± 0.46) × 10^{-8} mol cm^{-2}, Γ_{Ni} = 5.76 (± 1.48) × 10^{-8} mol cm^{-2}) and ITO_{por} (Γ_{Ni}= 1.09 (± 0.41) × 10^{-8} mol cm^{-2}) electrodes (0.4 cm^2) in 1 mM $NiSO_4$, 5 mM $Na_2C_2O_4$, 0.1 M $NaSO_4$ and 0.1 M H_3BO_3 solution.

The metallic nanoparticles of nickel present on ITO_{por}/**PPN$^+$** and ITO_{por} electrodes were then electro-oxidized into nickel oxide (**NiO_x**) by fifty successive anodic sweeps between 0.0 to +1.2 V *vs* Ag/AgCl at scan rate of 50 mV s^{-1}, after transfer of the ITO_{por}/**PPN$^+$-Ni^0** electrode into a borate buffer solution at pH 9.2 (Scheme 3 (iv) and Figure 7). The oxidation of Ni^0 to higher oxidation states is observed in the CV by the growing redox waves nearby +0.6 V and +0.9 V in the case of the nickel nanocomposite ITO_{por}/**PPN$^+$**, and +0.8 V and +0.7 V for the ITO_{por}. These values correlate to the ones obtained previously on the glassy carbon electrodes.[11] The waves ascribed to the $Ni^{II}(OH)_2/Ni^{III}(O)(OH)$ redox process attest the formation of NiO_x,[18] which is known to only appears when cycling until +1.2 V *vs* Ag/AgCl. In the case of the nanocomposite, the wide signal centered at +0.8 V, followed by the second broad one at +1.0 V observed in the first scan of the electro-oxidation process, correspond to the oxidation and overoxidation of the polypyrrole, respectively. Consequently, after the first scan, the polypyrrole film is fully overoxidized and has lost its conductivity. This is the reason why its related reversible wave has fully disappeared on the second scan. The overoxidation mechanism of polypyrrole was proposed by Beck et al.[19]

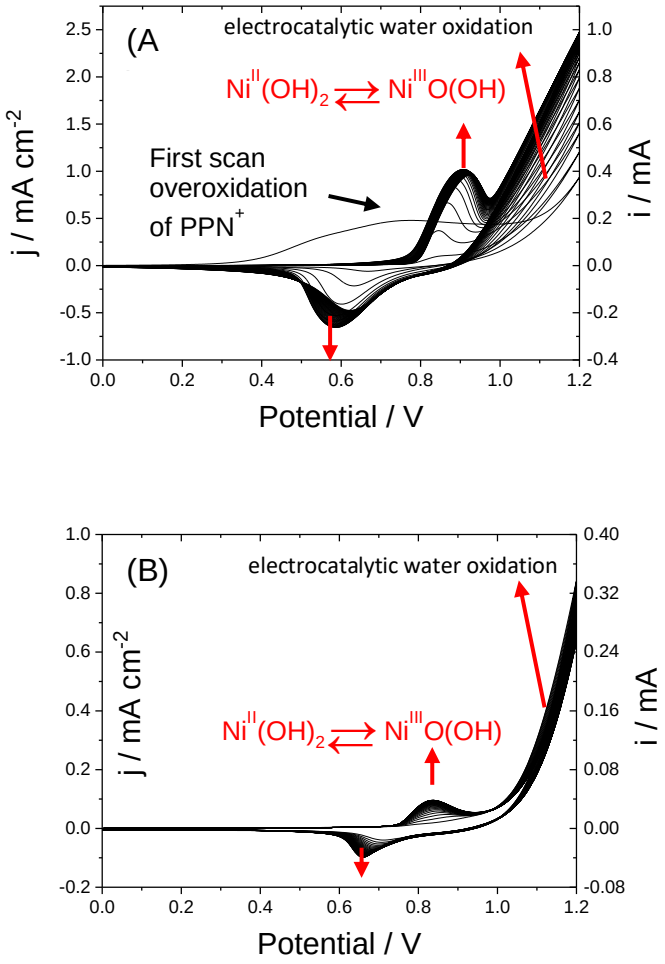

Figure 7: Electro-induced generation of NiO_x from Ni^0 by 50 repeated cyclic voltammetry (CV) scans in aqueous 0.1 M sodium borate buffer solution (pH 9.2) at ITO_{por}/**PPN^+-NiO_x** (Γ_{N^+} = 9.36 (± 0.46) × 10^{-8} mol cm^{-2}, Γ_{Ni} = 5.76 (± 1.48) × 10^{-8} mol cm^{-2}) (A) and ITO_{por}/**NiO_x** (Γ_{Ni} = 1.09 (± 0.41) × 10^{-8} mol cm^{-2}) (B), scan rate 50 mV s^{-1}.

In their mechanism, the β-carbon of the pyrrole unit was attacked by a nucleophilic hydroxide ion under the application of a highly positive potential as shown in Scheme 4. As a result, the carbonyl group is introduced at the β-carbon posit ion. The nucleophilic attack occurs irreversibly at an active site of the positive charged bipolaron.[20] Therefore, the polymer films acts only as a matrix at this stage, the nickel nanoparticles ensuring the conductivity of the nanocomposite material, while the nanostructuration of the ITO substrate prevents the film detachment. Indeed, it is important to note that we did not observe any desorption of the **PPN^+** films from the surface of the ITO_{por} during the steps of incorporation of **Ni^0** and oxidation of **Ni^0** into **NiO_x**, as it is often the case when **PPN^+** films are deposited on regular ITO. In fact, these two steps are accompanied by the formation of gas bubbles (H_2 for Ni deposition and O_2

for its oxidation into **NiO_x** due to the concomitant reduction and oxidation of water, respectively) which promotes the desorption of the **PPN^+** films from the electrode surface.

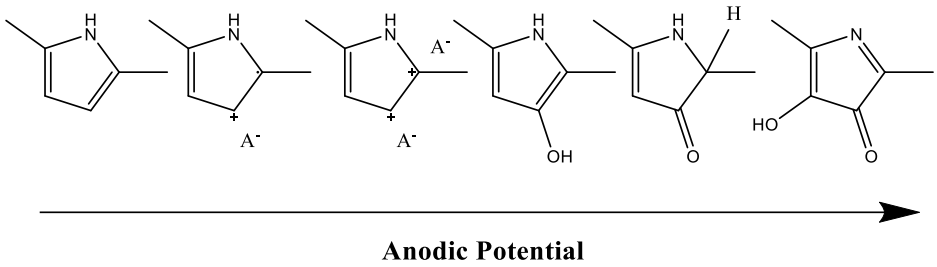

Scheme 4: Mechanism of the overoxidation of pyrrole by Beck[19].

II.2.2. Characterization of the ITO_{por}/PPN^+-NiO_x by AFM and SEM-EDX

For better understanding of the change of the morphology of the resultant material through every stage of the process, SEM images were recorded after each step. A cross-section view of the as-deposited ITO_{por}/**PPN^+** electrode and of ITO_{por}/**PPN^+-NiO_x** are shown in Figures 2(F) and 8. In both cases, the deposition of the film is uniform through the surface of the ITO_{por} electrode, which was not the case using simple ITO electrodes since the detachment of the PPN^+ occurred as soon as the polymeric film was transferred in an aqueous solution, owing to the poor adhesion of the film on the flat ITO surface. By measuring the length of layer of the polymer coating the electrode, we can observe an almost three-fold increase of the thickness (from 0.29 µm to 0.79 µm) after soaked in the nickel oxalate aqueous solution for the electroprecipitation of Ni^0 and its subsequent oxidation into NiO_x. The resulting ITO_{por}/**PPN^+-NiO_x** film appears to be bloated (0.79 µm), in contrast of the dehydrated sample that was taken from the inert and dry atmosphere of the glove-box (0.29 µm). Another interesting fact is that the layer of nanocomposite suffered during the voltammetry cycles realized for **Ni^0** oxidation, which reorganizes the polymer chains into two or three thinner layers through the surface of the ITO. The thickness of the **PPN^+-NiO_x** film is close to that of a **PPN^+-IrO_x** nanocomposite previously reported by our group. A thickness in the range of 0.10- 0.150 µm was measured by TEM for **PPN^+-IrO_x** films with a PPN^+ electrodeposited at +0.85 V *vs* Ag/AgCl and with a coverage surface in polypyrrole of $\Gamma_{N+} = 2.0 - 6.0 \times 10^{-8}$ mol cm^{-2}).[21] Since in the present work the amount of PPN^+ is slightly higher ($\Gamma_{N+} = 9.36 \times 10^{-8}$ mol cm^{-2}), it make sense to have slighlty thicker films.

Although nickel nanoparticles are not visible in the SEM cross-section images (Figure 9), complementary EDX experiments corroborate the successful electrodeposition of NiO_x (see below the Figure 11(A)).

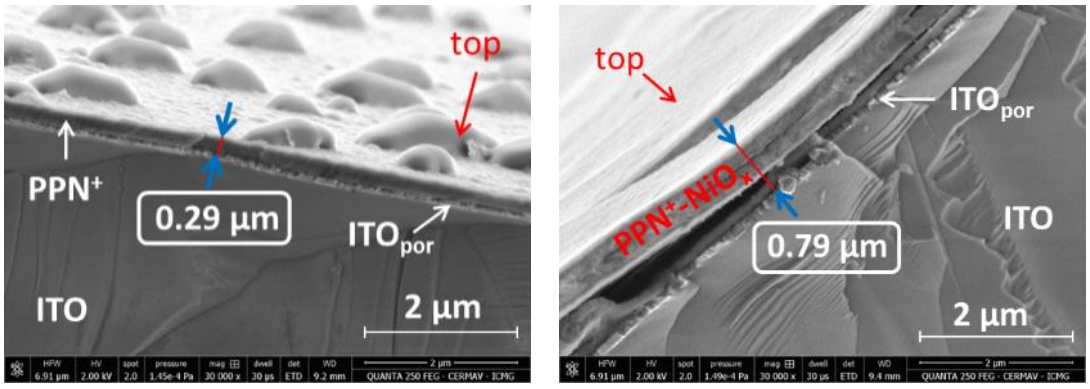

Figure 8: SEM images of the cross-section of ITO_{por}/$\mathbf{PPN^+}$ (left) and ITO_{por}/$\mathbf{PPN^+}$-$\mathbf{NiO_x}$ (right).

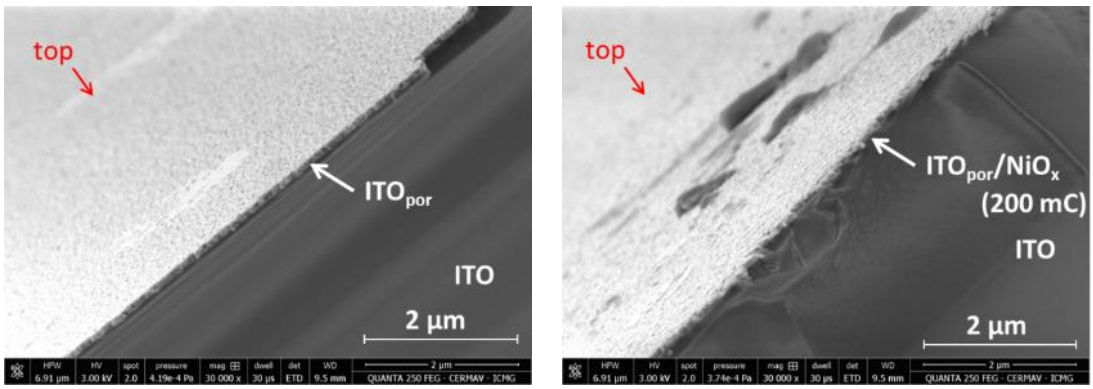

Figure 9: SEM images of the cross-section of naked ITO_{por} (A) and ITO_{por}/$\mathbf{NiO_x}$ (200 mC for deposition of Ni^0) (B).

Several studies regarding the electrodeposition of poly(pyrrole-alkylammonium) as a protective matrix for metal nanoparticles have been reported in our team. However, it is very difficult to achieve TEM images of a cross-section area of a film since it requires delicate preparation of the sample which must be cut into thin slices of less than 100 nm. Such images have been only successfully obtained for thin film (100 nm) of $\mathbf{PPN^+}$-$\mathbf{IrO_x}$. These images have revealed $\mathbf{IrO_x}$ particles with size ranging from 1-2 nm with a concentration of iridium similar over the whole structure and thus that the $\mathbf{IrO_x}$, particles are well distributed throughout the $\mathbf{PPN^+}$ film. By contrast, large aggregates of $\mathbf{IrO_x}$ particles with an average diameter from 100 to 200 nm have been observed when $\mathbf{IrO_x}$ is directly electrodeposited onto a naked ITO electrode. Regarding the $\mathbf{PPN^+}$-$\mathbf{NiO_x}$, TEM images of the $\mathbf{PPN^+}$-$\mathbf{NiO_x}$ film scratched off from a regular ITO electrode showed a network of well-dispersed nanoparticles of about 20 nm with a very narrow particle size distribution (22.4 ± 4.0 nm) while bigger $\mathbf{NiO_x}$ nanoparticles where obtained for NiO_x films directly deposited on the electrode surface with an average particle size of a hundred nanometers associated with a larger size distribution (*i.e.* 99.9 ± 42.5 nm, 125.9 ± 33.6 nm and 106.7 ± 33.7 nm).[11] Therefore, although nickel oxide particles were not seen in the SEM images

(Figure 8), previous evidence on the different metal oxide particles behaviour in the poly(pyrrole-alkylammonium) suggests that the NiO_x particles are well-dispersed into the film and are not concentrated on the interface ITO_{por}/**PPN$^+$**.[13]

We have also analyzed by SEM the NiO_x particles directy deposited onto a porous ITO electrode to observe the nanoparticles without the PPN^+ polymer. However there were no perceptible changes in the SEM images by comparing the naked ITO_{por} and the ITO_{por}/**NiO_x** (22.4 mC). Thus, a 10-fold increase in the cathodic charge (200 mC) was performed to evidence any visual changes, since the presence of nickel oxide is confirmed by EDX measurements (see below, Figure11(A)). The comparison of the cross-sectional SEM images of the naked ITO_{por} and ITO_{por}/**NiO_x** (200 mC) is shown in figure 9. Nevertheless, no nickel particles were able to be observed by SEM, which leads us to believe the particles grows inside de porous surface of the electrode even for a charge of 200 mC, and therefore fills the gaps of the nanostructurated ITO with conductive material, as hypothesized by Zhang.[13] In fact, an apparent change in the morphology is barely observed when the electrodeposition meet a 10-fold increase (200 mC), as shown in Figure 9(B).

An indirect proof of the NiO_x particles filling the holes of the porosity is the roughness measured by AFM. As mention in section II.1.2, the roughness measured previously in the group by AFM of bare ITO was calculated to be 1.1 nm and increased to 2.35 nm when porosity was introduced. Once the NiO_x coats ITO_{por} surface, the roughness was measured to be 3.0 nm with a granular topology with grain boundaries (Figure 10(B)). When the ITO_{por} surface is modified with **PPN$^+$-NiO_x**, the roughness number increased to 4.8 nm, with an ambiguous nodular topography, in which a cauliflower-like morphology observed in the Figure 10(A) is typical when a polypyrrole film is synthetized by electrodeposition.

Complementary EDX were assessed to corroborate the successful electrodeposition of NiO_x particles in the ITO_{por} and ITO_{por}/**PPN$^+$**, although the particles are not visible by SEM microscopy. As it is observed in Figure 11, SEM images are shown on the left, along with their corresponding EDX spectra, shown on the right. EDX on ITO_{por}/**NiO_x** confirmed the successful electrodeposition of NiO_x inside the holes of the nanostructuration of the eletrode with a small signal of nickel, either for a small amount of the catalysts or due to the beam was not able to reach and hit easily the nickel particle as it is inside and protected by the ITO rough surface.

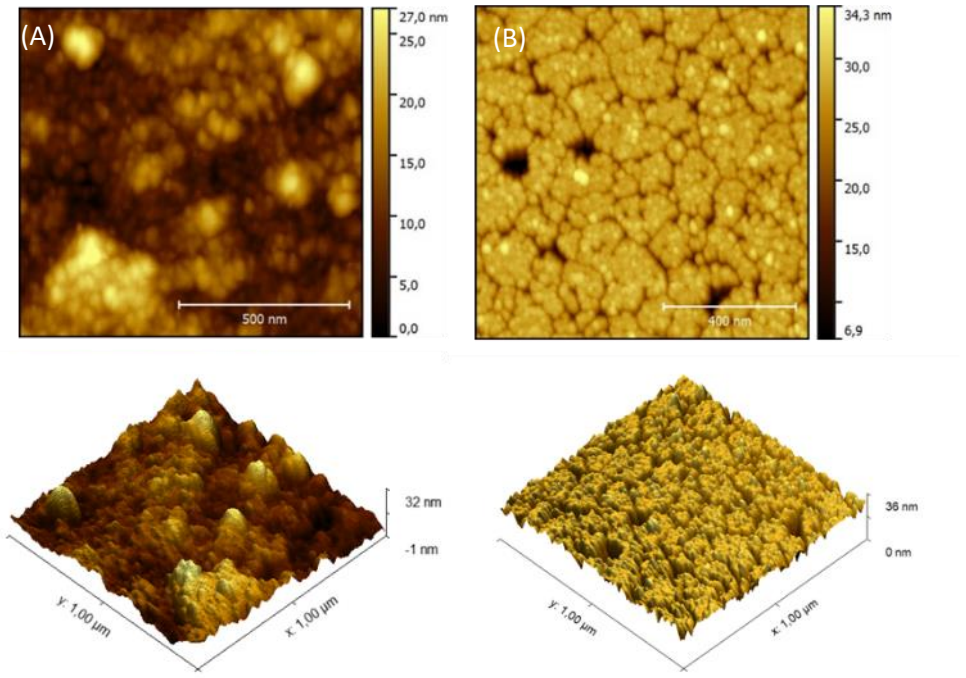

Figure 10: AFM images in tapping mode (top) and corresponding 3D profile (bottom) of ITO_{por}/**PPN^+-NiO_x** (22.4 mC for deposition of PPN^+ and Ni^0) (A) and ITO_{por}/**NiO_x** (22.4 mC for deposition of Ni^0) (B).

The large signals of oxygen, indium and silicium corresponds to the glass electrode and the carbon, sodium, aluminum and magnesium to the impurities from the buffers used in the nanostructuration process and the nanoparticles synthesis (Figure 11(A)). The polymer matrix shows thereafter strong EDX signals corresponding to carbon and nitrogen of the polypyrrole and a tinny peak of oxygen (Figure 11(B)). This last peak grows as the pyrrole is oxidized into pyrrolinone when the nickel oxide nanoparticles are incorporated in the polymer matrix by cycling (Figure 11(C)), resulting in the overoxidation of the polymeric film, as discussed previously in the mechanism proposed by Beck displayed in Scheme 4. The nickel peak, which is absent in the ITO_{por}/**PPN^+** EDX spectra, appears greater when the nickel is dispersed through the polymer film compared to NiO_x directly electrodeposited on the ITO_{por} (Figure 11(A)) attesting the higher amount of metal in this material than in ITO_{por}/**NiO_x,** where the NiO_x are mainly deposited inside the holes and thus difficult to detect.

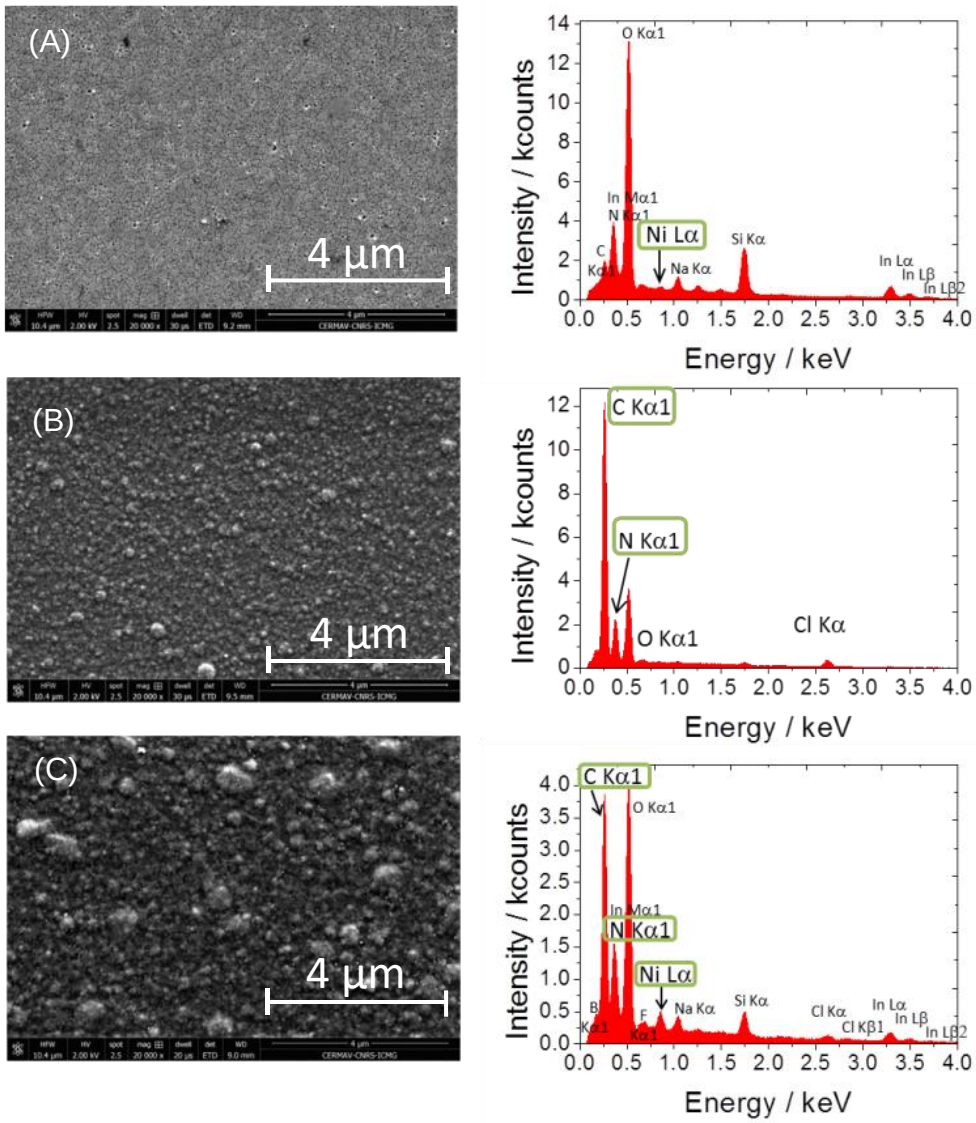

Figure 11: SEM images (left) and EDX spectrum (right) of ITO_{por}/**NiO_x** (22.4 mC for deposition of Ni^0) (A), ITO_{por}/**PPN^+** (B) and ITO_{por}/**PPN^+-NiO_x** (22.4 mC for deposition of PPN^+ and Ni^0) (C)

II.3. Electrocatalytic performance for OER of the nickel oxide-poly(pyrrole-alkylammonium) nickel oxide nanocomposite electrode materials deposited on porous ITO

The electrocatalytic activity and stability of ITO_{por}/**NiO_x** and ITO_{por}/**PPN^+-NiO_x** were evaluated by cyclic voltammetry and chronoamperometry in borate buffer at pH 9.2 (Figure 12). The nanocomposite ITO_{por}/**PPN^+-NiO_x** shows a higher catalytic current density than ITO_{por}/**NiO_x** (2.5 mA cm^{-2} *vs* 0.63 mA cm^{-2}) (Figure 12(A)). However since the amount of metal catalyst is 5.3 times higher when PPN^+ is present (5.76 x 10^{-8} *vs* 1.09 x 10^{-8} mol cm^{-2} respectively), and the NiO_x is deposited in the holes of the ITO_{por} electrode in the absence of

PPN$^+$, comparing the efficiency of the **PPN**$^+$**-NiO$_x$** and **NiO$_x$** is not relevant on such electrode material. Another reason of the weaker behavior of the ITO$_{por}$/**NiO$_x$** electrode is that the NiO_x particles inside the holes of the nanostructured ITO might be less accessible for the catalysis to occur. Anyway, the performance of the ITO$_{por}$/**PPN**$^+$**-NiO$_x$** anode with a mass activity for 490 mA mg^{-1} at overpotential of 0.61 V (*i.e.* 1.1 V *vs* Ag/AgCl) at pH 9.2, supports the positionning of the nanocomposite **PPN**$^+$**-NiO$_x$** anode material among the best reported nickel oxide-based anodes for water oxidation operating in a 0.1 M borate buffer solution under mild basic conditions,.

The stability of **PPN**$^+$**-NiO$_x$** is considerably improved by the nanostructuration of the ITO substrate compared to similar films deposited on carbon electrode (Figure 1(B)), since the catalytic current is stable over a period of 3 days at an applied potential of 1.2 V *vs* Ag/AgCl (Figure 12(B)) even under strong stirring conditions to prevent the resistance related to the mass transport and the variation in the pH in the proximity of the electrode, as well as the formation of large bubbles of O_2 which stay on the electrode surface. The noisy but stable signal of ITO$_{por}$/**PPN**$^+$**-NiO$_x$** is indeed explained by the strong bubbling of the anode, which blocks briefly the active sites of the nickel particles inside the polymeric matrix and therefore diminishes the catalytic response momentarily. After 3 days of electrolysis, the borate buffer solution was changed to a fresh one, since after several days the hydroxides are consumed and the pH drops to more acidic conditions; the reaction was resumed until the catalyst completed 7 days of activity. In the case of ITO$_{por}$/**NiO$_x$**, the stability is enhanced as well as for the nanocomposite since the stability does not exceed 1-2 h for a C/**PPN**$^+$**-NiO$_x$** and less than one 30 min for C/**NiO$_x$**[11]. However, the increase for ITO$_{por}$/**NiO$_x$** is less important compared to that obtained with ITO$_{por}$/**PPN**$^+$**-NiO$_x$**, since the catalytic current starts to gradually decline and after half a day and lost of activity by half is observed after only one day. This is probably due to the progressive detachement of the NiO_x particles from the ITO$_{por}$ surface. Thus, we were able to prevent the problem of the film detachment from the electrode (C or ITO) surface by using porous ITO electrodes which increase considerable the adherence of the polymeric film on the electrode surface. These results also confirm unambiguously that nanocomposite **PPN**$^+$**-NiO$_x$** based electrodes are more stable and robust for the OER reaction than bare **NiO$_x$** electrodes due to the beneficial role of the polypyrrole matric which prevents the corrosion and the release of NiO_x nanoparticles in solution.

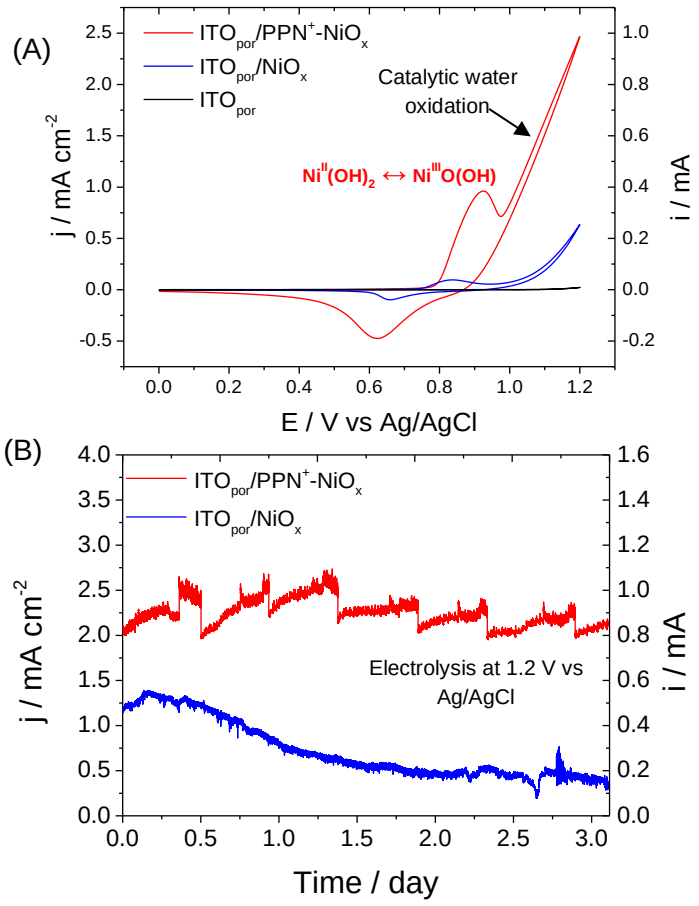

Figure 12: Overlay of the 50th scans of ITO$_{por}$/**PPN$^+$-NiO$_x$** (red) and ITO$_{por}$/**NiO$_x$** (blue) in 0.1 M borate buffer solution (pH 9.2) (in black, the electroactivity of a naked ITO$_{por}$ electrode of 0.4 cm^2) (A), and chronoamperograms in a stirred 0.1 M sodium borate aqueous solution (pH 9.2) at a constant potential of +1.2 V vs Ag/AgCl (B). Γ_{Ni} = 5.76 (± 1.48) × 10^{-8} and 1.09 (± 0.41) × 10^{-8} mol cm^{-2} respectively for ITO$_{por}$/**PPN$^+$-NiO$_x$** and ITO$_{por}$/**NiO$_x$**.

III – Conclusions

We report a very reproducible and cheap procedure to avoid the detachment of electrodeposition polymeric films from ITO electrodes by introducing porosity into the electrode surface with high mechanical stability. When the **PPN^+-NiO_x** nanocomposite is deposited in such electrode surfaces, its physisorption is considerably improved. Indeed, this treatment allows our efficient OER ITO_{por}/**PPN^+-NiO_x** anode to remain operational during a week during an electrolysis at 1.2 V *vs* Ag/AgCl, as long as the borate buffer solution at pH 9.2 is renewed to elude the pH drop, even under strong stirring conditions as well as with the formation of large bubbles of O_2. These results also confirm unambiguously that nanocomposite **PPN^+-NiO_x** based electrodes are more stable and robust for the OER reaction than bare **NiO_x** electrodes due to the beneficial role of the polypyrrole matric which prevents the corrosion and the release of **NiO_x** nanoparticles in solution.

This easy and reproducible method to nanostructured ITO electrodes inspired by the work of Zhang, which uses electrochemical reduction in neutral phosphate buffer and acid stripping, solves one of the most important problems concerning the use of modified ITO electrodes in practical applications: the poor adhesion of films on such electrode surface. The nanostructuration was well observed through SEM and AFM images of ITO_{por} in comparison with regular ITO. The roughness number of ITO_{por} increased from 1.1 nm to 2.35 nm compared to regular ITO. In addition, the conductivity of the resulting electrode is retained after treatment and the electro-polymerization of the pyrrole ammonium as well as the following electrochemical steps to electrogenerate the **NiO_x** particles inside the **PPN^+** film are not affected by the pre-treatment of the electrode. Furthermore, we did not observe the desorption of the **PPN^+** film during these two steps, which is often the case for non-nanostructured ITO electrodes. Finally, EDX and ICP-MS studies on the porous ITO surface confirm the presence of nickel although SEM and AFM images are unable to observe the nanoparticles.

References

1. Li, P., Zhao, R., Chen, H., Wang, H., Wei, P., Huang, H., Liu, Q., Li, T., Shi, X., Zhang, Y., Liu, M., & Sun, X. Recent Advances in the Development of Water Oxidation Electrocatalysts at Mild pH. *Small* **15**, 1–27 (2019).
2. Shifrina, Z. B., Matveeva, V. G., & Bronstein, L. M. Role of Polymer Structures in Catalysis by Transition Metal and Metal Oxide Nanoparticle Composites. *Chem. Rev.* **120**, 1350–1396 (2020).
3. Miodek, A., Mejri-Omrani, N., Khoder, R., & Korri-Youssoufi, H. Electrochemical functionalization of polypyrrole through amine oxidation of poly(amidoamine) dendrimers: Application to DNA biosensor. *Talanta* **154**, 446–454 (2016).
4. Ramanavičius, A., Ramanavičiene, A., & Malinauskas, A. Electrochemical sensors based on conducting polymer-polypyrrole. *Electrochim. Acta* **51**, 6025–6037 (2006).
5. Jain, R., Jadon, N., & Pawaiya, A. Polypyrrole based next generation electrochemical sensors and biosensors: A review. *TrAC - Trends Anal. Chem.* **97**, 363–373 (2017).
6. Cosnier, S., Deronzier, A., Moutet, J. C., & Roland, J. F. Alkylammonium and pyridinium group-containing polypyrroles, a new class of electronically conducting anion-exchange polymers. *J. Electroanal. Chem.* **271**, 69–81 (1989).
7. Zouaoui, A., Stéphan, O., Carrier, M., & Moutet, J. C. Electrodeposition of copper into functionalized polypyrrole films. *J. Electroanal. Chem.* **474**, 113–122 (1999).
8. Sánchez, J. A., Rivas, B. L., Pooley, S. A., Basaez, L., Pereira, E., Pignot-Paintrand, I., Bucher, C., Royal, G., Saint-Aman, E., & Moutet, J.-C. Electrocatalytic oxidation of As(III) to As(V) using noble metal–polymer nanocomposites. *Electrochim. Acta* **55**, 4876–4882 (2010).
9. De Gregori, I., Carrier, M., Deronzier, A., Moutet, J. C., Bedioui, F., & Devynck, J. Incorporation of anionic cobalt porphyrin by anion exchange into polypyrrole films containing alkylammonium groups. *J. Chem. Soc. Faraday Trans.* **88**, 1567–1572 (1992).
10. Lattach, Y., Rivera, J. F., Bamine, T., Deronzier, A., & Moutet, J.-C. Iridium Oxide–Polymer Nanocomposite Electrode Materials for Water Oxidation. *ACS Appl. Mater. Interfaces* **6**, 12852–12859 (2014).
11. Morales, D. V., Astudillo, C. N., Lattach, Y., Urbano, B. F., Pereira, E., Rivas, B. L., Arnaud, J., Putaux, J. L., Sirach, S., Cobo, S., Moutet, J. C., Collomb, M. N., & Fortage, J. Nickel oxide-polypyrrole nanocomposite electrode materials for electrocatalytic water oxidation. *Catal. Sci. Technol.* **8**, 4030–4043 (2018).
12. Morales Montecinos, D. V. Polypyrrole-metal oxide nanocomposite materials for electro- and photocatalytic water oxidation into oxygen. (Université Grenoble Alpes, 2018). doi:2018GREAV012.
13. Zhang, X., Lou, B., Li, D., Hong, W., Yu, Y., Li, J., & Wang, E. A universal method for the preparation of functional ITO electrodes with ultrahigh stability. *Chem. Commun.* **51**, 6788–6791 (2015).
14. Wu, M. S., Yuan, D. J., Xu, J. J., & Chen, H. Y. Sensitive electrochemiluminescence biosensor based on Au-ITO hybrid bipolar electrode amplification system for cell surface protein detection. *Anal. Chem.* **85**, 11960–11965 (2013).
15. Zhang, X., Li, J., Jia, X., Li, D., & Wang, E. Full-featured electrochemiluminescence sensing platform based on the multichannel closed bipolar system. *Anal. Chem.* **86**,

5595–5599 (2014).

16. Musselman, K. P., Mulholland, G. J., Robinson, A. P., Schmidt-Mende, L., & MacManus-Driscoll, J. L. Low-temperature synthesis of large-area, free-standing nanorod arrays on ITO/glass and other conducting substrates. *Adv. Mater.* **20**, 4470–4475 (2008).
17. Zouaoui, A., Stéphan, O., Ourari, A., & Moutet, J. C. Electrocatalytic hydrogenation of ketones and enones at nickel microparticles dispersed into poly(pyrrole-alkylammonium) films. *Electrochim. Acta* **46**, 49–58 (2000).
18. Doyle, R. L., Godwin, I. J., Brandon, M. P., & Lyons, M. E. G. Redox and electrochemical water splitting catalytic properties of hydrated metal oxide modified electrodes. *Phys. Chem. Chem. Phys.* **15**, 13737 (2013).
19. Beck, F., Braun, P., & Oberst, M. Organic Electrochemistry in the Solid State-Overoxidation of Polypyrrole. *Berichte der Bunsengesellschaft/Physical Chem. Chem. Phys.* **91**, 967–974 (1987).
20. Osaka, T., Momma, T., Komaba, S. ichi, Kanagawa, H., & Nakamura, S. Electrochemical process of formation of an insulating polypyrrole film. *J. Electroanal. Chem.* **372**, 201–207 (1994).
21. Rivera, J. F., Pignot-Paintrand, I., Pereira, E., Rivas, B. L., & Moutet, J. C. Electrosynthesized iridium oxide-polymer nanocomposite thin films for electrocatalytic oxidation of arsenic(III). *Electrochim. Acta* **110**, 465–473 (2013).

CHAPTER III

Cobalt oxide-polypyrrole nanocomposite as efficient and stable electrode material for electrocatalytic water oxidation

Index

I – Introduction

As we introduced in Chapter I of the manuscript, several earth-abundant metal oxides such as Fe, Mn, Cu, Co and Ni and their alloys have been investigated as electrocatalysts for OER under mild pH conditions.[1] Among them, cobalt oxide (CoO_x) has been intensively studied by many groups under alkaline conditions.[2-31] Originally identified as an electrocatalyst for water oxidation at pH 14 in 1950 by El Wakkad and Hickling,[32] CoO_x received a renewed interest in 2008, owing to the work of Nocera and co-workers demonstrating that thin films of this earth-abundant metal oxide electrodeposited in a proton-accepting phosphate (pH 7)[9,10] or borate (pH 9.2)[10] buffer are also very active OER electrocatalysts in such neutral or near-neutral conditions.

As we described in Chapter II, a key and important factor in the performance of an electrocatalyst for the OER is its nanostructuration, as it was helpful when introduced in iridium and nickel oxide nanoparticles of small sizes (2 – 21 nm), into a polypyrrole-alkylammonium matrix to generate the electrocatalyst by an electrochemical approach to design nanocomposite electrode materials.[33,34] In this context, we have extended this interesting strategy to cobalt oxide and we report in this chapter a very active and stable anode for OER operating at pH 9.2 based on a cobalt oxide-poly(pyrrole-alkylammonium) nanocomposite (denoted **PPN^+-CoO_x**). This work was initiated during Daniela Morales' thesis,[35] which has optimized the conditions for the incorporation of the cobalt oxalate complex into the nanocomposite, and obtained AFM and TEM images of the **PPN^+-CoO_x** nanocomposite deposited on ITO.

We will first describe the electrodeposition of the **PPN^+-CoO_x** nanocomposite material onto vitreous carbon (denoted C) as well as on porous indium tin oxide (ITO_{por}) electrodes, using similar procedures to those introduced in the previous chapter. The material has been then characterized by various electrochemical and microscopy techniques (SEM-EDX and XPS), and the amount of cobalt was also quantified by inductively coupled plasma mass spectrometry (ICP-MS). Finally, the electrocatalytic properties of this nanocomposite material toward water oxidation have been evaluated in a 0.1 M borate buffer at pH 9.2 and compared with those of **CoO_x**-based anodes of literature under similar catalytic conditions and with that of **CoO_x** films directly deposited on a naked electrode by the same electrochemical procedure, in order to highlight the

beneficial role of the PPN^+ matrix in generating non-agglomerated **CoO_x** particles with higher OER activity.

II – Results

II.1. Electrosynthesis and Electrochemical Characterization of Cobalt Oxide and Poly(pyrrole-alkylammonium)-Cobalt Oxide Nanocomposite Electrode Materials.

The four-step electrochemical procedure used to prepare the C or ITO_{por}/**PPN^+-CoO_x** modified electrodes depicted in Scheme 1, are comparable to the one used to prepare the nickel oxide-based nanocomposite described in Chapter II. The main difference is the concentration of the metal salt and oxalate which have been multiplied by four compared for cobalt (4 mM $CoSO_4$, and 20 mM $Na_2C_2O_4$) compared to nickel using lower concentrations (1 mM $NiSO_4$, and 5 mM $Na_2C_2O_4$).

Scheme 1: General strategy for the electrosynthesis of poly(pyrrole-alkylammonium)/CoO_x nanocomposite film modified electrodes. (i) Formation of **PPN^+** by oxidative electropolymerization of monomer **PN^+** (4 mM) at E_{app} = +0.95 and +1.1 V *vs* Ag/$AgNO_3$ in CH_3CN, 0.1 M $[Bu_4N]ClO_4$, respectively for C and ITO_{por} electrodes; (ii) incorporation of $[Co(C_2O_4)_2]^{2-}$ into **PPN^+** upon soaking during 1h in a 0.1 M borate buffer solution (pH 6) of 4 mM $CoSO_4$, 20 mM $Na_2C_2O_4$ and 0.1 M Na_2SO_4; (iii) electroprecipitation of **Co^0** within PPN^+ at E_{app} = -1.3 and -1.5 V *vs* Ag/AgCl, respectively for C and ITO_{por} electrodes, in the 0.1 M borate buffer solution (pH 6) of cobalt oxalate; (iv) air oxidation and electro-oxidation of **Co^0** to **CoO_x** *via* 5 consecutive cycles between 0 and +1.2 V *vs* Ag/AgCl in a 0.1 M borate buffer solution (pH 9.2).

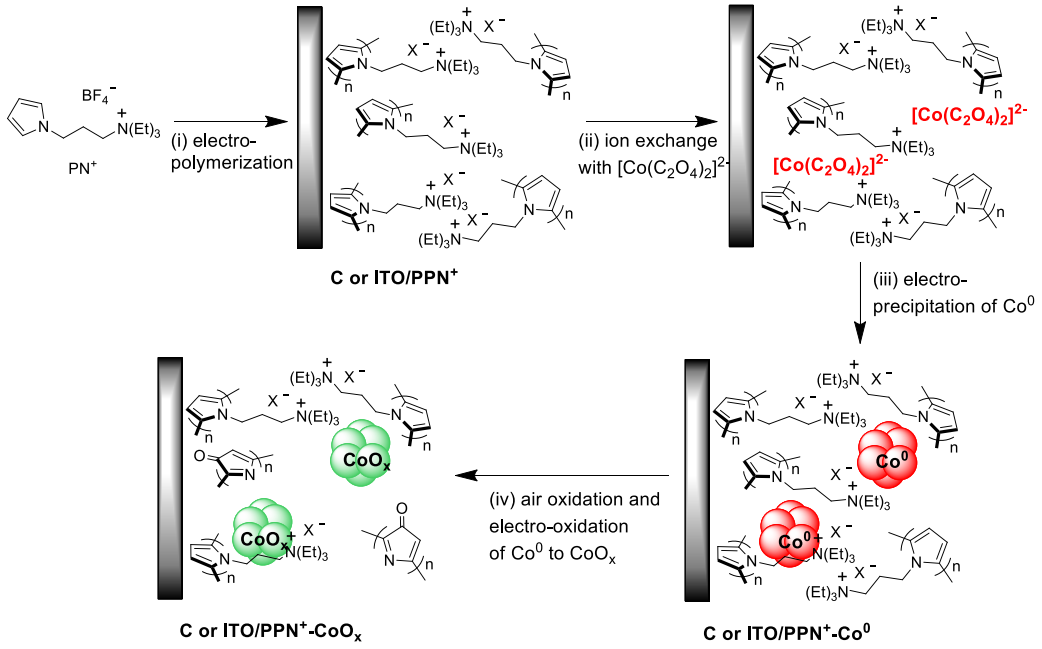

For analytical electrochemistry studies, C electrodes (diameter 3 mm,surface of 0.071 cm^2) were used for films deposition, while large-surface ITO_{por} electrodes (surface of 0.40 cm^2) nanostructured as described in the previous chapter were employed for microscopy and spectroscopy studies as well as for electrocatalytic experiments (see below). As explained before, the first step consists in the electropolymerization in acetonitrile of the pyrrole-alkylammonium monomer (PN^+; 4 mM) at the electrode surface at an applied potential of +0.95 V *vs* $Ag/AgNO_3$ for a C electrode (anodic charge of 4 mC) and +1.1 V *vs* $Ag/AgNO_3$ for an ITO_{por} electrode (anodic charge of 22.4 mC); the charge corresponding in both cases to 56 mC cm^{-2}.[34] The surface coverage in ammonium units Γ_{N^+} (mol cm^{-2}) corresponding to the amount of polypyrrole deposited on electrode, was estimated by integration of the reversible redox process of polypyrrole (see Chapter II) and the values obtained of 1.20 (± 0.1) × 10^{-7} mol cm^{-2} and 9.32 (± 0.56) × 10^{-8} mol cm^{-2} for C and ITO_{por}, respectively, are very similar to those obtained in Chapter II. In a second step, the PPN^+ electrodes are dipped for one hour in an aqueous borate buffer at pH 6 (0.1 M Na_2SO_4 and 0.1 M H_3BO_3) containing $CoSO_4$ (4 mM) and $Na_2C_2O_4$ (20 mM), to incorporate the anionic cobalt oxalate complex, $[Co(C_2O_4)_2]^{2-}$ generated *in situ,* by ion exchange within the cationic polypyrrole film.[33,34,36-38] The Co^0 nanoparticles were then electrogenerated *in situ* within the film by reduction of $[Co(C_2O_4)_2]^{2-}$ inserted into the polymer at an applied potential of -1.3 V *vs* Ag/AgCl for a C electrode (cathodic charge of 4 mC) and -1.5 V *vs* Ag/AgCl for an ITO_{por} electrode (cathodic charge of 22.4 mC). During this electroreduction step, the C or ITO_{por}/**PPN**$^+$ modified electrode is maintained into the cobalt oxalate solution (0.1 M borate buffer at pH 6). For comparison purposes, Co^0 particles were also electrodeposited on naked C and ITO_{por} electrodes (without PPN^+) from the same cobalt oxalate aqueous solution also using a cathodic charge of 4 or 22.4 mC, respectively. Typically for the Co^0 electrodeposition on C and C/**PPN**$^+$ electrodes, about 130-170 seconds are required to pass a cathodic charge of 4 mC (Figure 1).

The Co loading (Γ_{Co}) on the C/**PPN**$^+$ and C electrodes was estimated to 2.27 (± 0.45) × 10^{-8} and 5.07 (± 0.33) × 10^{-8} mol cm^{-2} by ICP-MS measurements, corresponding to deposition yields of 7.8 and 17.4%, respectively. Thus, for the same quantity of charge (4 mC), the amount of Co^0 deposited on the C/**PPN**$^+$ film is 2.23 times smaller than that deposited on the naked C electrode. In the case of the Co loading on ITO_{por} electrodes, the estimated quantity was of 3.24 (± 0.72) × 10^{-8} mol cm^{-2} and 1.93 (± 0.10) × 10^{-8} mol cm^{-2}, for ITO_{por}/**PPN**$^+$ and ITO_{por}, giving an efficiency of 11.2 and

6.6 % for the same quantity of charge (22.4 mC). In this case, the amount of cobalt is 1.8 times larger in the nanocomposite than the naked ITO_{por}.

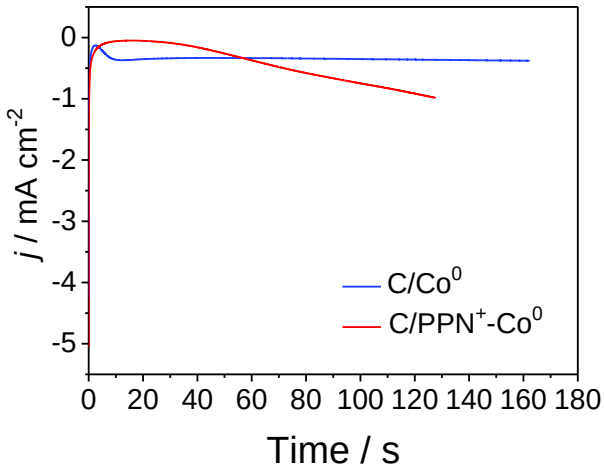

Figure 1: Cobalt deposition (E_{appl} = –1.3 V, $Q_{deposition}$ = 4 mC) on C (Γ_{Co} = 5.07 (± 0.33) × 10^{-8} mol cm^{-2}) and C/**PPN**$^+$ (Γ_{N^+} = 1.2 (± 0.1) × 10^{-7} mol cm^{-2}, Γ_{Co} = 2.27 (± 0.45) × 10^{-8} mol cm^{-2}) electrodes (3 mm of diameter) in 0.1 M borate buffer + 0.1 M $NaSO_4$ (pH 6) containing 4 mM $CoSO_4$ and 20 mM $Na_2C_2O_4$

The maximal amount of cobalt incorporated within the **PPN**$^+$ film has been also estimated considering that two ammonium units interact with one di-anionic $[Co(C_2O_4)_2]^{2-}$ complex during the Co loading in the film. Therefore, the Γ_{Co}/Γ_{N^+} ratio should be equal to 0.5 when the incorporation efficiency of cobalt is 100%. For the C/**PPN**$^+$**-CoO$_x$** electrodes, the average surface coverage values of Co and **PPN**$^+$ were determined to be respectively Γ_{Co} = 2.27 × 10^{-8} mol cm^{-2} and Γ_{N^+} = 1.2 × 10^{-7} mol cm^{-2} which corresponds to an average Γ_{Co}/Γ_{N^+} ratio of 0.19 and thus to an incorporation efficiency of cobalt of 38%. As for ITO_{por}/**PPN**$^+$**-CoO$_x$**, values of Γ_{Co} = 3.24 × 10^{-8} mol cm^{-2} and Γ_{N^+} = 9.32 × 10^{-8} mol cm^{-2} were found, giving an average Γ_{Co}/Γ_{N^+} ratio of 0.35, therefore an incorporation efficiency of cobalt of 70%. Incorporation efficiencies within **PPN**$^+$ were obtained by our group in the past with other materials, such as NiO_x (56%),[34] IrO_x (60%)[33] and MoS_x (*ca.* 58%).[38]

Finally, the last step is the oxidation of Co^0 into cobalt oxide. Firstly, a partial oxidation of Co^0 to CoO occurs almost instantaneously under air exposure during the transfer of the C or ITO_{por}/**PPN**$^+$**-Co^0** and C or ITO_{por}/**Co^0** electrodes into an aqueous borate buffer solution at pH 9.2. The spontaneous air oxidation of **Co^0** into **CoO** is well known and was previously reported by the groups of Rice[39] and Zhao.[40] Then, to oxidize **CoO** into higher oxidation states than II (*i.e.* to **CoO$_x$**), five consecutive cycles between 0 and +1.2 V were performed in a 0.1 M borate buffer

solution (pH 9.2) (Figure 2 and Scheme 1 (iv)). The generation of cobalt oxide is evidenced by the appearance of its typical small intensity reversible Co^{II}/Co^{III} redox process[41-43] with anodic and cathodic peaks respectively located at +0.58 and +0.53 V for C/**PPN$^+$-CoO$_x$**, and at +0.56 and +0.51 V for C/**CoO$_x$** (Figure 2(D)). Increasing the number of anodic cycles does not lead to a significant increase of the Co^{II}/Co^{III} redox process. The similarity of the Co^{II}/Co^{III} redox processes for C/**PPN$^+$-CoO$_x$** and C/**CoO$_x$** suggests that the same nature of cobalt oxide is generated on both electrodes (Figure 2(D)). X-ray photoelectron spectroscopy (XPS) measurements performed on C/**PPN$^+$-CoO$_x$** after the electro-oxidation of **CoO** particles indeed indicate a mixture of a mixed valence cobalt oxide (Co_3O_4) and a cobalt oxyhydroxide (CoOOH) (see below). Note that a similar Co^{II}/Co^{III} redox process in the same potential range was obtained by the group of Spiccia[44] for cobalt oxide electrodeposited in a borate buffer (pH 9.2) from solutions of negatively charged cobalt complexes.

It is also noteworthy that on the first scan from 0 to +1.2 V of the C/**PPN$^+$-CoO** electrode (Figure 2(A)), two broad anodic processes are observed at +0.67 and +0.95 V on the cyclic voltammogram which correspond respectively to the oxidation and the overoxidation of polypyrrole. Consequently, after the first scan, only the Co^{II}/Co^{III} redox process is observed in the CV below +0.7 V and the redox behavior of the polypyrrole has disappeared, meaning that the polymer conductivity is fully destroyed owing to its complete overoxidation. Consequently, the electronic conductivity of the **PPN$^+$-CoO$_x$** film, which is effective for potentials above +0.3 V (Figure 2(D)), is only ensured by the cobalt oxide nanoparticles, presumably *via* their percolation, while the overoxidized PPN^+ acts as a nonconductive matrix maintaining the nanoparticles at the surface of the electrode, as we previously observed for C/**PPN$^+$-NiO$_x$** electrodes.[34]

The generation of the CoO_x particles on C and C/**PPN$^+$** electrodes is also quasi-concomitant with the catalytic water oxidation observed in their CVs (Figure 2) by a growing catalytic current above +0.80 V. It is important to note that the catalytic current density (j) of the C/**PPN$^+$-CoO$_x$** electrode at +1.2 V is higher than that of C/**CoO$_x$** electrode, with 5.77 *vs* 4.76 mA cm^{-2}, respectively (Figures 2(A) and (B)), evidencing the better catalytic performance of C/**PPN$^+$-CoO$_x$** in spite of the lower loading of cobalt within the polymer film. This result could be ascribed to the greater nanostructuration of the **CoO$_x$** embedded into the polymeric **PPN$^+$** matrix.

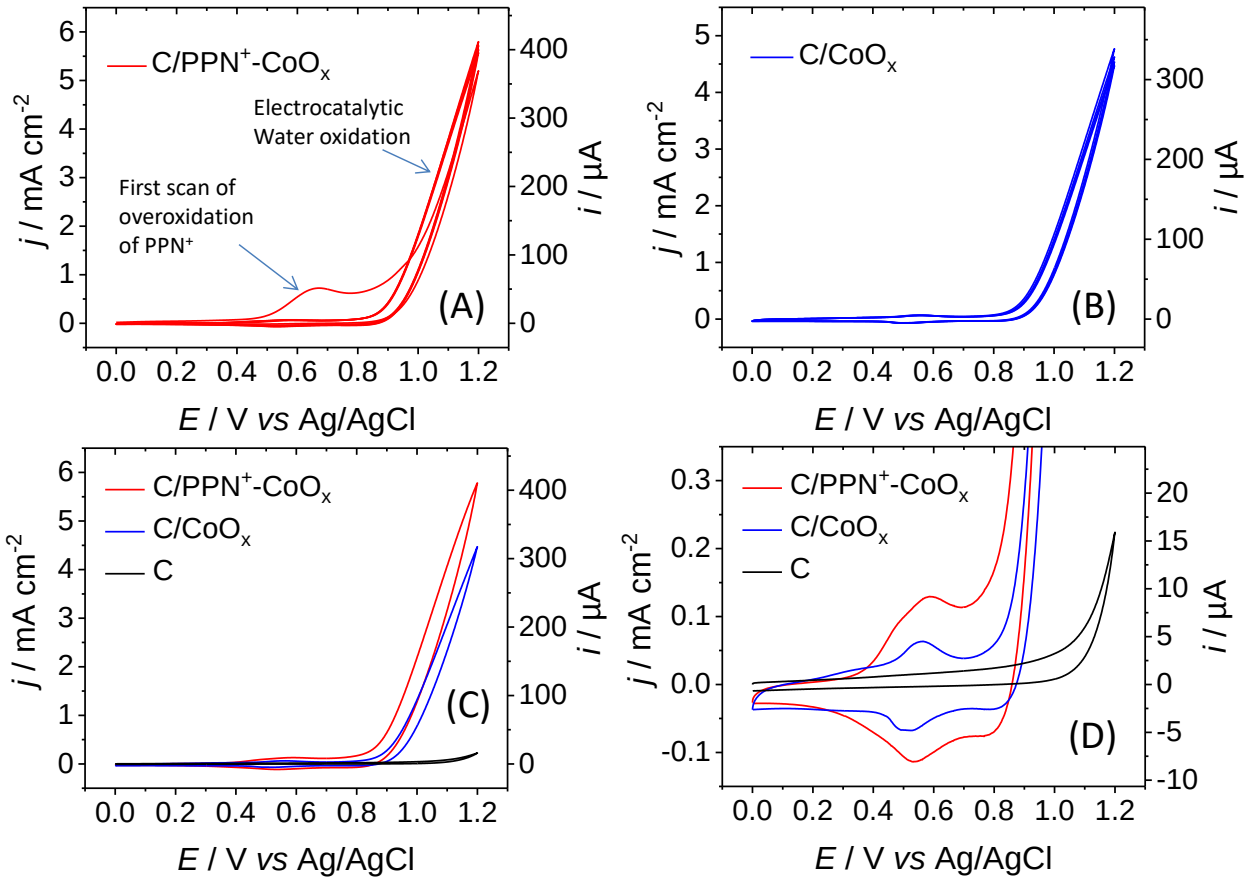

Figure 2: Electro-induced generation of **CoO_x** from **CoO** by repeated cyclic voltammetry (CV) scans (5 consecutive scans; scan rate of 50 mV s^{-1}) in a 0.1 M borate buffer solution (pH 9.2) at (A) C/**PPN^+-CoO** electrode (Γ_{N^+} = 1.2 (± 0.1) × 10^{-7} mol cm^{-2}, Γ_{Co} = 2.27 (± 0.45) × 10^{-8} mol cm^{-2}) and (B) C/**CoO** electrode (Γ_{Co} = 5.07 (± 0.33) × 10^{-8} mol cm^{-2}). (C) Overlay of 5th scans of the C/**PPN^+-CoO** (red) and C/**CoO** (blue) electrodes (in black, the electroactivity of a naked C electrode of 3 mm diameter) and (D) zoom of part (C) showing the redox process of the cobalt oxide.

The difference of nanostructuration between C/**PPN^+-CoO_x** and C/**CoO_x**, which is related to their electrochemically active surface area, can be qualitatively estimated from their CVs. The integration of the overall current of the CVs for both electrodes between +0.3 and +0.7 V (Figure 2(D)) indicates that the charge involved in the redox processes leading to the insulator/conductor conversion[45] of C/**PPN^+-CoO_x** as well as the Co^{II}/Co^{III} conversion of redox active sites exposed to the electrolyte[42] is 1.81 times greater than that of C/**CoO_x**. Given that there is 2.23 less cobalt in C/**PPN^+-CoO_x** compared to C/**CoO_x** (see above), the electrochemically active surface area of the nanocomposite electrode is then estimated to be greater than that of the simple cobalt oxide electrode.

In order to confirm the greater nanostructuration of the composite material, the capacitance of C/**PPN$^+$-CoO$_x$** and C/**CoO$_x$** electrodes was estimated by electrochemical impedance spectroscopy (EIS). Indeed, the capacitance of an electrode is directly correlated to its electrochemically active surface area and thus to its structuration.[46-48] Bode phase and Nyquist plots (Figures 3 and 4) were recorded with both electrodes in borate buffer solution at pH 9.2 for different potentials (0.2, 0.6, 0.8, 0.9 and 1.0 V). The impedance spectra obtained were fitted with the equivalent circuit conventionally used for the catalytic oxidation of water.[41,49-51] The equivalent circuit is shown in the inset of Figure 3(C) and is composed of the resistance of the electrolyte (R_s) between the working and reference electrodes, the double layer capacitance of the working electrode (C_{dl}), the electron transport resistance (R_{tr}, also called polarization resistance) of the film (*i.e.* **PPN$^+$-CoO$_x$** or **CoO$_x$**), the capacitance (C_{sub}) and resistance (R_{sub}) related to the charge transfer between the cobalt oxide particle and its surface intermediates involved in the water oxidation process. For the curve fitting, we chose to replace the capacities with constant phase elements (CPE) in order to take into account the inhomogeneity of the system which is commonly associated with nanostructured electrodes with high roughness factor (see the section 5 of the experimental part).[51-54] The values of the equivalent circuit elements obtained by the experimental data fitting are reported in Table 1 and are averages calculated from measurements performed on three different electrodes for each film.

Table 1: Values of equivalent circuit elements (R_{tr}, C_{dl}, n_1, and R_{sub}, C_{sub}, n_2) obtained for the fitting of the experimental data obtained for various potentials with C/**PPN$^+$-CoO$_x$** and C/**CoO$_x$** in a 0.1 M borate buffer at pH 9.2.

E (V)[a]	R_{tr} (Ω cm^{-2})	C_{dl} (mF cm^{-2})	n_1	R_{sub} (Ω cm^{-2})	C_{sub} (mF cm^{-2})	n_2
C/PPN$^+$-CoO$_x$						
0.6	12 ± 1	0.67 ± 0.06	0.936 ± 0.004	> 10^{17}	---	---
0.8	10 ± 1	1.1 ± 0.1	0.930 ± 0.006	> 10^{14}	---	---
0.9	7.2 ± 0.5	1.2 ± 0.1	0.89 ± 0.01	145 ± 9	1.32 ± 0.09	0.905 ± 0.006
1.0	5.6 ± 0.7	0.8 ± 0.2	0.875 ± 0.006	30 ± 1	1.4 ± 0.1	0.91 ± 0.01
C/CoO$_x$						
0.6	18 ± 1	0.15 ± 0.03	0.956 ± 0.003	> 10^{17}	---	---
0.8	16 ± 1	0.30 ± 0.05	0.958 ± 0.003	> 10^{15}	---	---
0.9	14 ± 1	0.38 ± 0.06	0.952 ± 0.003	350 ± 40	0.34 ± 0.06	0.922 ± 0.002
1.0	8.2 ± 0.8	0.30 ± 0.03	0.929 ± 0.007	40 ± 0.5	0.39 ± 0.07	0.901 ± 0.095

[a]Potentials are given *versus* Ag/AgCl

Three potential domains with different electrochemical behaviours for C/**PPN$^+$-CoO$_x$** and C/**CoO$_x$** were observed by EIS, the latter being correlated to their CVs: the regions around +0.2 V, between

+0.6 and +0.8 V and above +0.9 V. At the potential of +0.2 V, the impedance spectra of C/**PPN$^+$-CoO$_x$** and C/**CoO$_x$** could not be correctly fitted because the impedance measured at this potential is very high and different from those of the other spectra obtained with potentials between +0.6 and +1.0 V (Figures 3(C) and 4(C)). Therefore only the values of the equivalent circuit elements obtained between +0.6 and +1.0 V are reported in the Table 1. This corroborates that no redox process of cobalt is observable in the CVs of C/**PPN$^+$-CoO$_x$** and C/**CoO$_x$** in the region of +0.2 V (Figure 1(D)) and both electrodes are mainly insulating in this potential region. Hence, EIS measurements confirm that the conductivity within the **PPN$^+$-CoO$_x$** film is only ensured by the cobalt oxide particles and not by the overoxidized polypyrrole matrix. This means that, in the range of cathodic potential at +0.2 V, the insulating overoxidized polypyrrole prevents the electron transport through the film, while above this potential region the electron transport is promoted by the various oxidation states of cobalt (*i.e.* Co^{II}/Co^{III} and Co^{III}/Co^{IV}).

In the region between +0.6 and +0.8 V, the EIS spectra allow recovering only the C_{dl} and R_{tr} parameters which are here related to the Co^{II}/Co^{III} redox system. Since the water oxidation catalysis is weak or non-operative between +0.6 and +0.8 V, R_{sub} and C_{sub} cannot be determined. In contrast, EIS measurements reveal that, whatever the potential, the R_{tr} resistance is weaker for the C/**PPN$^+$-CoO$_x$** electrode than for the C/**CoO$_x$** electrode, and conversely, the C_{dl} value of C/**PPN$^+$-CoO$_x$** is higher than those of C/**CoO$_x$**. At +0.6 V on the Co^{II}/Co^{III} redox process (see Figure 2(D)), C_{dl} value of C/**PPN$^+$-CoO$_x$** (670 µF cm^{-2}) is 4.5 times greater than that of C/**CoO$_x$** (150 µF cm^{-2}). Therefore, EIS measurements confirm that C/**PPN$^+$-CoO$_x$** exhibits a greater nanostructuration than that of C/**CoO$_x$**. At +0.8 V, C_{dl} values drastically increase to 1100 and 300 µF cm^{-2}, respectively for C/**PPN$^+$-CoO$_x$** and C/**CoO$_x$**, most probably due to further oxidation of cobalt active sites leading to the onset of OER (Figure 2(D)).[41]

For potentials above +0.9 V, all the parameters of the equivalent circuit were recovered from the spectra. Indeed, the $R_{sub}C_{sub}$ loop in the equivalent circuit correctly models the interfacial charge transfer with the surface intermediates produced during OER,[41] the latter operating efficiently above +0.9 V. C_{dl} values are higher at +0.9 V (1200 µF cm^{-2} for C/**PPN$^+$-CoO$_x$** and 380 µF cm^{-2} for C/**CoO$_x$**) than those at +0.6 and +0.8 V for both films for the reason mentioned above. It is worth noting that, when the potential goes from 0.9 to 1.0 V, the decrease in C_{dl} (800 µF cm^{-2} for C/**PPN$^+$-CoO$_x$** and 300 µF cm^{-2} for C/**CoO$_x$** at 1.0 V), was ascribed by Bisquert et coll.[55] to the

strong release of O_2 bubbles obtained at the higher potentials that diminish the electrode surface area exposed to the substrate and thus reduce its capacitive behavior. The values of n_1 and n_2 are the parameters associated with the transition from the CPE to a pure capacity.[52] When n is close to 1, it means that we are approaching a pure capacity. Here, the n values are all greater than 0.87 indicating a relatively good homogeneity[52] of both film/solution interfaces, **PPN$^+$-CoO$_x$** and **CoO$_x$**. This may reflect the fact that the catalytic sites are certainly distributed relatively homogeneously. In addition, the n value associated with the double-layer capacitance is slightly lower for the **PPN$^+$-CoO$_x$** film, which shows that in the presence of the polymer, the roughness at the film/solution interface is slightly greater. This increase in the roughness of the film surface was also observed by scanning electron microscopy (SEM) (see below and Figure 6). Therefore it can be assumed that, even if the catalytic sites are distributed in a homogeneous manner, the roughness of the polymer lowers very slightly the value of n_1.

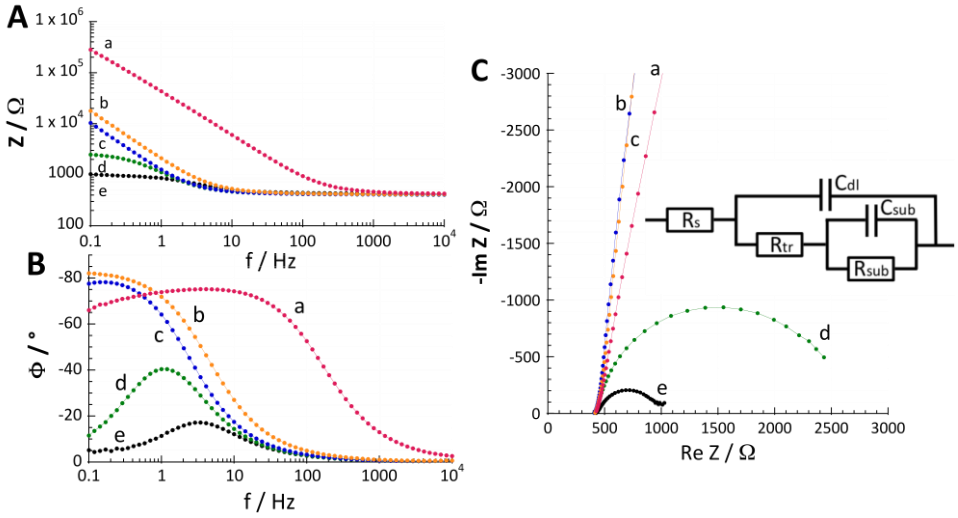

Figure 3: Bode (module (A), phase (B)) and Nyquist plots (C) recorded at the C/**PPN$^+$-CoO$_x$** (Γ_{N^+} = 1.2 (± 0.1) × 10^{-7} mol cm^{-2}, Γ_{Co} = 2.27 (± 0.45) × 10^{-8} mol cm^{-2}) electrode (3 mm of diameter) in a 0.1 M borate buffer solution (pH 9.2) at different potentials 0.2 (a), 0.6 (b), 0.8 (c), 0.9 (d) and 1.0 V (e) *vs* Ag/AgCl; inset in (C) shows the equivalent circuit model used to fit the EIS data.

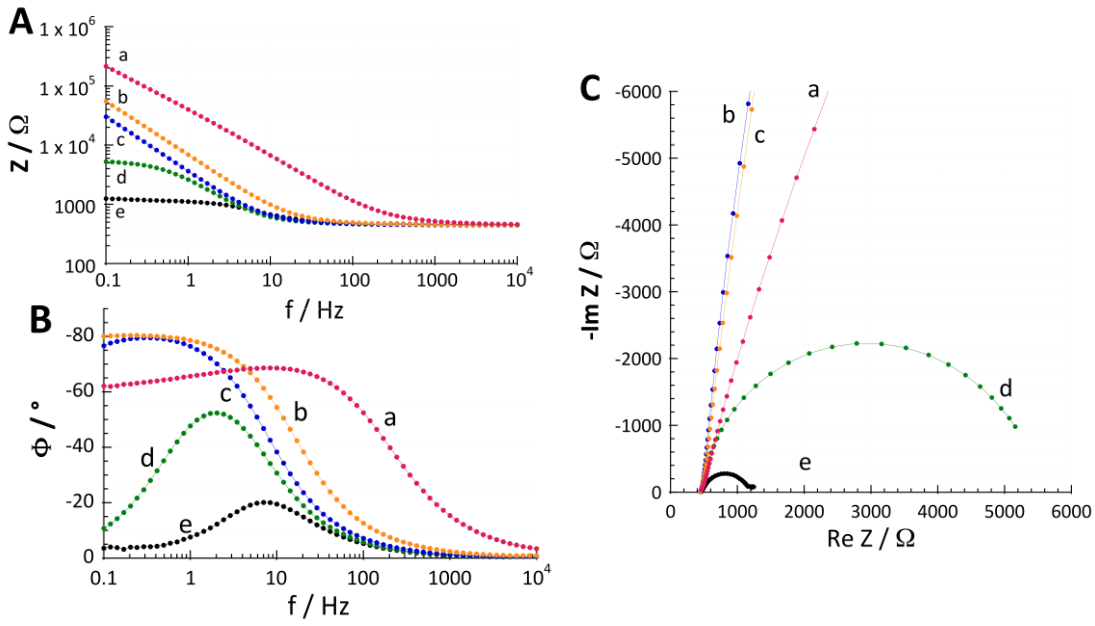

Figure 4: Bode (module (A), phase (B)) and Nyquist plots (C) recorded at the C/**CoO$_x$** (Γ_{Co} = 5.07 (± 0.33) × 10^{-8} mol cm^{-2}) electrode (3 mm of diameter) in a 0.1 M borate buffer solution (pH 9.2) at different potentials 0.2 (a), 0.6 (b), 0.8 (c), 0.9 (d) and 1.0 V (e) *vs* Ag/AgCl

II.2. Characterization of Cobalt Oxide and Poly(Pyrrole-alkylammonium) Cobalt Oxide Nanocomposite by SEM-EDX and XPS.

For scanning electron microscopy (SEM) studies, the films of **PPN$^+$-CoO$_x$** or **CoO$_x$** were deposited on ITO$_{por}$ electrodes (surface of 0.40 cm^2). As discussed above, ITO$_{por}$/**PPN$^+$-CoO$_x$** and ITO$_{por}$/**CoO$_x$** electrodes were prepared with a charge of 22.4 mC for both the **PPN$^+$** and **Co^0** deposition to obtain a charge density of 56 mC cm^{-2}, similar to that used for the preparation of the C/**PPN$^+$-CoO$_x$** and C/**CoO$_x$** electrodes (4 mC for a C electrode with a surface of 0.071 cm^2). Previous studies[35] using atomic force microscopy (AFM) on the ITO/**PPN$^+$-CoO$_x$** and ITO/**CoO$_x$** showed characteristic features of both materials: an ill-defined cauliflower-like topography and a homogeneous nodular topography composed of aggregated **CoO$_x$** particles, respectively. SEM images performed herein confirmed this results in which nodular and cauliflower morphologies have been observed for ITO$_{por}$/**CoO$_x$** (Figure 5) and ITO$_{por}$/**PPN$^+$-CoO$_x$** (Figure 6), respectively. In contrast to the nickel oxide nanoparticles electrodeposited in similar conditions without polypyrrole matrix (Chapter II), the cobalt oxide nanoparticles grow outside the pores introduced on the ITO electrode in a droplet conformation. The nanoparticles were sized as 34.8 ± 8.7 nm and

gathered in large aggregates (> 100 nm) . This result is similar to the one found in previous TEM images obtained by our group, which has revealed large agglomerates (> 100 nm) of **CoO_x** nanoparticles for ITO/**CoO_x**. However this agglomeration is not observed when the polymer is present. In ITO/**PPN^+-CoO_x** synthetized previously by our group, the cobalt nanoparticles are well-dispersed in the polymer film with an average particle size of 31 ± 20 nm, demonstrating once again the nanostructuration that the polymer imparts to the metal oxide nanoparticles.[35] Further energy dispersive X-ray (EDX) spectroscopy on a droplet of the ITO_{por}/**CoO_x** confirmed the presence of cobalt species, as well as in the nanocomposite the ITO_{por}/**PPN^+-CoO_x** (Figure 7).

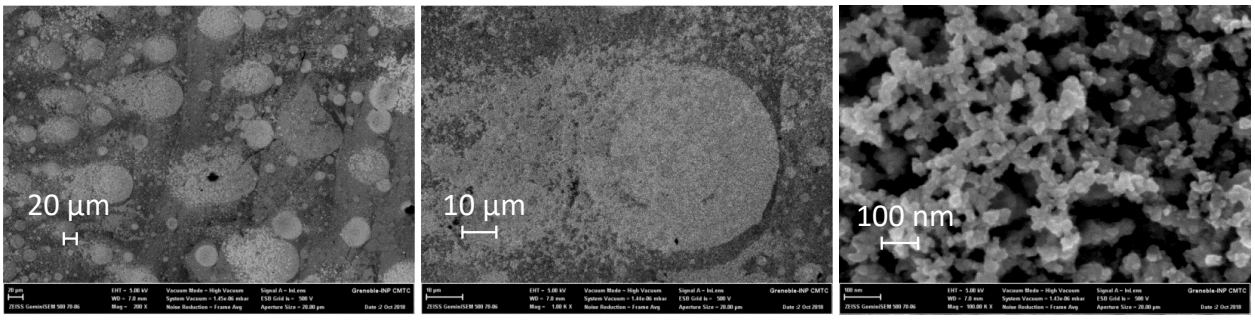

Figure 5: SEM images of the top view of the ITO_{por}/**CoO_x** at different scales: 20, 10 and 0.1 µm.

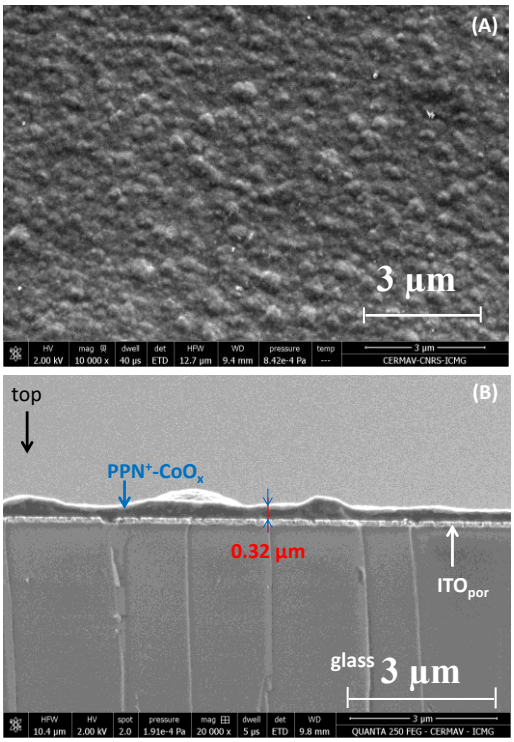

Figure 6: SEM images of the top view (A) and the cross section (B) of ITO_{por}/**PPN^+-CoO_x**

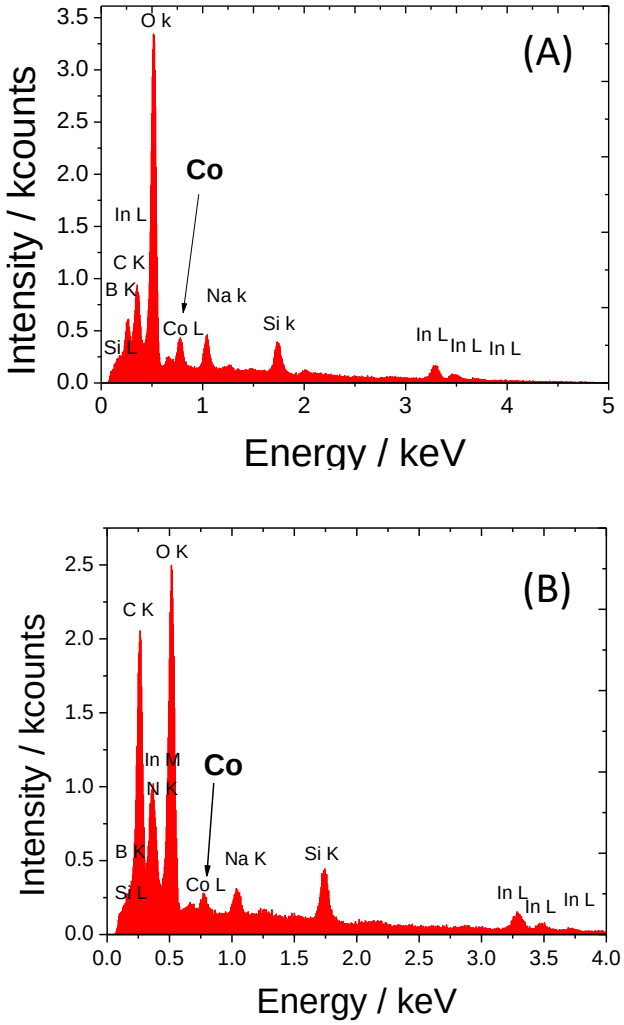

Figure 7: EDX spectrum of (A) ITO_{por}/**CoO_x** and (B) ITO_{por}/**PPN^+-CoO_x.**

The nature of the electrogenerated cobalt oxide particles within the PPN^+ film, after 5 cycles between 0 and +1.2 V in 0.1 M borate buffer (pH 9.2), was also studied by X-ray photoelectron spectroscopy (XPS) measurements (Figure 8). For XPS analysis, **PPN^+-CoO_x** was electrodeposited on carbon pellets (6 mm of diameter, denoted C_{pel}) which can be easily removed from the electrode support by unscrewing and placed in the vacuum chamber of the spectrometer. High resolution XPS spectroscopy of Co $2p_{3/2}$ region reveals a broad signal, which could be deconvoluted into a series of peaks corresponding to various transitions (shake-up, plasmon loss, satellites, *etc.*) due to the complex nature of this transition metal (Figure 8). The deconvolution of the peak at *ca.* 781 eV indicates that the cobalt deposit for the C_{pel}/**PPN^+-CoO_x** anode could be a mixture of a mixed

valence cobalt oxide (Co_3O_4) and a cobalt oxyhydroxide (CoOOH).[56] Foelske et al[57] demonstrated by coupling electrochemical experiments with XPS measurements that poising an electrode of metallic cobalt at a potential superior to +1.18 V *vs* Ag/AgCl in a borate buffer at pH 9.3 results in the formation of a Co_3O_4 layer on its surface. In parallel, the group of Spiccia[44] demonstrated by X-ray absorption fine structure measurements (EXAFS) that cobalt oxide, electrodeposited in a borate buffer (pH 9.2) by oxidizing a cobalt complex, closely resembles the heterogeneous CoOOH phase. Given the similarities between our study and that of Spiccia[44] in the electrochemical behavior of CoO_x in borate buffer at the same pH 9.2 (see discussion above), as well as with the study of Foelske[57] in the electrogeneration of CoO_x from Co^0 in borate buffer, we can assume that our cobalt oxide within PPN^+ could indeed contain a mixture of both Co_3O_4 and CoOOH species.

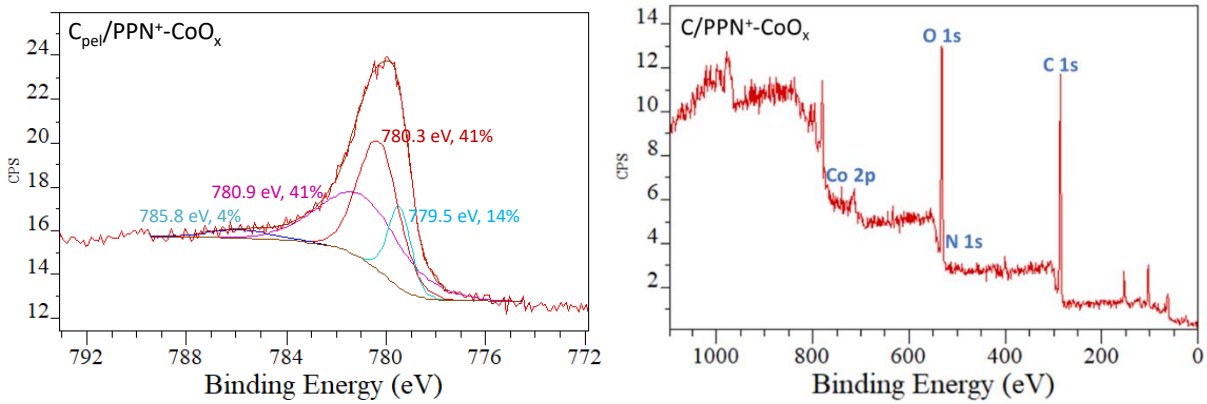

Figure 8: XPS spectrum in the Co $2p_{3/2}$ region (left) and full XPS spectrum (right) of the electrode surfaces of C_{pel}/**PPN^+-CoO_x** after 5 cycles between 0 to +1.2 V *vs* Ag/AgCl in a 0.1 M borate buffer (pH 9.2)

II.3. Electrocatalytic Performances for OER of Cobalt Oxide and Poly(pyrrole-alkylammonium) Cobalt Oxide Nanocomposite Electrodes.

The electrocatalytic activity of C/**PPN^+-CoO_x** and C/**CoO_x** electrodes has been investigated by cyclic voltammetry under mild basic conditions in a borate buffer solution at pH 9.2 (Figure 2). Table 2 summarizes the catalytic OER performances of these modified electrodes and that of C/**PPN^+-NiO_x** recently reported by our group[34] in a 0.1 M borate buffer solution at pH 9.2 together with those of cobalt oxide-based electrodes reported in literature in a similar medium. In all reported cases, the cobalt oxide was electrogenerated on the surface of fluorine doped tin oxide electrodes (FTO). Developing electrolyzers operating at nearly neutral pH, such as pH 9.2, is of

utmost importance in view to avoid corrosion issue under strongly acidic or alkaline conditions.[1] Herein, the C/**PPN$^+$-CoO$_x$** anode exhibits a *j* value of 4.04 mA cm^{-2} at η of +0.61 V (*i.e.* 1.1 V *vs* Ag/AgCl) and a η value of +0.44 V at 1 mA cm^{-2} with a cobalt mass loading of 1.34 μg cm^{-2}. This performance places our nanocomposite anode among the best reported cobalt oxide-based anodes for water oxidation operating in a 0.1 M borate buffer solution at pH 9.2.

For comparison, the C/**CoO$_x$** anode presents a *j* value of 3.40 mA cm^{-2} at η of +0.61 V and a η value of +0.46 V at 1 mA cm^{-2} with a cobalt mass loading of 2.99 μg cm^{-2}. The C/**PPN$^+$-CoO$_x$** nanocomposite electrode presents a higher *j* and a lower η values compared to those of C/**CoO$_x$** with ~2.2 times less cobalt loading, demonstrating the beneficial effect of using a poly(pyrrole-alkylammonium) matrix to enhance the nanostructuration of the electrode material and thus its electrocatalytic performance. Indeed, according to previous TEM analysis and EIS measurements, C/**PPN$^+$-CoO$_x$** contains small **CoO$_x$** particles (31 nm) with a capacitance of 670 μF cm^{-2}, while C/**CoO$_x$** exhibits big agglomerates of **CoO$_x$** particles (> 100 nm) associated with a lower capacitance of 150 μF cm^{-2} (see above). Hence the higher catalytic activity of the C/**PPN$^+$-CoO$_x$** nanocomposite compared to the direct deposition C/**CoO$_x$** can be directly correlated to a greater nanostructuration of the nanocomposite that increases the electrochemically active surface area of the anode and ensures a great accessibility of the active catalytic sites towards substrates as water or OH$^-$ ions. The greater values of mass activity and turnover frequency (TOF) of C/**PPN$^+$-CoO$_x$** (3.01 A mg^{-1} and 0.46 s^{-1}) compared to those of C/**CoO$_x$** (1.14 A mg^{-1} and 0.17 s^{-1}) at pH 9.2 at an overpotential of 0.61 V confirm the higher OER catalytic activity of the nanocomposite **PPN$^+$-CoO$_x$** material (Table 2).

Carefully analyzing the catalytic performances of the previously reported anodes based on cobalt oxide operating at pH 9.2 with a 0.1 M borate buffer (Table 2), one can see that the C/**PPN$^+$-CoO$_x$** electrode is also clearly superior in terms of mass activity and TOF for cobalt oxide deposits in the same range of mass loading (1-4 μg cm^{-2}). It is also interesting to note that the OER performance of C/**PPN$^+$-CoO$_x$** is greater than that of the analogous C/**PPN$^+$-NiO$_x$** previously reported by our group,[34] which displays lower values of *j* (2.17 mA cm^{-2}), mass activity (1.12 A mg^{-1}) and TOF (0.17 s^{-1}) for an overpotential of 0.61 V. If we consider a similar nanostructuration for C/**PPN$^+$-CoO$_x$** and C/**PPN$^+$-NiO$_x$** anodes (particle sizes of **CoO$_x$** and **NiO$_x$**[34] within **PPN$^+$** of 31 and 21 nm, respectively) and a lower metal loading for cobalt compared to that for nickel (Γ_{Co}

~ 23 nmol cm^{-2} *vs* Γ_{Ni} ~ 33 nmol cm^{-2}),[34] CoO_x particles display a higher intrinsic catalytic activity than that of NiO_x for water oxidation in borate buffer at pH 9.2.

Table 2. OER performances of C/**PPN$^+$-CoO$_x$** and C/**CoO$_x$** anodes prepared in this work compared to those of C/**PPN$^+$-NiO$_x$** and FTO/**CoO$_x$** anodes previously reported with a 0.1 M borate buffer solution at pH 9.2

Catalyst/electrode	j (mA cm^{-2}) @η (V)	η (V) @j (mA cm^{-2})	Metal mass loading (µg cm^{-2})	Mass activity (A mg^{-1}) @η (V)	TOF$_{min}$(s^{-1}) @η (V)	Author^{ref}
C/**PPN$^+$-CoO$_x$**	4.04@0.61	0.44@1	1.34	3.01@0.61	0.46@0.61	This work
C/**PPN$^+$-CoO$_x$**	2.17@0.51		1.34	1.62@0.51	0.25@0.51	This work
C/**PPN$^+$-CoO$_x$**	0.53@0.40		1.34	0.40@0.40	0.06@0.40	This work
C/**CoO$_x$**	3.40@0.61	0.46@1	2.99	1.14@0.61	0.17@0.61	This work
C/**CoO$_x$**	1.32@0.51		2.99	0.44@0.51	0.07@0.51	This work
C/**CoO$_x$**	0.22@0.40		2.99	0.07@0.40	0.01@0.40	This work
C/**PPN$^+$-NiO$_x$**	2.17@0.61	0.51@1	1.9	1.12@0.61	0.17@0.61	Fortage[34]
FTO/CoO_x	2.89[a]@0.51	0.37[a]@1	nd	nd	nd	Nocera[10]
FTO/CoO_x	0.41@0.40	0.53@1	46.0	0.009[b]@0.40	0.001[b]@0.40	Nocera[14]
FTO/CoO_x	1.90[a]@0.61	0.51[a]@1	1.11	1.71[b]@0.61	0.26[b]@0.61	Spiccia[44]
FTO/CoO_x	0.39[a]@0.61	0.75[a]@1	0.003	130[b]@0.61	20@0.61	Sun[58]
FTO/CoO_x	2.60@0.61	nd	nd	nd	nd	Du[59]
FTO/CoO_x	1.40@0.61	0.51[a]@1	3.53	0.40[b]@0.61	0.06[b]@0.61	Du[60]

[a]Values were extrapolated from the cyclic voltammograms reported by the authors. [b]Data non calculated by the authors but estimated herein from the current density (j) at defined overpotentials (η) and the mass loading of Co given in the article. nd: not determined. FTO: Fluorine doped Tin Oxide electrode.

The stability of C/**PPN$^+$-CoO$_x$** and C/**CoO$_x$** electrodes at pH 9.2 in a 0.1 M borate buffer was evaluated previously[35] by chronoamperometry measurements at an applied potential of +1.2 V *vs* Ag/AgCl and was stable only over a period of about 2h (not shown). To avoid the film detachment from the electrode surface under prolonged electrolysis at +1.2 V, the physisorption of the polypyrrole film on the electrode has been increased by the electrodeposition of the **PPN$^+$-CoO$_x$** material on a porous ITO plate (ITO$_{por}$, surface of 0.4 cm^2) following the same all-electrochemical procedure described above (Scheme 1). In such conditions, no **PPN$^+$-CoO$_x$** film detachment is observed and the catalytic current of ITO$_{por}$/**PPN$^+$-CoO$_x$** is stable over more than 24

h (Figure 9). The **PPN**$^+$ film confers a great stability to the nanocomposite material by preventing the corrosion and the degradation of **CoO$_x$** nanoparticles, in addition to the phenomenon of self-healing that is known for cobalt oxide in a borate buffer.[11,61,62] In the case of the ITO$_{por}$/**CoO$_x$** material, as we have seen in the SEM images (Figure 5), the growth of aggregates outside the pores of the electrode might play an important role in our incapacity to perform stability tests under the same conditions as in the nanocomposite, since the material is too exposed to the OER conditions and therefore dissolves into the solution.

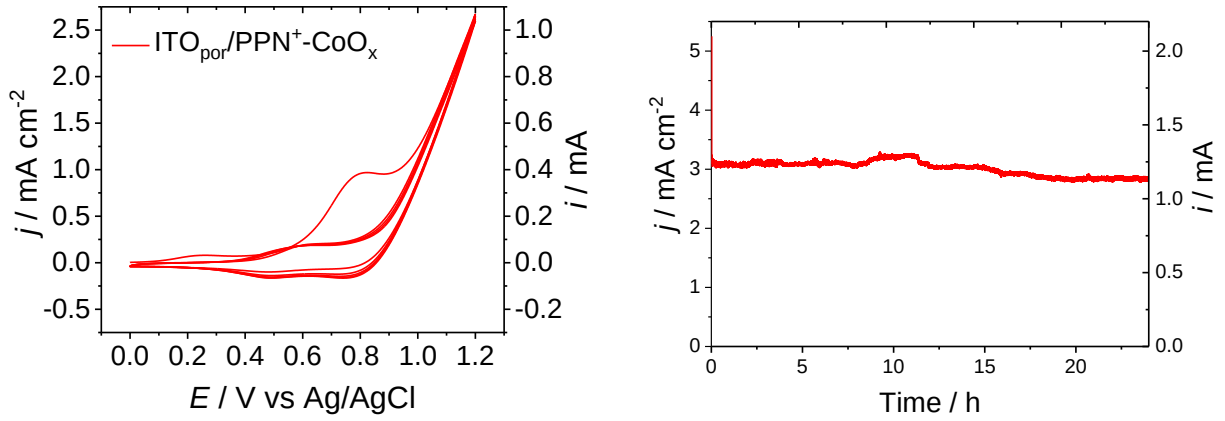

Figure 9: Electro-induced generation of CoO$_x$ from CoO by repeated cyclic votammetry (CV) scans (5 consecutive scans; scan rate of 50 mV s^{-1}) in a 0.1 M borate buffer solution (pH 9.2) at ITO$_{por}$/**PPN$^+$-CoO** electrode (Γ_{N^+} = 9.32 (± 0.56) × 10^{-8} mol cm^{-2}, Γ_{Co} = 3.2 (± 0.72) × 10^{-8} mol cm^{-2}) (left); Chronoamperogram recorded at ITO$_{por}$/**PPN$^+$-CoO$_x$** (Γ_{N^+} = 9.32 (± 0.56) × 10^{-8} mol cm^{-2}, Γ_{Co} = 3.24 (± 0.72) × 10^{-8} mol cm^{-2}) electrode (0.4 cm^2) in a stirred 0.1 M borate buffer solution (pH 9.2) at a constant potential of +1.2 V *vs* Ag/AgCl (right).

To obtain some mechanistic information, Tafel analysis was performed through stepwise chronoamperometry at pH 9.2 on C/**PPN$^+$-CoO$_x$** and C/**CoO$_x$** electrodes (Figure 10). A Tafel slope value of 56 mV dec^{-1} was determined for C/**CoO$_x$** corresponding to a fast equilibrated electron transfer. The catalytic process is thus not controlled by an electron transfer but by a chemical step following this electron transfer.[12,41,63] Similar values were reported with cobalt oxide catalysts in borate buffer at pH 9.2 by several groups as those of Nocera,[14] Du[59,60] and Spiccia.[44] For C/**PPN$^+$-CoO$_x$**, a Tafel slope of 65 mV dec^{-1}, close to that of C/**CoO$_x$**, was estimated within a region of corrected overpotentials between +0.41 and +0.47 V (*i.e.* between +0.9 and +1.02 V *vs* Ag/AgCl). Above +0.47 V, the Tafel plot of C/**PPN$^+$-CoO$_x$** deviates from linearity most probably due to the mass transport issue related to O_2 release within the polypyrrole film, that could not be easily obviated by the rotation of the electrode.[64] However, the similar Tafel slopes of C/**PPN$^+$-CoO$_x$** and

C/**CoO$_x$** confirm that the O_2 evolution occurring with these two electrodes involves the same catalytic mechanism.

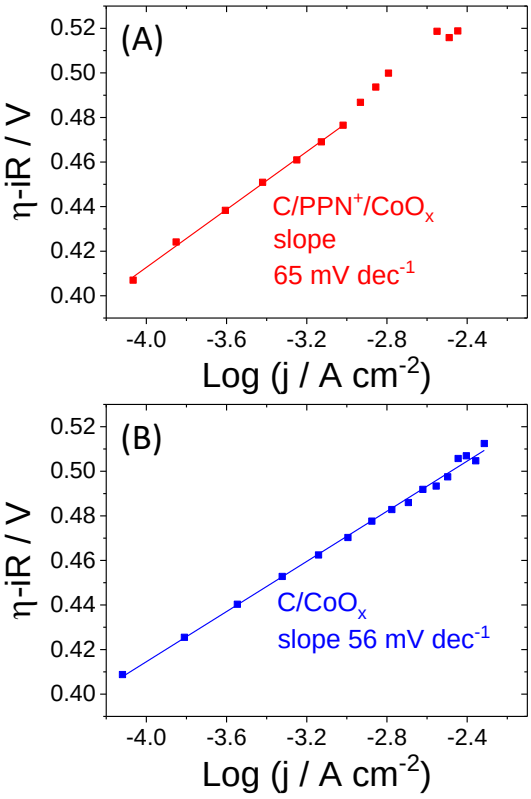

Figure 10: Tafel plots recorded at the C/**PPN$^+$-CoO$_x$** (Γ_{N^+} = 1.2 (± 0.)1 × 10^{-7} mol cm^{-2}, Γ_{Co} = 2.27 (± 0.45) × 10^{-8} mol cm^{-2}) (A) and C/**CoO$_x$** (Γ_{Co} = 5.07 (± 0.33) × 10^{-8} mol cm^{-2}) (B) rotating disc electrodes (3 mm of diameter) in a 0.1 M borate buffer solution (pH 9.2) under rotation (1200 rpm).

III – Conclusion

We prepared a very efficient OER anode material based on a poly(pyrrole-alkylammonium)-cobalt oxide nanocomposite (**PPN$^+$-CoO$_x$**) deposited at an electrode surface by an easy all-electrochemical procedure. For analytical electrochemical studies, C electrodes (diameter 3 mm, surface area 0.071 cm^2) were used for films deposition, while ITO_{por} electrodes (surface area 0.4 cm^2) were used for microscopic and spectroscopic studies as well as electrocatalytic experiments.

Electrodeposition procedures similar to those presented in the previous chapter for the nickel were used. However, the concentration of the $[Co(C_2O_4)_2]^{2-}$ complex is multiplied by four compared to $[Ni(C_2O_4)_2]^{2-}$ to facilitate the incorporation of cobalt. In addition, unlike **Ni^0**

nanoparticles, **Co^0** nanoparticles present in the composite are partially oxidized to cobalt oxide **CoO** under exposure to air and then fully oxidized to **CoO_x** by only 5 successive scans between 0 and 1.2 V *vs* Ag/AgCl in a borate buffer (0.1 M) at pH 9.2. For comparison, **CoO_x** films were also deposited on naked C and ITO_{por} electrodes without prior deposition of **PPN^+**.

The materials were characterized by various electrochemical (cyclic voltammetry, electrochemical impedance spectroscopy (ESI), chronoamperometry, Tafel curve) and microscopic (SEM-EDX and XPS) techniques. The nature of the cobalt oxide has been identified by XPS as a mixture of Co_3O_4/CoOOH. EIS measurements evidenced the high nanostructuration of the **PPN^+-CoO_x** nanocomposite, confirming to what was observed previously by TEM studies with small **CoO_x** nanoparticles of *ca.* 30 nm well dispersed into the polypyrrole film and not aggregated.

We demonstrated that the high nanostructuration of the composite material, is at the origin of the higher OER electrocatalytic performances. The nanocomposite material exhibits exceptional mass activity of 3.01 A mg^{-1} and TOF values of 0.46 s^{-1} for water oxidation at mildly basic pH 9.2 at an overpotential of 0.61 V, and a Tafel slope of 65 mV dec^{-1}. These performances outperforms not only most of the cobalt oxide-based anodes previously reported operating in a 0.1 M borate buffer solution at pH 9.2, but also the cobalt oxide electrogenerated on a naked electrode surface by the same electrochemical procedure. In addition, when the **PPN^+-CoO_x** material is electrodeposited on porous ITO, the physisorption of the film is considerably enhanced and consequently its catalytic activity is very stable beyond 24 h of electrocatalysis at 1.2 V.

This work confirms again the beneficial role of positively charged polypyrrole matrix in the preparation of small particles of cobalt oxide and in the achievement of a highly stable and active anode for water oxidation. The elaboration of such polypyrrole-metal oxide nanocomposite material could be easily extended to the preparation of mixed metal oxides such as **$NiFeO_x$** or **$CoFeO_x$**, which are the most efficient OER catalysts in alkaline or mildly basic conditions. This will be the subject of Chapter IV, with the development of poly(pyrrole-alkylammonium)-NiFe oxide nanocomposite electrode materials for OER.

References

1 Li, P., Zhao, R., Chen, H., Wang, H., Wei, P., Huang, H., Liu, Q., Li, T., Shi, X., Zhang, Y., Liu, M. & Sun, X. Recent Advances in the Development of Water Oxidation Electrocatalysts at Mild pH. *Small* **15**, 1805103 (2019).

2 Benson, P., Briggs, G. W. D. & Wynne-Jones, W. F. K. The cobalt hydroxide electrode—II. Electrochemical behaviour. *Electrochim. Acta* **9**, 281-288 (1964).

3 Shafirovich, V. Y. & Strelets, V. V. Catalytic-Oxidation of Water by Cobalt Complexes. *Nouv. J. Chim.* **2**, 199-201 (1978).

4 Jasem, S. M. & Tseung, A. C. C. A Potentiostatic Pulse Study of Oxygen Evolution on Teflon-Bonded Nickel-Cobalt Oxide Electrodes. *J. Electrochem. Soc.* **126**, 1353-1360 (1979).

5 Burke, L. D., Lyons, M. E. & Murphy, O. J. Formation of hydrous oxide films on cobalt under potential cycling conditions. *J. Electroanal. Chem.* **132**, 247-261 (1982).

6 Chen, Y. W. D. & Noufi, R. N. Electrodeposition of Nickel and Cobalt Oxides onto Platinum and Graphite Electrodes for Alkaline Water Electrolysis. *J. Electrochem. Soc.* **131**, 731-735 (1984).

7 Jiang, S. P. & Tseung, A. C. C. Reactive Deposition of Cobalt Electrodes: IV . Alkaline Water Electrolysis. *J. Electrochem. Soc.* **138**, 1216-1222 (1991).

8 Castro, E. B., Gervasi, C. A. & Vilche, J. R. Oxygen evolution on electrodeposited cobalt oxides. *J. Appl. Electrochem.* **28**, 835-841 (1998).

9 Kanan, M. W. & Nocera, D. G. In situ formation of an oxygen-evolving catalyst in neutral water containing phosphate and Co2+. *Science* **321**, 1072-1075 (2008).

10 Surendranath, Y., Dinca, M. & Nocera, D. G. Electrolyte-Dependent Electrosynthesis and Activity of Cobalt-Based Water Oxidation Catalysts. *J. Am. Chem. Soc.* **131**, 2615-2620 (2009).

11 Lutterman, D. A., Surendranath, Y. & Nocera, D. G. A Self-Healing Oxygen-Evolving Catalyst. *J. Am. Chem. Soc.* **131**, 3838-3839 (2009).

12 Surendranath, Y., Kanan, M. W. & Nocera, D. G. Mechanistic Studies of the Oxygen Evolution Reaction by a Cobalt-Phosphate Catalyst at Neutral pH. *J. Am. Chem. Soc.* **132**, 16501-16509 (2010).

13 Kanan, M. W., Yano, J., Surendranath, Y., Dinca, M., Yachandra, V. K. & Nocera, D. G. Structure and Valency of a Cobalt-Phosphate Water Oxidation Catalyst Determined by in Situ X-ray Spectroscopy. *J. Am. Chem. Soc.* **132**, 13692-13701 (2010).

14 Esswein, A. J., Surendranath, Y., Reece, S. Y. & Nocera, D. G. Highly active cobalt phosphate and borate based oxygen evolving catalysts operating in neutral and natural waters. *Energy Environ. Sci.* **4**, 499-504 (2011).

15 Gerken, J. B., Landis, E. C., Hamers, R. J. & Stahl, S. S. Fluoride-Modulated Cobalt Catalysts for Electrochemical Oxidation of Water under Non-Alkaline Conditions. *ChemSusChem* **3**, 1176-1179 (2011).

16 Gerken, J. B., McAlpin, J. G., Chen, J. Y. C., Rigsby, M. L., Casey, W. H., Britt, R. D. & Stahl, S. S. Electrochemical Water Oxidation with Cobalt-Based Electrocatalysts from pH

0–14: The Thermodynamic Basis for Catalyst Structure, Stability, and Activity. *J. Am. Chem. Soc.* **133**, 14431-14442 (2011).

17 Liang, Y., Li, Y., Wang, H., Zhou, J., Wang, J., Regier, T. & Dai, H. Co3O4 nanocrystals on graphene as a synergistic catalyst for oxygen reduction reaction. *Nat. Mater.* **10**, 780-786 (2011).

18 Surendranath, Y., Lutterman, D. A., Liu, Y. & Nocera, D. G. Nucleation, Growth, and Repair of a Cobalt-Based Oxygen Evolving Catalyst. *J. Am. Chem. Soc.* **134**, 6326-6336 (2012).

19 Cobo, S., Heidkamp, J., Jacques, P.-A., Fize, J., Fourmond, V., Guetaz, L., Jousselme, B., Ivanova, V., Dau, H., Palacin, S., Fontecave, M. & Artero, V. A Janus cobalt-based catalytic material for electro-splitting of water. *Nat. Mater.* **11**, 802-807 (2012).

20 Farrow, C. L., Bediako, D. K., Surendranath, Y., Nocera, D. G. & Billinge, S. J. L. Intermediate-Range Structure of Self-Assembled Cobalt-Based Oxygen-Evolving Catalyst. *J. Am. Chem. Soc.* **135**, 6403-6406 (2013).

21 Ma, T. Y., Dai, S., Jaroniec, M. & Qiao, S. Z. Metal–Organic Framework Derived Hybrid Co3O4-Carbon Porous Nanowire Arrays as Reversible Oxygen Evolution Electrodes. *J. Am. Chem. Soc.* **136**, 13925-13931 (2014).

22 Liu, Y. & Nocera, D. G. Spectroscopic Studies of Nanoparticulate Thin Films of a Cobalt-Based Oxygen Evolution Catalyst. *J. Phys. Chem. C* **118**, 17060-17066 (2014).

23 Jiang, N., You, B., Sheng, M. & Sun, Y. Electrodeposited Cobalt-Phosphorous-Derived Films as Competent Bifunctional Catalysts for Overall Water Splitting. *Angew. Chem., Int. Ed.* **54**, 6251-6254 (2015).

24 Kim, H., Park, J., Park, I., Jin, K., Jerng, S. E., Kim, S. H., Nam, K. T. & Kang, K. Coordination tuning of cobalt phosphates towards efficient water oxidation catalyst. *Nat. Commun.* **6**, 8253 (2015).

25 Zhao, Y., Chen, S., Sun, B., Su, D., Huang, X., Liu, H., Yan, Y., Sun, K. & Wang, G. Graphene-Co3O4 nanocomposite as electrocatalyst with high performance for oxygen evolution reaction. *Sci. Rep.* **5**, 7629 (2015).

26 Gardner, G., Al-Sharab, J., Danilovic, N., Go, Y. B., Ayers, K., Greenblatt, M. & Charles Dismukes, G. Structural basis for differing electrocatalytic water oxidation by the cubic, layered and spinel forms of lithium cobalt oxides. *Energy Environ. Sci.* **9**, 184-192 (2016).

27 Chen, H., Gao, Y. & Sun, L. A Cobalt-Based Film for Highly Efficient Electrocatalytic Water Oxidation in Neutral Aqueous Solution. *ChemCatChem* **8**, 2757-2760 (2016).

28 Han, L., Dong, S. & Wang, E. Transition-Metal (Co, Ni, and Fe)-Based Electrocatalysts for the Water Oxidation Reaction. *Adv. Mater.* **28**, 9266-9291 (2016).

29 Wang, J., Cui, W., Liu, Q., Xing, Z., Asiri, A. M. & Sun, X. Recent Progress in Cobalt-Based Heterogeneous Catalysts for Electrochemical Water Splitting. *Adv. Mater.* **28**, 215-230 (2016).

30 Chen, Y., Hu, J., Diao, H., Luo, W. & Song, Y.-F. Facile Preparation of Ultrathin Co3O4/Nanocarbon Composites with Greatly Improved Surface Activity as a Highly Efficient Oxygen Evolution Reaction Catalyst. *Chem. Eur. J.* **23**, 4010-4016 (2017).

31 Roger, I., Shipman, M. A. & Symes, M. D. Earth-abundant catalysts for electrochemical and photoelectrochemical water splitting. *Nat. Rev. Chem.* **1**, 0003 (2017).

32 El Wakkad, S. E. S. & Hickling, A. The anodic behaviour of metals. Part VI.—Cobalt. *Trans. Faraday Soc.* **46**, 820-824 (1950).

33 Lattach, Y., Rivera, J. F., Bamine, T., Deronzier, A. & Moutet, J.-C. Iridium Oxide–Polymer Nanocomposite Electrode Materials for Water Oxidation. *ACS Appl. Mater. Interfaces* **6**, 12852-12859 (2014).

34 Morales, D. V., Astudillo, C. N., Lattach, Y., Urbano, B. F., Pereira, E., Rivas, B. L., Arnaud, J., Putaux, J.-L., Sirach, S., Cobo, S., Moutet, J.-C., Collomb, M.-N. & Fortage, J. Nickel oxide–polypyrrole nanocomposite electrode materials for electrocatalytic water oxidation. *Catal. Sci. Technol.* **8**, 4030-4043 (2018).

35 Morales Montecinos, D. V. *Matériaux nanocomposites polypyrrole-oxyde métallique pour l'oxydation de l'eau en oxygène par voie électrocatalytique et photocatalytique*, PhD thesis, Université Grenoble Alpes, (2018).

36 Zouaoui, A., Stephan, O., Carrier, M. & Moutet, J. C. Electrodeposition of copper into functionalized polypyrrole films. *J. Electroanal. Chem.* **474**, 113-122 (1999).

37 Zouaoui, A., Stephan, O., Ourari, A. & Moutet, J. C. Electrocatalytic hydrogenation of ketones and enones at nickel microparticles dispersed into poly(pyrrole-alkylammonium) films. *Electrochim. Acta* **46**, 49-58 (2000).

38 Lattach, Y., Deronzier, A. & Moutet, J.-C. Electrocatalytic Hydrogen Evolution from Molybdenum Sulfide–Polymer Composite Films on Carbon Electrodes. *ACS Appl. Mater. Interfaces* **7**, 15866-15875 (2015).

39 Rice, D. W., Phipps, P. B. P. & Tremoureux, R. Atmospheric Corrosion of Cobalt. *J. Electrochem. Soc.* **126**, 1459-1466 (1979).

40 Suryanto, B. H. R., Lu, X., Chan, H. M. & Zhao, C. Controlled electrodeposition of cobalt oxides from protic ionic liquids for electrocatalytic water oxidation. *RSC Advances* **3**, 20936-20942 (2013).

41 Doyle, R. L., Godwin, I. J., Brandon, M. P. & Lyons, M. E. G. Redox and electrochemical water splitting catalytic properties of hydrated metal oxide modified electrodes. *PhysChemChemPhys* **15**, 13737-13783 (2013).

42 Costentin, C., Porter, T. R. & Savéant, J.-M. Conduction and Reactivity in Heterogeneous-Molecular Catalysis: New Insights in Water Oxidation Catalysis by Phosphate Cobalt Oxide Films. *J. Am. Chem. Soc.* **138**, 5615-5622 (2016).

43 Brodsky, C. N., Bediako, D. K., Shi, C., Keane, T. P., Costentin, C., Billinge, S. J. L. & Nocera, D. G. Proton–Electron Conductivity in Thin Films of a Cobalt–Oxygen Evolving Catalyst. *ACS Appl. Energy Mater.* **2**, 3-12 (2019).

44 Bonke, S. A., Wiechen, M., Hocking, R. K., Fang, X.-Y., Lupton, D. W., MacFarlane, D. R. & Spiccia, L. Electrosynthesis of Highly Transparent Cobalt Oxide Water Oxidation Catalyst Films from Cobalt Aminopolycarboxylate Complexes. *ChemSusChem* **8**, 1394-1403 (2015).

45 Costentin, C., Porter, T. R. & Savéant, J.-M. Nature of Electronic Conduction in "Pseudocapacitive" Films: Transition from the Insulator State to Band-Conduction. *ACS Appl. Mater. Interfaces* **11**, 28769-28773 (2019).

46 Trasatti, S. & Petrii, O. A. Real Surface-Area Measurements in Electrochemistry. *Pure Appl. Chem.* **63**, 711-734 (1991).

47 Louie, M. W. & Bell, A. T. An Investigation of Thin-Film Ni-Fe Oxide Catalysts for the Electrochemical Evolution of Oxygen. *J. Am. Chem. Soc.* **135**, 12329-12337 (2013).

48 McCrory, C. C. L., Jung, S., Peters, J. C. & Jaramillo, T. F. Benchmarking Heterogeneous Electrocatalysts for the Oxygen Evolution Reaction. *J. Am. Chem. Soc.* **135**, 16977-16987 (2013).

49 Singh, A., Fekete, M., Gengenbach, T., Simonov, A. N., Hocking, R. K., Chang, S. L. Y., Rothmann, M., Powar, S., Fu, D. C., Hu, Z., Wu, Q., Cheng, Y. B., Bach, U. & Spiccia, L. Catalytic Activity and Impedance Behavior of Screen-Printed Nickel Oxide as Efficient Water Oxidation Catalysts. *ChemSusChem* **8**, 4266-4274 (2015).

50 Klahr, B., Gimenez, S., Fabregat-Santiago, F., Hamann, T. & Bisquert, J. Water Oxidation at Hematite Photoelectrodes: The Role of Surface States. *J. Am. Chem. Soc.* **134**, 4294-4302 (2012).

51 Anantharaj, S. & Noda, S. Appropriate Use of Electrochemical Impedance Spectroscopy in Water Splitting Electrocatalysis. *ChemElectroChem* **n/a**, DOI:10.1002/celc.202000515 (2020).

52 Doyle, R. L. & Lyons, M. E. G. An electrochemical impedance study of the oxygen evolution reaction at hydrous iron oxide in base. *PhysChemChemPhys* **15**, 5224-5237 (2013).

53 Orazem, M. E., Pébère, N. & Tribollet, B. Enhanced Graphical Representation of Electrochemical Impedance Data. *J. Electrochem. Soc.* **153**, B129-B136 (2006).

54 Pajkossy, T. Impedance spectroscopy at interfaces of metals and aqueous solutions — Surface roughness, CPE and related issues. *Solid State Ionics* **176**, 1997-2003 (2005).

55 Terezo, A. J., Bisquert, J., Pereira, E. C. & Garcia-Belmonte, G. Separation of transport, charge storage and reaction processes of porous electrocatalytic IrO2 and IrO2/Nb2O5 electrodes. *J. Electroanal. Chem.* **508**, 59-69 (2001).

56 Biesinger, M. C., Payne, B. P., Grosvenor, A. P., Lau, L. W. M., Gerson, A. R. & Smart, R. S. C. Resolving surface chemical states in XPS analysis of first row transition metals, oxides and hydroxides: Cr, Mn, Fe, Co and Ni. *Appl. Surf. Sci.* **257**, 2717-2730 (2011).

57 Foelske, A. & Strehblow, H.-H. Passivity of cobalt in borate buffer at pH 9.3 studied by x-ray photoelectron spectroscopy. *Surf. Interface Anal.* **29**, 548-555 (2000).

58 Daniel, Q., Ambre, R. B., Zhang, B., Philippe, B., Chen, H., Li, F., Fan, K., Ahmadi, S., Rensmo, H. & Sun, L. Re-Investigation of Cobalt Porphyrin for Electrochemical Water Oxidation on FTO Surface: Formation of CoOx as Active Species. *ACS Catal.* **7**, 1143-1149 (2017).

59 Han, A., Wu, H., Sun, Z., Jia, H. & Du, P. Facile deposition of nanostructured cobalt oxide catalysts from molecular cobaloximes for efficient water oxidation. *PhysChemChemPhys* **15**, 12534-12538 (2013).

60 Chen, H., Sun, Z., Liu, X., Han, A. & Du, P. Cobalt–Salen Complexes as Catalyst Precursors for Electrocatalytic Water Oxidation at Low Overpotential. *J. Phys. Chem. C* **119**, 8998-9004 (2015).

61 Costentin, C. & Nocera, D. G. Self-healing catalysis in water. *Proc. Natl. Acad. Sci.* **114**, 13380-13384 (2017).

62 Bediako, D. K., Ullman, A. M. & Nocera, D. G. in *Solar Energy for Fuels* (eds Harun Tüysüz & Candace K. Chan) 173-213 (Springer International Publishing, 2016).

63 Suen, N.-T., Hung, S.-F., Quan, Q., Zhang, N., Xu, Y.-J. & Chen, H. M. Electrocatalysis for the oxygen evolution reaction: recent development and future perspectives. *Chem. Soc. Rev.* **46**, 337-365 (2017).

64 Anantharaj, S., Ede, S. R., Karthick, K., Sam Sankar, S., Sangeetha, K., Karthik, P. E. & Kundu, S. Precision and correctness in the evaluation of electrocatalytic water splitting: revisiting activity parameters with a critical assessment. *Energy Environ. Sci.* **11**, 744-771 (2018).

CHAPTER IV

Iron doping of Nickel Oxide-Polypyrrole Nanocomposite Material to Improve the Electrocatalytic Performance of Water Oxidation

Index

I – Introduction

As we introduced in the Chapter I, mixed nickel/iron oxide (denoted **$NiFeO_x$**), which is only composed of earth abundant elements, is considered as one of the best electrocatalysts for water oxidation and a promising alternative to rare metal-based catalysts as ruthenium and iridium oxide, due to the fact that **$NiFeO_x$** displays high catalytic current densities at low overpotential with a great stability in an alkaline electrolyte.[1] Since the pioneer work of Tichenor[2] in 1952, followed by Troilus,[3] Radniecka[4] and Corrigan,[5] many groups studied the positive effect of iron inserted into nickel oxide films on their OER electrocatalytic activity, even if the real role of iron in OER catalysis is still under debate.[1] Basically, two theories stand out. The first one is based on the fact that iron oxide is the catalytic centre for the water oxidation within **$NiFeO_x$**, with nickel oxide serving only as an electronically conductive matrix for the iron oxide, which has a low conductivity.[6-9] The second advocates that the active species for the water oxidation in **$NiFeO_x$** is Ni(IV)-oxo (*i.e.* Ni(IV)=O present in the γ-NiOOH phase) which is promoted by the presence of a strong Lewis acid such as Fe^{3+} and has a strong oxyl radical resonance character (*i.e.* Ni(III)-O•).[10] The latter has been identified as being involved in the formation of the O-O bond *via* a PCET mechanism leading to the hydroperoxide intermediate responsible for the release of oxygen. In view of literature, **$NiFeO_x$** catalyst has been obtained under various morphologies and nanostructures *via* different synthetic methods such as solvothermal deposition, co-precipitation and electrodeposition. We do believe that electrochemical synthesis is a method of choice to deposit mixed metal oxides onto conductive electrodes due to its easiness of implementation and its propensity to electrogenerate nano-sized metal oxide particles.

Inspired by our work described in Chapters II and III dealing with the design of anodes based on nickel and cobalt oxides-polypyrrole nanocomposites (**PPN^+-NiO_x** and **PPN^+-CoO_x**) we extend our approach to the elaboration of a nanocomposite composed of mixed nickel/iron oxide dispersed into a poly(pyrrole-alkyl ammonium) film (denoted **PPN^+-$NiFeO_x$**). The aim was to further improve the OER performance of anodes using a **PPN^+-NiO_x** nanocomposite described in the Chapter II by the intentional introduction of some iron amounts. Among the various possible methods to introduce iron, we have chosen the electrodeposition from solutions containing a mixture of anionic nickel oxalate and iron citrate complexes in different concentrations. Besides, unlike to the procedure used in the previous chapters, where the anionic metal complexes were incorporated into the cationic **PPN^+** polymer by electro-reduction to generate metal(0) nanoparticles, which were then electro-oxidized to metal oxide,

herein we have simplified the electrodeposition by electrogenerating directly the **$NiFeO_x$** nanoparticles into the **PPN^+** film by electro-oxidizing the anionic nickel and iron complexes previously incorporated within the polymer. We adopted this simpler strategy since the groups of Boettcher,[11] Nocera[10] and Halaoui[12] already showed that the electrodeposition of **$NiFeO_x$** on electrode from nickel and iron salts from an anodic potentiostatic experiment in borate buffer at pH 9.2 is easy and efficient.

For comparison, we also prepared **PPN^+-NiO_x** nanocomposite materials in this chapter by a similar anodic potentiostatic method from a borate solution containing only nickel oxalate. However the nanocomposite obtained contains some amount of iron which has been "involuntary" incorporate because of iron ions are naturally present in the electrolytes. As introduced in the Chapter I, the groups of Corrigan[5,13] and more recently that of Boettcher[6] investigated the unintentional introduction of iron into nickel oxide, even in large quantities, especially during anodic electrochemical processes in basic media (1 M KOH or 0.1 M borate buffer), that contain trace Fe impurities. Of note, the quantity of iron present in the **PPN^+-NiO_x** nanocomposite described in Chapter II of this manuscript has not been evaluated and has to be done in a near future.

So, in this chapter, we will first present preliminary results on the electrosynthesis and the electrocharacterization of polypyrrole-nickel oxide nanocomposite electrodes, prepared from a borate buffer solution (pH 9.2) only containing nickel oxalate, by an anodic potentiostatic procedure. The quantity of iron unintentionally introduced into these electrodes will be analyzed by ICPMS in order to estimate the Ni/Fe ratio and will be discussed in view of the OER electrocatalytic activities. Such electrodes will serve as reference. Then, the electrosynthesis and the electrocharacterization of polypyrrole-nickel/iron oxide nanocomposite electrodes, prepared from a mixture of nickel oxalate and iron citrate complexes, will be discussed in the light of the iron quantity intentionally introduced. Finally, future pathways for improvement in the preparation of these **$NiFeO_x$** nanocomposites anodes and future characterizations will be proposed.

II – Results

II.1 – Electrochemical study of nickel oxalate complex in a borate buffer (pH 9.2)

In view to electrogenerate nickel oxide particles into the polypyrrole film from a nickel oxalate complex by an anodic potentiostatic experiment, we first investigated the cyclic voltammogram (CV) of nickel oxalate in a 0.1 M borate buffer at pH 9.2 (Figure 1).

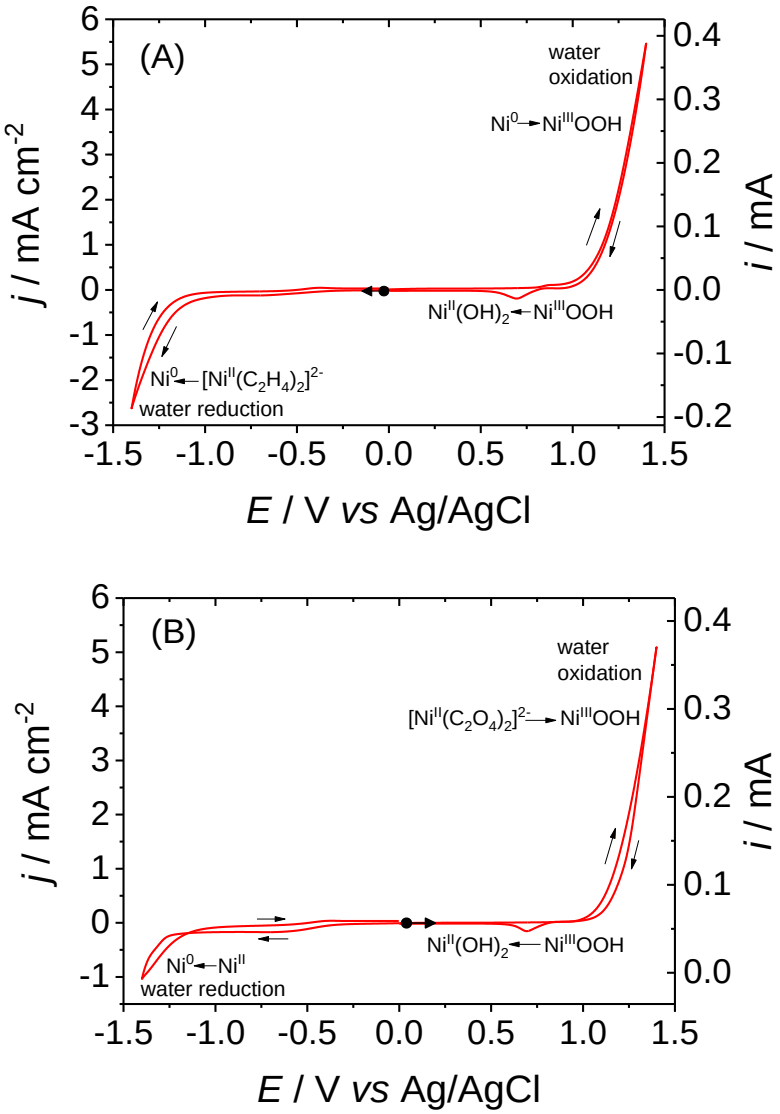

Figure 1: Cyclic voltammograms recorded at C electrode (3 mm of diameter) in a 0.1 M borate buffer solution (pH 9.2) of 1 mM $NiSO_4$, and 5 mM $Na_2C_2O_4$ (A) scanning first to the cathodic potentials and then to the anodic potentials or (B) scanning first to the anodic potentials and then to the cathodic potentials. Scan rate: 50 mV s^{-1}.

The di-anionic nickel oxalate $[Ni^{II}(C_2O_4)_2]^{2-}$ is generated *insitu* from the aqueous borate buffer (0.1 M) solution containing 1 mM $NiSO_4$ and 5 mM $Na_2C_2O_4$. In this electrolyte, $[Ni^{II}(C_2O_4)_2]^{2-}$

is considered as the dominant species. Indeed, the aqueous solution of 1 mM $NiSO_4$ and 5 mM $Na_2C_2O_4$ can lead to various species of nickel oxalate, such as $[Ni^{II}(C_2O_4)]$, $[Ni^{II}(C_2O_4)_2]^{2-}$ and $[Ni^{II}(C_2O_4)_3]^{4-}$, and the distribution diagram for the nickel oxalate system in aqueous solution previously calculated by Moutet[14] shows that $[Ni^{II}(C_2O_4)_2]^{2-}$ predominates in a large pH range between 3 and 11. This negative charge of the dianionic nickel oxalate will ensure its efficient incorporation by anion exchange into the cationic poly(pyrrole-alkyl ammonium) film.

The cyclic voltammogram shown in Figure 1(A) was thus recorded at a carbon (C) electrode in an aqueous borate buffer solution (pH 9.2) containing 1 mM $NiSO_4$ and 5 mM $Na_2C_2O_4$, scanning from 0 to -1.4 V *vs* Ag/AgCl in the cathodic region, then from -1.4 to 1.4 V towards the anodic region, and finally from 1.4 to 0 V. The cathodic part of the cyclic voltammogram of $[Ni^{II}(C_2O_4)_2]^{2-}$ exhibits a strong irreversible process below -1.0 V ascribed to the reduction of $[Ni^{II}(C_2O_4)_2]^{2-}$ to Ni^0, which is deposited on the electrode surface, and to the concomitant water reduction to hydrogen (H_2) catalyzed by Ni^0. In the reverse scan towards the anodic region, the strong irreversible process above 1.0 V evolves the sequential three-electron oxidation of Ni^0 to Ni^{3+}, which generates in basic electrolyte a nickel(III) oxyhydroxide species ($Ni^{III}OOH$) at the surface of the electrode. As evidence of its formation, this $Ni^{III}OOH$ is reduced to $Ni^{II}(OH)_2$ at 0.70 V in the reverse scan towards 0 V. This $Ni^{II}(OH)_2/Ni^{III}OOH$ redox couple is well known[15] and we also observed it in Chapter II of this manuscript when NiO_x (*i.e.* $Ni^{III}OOH$) is electrogenerated on porous ITO from Ni^0 by cycling between 0 and 1.2 V *vs* Ag/AgCl in a 0.1 M borate buffer (pH 9.2).

The cyclic voltammogram shown in Figure 1(B), scanning first in the anodic region and then to cathodic region, displays relatively similar features than those of Figure 1(A) but with slightly different attributions. In the anodic region, the irreversible one-electron oxidation of $[Ni^{II}(C_2O_4)_2]^{2-}$, above 1.0 V *vs* Ag/AgCl, leads to its decomposition and the deposition of $Ni^{III}OOH$ at the electrode surface. In addition, the reduction of $Ni^{III}OOH$ to $Ni^{II}(OH)_2$ in the reverse scan occurs at 0.69 V as previously observed in Figure 1(A). In the cathodic region, an irreversible process below -1.0 V is assigned to the reduction of $Ni^{II}(OH)_2$ and $[Ni^{II}(C_2O_4)_2]^{2-}$ to Ni^0, which is concomitant to water reduction to H_2 promoted by Ni^0. Therefore, for the preparation of **PPN^+-NiO_x** nanocomposite materials, we will carry out the oxidation of $[Ni^{II}(C_2O_4)_2]^{2-}$ at 1.0 V *vs* Ag/AgCl to generate NiO_x nanoparticles inside the polypyrrole film. It is worth noting that the group of Spiccia reported the preparation of **NiO_x** films based on the electro-oxidation/decomposition of several nickel complexes solubilized in borate buffer at pH 9.2 for robust and efficient anodes for electrocatalytic OER.[16,17]

II. 2 – Electrosynthesis and electrocharacterization of the poly(pyrrole-alkyl ammonium)-nickel oxide nanocomposite material on carbon electrode

The electrosynthesis of the **PPN$^+$-NiO$_x$** nanocomposite material on C electrode was performed in three steps (Scheme 1). In order to evaluate the reproducibility of the procedure, we prepared four electrodes of C/**PPN$^+$-NiO$_x$** (with the carbon electrodes named C1, C2, C3 and C4). As in the Chapter III, the first step consists in the oxidative electropolymerization of **PN$^+$** (4 mM) at a controlled potential of 0.95 V *vs* Ag/AgNO$_3$ in CH$_3$CN on C electrode (3 mm of diameter; S = 0.071 cm^2) under inert atmosphere into a glovebox. For an anodic charge of 4 mC passed for the electro-oxidation of **PN$^+$**, the quantity of monomer electrodeposited on the C electrodes, Γ_{N^+}, was estimated to be 1.2 ± 0.1 x 10^{-7} mol cm^{-2}, from the integration of the reversible redox process of polypyrrole recorded by cyclic voltammetry in the same electrolyte (see the Chapter II and the experimental part).

Scheme 1: Electrosynthesis of poly(pyrrole-alkylammonium)/**NiO$_x$** nanocomposite film modified electrodes. (i) Formation of **PPN$^+$** on C electrode by oxidative electropolymerization of monomer **PN$^+$** (4 mM) at +0.95 V *vs* Ag/AgNO$_3$ in CH$_3$CN, 0.1 M [Bu$_4$N]ClO$_4$; (ii) incorporation of [Ni(C$_2$O$_4$)$_2$]$^{2-}$ into **PPN$^+$** upon soaking during 1h in a 0.1 M aqueous borate buffer solution (pH 9.2) of 1 mM NiSO$_4$ and 5 mM Na$_2$C$_2$O$_4$; (iii) electro-oxidation followed by an electroprecipitation of **NiO$_x$** particles at +1.0 V *vs* Ag/AgCl in a 0.1 M borate buffer solution (pH 9.2) of nickel(II) oxalate complex.

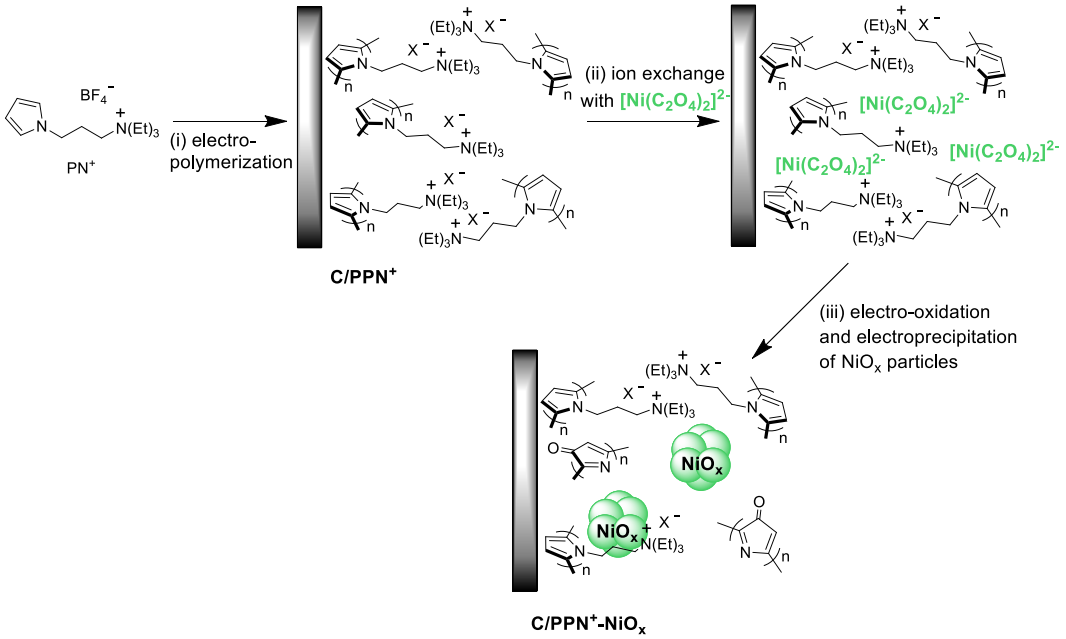

In the second step, the C/**PPN$^+$** electrodes are then loaded with [Ni^{II}(C$_2$O$_4$)$_2$]$^{2-}$ by anion exchange, dipping the electrodes during 1 h in a 0.1 M borate buffer solution (pH 9.2) containing 1 mM NiSO$_4$ and 5 mM Na$_2$C$_2$O$_4$ (see the discussion above). Then, for the last step, the C/**PPN$^+$** electrodes loaded with [Ni^{II}(C$_2$O$_4$)$_2$]$^{2-}$ undergo an oxidation at a controlled potential

of 1.0 V *vs* Ag/AgCl in the same electrolyte by passing 2 mC, to generate nickel oxide particles within the polypyrrole film (Figure 2(A)). This oxidation potential of $[Ni^{II}(C_2O_4)_2]^{2-}$ was chosen from the cyclic voltammogram recorded at C electrode in the (0.1 M) borate buffer solution with nickel and oxalate salts (see above Figure 1(B)). The chronoamperometry of the oxidation of the nanocomposite deposited on 4 electrodes (denoted C1-C4) electrodes in Figure 2(A) shows the good reproducibility of the anodic procedure with an oxidation time ranging from 92 to 105 s. Then, the redox behavior and the OER catalytic activity of the four C/**PPN^+-NiO_x** electrodes were characterized by cyclic voltammetry in a 0.1 M borate buffer at pH 9.2, without $NiSO_4$ and $Na_2C_2O_4$ in solution (Figures 2(B-C)).

Before discussing the cycling votltammograms, it is important to mention that all nanocomposite materials were dissolved in an aqueous nitric acid solution (0.45 M) after the electrochemical characterization and analyzed by ICP-MS to determine the quantity of metal deposited on electrode (Table 1). These measurements reveal that nickel is present on C/**PPN^+** electrode, thus the deposition of nickel succeeded following this new procedure, and all **PPN^+-NiO_x** nanocomposite films prepared by this anodic potentiostatic procedure contain iron in different proportions. This involuntary introduction of Fe into NiO_x was investigated in-depth by Boettcher in mildly and strongly basic media as a 0.1 M borate buffer[11] and a 1 M KOH solution,[6] respectively. Specifically, they showed that iron present even as trace in borate buffer (pH 9.2) can be introduced easily during a procedure of electrodeposition/anodization of nickel oxide on electrode (see the discussion below). Consequently in our study, these first series of electrodes based on nickel oxide-polypyrrole nanocomposite, containing an involuntary amount of iron, have been named C/**PPN^+-Ni(Fe)O_x**. The surface coverage of Ni (Γ_{Ni}) and Fe (Γ_{Fe}) within C/**PPN^+-Ni(Fe)O_x** has been estimated to be $1.13 \pm 0.29 \times 10^{-7}$ and $3.55 \pm 1.00 \times 10^{-8}$ mol cm^{-2}, respectively, from ICPMS (Table 1). Anyway, these values should be considered with caution, since the margin of error on Γ_{Ni} and Γ_{Fe} of 26% and 28% are quite important. This can be due to the too small number of prepared electrodes (too narrow sampling) and the fact that the Γ values are at the detection limit of ICPMS.

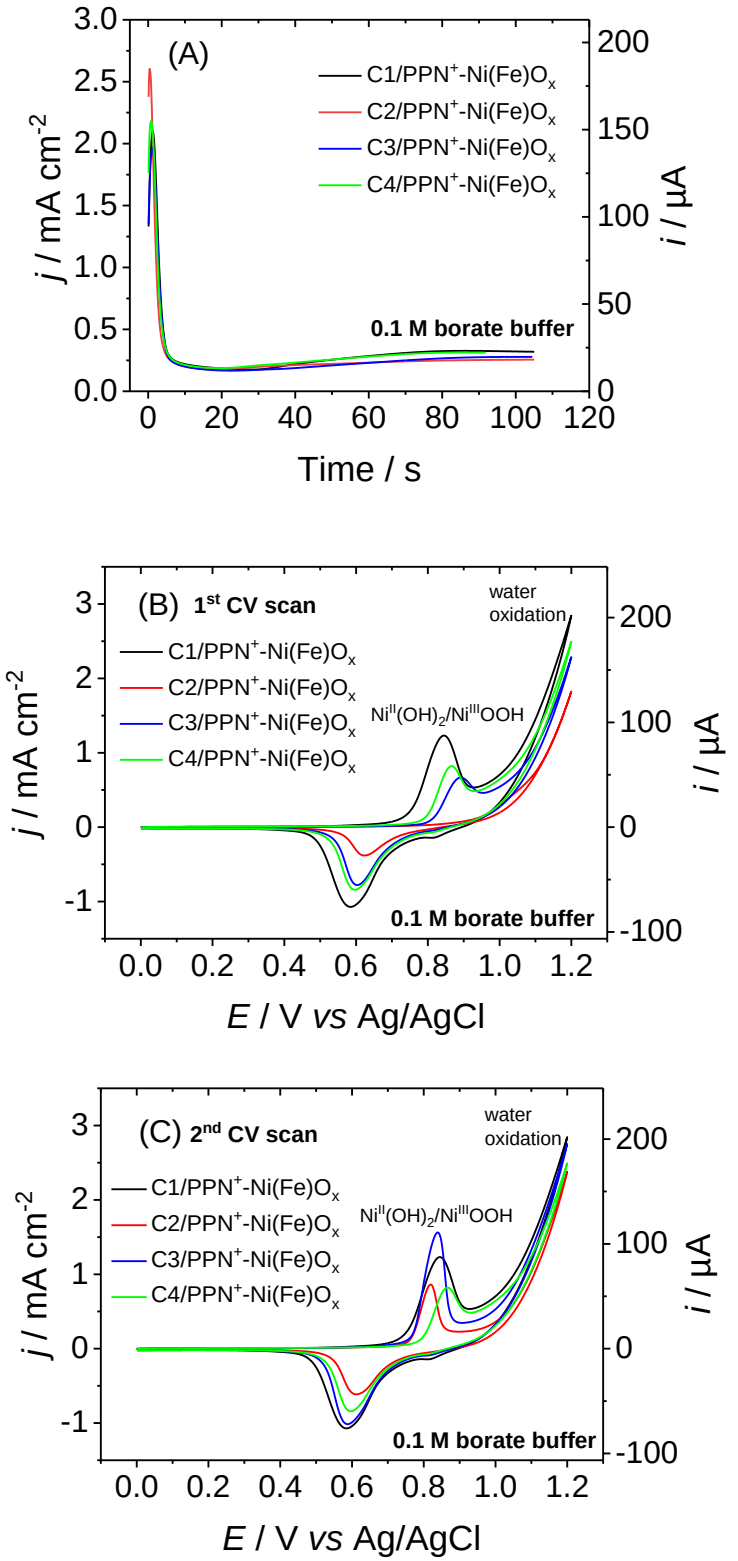

Figure 2. (A) Electro-induced generation of **Ni(Fe)O$_x$** with involuntary introduction of iron by potentiostatic experiment at +1.0 V *vs* Ag/AgCl (2 mC) on four C/**PPN**$^+$ electrodes (3 mm of diameter; Γ_{N^+} = 1.2 ± 0.1 x 10^{-7} mol cm^{-2}) in a 0.1 M borate buffer solution (pH 9.2) of 1 mM $NiSO_4$ and 5 mM $Na_2C_2O_4$. After electrogeneration of **Ni(Fe)O$_x$**, the first (B) and second (C) CV scans of four C/**PPN**$^+$-**Ni(Fe)O$_x$** electrodes (Γ_{Ni} = 1.13 ± 0.29 x 10^{-7} mol cm^{-2}, Γ_{Fe} = 3.55 ± 1.00 x 10^{-8} mol cm^{-2}) in a 0.1 M borate buffer solution (pH 9.2). Scan rate: 50 mV s^{-1}.

Besides, the amount of iron present in the blank is higher than those found in the nanocomposite, which contributes to increase the margin of error (Table 1). Although the margin of error is significant, three of the samples exhibit the same formula $Ni_{0.77}Fe_{0.23}$ with 23% of Fe (relative to Ni), the fourth one displaying a close formula of $Ni_{0.69}Fe_{0.31}$ with 31% of Fe. These high percentages of iron into **NiO_x** after deposition is surprising and differs from the study reported by the group of Boettcher[11] which showed that no iron is detected by XPS inside the NiO_x films after an anodic deposition at controlled potential (1.108 V *vs* Ag/AgCl, passing 10 mC cm^{-2}) in 0.1 M borate buffer (pH 9.2) containing 0.4 mM $Ni(NO_3)_2$. Nevertheless, they observed iron quantities until 14% molar (relative to Ni) into the **NiO_x** film after its anodization at a controlled potential of 1.055 V *vs* Ag/AgCl maintained 2h in a 0.5 M borate buffer (pH 9.2). In our study, the presence of iron into the **NiO_x** particles just after its deposition could be explained by the use of sodium oxalate in borate buffer that presents a higher iron concentration (30% higher) than a simple borate buffer (blank not shown in the Table 1).

Table 1. Loading of nickel and (involuntary introduced) iron electrodeposited in the nanocomposite electrode (C/PPN^+) and the composition of nickel iron oxide films, estimated from ICPMS measures

Carbon electrode N°	Nature of electrode	[Fe][c] µmol/L (without blank)[d]	Γ_{Fe}[e] nmol/cm² (without blank)[d]	[Ni][c] µmol/L (without blank)[d]	Γ_{Ni}[e] nmol/cm² (without blank)[d]	Formula
Blank[a]	-	8.69 ± 0.11	122.4 ± 1.6	0.03 ± 0.01	0.4 ± 0.1	
C1	C/**PPN^+-Ni(Fe)O_x** without anodization	10.71 (2.02)	150.8 (28.5)	6.86 (6.83)	96.6 (96.2)	$Ni_{0.77}Fe_{0.23}O_x$
C2		11.67 (2.98)	164.4 (42.0)	10.11 (10.08)	142.4 (142.0)	$Ni_{0.77}Fe_{0.23}O_x$
C3		9.87 (1.81)	139.0 (25.5)	6.00 (5.97)	84.4 (84.0)	$Ni_{0.77}Fe_{0.23}O_x$
C4		11.93 (3.24)	168.0 (45.6)	7.16 (7.13)	100.8 (100.4)	$Ni_{0.69}Fe_{0.31}O_x$
C5	C/**PPN^+-Ni(Fe)O_x** after anodization[b]	9.35 (0.66)	131.7 (9.3)	2.90 (2.87)	40.9 (40.5)	$Ni_{0.81}Fe_{0.19}O_x$
C6		11.30 (2.61)	159.2 (36.8)	3.41 (3.38)	48.0 (47.6)	$Ni_{0.56}Fe_{0.44}O_x$
C7		12.15 (3.46)	171.1 (48.7)	3.38 (3.35)	47.6 (47.2)	$Ni_{0.49}Fe_{0.51}O_x$
C8		9.59 (0.90)	135.1 (12.7)	2.38 (2.35)	33.5 (33.1)	$Ni_{0.72}Fe_{0.28}O_x$

[a] The blank corresponds to 1 mL solution of nitric acid (0.45 M); [b] anodization performed at 0.95 V *vs* Ag/AgCl in 1.0 M borate buffer during 45 min; [c] concentration of Fe and Ni measured by ICPMS in a 1 mL solution of nitric acid (0.45 M) in which the PPN^+-Ni(Fe)O_x films were dissolved; [d] values subtracted by the value of the blank; [e] surface coverage of Fe and Ni on carbon electrode (S = 0.071 cm²)

This amount of Fe into the **PPN^+-NiO_x** nanocomposite material has an impact on the redox behavior and the OER catalytic activity of **NiO_x**. The first (Figure 2(B)) and second (Figure 2(C)) CV scans recorded at the four C/**PPN^+-Ni(Fe)O_x** electrodes in 0.1 M borate buffer (pH 9.2), just after the anodic deposition of **Ni(Fe)O_x**, display the well-known $Ni^{II}(OH)_2/Ni^{III}OOH$ redox process between 0.5 and 0.9 V *vs* Ag/AgCl along with the catalytic current of water oxidation above 1 V. These cyclic voltammograms confirm that the anodic deposition of

Ni(Fe)O$_x$ within the **PPN$^+$** film, from a solution of nickel oxalate, is effective. Otherwise, the first and second CV scans exhibit a slightly different profile on the $Ni^{II}(OH)_2/Ni^{III}OOH$ process, specifically its anodic peak that could be very small or inexistent in the first scan (*e.g.* the C2 electrode in Figure 2(B)) due to the various proportions of $Ni^{II}(OH)_2$ present within the different nanocomposite electrodes after maintaining these electrodes at 1.0 V during *ca.* 100 s. After the first scan, the anodic peak in the second scan (Figure 2(C)) is magnified and cathodically shifted, most probably owing to the change of the oxidation state of **Ni(Fe)O$_x$** occurring during the first scan and to the nature change of the active surface states of metal oxide particles, also named *surfaquo* groups, that could govern the redox behavior of metal oxides and also their OER catalytic activity. The concept of *surfaquo* groups, largely developed by Lyons,[15] described the surface of metal oxide in alkaline water as a network of hydrated surface bound oxymetal complexes, such as metal oxyhydroxide network, that behaves as homogenous molecular catalysts. Further characterizations have to be carried out on the C/**PPN$^+$-Ni(Fe)O$_x$** electrode in view to observe the film morphology (SEM and AFM), to measure the size of **Ni(Fe)O$_x$** particles electrogenerated within the polymer film (TEM) and to determine the nature of the metal oxide such as their crystallinity and oxidation states by TEM-SAED, SEM-EDX, XPS, XANES and EXAFS).

The OER performance of the four C/**PPN$^+$-Ni(Fe)O$_x$** electrodes at 1.2 V *vs* Ag/AgCl, corresponding to an overpotential of 0.71 V, is relatively high in a borate buffer at pH 9.2 with a catalytic current density that does up to 2.82 mA cm^{-2} (Figure 2(C)). The current density of C/**PPN$^+$-Ni(Fe)O$_x$** is lower than that of the previous C/**PPN$^+$-NiO$_x$** anodes (3.6 mA cm^{-2}) prepared by our group[18] *via* a successively cathodic and anodic process in borate buffer but the amount of nickel is more than three-fold higher. Of note, we cannot exclude the presence of iron inside the C/**PPN$^+$-NiO$_x$** anodes previously reported by our group[18] and described briefly in Chapter II. In a near future, in order to observe the real effect of iron inside polypyrrole-nickel oxide nanocomposite material on the OER catalytic activity, we will have to prepare real blank electrodes with **PPN$^+$-NiO$_x$** films without trace of iron, by using ultra-pure reagents (*i.e.* $NiSO_4$, $Na_2C_2O_4$, H_3BO_3, NaOH) and ultra-pure nitric acid for the dissolution of the nanocomposite materials for ICPMS measurements.

So, in view to improve the performance of C/**PPN$^+$-Ni(Fe)O$_x$** electrodes, they underwent an anodization in borate buffer at 1.0 M. The anodization process in borate buffer of anodes based on **NiO$_x$** and **NiFeO$_x$**, first described by Nocera[10,19] and then by Boettcher[11] and Halaoui,[12] consists in maintaining these electrodes during several minutes or hours at an

anodic potential (*ca.* 1 V *vs* Ag/AgCl) in a borate buffer with a high ionic strength at 1.0 M. Consequently, we prepared four new C/**PPN$^+$-Ni(Fe)O$_x$** electrodes (C5-C8) by the anodic procedure described above in a 0.1 M borate buffer (pH 9.2) with 1 mM $NiSO_4$ and 5 mM $Na_2C_2O_4$. The latters were then characterized by cyclic voltammetry first in the same electrolyte without the nickel oxalate complex (Figure 3(A)) and then in a 1.0 M borate buffer (pH 9.2, Figure 3(B)).

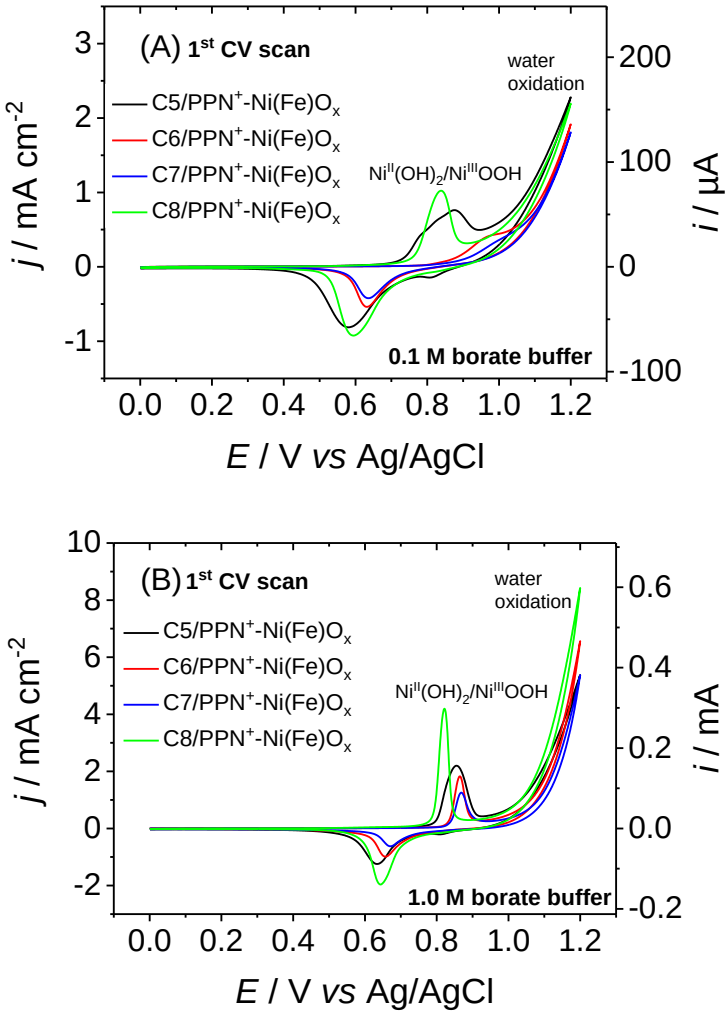

Figure 3: Cyclic voltammogram of four C/**PPN$^+$-Ni(Fe)**O$_x$ electrodes (3 mm of diameter; Γ_{N^+} = 1.2 ± 0.1 x 10^{-7} mol cm^{-2}) in a 0.1 M (A) and 1.0 M (B) borate buffer solution (pH 9.2), after electrogeneration of **Ni(Fe)O$_x$** by potentiostatic experiment at +1.0 V *vs* Ag/AgCl (2 mC) on C/**PPN$^+$** electrodes in a 0.1 M borate buffer solution (pH 9.2) of 1 mM $NiSO_4$ and 5 mM $Na_2C_2O_4$. Scan rate: 50 mV s^{-1}.

The redox behavior and the OER catalytic current in a 0.1 M borate buffer (pH 9.2) of this new series of C/**PPN$^+$-Ni(Fe)O$_x$** electrodes (Figure 3(A)) is very similar to that of the previous series of electrodes described above (see the electrodes C1, C2, C3 and C4, in Figure 2(B)). When the electrodes are studied in an electrolyte with a higher ionic strength (1.0 M borate buffer, Figure

3(B)), the anodic and cathodic peaks of the $Ni^{II}(OH)_2/Ni^{III}OOH$ process as-well-as the OER catalytic current are magnified, to reach *ca.* 8.4 mA cm^{-2} for the latter at 1.2 V *vs* Ag/AgCl (*vs* 2.25 mA cm^{-2} in a 0.1 M borate buffer, Figure 3(A)). The increase of measured current in function of the ionic strength of the electrolyte have been previously observed by Spiccia for OER electrocatalysts of cobalt oxide.[20] Then, the new series of C/**PPN^+-Ni(Fe)O_x** electrodes were anodized at 0.95 V *vs* Ag/AgCl in the 1.0 M borate buffer during 45 min (Figure 4(A)) and studied by CV in the same electrolyte (Figure 4(B)).

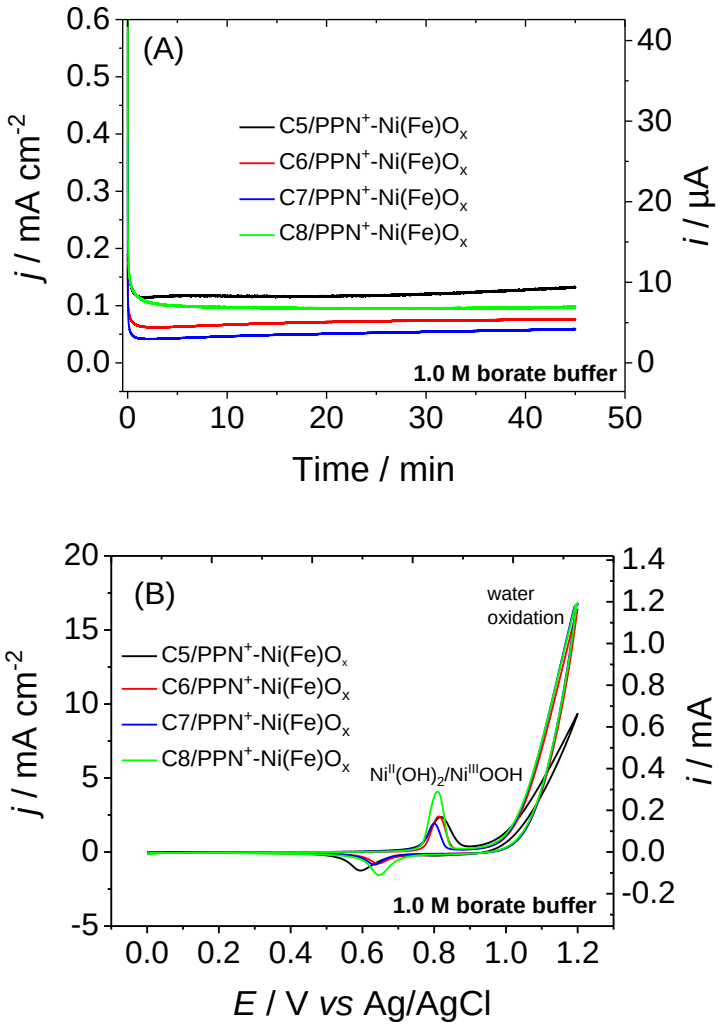

Figure 4: (A) Anodization of four C/**PPN^+-Ni(Fe)O_x** electrodes (3 mm of diameter; Γ_{N^+} = 1.2 ± 0.1 x 10^{-7} mol cm^{-2}, Γ_{Ni} = 4.03 ± 0.72 x 10^{-8} mol cm^{-2}, Γ_{Fe} = 2.90 ± 1.97 x 10^{-8} mol cm^{-2}) by potentiostatic experiment at +0.95 V *vs* Ag/AgCl during 45 min in a 1.0 M borate buffer solution (pH 9.2), (B) followed by their cyclic voltammetry recorded in the same solution. Scan rate: 50 mV s^{-1}.

Although the current of the anodic and cathodic peaks of Ni^{II}/Ni^{III} process remains almost unchanged in the 1.0 M borate buffer (Figure 4(B)), the OER catalytic current significantly increases until 16.9 mA cm^{-2} (*vs* 8.4 mA cm^{-2} before anodization, Figure 3(B)). Of note, the C5

electrode exhibits a weak increase of its OER catalytic current in the 1.0 M borate buffer for an unknown reason. In order to find explanations of its drastic increase of their OER performance, the anodized **PPN$^+$-Ni(Fe)O$_x$** materials were dissolved in an aqueous nitric acid solution (0.45 M) and analyzed by ICPMS (Table 1). For this new series of electrodes, the Γ_{Ni} and Γ_{Fe} values have been estimated to be 4.03 ± 0.73 x 10^{-8} and 2.90 ± 1.97 x 10^{-8} mol cm^{-2}, respectively. As previously observed, the margin of error on Γ_{Ni} and Γ_{Fe} are again significant with values of 18 and 67%. In addition, the amount of Ni in these anodized C/**PPN$^+$-Ni(Fe)O$_x$** electrodes are three time less than that of non-anodized electrodes (1.13 ± 0.29 x 10^{-7} mol cm^{-2}), while the amount of iron remains almost unchanged for two of them (3.68 – 4.87 x 10^{-8} cm^{-2}) and even less for the other two (0.93 – 1.27 x 10^{-8} cm^{-2}). All in all, after anodization, the percentage of Fe within the **NiO$_x$** particles increased for two of them (*i.e.* $Ni_{0.56}Fe_{0.44}O_x$ and $Ni_{0.49}Fe_{0.51}O_x$) and was unchanged for the other two (*i.e.* $Ni_{0.81}Fe_{0.19}O_x$ and $Ni_{0.72}Fe_{0.28}O_x$). Therefore, the increase of the OER activity of the anodized C/**PPN$^+$-Ni(Fe)O$_x$** electrodes could be due to the introduction of Fe within **NiO$_x$** during anodization. Considering the significant margin of error cited above, it's hard to draw definitive conclusions, but the introduction of Fe into **NiO$_x$** appears to be poorly controlled *via* anodization. One way to improve the control on the quantity of Fe in **NiO$_x$** is to electrogenerate the **NiFeO$_x$** particles within the cationic polypyrrole film from a mixed solution of anionic iron and nickel complexes. Ammonium iron(III) citrate mixed with nickel oxalate is a good candidate to make this electro-deposit in the polymer film.

II.3 – Electrochemical study of ammonium Iron(III) citrate in a borate buffer

Ammonium iron(III) citrate is the commercial reagent chosen to electrogenerate the nanoparticles of nickel-iron oxide inside the poly(pyrrole-alkyl ammonium) film. Sold with the formula $[Fe_x(C_6H_8O_7)(NH_3)_y]$, this species usually used as food additive to regulate the acidity (E381), is very soluble in water. The structure of the iron citrate complexes is intricate and depends on the deprotonation of the citrate ligand which can vary in function of the pH. It is worth noting that the pKa values of the carboxylic acid groups of citric acid are 3.13, 4.76, and 6.40, and that of the hydroxyl function is 14.4.[21-23] The group of Pierre reviewed the different modes of coordination of the iron salt by citric acid and the various structures of iron-citrate complexes reported in literature.[24] Particularly, the group of Salifoglou isolated in 1998 the structure of the

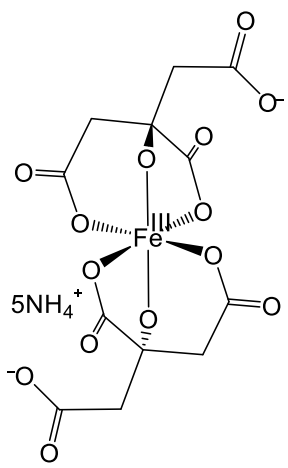

Scheme 2. Isolated structure of ammonium iron(III) citrate by the group of Salifoglou, with the formula $(NH_4)_5[Fe(C_6H_4O_7)_2]\bullet 2H_2O$

first mononuclear anionic iron(III) citrate complex containing ammonium salt (*i.e.* $(NH_4)_5[Fe(C_6H_4O_7)_2]\bullet 2H_2O$), from an aqueous solution at pH 8.[25] The latter displays two deprotonated citric acid coordinating an iron(III) salt by four carboxylate functions and two hydroxylate, the third carboxylate group of each citrate anion being linked to the ammonium moieties (Scheme 2).

Given that the $[Fe_x(C_6H_8O_7)(NH_3)_y]$ sample will be used herein in an aqueous solution buffered at pH 9.2 (close to pH 8) for the electrosynthesis of **$NiFeO_x$** particles, we can consider that in our study this iron complex is under the form of $[Fe(C_6H_4O_7)_2]^{5-}$. This negative charge of 5^- will promote its incorporation into the positively charged poly(pyrrole-alkyl ammonium) film. Before the incorporation of $[Fe_x(C_6H_8O_7)(NH_3)_y]$ into the polymer and its electro-oxidation, its redox behavior was investigated by cyclic voltammetry in a 0.1 M borate buffer at pH 9.2 (Figure 5), that is the electrolyte employed to electrogenerate the particle of $NiFeO_x$. Since the first studies of the redox properties of iron citrate solutions by polarography of Lingane,[26] Meites[27] and Grant,[28] only few studies were performed by CV and they were essentially focused on the cathodic region.[21,29-31]

Figure 5(A) shows the cyclic voltammogram of $[Fe_x(C_6H_8O_7)(NH_3)_y]$ sweeping in the cathodic region from 0 to -1.4 V *vs* Ag/AgCl, then from -1.4 to +1.4 V in the anodic region, and from 1.4 to 0 V.

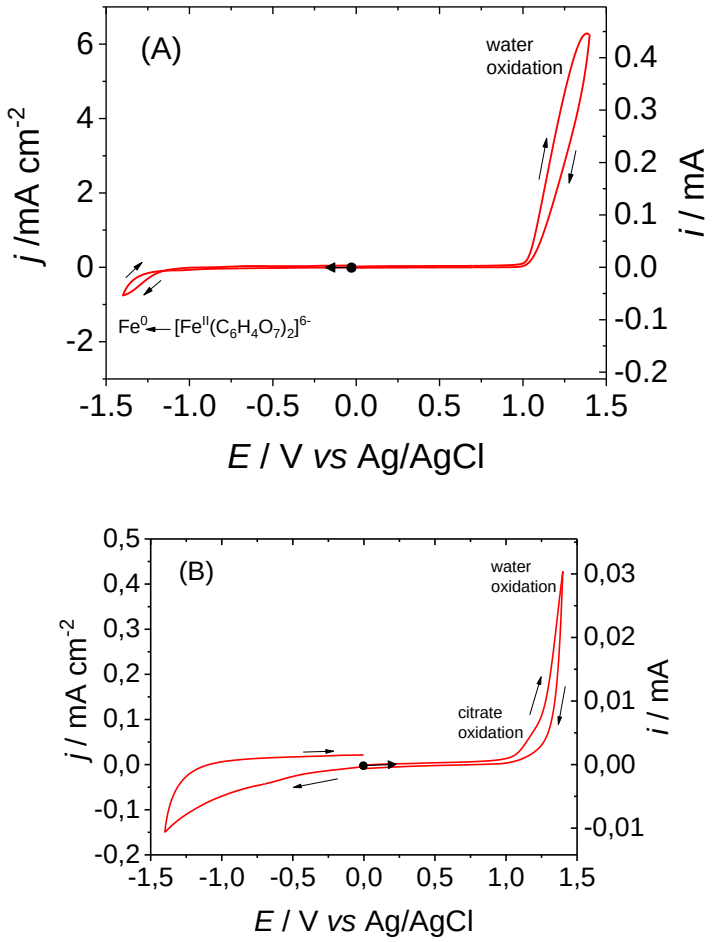

Figure 5: Cyclic voltammograms recorded at C electrode (3 mm of diameter) in a 0.1 M borate buffer solution (pH 9.2) of 5 mM ammonium iron(III) citrate ($[Fe_x(C_6H_8O_7)(NH_3)_y]$) (A) scanning first to the cathodic potentials and then to the anodic potentials or (B) scanning first to the anodic potentials and then to the cathodic potentials. Scan rate: 50 mV s^{-1}.

The cathodic part of CV (Figure 5(B)) is complex and was barely ascribed to the reductions of $[Fe^{III}(C_6H_4O_7)_2]^{5-}$ to $[Fe^{II}(C_6H_4O_7)_2]^{6-}$ and $[Fe^{II}(C_6H_4O_7)_2]^{6-}$ to metallic Fe^0. The irreversible process above 1.0 V in the anodic region is undoubtedly the catalytic wave of water oxidation promoted by iron oxide generated in the first cathodic scan (Figure 5(A)).

Figure 5(C) shows the cyclic voltamogram of $[Fe_x(C_6H_8O_7)(NH_3)_y]$ sweeping first in the anodic region from 0 to 1.4 V *vs* Ag/AgCl, then from 1.4 V to -1.4 V in the cathodic region, and from -1.4 to 0 V. The pre-peak in the anodic part at *ca.* 1.16 V could be ascribed to the oxidation of citrate leading to the decomposition of the iron citrate complex and the concomitant formation of iron oxide. Water oxidation catalyzed by iron oxide occurs above this pre-peak. The reverse scan in the cathodic region is featureless with an irreversible process below -1.0 V potentially ascribed to the reduction of iron oxide to metallic iron. So, according to the CV in

Figure 5(C), the electrosynthesis of **$NiFeO_x$** nanoparticles inside the polymer film could be carried out at potential of 1.0 V *vs* Ag/AgCl, on the foot of citrate oxidation wave.

II.4 - Electrosynthesis and electrocharacterization of the poly(pyrrole-alkyl ammonium)-nickel/iron oxide nanocomposite material on carbon electrode

The preparation of the poly(pyrrole-alkyl ammonium)-nickel and iron oxide nanocomposite material was also performed in three steps (Scheme 3). As described above, the first step is the oxidative polymerization of **PN^+** on C electrode (3 mm of diameter; S = 0.071 cm^2) in acetonitrile under inert atmosphere into a glovebox, passing 4 mC. For the second step, the C/**PPN^+** modified electrode is dipped during 1 h in a 0.1 M borate buffer solution with 1 mM $Ni(SO_4)$, 5 mM $Na_2C_2O_4$ and 0.4 mM (or 0.8 mM) $[Fe_x(C_6H_8O_7)(NH_3)_y]$. Finally, the **$NiFeO_x$** particles are electrogenerated within **PPN^+** film *via* an anodic process by maintaining the C/**PPN^+** electrode charged with nickel oxalate and iron citrate complexes at 1.0 V *vs* Ag/AgCl in the electrolyte cited above, passing 4 mC of charge. This series of modified electrodes will be named C/**PPN^+-$NiFeO_x$** (without parenthesis around Fe). Besides, for this preliminary work, three C/**PPN^+-$NiFeO_x$** electrodes have been prepared to show the reproducibility of the process (C9, C10, C11 for **$NiFeO_x$** generation from 0.4 mM iron citrate; C12, C13, C14 for **$NiFeO_x$** generation from 0.8 mM iron citrate), even if more electrodes will be needed in a future work in order to obtain a more representative sampling. The electrogeneration of **$NiFeO_x$** particles was carried out from two different concentrations of iron citrate, 0.4 and 0.8 mM, in order to evaluate the influence of its concentration in the deposition solution on the percentage of iron introduced into **NiO_x** and thus on the OER catalytic performance of the nanocomposite material. The deposition time of **$NiFeO_x$** particles, from a 0.1 M borate buffer solution with 0.4 mM $[Fe_x(C_6H_8O_7)(NH_3)_y]$, 1 mM $NiSO_4$ and 5 mM $Na_2C_2O_4$, varies between 137 and 350 s for 4 mC of charge, as observed in the chronoamperograms in Figure 6(A). Then the three C/**PPN^+-$NiFeO_x$** electrodes (C9, C10, C11) were studied by cyclic voltammetry in a 0.1 M (Figure 6(B)) and 1.0 M (Figure 6(C)) borate buffer at pH 9.2, without nickel oxalate and iron citrate. As previously observed for the 0.1 M borate buffer, the CVs of C/**PPN^+-$NiFeO_x$** exhibit the $Ni^{II}(OH)_2/Ni^{III}OOH$ process along with a strong OER catalytic current above *ca.* 0.9 V *vs* Ag/AgCl (Figure 6(B)). This confirms the effective generation of **$NiFeO_x$** particles within the **PPN^+** film. Even if more electrodes have to be prepared in a near future, the reproducibility on three electrodes seems relatively good since the potential Ni^{II}/Ni^{III} redox process and the catalytic current are quite similar for all electrodes.

Scheme 3: Electrosynthesis of poly(pyrrole-alkylammonium)/**NiFeO$_x$** nanocomposite film modified electrodes. (i) Formation of **PPN$^+$** on C electrode by oxidative electropolymerization of monomer PN$^+$ (4 mM) at +0.95 V *vs* Ag/AgNO$_3$ in CH$_3$CN, 0.1 M [Bu$_4$N]ClO$_4$; (ii) incorporation of $[Ni(C_2O_4)_2]^{2-}$ and $[Fe_x(C_6H_8O_7)(NH_3)_y]$ into PPN$^+$ upon soaking during 1h in a 0.1 M aqueous borate buffer solution (pH 9.2) of 1 mM NiSO$_4$, 5 mM Na$_2$C$_2$O$_4$ and 0.4 mM (or 0.8 mM) $[Fe_x(C_6H_8O_7)(NH_3)_y]$; (iii) electro-oxidation followed by an electroprecipitation of **NiFeO$_x$** particles at +1.0 V *vs* Ag/AgCl in a 0.1 M borate buffer solution (pH 9.2) of nickel(II) oxalate and ammonium iron(III) citrate complexes.

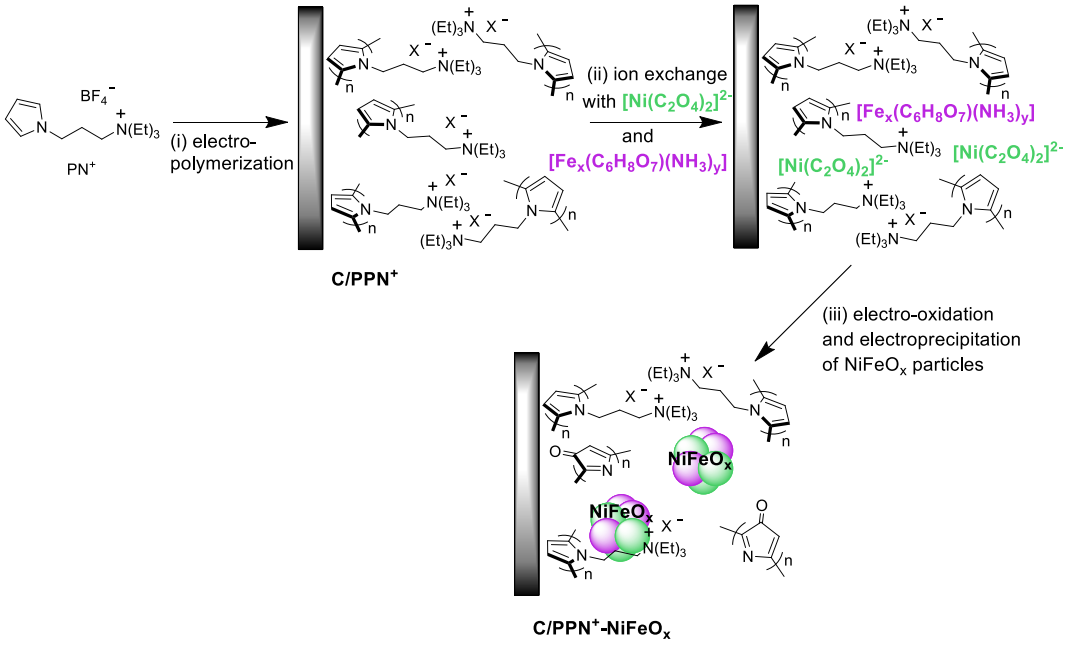

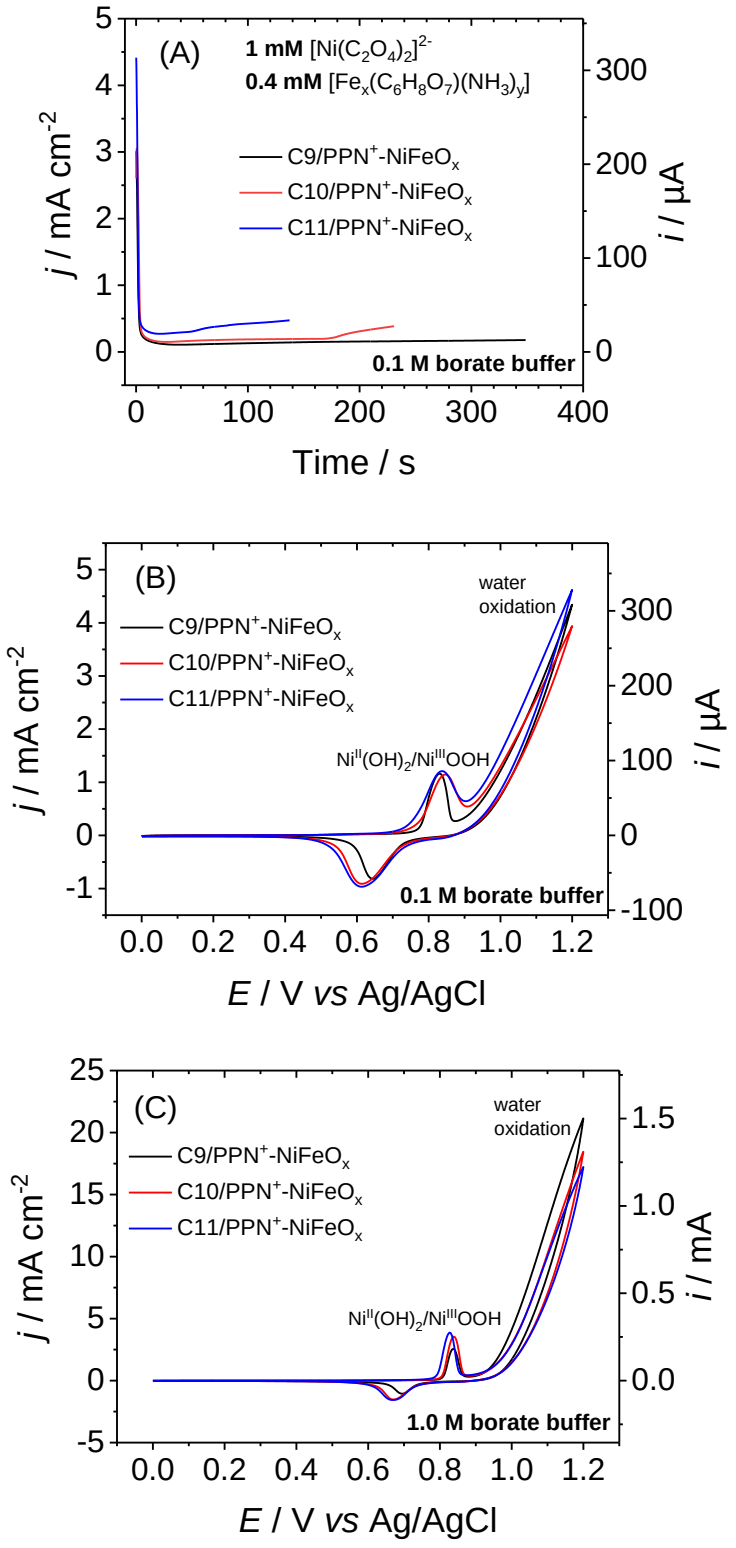

Figure 6: (A) Electro-induced generation of **$NiFeO_x$** by potentiostatic experiment at +1.0 V *vs* Ag/AgCl (4 mC) on three C/**PPN^+** electrodes (3 mm of diameter; $\Gamma_{N^+} = 1.2 \pm 0.1 \times 10^{-7}$ mol cm^{-2}) in a 0.1 M borate buffer solution (pH 9.2) of 1 mM $NiSO_4$, 5 mM $Na_2C_2O_4$ and 0.4 mM $[Fe_x(C_6H_8O_7)(NH_3)_y]$. After electrogeneration of $NiFeO_x$, cyclic voltammograms of three C/**PPN^+-$NiFeO_x$** electrodes ($\Gamma_{Ni} = 4.19 \pm 0.74 \times 10^{-8}$ mol cm^{-2}, $\Gamma_{Fe} = 5.11 \pm 0.74 \times 10^{-8}$ mol cm^{-2}) in a 0.1 M (B) and 1.0 M (C) borate buffer solution (pH 9.2). Scan rate: 50 mV s^{-1}.

Table 2: Loading of nickel and (intentionally introduced) iron electrodeposited in the nanocomposite electrode (C/**PPN**$^+$) and the composition of nickel iron oxide films, estimated from ICPMS measures

Carbon electrode N°	Nature of electrode and [Ni:Fe] (mM) solution for deposition	[Fe][c] µmol/L (without blank)[d]	Γ_{Fe}[e] nmol/cm² (without blank)[d]	[Ni][c] µmol/L (without blank)[d]	Γ_{Ni}[e] nmol/cm² (without blank)[d]	Formula
Blank[a]	-	1.02 ± 0.10	71.8 ± 7.0	0.03 ± 0.01	2.1 ± 0.7	
C9	C/**PPN$^+$-NiFeO$_x$** [1:0.4]	1.68 (0.66)	118.3 (46.5)	0.52 (0.49)	36.6 (34.5)	$Ni_{0.43}Fe_{0.57}O_x$
C10		1.64 (0.62)	115.5 (43.7)	0.62 (0.59)	43.7 (41.6)	$Ni_{0.49}Fe_{0.51}O_x$
C11		1.85 (0.83)	130.3 (58.5)	0.73 (0.70)	51.4 (49.3)	$Ni_{0.46}Fe_{0.54}O_x$
C12	C/**PPN$^+$-NiFeO$_x$** [1:0.8]	1.62 (0.60)	114.1 (42.3)	0.44 (0.41)	31.0 (28.9)	$Ni_{0.41}Fe_{0.59}O_x$
C13		1.57 (0.55)	110.6 (38.8)	0.49 (0.46)	34.5 (32.4)	$Ni_{0.46}Fe_{0.54}O_x$
C14		1.48 (0.46)	104.2 (32.4)	0.48 (0.45)	33.8 (31.7)	$Ni_{0.49}Fe_{0.51}O_x$

[a] The blank corresponds to 5 mL solution of nitric acid (0.45 M); [b] anodization performed at 0.95 V *vs* Ag/AgCl in 1.0 M borate buffer (pH 9.2) during 45 min; [c] concentration of Fe and Ni measured by ICPMS in a 5 mL solution of nitric acid (0.45 M) in which the **PPN$^+$-NiFeO$_x$** films were dissolved; [d] values subtracted by the value of the blank; [e] surface coverage of Fe and Ni on carbon electrode (S = 0.071 cm²)

Besides, this reproducibility was also observed for the Γ_{Ni} and Γ_{Fe} values of these electrodes, which have been estimated by ICPMS after their dissolution in nitric acid (0.45 M) to be 4.19 ± 0.74 x 10^{-8} and 5.11 ± 0.74 x 10^{-8} mol cm^{-2}, respectively (Table 2). Of note, the margins of error on the Γ_{Ni} and Γ_{Fe} values (18 and 14 % respectively, Table 2) are slightly smaller than those of the previous series of C/**PPN$^+$-Ni(Fe)O$_x$** electrodes (26 and 28 % respectively, Table 1) with involuntary introduction of iron. This suggests that the electrogeneration of **NiFeO$_x$** with a mixture of iron citrate and nickel oxalate allows a better control on the iron quantity introduced into **NiO$_x$**, compared to the involuntary introduction of iron. The best OER performance was obtained with percentages of iron comprise between 51 and 57 %. The group of Bell demonstrated that the best OER activity with **NiFeO$_x$**-based anodes has been reached with 40 % of iron inside the **NiO$_x$** films.[32] Given the margins of error of our ICPMS measurements, our nanocomposite materials most certainly have iron and nickel compositions very similar to those of Bell's anodes.

In the 1.0 M borate buffer (Figure 6(C)), similar $Ni^{II}(OH)_2/Ni^{III}OOH$ redox process is observed for the three C/**PPN$^+$-NiFeO$_x$** electrodes with higher currents, and the OER catalytic current at 1.2 V *vs* Ag/AgCl (overpotential 0.71 V) is multiplied by a factor of 4.55 to reach 21.0 mA cm^{-2} (*vs* 4.61 mA cm^{-2} in a 0.1 M borate buffer, Figure 6(B)) owing to the higher ionic strength of the electrolyte (see above). This OER catalytic activity is very impressive and is among the best in literature (see the discussion below).

For the electrogeneration of **$NiFeO_x$** particles from a mixture of 0.8 mM $[Fe_x(C_6H_8O_7)(NH_3)_y]$, 1 mM $NiSO_4$ and 5 mM $Na_2C_2O_4$, the deposition times monitored by chronoamperometry (Figure 7(A)), the redox behavior and the OER performance of the three C/**PPN^+-$NiFeO_x$** electrodes studied by cyclic voltammetry in 0.1 M (Figure 7(B)) and 1.0 M (Figure 7(C)) borate buffers, are very similar to those obtained from a solution containing 0.4 mM iron citrate complex (Figure 6). In addition to these similarities, the OER performance of C/**PPN^+-$NiFeO_x$** electrodes prepared with 0.8 mM iron citrate is highly reproducible with catalytic currents in a narrow range between 4.28-4.69 mA cm^{-2} in 0.1 M borate buffer, and between 21.55-22.61 mA cm^{-2} in a 1.0 M borate buffer, at a potential of 1.2 V *vs* Ag/AgCl (*i.e.* an overpotential of 0.71 V). This reproducibility is also observed with the Γ_{Ni} and Γ_{Fe} values of $3.07 \pm 0.18 \times 10^{-8}$ and $3.74 \pm 0.75 \times 10^{-8}$ mol cm^{-2}, respectively (Table 2), which display the lowest margins of error in the study (6 and 13 % respectively). Consequently, the use of 0.8 mM iron citrate with 1 mM nickel oxalate is the best mixture to prepare a reproducible **PPN^+-$NiFeO_x$** nanocomposite material for OER.

A comparison between the cyclic voltammograms of C/**PPN^+-$NiFeO_x$** and C/**PPN^+-Ni(Fe)O_x** (*i.e.* intentional *vs* involuntary introduction of iron) in the 0.1 M borate buffer (Figure 8(A)) shows that the OER catalytic activity of C/**PPN^+-$NiFeO_x$** (4.73 mA cm^{-2}, with C13) is 1.66 times higher than that of C/**PPN^+-Ni(Fe)O_x** (2.84 mA cm^{-2}, with C1) without anodization. This is directly correlated to the percentage of iron inside the NiO_x particles, which is higher in C13/**PPN^+-$NiFeO_x$** ($Ni_{0.46}Fe_{0.54}O_x$) than in C1/**PPN^+-Ni(Fe)O_x** ($Ni_{0.77}Fe_{0.23}O_x$). In the same way, with a 1.0 M borate buffer, C13/**PPN^+-$NiFeO_x$** with intentional introduction of iron present an OER catalytic current 3.45 times higher (22.61 mA cm^{-2}) than that of C6/**PPN^+-Ni(Fe)O_x** with involuntary introduction of iron (6.55 mA cm^{-2}) at 1.20 V *vs* Ag/AgCl. Nevertheless, when the C6/**PPN^+-Ni(Fe)O_x** electrode is anodized at 0.95 V *vs* Ag/AgCl the catalytic current is raised until 16.32 mA cm^{-2} at 1.2 V, most probably due to the iron introduction during the anodization process to achieve 44 % of iron (*i.e.* $Ni_{0.56}Fe_{0.44}O_x$), but stays below the performance of C13/**PPN^+-$NiFeO_x$** containing 54 % of iron ($Ni_{0.46}Fe_{0.54}O_x$). Consequently the intentional introduction of iron *via* the mixture of 0.8 mM iron citrate and 1 mM nickel oxalate is the most adequate method to prepare **PPN^+-$NiFeO_x$** nanocomposite materials with the highest OER performance.

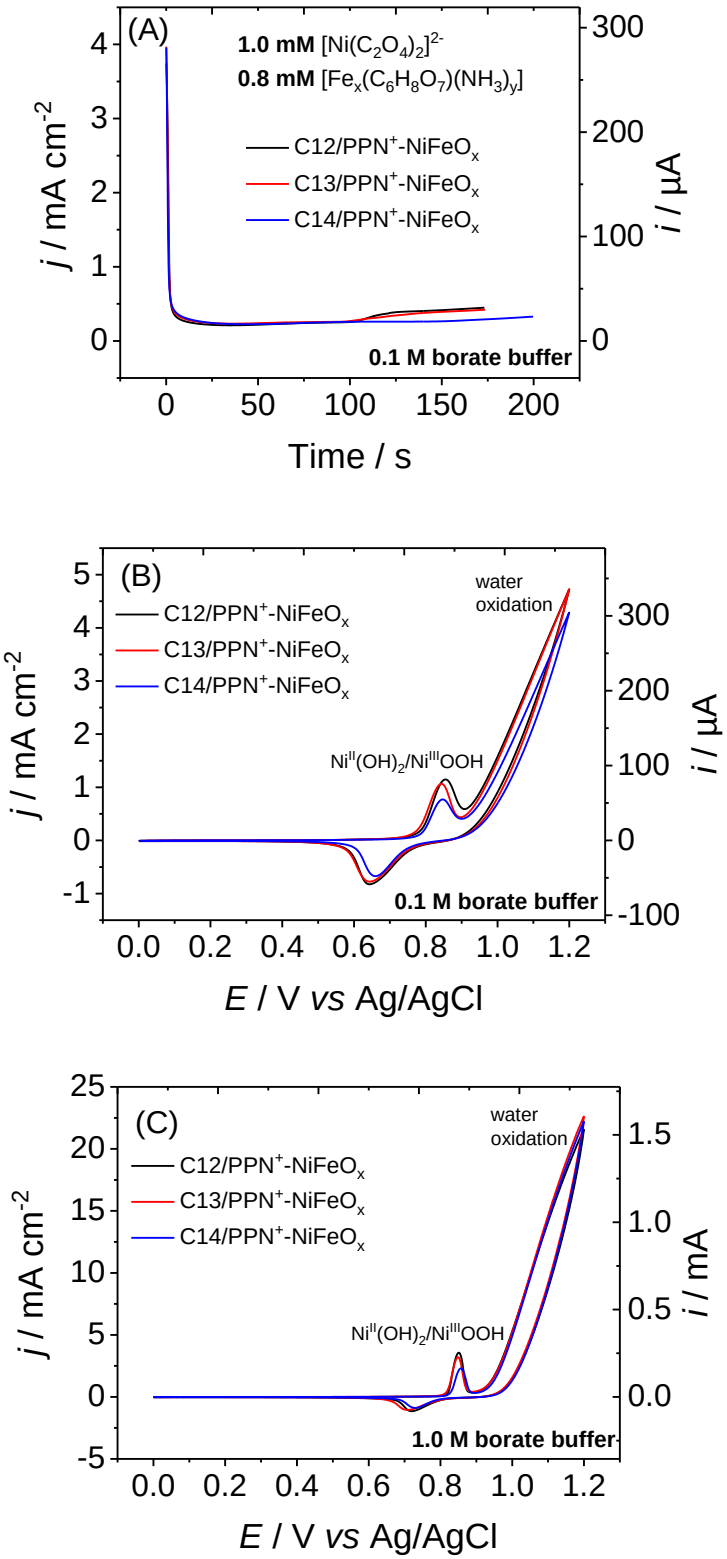

Figure 7: (A) Electro-induced generation of **NiFeO$_x$** by potentiostatic experiment at +1.0 V *vs* Ag/AgCl (4 mC) on three C/PPN$^+$ electrodes (3 mm of diameter; Γ_{N^+} = 1.2 ± 0.1 x 10^{-7} mol cm^{-2}) in a 0.1 M borate buffer solution (pH 9.2) of 1 mM $NiSO_4$, 5 mM $Na_2C_2O_4$ and 0.8 mM $[Fe_x(C_6H_8O_7)(NH_3)_y]$. After electrogeneration of **NiFeO$_x$**, cyclic voltammograms of three C/**PPN$^+$-NiFeO$_x$** electrodes (Γ_{Ni} = 3.06 ± 0.17 x 10^{-8} mol cm^{-2}, Γ_{Fe} = 3.73 ± 0.49 x 10^{-8} mol cm^{-2}) in a 0.1 M (B) and 1.0 M (C) borate buffer solution (pH 9.2). Scan rate: 50 mV s^{-1}.

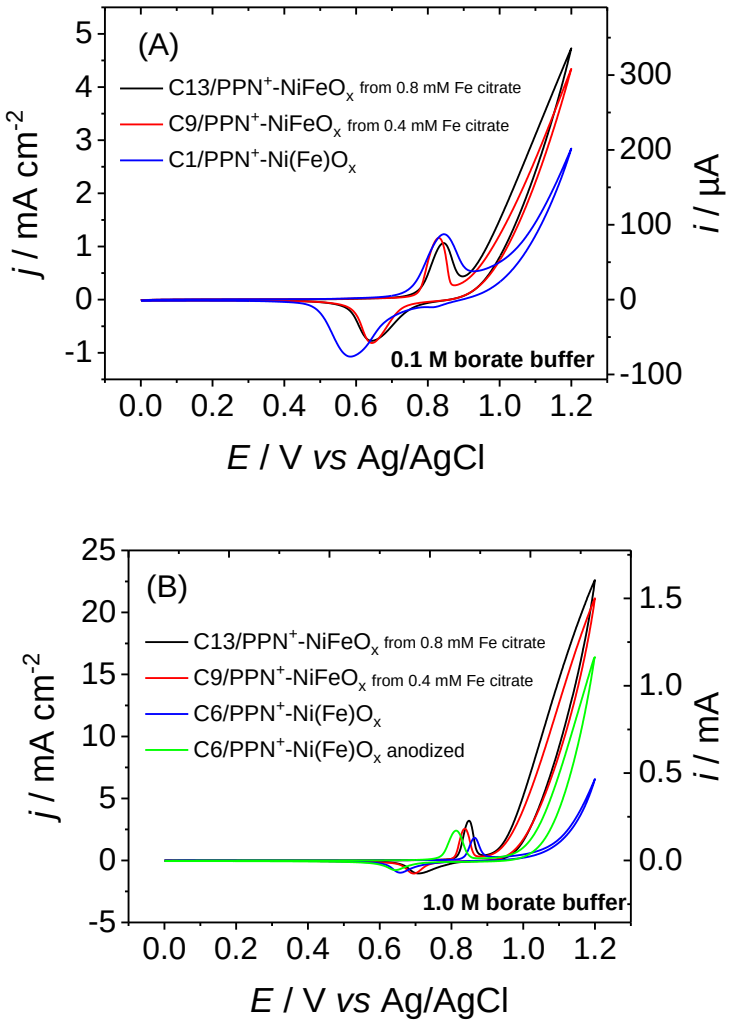

Figure 8: Cyclic voltammograms recorded in a 0.1 M (A) and 1.0 M (B) borate buffer solution (pH 9.2) at C13/**PPN$^+$-NiFeO$_x$** (with intentional addition of iron, black trace, Formula: $Ni_{0.46}Fe_{0.54}O_x$ in (A) and (B), Γ_{N^+} = 1.2 ± 0.1 x 10^{-7} mol cm^{-2}, Γ_{Ni} = 3.24 x 10^{-8} mol cm^{-2}, Γ_{Fe} = 3.88 x 10^{-8} mol cm^{-2}), C9/PPN$^+$-NiFeO$_x$ (with intentional addition of iron, red trace, Formula: $Ni_{0.43}Fe_{0.57}O_x$ in (A) and (B), Γ_{N^+} = 1.2 ± 0.1 x 10^{-7} mol cm^{-2}, Γ_{Ni} = 3.45 x 10^{-8} mol cm^{-2}, Γ_{Fe} = 4.65 x 10^{-8} mol cm^{-2}), C1/**PPN$^+$-Ni(Fe)O$_x$** (with involuntary addition of iron, blue trace, Formula: $Ni_{0.77}Fe_{0.23}O_x$ in (A), Γ_{N^+} = 1.2 ± 0.1 x 10^{-7} mol cm^{-2}, Γ_{Ni} = 9.62 x 10^{-8} mol cm^{-2}, Γ_{Fe} = 2.85 x 10^{-8} mol cm^{-2}) and C6/**PPN$^+$-Ni(Fe)O$_x$** before (with involuntary addition of iron, blue trace in (B)) and after anodization at +0.95 V *vs* Ag/AgCl during 45 min in a 1.0 M borate buffer solution (pH 9.2) (green trace in (B), Formula: $Ni_{0.56}Fe_{0.44}O_x$ in (B), Γ_{N^+} = 1.2 ± 0.1 x 10^{-7} mol cm^{-2}, Γ_{Ni} = 4.76 x 10^{-8} mol cm^{-2}, Γ_{Fe} = 3.68 x 10^{-8} mol cm^{-2}). Scan rate: 50 mV s^{-1}.

II.5 – Comparison of electrocatalytic activities of C/PPN$^+$-NiFeO$_x$ anodes and NiFeO$_x$ anodes of literature

The OER performance of the C13/**PPN$^+$-NiFeO$_x$** electrode, prepared in a 0.1 M borate buffer with 0.8 mM iron citrate and 1 mM nickel oxalate, will be considered as our benchmark in our work since it presents the highest catalytic current at 1.2 V *vs* Ag/AgCl in 0.1 M and 1.0 M borate buffers (pH 9.2). Table 3 summarizes the catalytic performance of C13/**PPN$^+$-NiFeO$_x$** in 0.1 M and 1.0 M borate buffers (pH 9.2) and those of C/**PPN$^+$-NiO$_x$** previously reported by our group[18], and those of the rare examples of **NiFeO$_x$**-based anodes reported in literature at pH 9.2 in borate buffer. The figures of merit of anodes operating at pH 9.2 are generally the OER catalytic current density at overpotentials (η) between 0.40 and 0.61 V (*i.e.* at potentials between 0.89 and 1.1 V *vs* Ag/AgCl at pH 9.2) and the overpotential at a current density of 1 mA cm^{-2}. In addition, to be able to compare anodes with each other which do not have the same amount of electrocatalysts on the surface, the mass activity (A mg$^{-1}_{catalyst}$) and the turnover frequency (TOF in s^{-1}) of electrocatalysts are also provided.

In a 0.1 M borate buffer, the C13/**PPN$^+$-NiFeO$_x$** electrode displays a high catalytic current of 3.10 mA cm^{-2} at η of 0.61 V and a low η value of 0.48 V at 1 mA cm^{-2} with a Ni/Fe mass loading of 1.90/2.17 µg cm^{-2}. C13/**PPN$^+$-NiFeO$_x$** also displays a high mass activity and TOF of 1.63 A mg^{-1} and 0.25 s^{-1} respectively at a η value of 0.61 V. Compared to the previous C/**PPN$^+$-NiO$_x$** electrode reported by group that was prepared by a successively cathodic and anodic process,[18] the OER performance of C13/**PPN$^+$-NiFeO$_x$** are clearly superior in a 0.1 M borate buffer due to the incorporation of iron into the **NiO$_x$** particles. Another possible explanation of its superiority could be the smaller size of **NiFeO$_x$** electrodeposited by an anodic process compared to that of NiO$_x$ particles electrodeposited by the cathodic/anodic process. Recent work in our group on nanocomposite materials based on anionic poly(pyrrole-carboxylate)-metal oxide shows that it is possible to electrogenerate very small particles of metal oxide (<1 nm) within polymer film by an anodic process (unpublished results of the PhD student Baptiste Dautreppe). If it is true, smaller particles sizes of **NiFeO$_x$** into the **PPN$^+$** film would confer a higher nanostructuration to C13/**PPN$^+$-NiFeO$_x$**, thus a higher electroactive surface area and a higher OER catalytic current. Future TEM and XAS experiments will be necessary to measure the size of **NiFeO$_x$** particles embedded into the **PPN$^+$** film.

Although the examples of **NiFeO$_x$**-based anodes operating at pH 9.2 are rare, other groups such as that of Boettcher[11] reported a **NiFeO$_x$** anode deposited on Au-Ti coated glass

electrode rather active in a 0.1 M borate buffer with 7.4 mA cm^{-2} at η of 0.61 V and a η value of 0.43 V at 1 mA cm^{-2}. This anode (denoted Au-Ti/$Ni_{0.86}Fe_{0.14}O_x$) containing only 14% molar of iron outperforms the C13/**PPN^+-$NiFeO_x$** electrode, but if the high Ni mass loading of Au-Ti/$Ni_{0.86}Fe_{0.14}O_x$ (*ca.* 115 µg cm^{-2}) is considered, its mass activity and TOF values (0.064 A mg^{-1} and 0.04 s^{-1}) are much lower than those of C13/**PPN^+-$NiFeO_x$**. The Luo's anode, which corresponds to a 3D $NiFeO_x$ nanoarray electrodeposited on a large surface area of a carbon cloth electrode, displays the highest OER performance for an anode in a 0.1 M borate buffer at pH 9.2 with very low overpotentials of 0.365 and 0.444 V at 1 and 10 mA cm^{-2} respectively.[33] Nevertheless, it is not possible to compare its performance with C13/**PPN^+-$NiFeO_x$** and the other $NiFeO_x$-based anodes of literature, since they did not estimate the mass loading of nickel and iron deposited on electrode. The Strasser's group also reported a very active anode (C/$Ni_{0.62}Fe_{0.38}O_x$) in 0.1 M borate buffer with a very low overpotential of 0.37 V at 1 mA cm^{-2}, and high mass activity and TOF values of 1.9 A mg^{-1} and 0.29 s^{-1} respectively at η of 0.40 V.[34] Although its OER activity seems superior to that of C13/**PPN^+-$NiFeO_x$** (0.48 V@1 mA cm^{-2}, 0.24 A mg^{-1}@0.4V, 0.04 s^{-1}@0.4V, respectively), the comparison has to be considered with caution since the potential (*E*) measured by Strasser et al.[34] during cyclic voltammetry are corrected for the ohmic drop (*E-iR*) between the working and reference electrodes, while in our study the potentials are not corrected. For instance, at 3.89 mA cm^{-2} of current density estimated at η of 0.40 V, the potential correction (iR) with a resistance of 200 Ω (value measured by Strasser's group in the 0.1 M borate buffer) is significant with a value of 0.152 V. This means that, without correction of ohmic drop, this anode should display a catalytic current of 3.89 mA cm^{-2} at η of 0.552 V instead of 0.4 V, which is still superior to the performance of C13/**PPN^+-$NiFeO_x$** (2.17 mA cm^{-2} at 0.552 V, Figure 8A) but in the same order of magnitude.

In 1.0 M borate buffer with a higher ionic strength, C13/**PPN^+-$NiFeO_x$** present very high OER catalytic current of 14.6 mA cm^{-2} at η of 0.61 V and a relatively low η value of 0.44 V at 1 mA cm^{-2}. In this electrolyte, its mass activity and TOF are also significantly improved to achieve 7.7 A mg^{-1} and 1.17 s^{-1} respectively at η of 0.61 V. In literature, only the Halaoui's group reported an anode with nickel/iron oxide deposited on FTO (denoted FTO/$Ni_{0.6}Fe_{0.4}O_x$) catalyzing OER in a 1.0 M borate buffer at pH 9.2. Its catalytic current (2.33 mA cm^{-2}@0.61 V) is 6.27 times lower than that of C13/**PPN^+-$NiFeO_x$**, but this is ascribed to the lower mass loading of nickel on their electrode (0.083 µg cm^{-2} *vs* 1.90 µg cm^{-2}). Conversely, this low nickel mass loading confers greater mass activity and TOF values (28 A mg^{-1}@0.61 V and 1.17 s^{-1}@0.61 V respectively).

All-in-all, the C13/**PPN$^+$-NiFeO$_x$** electrode presents very high OER catalytic activity in both 0.1 M and 1.0 M borate buffers at pH 9.2, and its performance place it among the best of **NiFeO$_x$** anodes of literature investigated in these electrolytes.

Table 3. OER performances of C/**PPN$^+$-NiFeO$_x$** anodes[a] prepared in this work compared to those of **NiFeO$_x$**-based anodes previously reported with 0.1 M and 1.0 M borate buffer solutions at pH 9.2

Catalyst/electrode	j (mA cm^{-2}) @η (V)	η (V) @j (mA cm^{-2})	Ni/Fe mass loading (µg cm^{-2})	Mass activity[b] (A mg^{-1}) @η (V)	TOF$_{min}$[b] (s^{-1}) @η (V)	Author[ref]
0.1 M borate buffer						
C/**PPN$^+$-Ni$_{0.46}$Fe$_{0.54}$O$_x$**	3.10@0.61	0.48@1	1.90/2.17	1.63@0.61	0.25@0.61	This work
C/**PPN$^+$-Ni$_{0.46}$Fe$_{0.54}$O$_x$**	0.46@0.40	-	1.90/2.17	0.24@0.40	0.04@0.40	This work
C/**PPN$^+$-NiO$_x$**	2.17@0.61	0.51@1	1.90	1.12@0.61	0.17@0.61	Fortage[18]
Au-Ti/Ni$_{0.86}$Fe$_{0.14}$O$_x$	7.4@0.61[c]	0.43@1[c]	115/15.3	0.064@0.61[d]	0.006@0.61[d]	Boettcher[11]
CC/NiFeO$_x$	nd	0.365@1	nd	nd	nd	Luo[33]
CC/NiFeO$_x$	nd	0.444@10	nd	nd	nd	Luo[33]
C/Ni$_{0.62}$Fe$_{0.38}$O$_x$	3.89@0.40[e]	0.37@1	1.26/0.74	1.9@0.40	0.29@0.40	Strasser[34]
1.0 M borate buffer						
C/**PPN$^+$-Ni$_{0.46}$Fe$_{0.54}$O$_x$**	14.63@0.61	0.44@1	1.90/2.17	7.7@0.61	1.17@0.61	This work
FTO/Ni$_{0.6}$Fe$_{0.4}$O$_x$	2.33@0.61[c]	0.52@1	0.083	28@0.61[d]	4.25@0.61[d]	Halaoui[12]

[a]Electro-generated by potentiostatic experiment at 1.0 V *vs* Ag/AgCl (4 mC) on C13/**PPN$^+$** electrodes (3 mm of diameter) in a 0.1 M borate buffer solution (pH 9.2) with 1 mM $NiSO_4$, 5 mM $Na_2C_2O_4$ and 0.8 mM [$Fe_x(C_6H_8O_7)(NH_3)_y$]. The formula of this nickel iron oxide was estimated to be $Ni_{0.46}Fe_{0.54}O_x$ with Ni and Fe contents of 32.4 and 38.8 nmol cm^{-2} respectively. [b]Values calculated for the Ni content. [c]Values were extrapolated from the cyclic voltammograms reported by the authors. [d]Data non calculated by the authors but estimated herein from the current density (j) at defined overpotentials (η) and the mass loading of Ni given in the article. [e]Data non calculated by the authors but estimated herein from the TOF value at defined overpotentials (η) and the mass loading of Ni/Fe given in the article. nd: not determined. Au-Ti: Au/Ti-coated glass electrodes; CC: Carbon cloth; FTO: Fluorine doped Tin Oxide electrode.

III – Conclusion

We report a very efficient nanocomposite material for OER in near neutral pH and based on nickel/iron oxide particles embedded into a poly(pyrrole-alkyl ammonium) film. This nanocomposite material was prepared by electrogeneration of the **$NiFeO_x$** particles into the cationic polymer film by an anodic process are at controlled potential from a borate buffer solution (pH 9.2) containing anionic iron citrate and nickel oxalate complexes. The incorporation of iron into nickel oxide particles by this anodic procedure is quite reproducible with *ca.* 54 % molar of Fe (relative to Ni) and the C/**PPN^+-$NiFeO_x$** electrode exhibits one of the best OER performance of literature in 1.0 M borate buffer (pH 9.2) with a very high catalytic current of 14.6 mA cm^{-2} at an overpotential of 0.61 V, a low overpotential of 0.44 at 1 mA cm^{-2}, and along with very high mass activity and TOF values of 7.7 A mg^{-1} and 1.17 s^{-1} respectively at η of 0.61 V.

For the comparison, nanocomposite materials have been prepared *via* the same procedure from borate buffer solution with only nickel oxalate. Nevertheless, the presence of iron trace in the electrolyte allows an involuntary incorporation of iron into nickel oxide particles with *ca.* 25 % of Fe. These electrodes, denoted C/**PPN^+-Ni(Fe)O_x**, present interesting OER performance but much lower than that of C/**PPN^+-$NiFeO_x$** with the intentional addition of iron into nickel oxide. Then, the catalytic activity of the C/**PPN^+-Ni(Fe)O_x** electrodes has been clearly improved by an anodization process to achieve 16.3 and 6.96 mA cm^{-2} at overpotentials of 0.71 and 0.61 V in a 1.0 M borate buffer, but their OER activity remains lower than that of C/**PPN^+-$NiFeO_x$**. The improvement of the OER performance of the C/**PPN^+-Ni(Fe)O_x** was ascribed to the additional incorporation of ion during the anodization for which the percentage of Fe into NiO_x increased until 51 % in an uncontrolled and non-reproducible manner.

This preliminary study revealed the very promising OER performance of the **PPN^+-$NiFeO_x$** nanocomposite material and further characterizations have to be carried out to confirm and rationalize this high performance. First of all, a larger number of electrodes has to be prepared in order to fine estimate the reproducibility of the all-electrochemical procedure in terms of redox behavior, OER catalytic activity and relative quantities of nickel and iron incorporated into the polymer film. Of note, the measure of quantities of nickel and iron electrodeposited on electrode, after their dissolution in nitric acid, will be more accurate by using Inductively Coupled Plasma Atomic Emission Spectroscopy (ICP-AES) instead of ICP-

MS, due to its lower limit of detection (µg L^{-1} for ICP-AES *vs* mg L^{-1} for ICP-MS). Then the **PPN^+-$NiFeO_x$** nanocomposite material has to be characterized by SEM and AFM to observe the morphology and nanostructuration of the film, by TEM and XAS to estimate the size of the **$NiFeO_x$** particles within **PPN^+**, by SEM-EDX, XPS and XANES to determine the composition and oxidation states of the mixed metal oxide, and by TEM-SAED and EXAFS to evaluate the nature and crystallinity of **$NiFeO_x$** particles. In addition, the redox behavior and OER electrocatalytic activity of C/**PPN^+-$NiFeO_x$** have to be further investigated by electrochemical impedance spectroscopy to evaluate its conductivity and capacitance, the latter being correlated to its nanostructuration, and by Tafel plot to gain some mechanistic information such as the rate determining step through the Tafel slope. In addition, long electrolysis at controlled potential or current will have to be performed with C/**PPN^+-$NiFeO_x$** electrodes in order to demonstrate the stability of the nanocomposite material under catalytic conditions. This work paves the way of a new generation of nanocomposite anodes composed of mixed metal oxides well dispersed into organic polymers, and very active for electrocatalytic OER. This type of nanocomposite material, rarely explored in literature to develop OER anodes, would be extended to the implementation of anodes containing others efficient multimetallic catalysts such as $CoFeO_x$, $NiCoFeO_x$ and $MnCaO_x$, the latter being able to mimic the natural oxygen evolving center (OEC) found in the photosystem II of the green plants.

References

1 Feng, C., Faheem, M. B., Fu, J., Xiao, Y., Li, C. & Li, Y. Fe-Based Electrocatalysts for Oxygen Evolution Reaction: Progress and Perspectives. *ACS Catalysis* **10**, 4019-4047 (2020).

2 Tichenor, R. L. Nickel Oxides-Relation Between Electrochemical and Foreign Ion Content. *Industrial & Engineering Chemistry* **44**, 973-977 (1952).

3 Troilus, G. & Alfelt, G. The migration of iron in alkaline nickel cadmium cells with pocket electrodes. *In Power Sources; Elsevier*, 337−347 (1967).

4 Młynarek, G., Paszkiewicz, M. & Radniecka, A. The effect of ferric ions on the behaviour of a nickelous hydroxide electrode. *J. Appl. Electrochem.* **14**, 145-149 (1984).

5 Corrigan, D. A. The Catalysis of the Oxygen Evolution Reaction by Iron Impurities in Thin Film Nickel Oxide Electrodes. *J. Electrochem. Soc.* **134**, 377-384 (1987).

6 Trotochaud, L., Young, S. L., Ranney, J. K. & Boettcher, S. W. Nickel–Iron Oxyhydroxide Oxygen-Evolution Electrocatalysts: The Role of Intentional and Incidental Iron Incorporation. *J. Am. Chem. Soc.* **136**, 6744-6753 (2014).

7 Burke, M. S., Zou, S., Enman, L. J., Kellon, J. E., Gabor, C. A., Pledger, E. & Boettcher, S. W. Revised Oxygen Evolution Reaction Activity Trends for First-Row Transition-Metal (Oxy)hydroxides in Alkaline Media. *The Journal of Physical Chemistry Letters* **6**, 3737-3742 (2015).

8 Zou, S., Burke, M. S., Kast, M. G., Fan, J., Danilovic, N. & Boettcher, S. W. Fe (Oxy)hydroxide Oxygen Evolution Reaction Electrocatalysis: Intrinsic Activity and the Roles of Electrical Conductivity, Substrate, and Dissolution. *Chem. Mater.* **27**, 8011-8020 (2015).

9 Friebel, D., Louie, M. W., Bajdich, M., Sanwald, K. E., Cai, Y., Wise, A. M., Cheng, M.-J., Sokaras, D., Weng, T.-C., Alonso-Mori, R., Davis, R. C., Bargar, J. R., Nørskov, J. K., Nilsson, A. & Bell, A. T. Identification of Highly Active Fe Sites in (Ni,Fe)OOH for Electrocatalytic Water Splitting. *J. Am. Chem. Soc.* **137**, 1305-1313 (2015).

10 Li, N., Bediako, D. K., Hadt, R. G., Hayes, D., Kempa, T. J., von Cube, F., Bell, D. C., Chen, L. X. & Nocera, D. G. Influence of iron doping on tetravalent nickel content in catalytic oxygen evolving films. *Proc. Natl. Acad. Sci.* **114**, 1486-1491 (2017).

11 Smith, A. M., Trotochaud, L., Burke, M. S. & Boettcher, S. W. Contributions to activity enhancement via Fe incorporation in Ni-(oxy)hydroxide/borate catalysts for near-neutral pH oxygen evolution. *Chem. Commun.* **51**, 5261-5263 (2015).

12 Fayad, R., Dhainy, J., Ghandour, H. & Halaoui, L. Electrochemical study of the promoting effect of Fe on oxygen evolution at thin 'NiFe–Bi' films and the inhibiting effect of Al in borate electrolyte. *Catalysis Science & Technology* **7**, 3876-3891 (2017).

13 Corrigan, D. A. & Bendert, R. M. EFFECT OF COPRECIPITATED METAL-IONS ON THE ELECTROCHEMISTRY OF NICKEL-HYDROXIDE THIN-FILMS - CYCLIC VOLTAMMETRY IN 1M KOH. *J. Electrochem. Soc.* **136**, 723-728 (1989).

14 Zouaoui, A., Stephan, O., Ourari, A. & Moutet, J. C. Electrocatalytic hydrogenation of ketones and enones at nickel microparticles dispersed into poly(pyrrole-alkylammonium) films. *Electrochim. Acta* **46**, 49-58 (2000).

15 Doyle, R. L., Godwin, I. J., Brandon, M. P. & Lyons, M. E. G. Redox and electrochemical water splitting catalytic properties of hydrated metal oxide modified electrodes. *PhysChemChemPhys* **15**, 13737-13783 (2013).

16 Singh, A., Chang, S. L. Y., Hocking, R. K., Bach, U. & Spiccia, L. Highly active nickel oxide water oxidation catalysts deposited from molecular complexes. *Energy Environ. Sci.* **6**, 579-586 (2013).

17 Singh, A., Chang, S. L. Y., Hocking, R. K., Bach, U. & Spiccia, L. Anodic deposition of NiOx water oxidation catalysts from macrocyclic nickel(ii) complexes. *Catal. Sci. Technol.* **3**, 1725-1732 (2013).

18 Morales, D. V., Astudillo, C. N., Lattach, Y., Urbano, B. F., Pereira, E., Rivas, B. L., Arnaud, J., Putaux, J.-L., Sirach, S., Cobo, S., Moutet, J.-C., Collomb, M.-N. & Fortage, J. Nickel oxide–polypyrrole nanocomposite electrode materials for electrocatalytic water oxidation. *Catal. Sci. Technol.* **8**, 4030-4043 (2018).

19 Bediako, D. K., Lassalle-Kaiser, B., Surendranath, Y., Yano, J., Yachandra, V. K. & Nocera, D. G. Structure–Activity Correlations in a Nickel–Borate Oxygen Evolution Catalyst. *J. Am. Chem. Soc.* **134**, 6801-6809 (2012).

20 Bonke, S. A., Wiechen, M., Hocking, R. K., Fang, X.-Y., Lupton, D. W., MacFarlane, D. R. & Spiccia, L. Electrosynthesis of Highly Transparent Cobalt Oxide Water Oxidation Catalyst Films from Cobalt Aminopolycarboxylate Complexes. *ChemSusChem* **8**, 1394-1403 (2015).

21 Adam, F. I., Bounds, P. L., Kissner, R. & Koppenol, W. H. Redox Properties and Activity of Iron–Citrate Complexes: Evidence for Redox Cycling. *Chemical Research in Toxicology* **28**, 604-614 (2015).

22 Hastings, A. B. & Van Slyke, D. D. The determination of the three dissociation constants of citric acid. *J. Biol. Chem.* **53**, 269-276 (1922).

23 Silva, A. M. N., Kong, X. & Hider, R. C. Determination of the pKa value of the hydroxyl group in the α-hydroxycarboxylates citrate, malate and lactate by 13C NMR: implications for metal coordination in biological systems. *BioMetals* **22**, 771-778 (2009).

24 Pierre, J. L. & Gautier-Luneau, I. Iron and citric acid: A fuzzy chemistry of ubiquitous biological relevance. *Biometals* **13**, 91-96 (2000).

25 Matzapetakis, M., Raptopoulou, C. P., Tsohos, A., Papaefthymiou, V., Moon, N. & Salifoglou, A. Synthesis, Spectroscopic and Structural Characterization of the First Mononuclear, Water Soluble Iron−Citrate Complex, (NH4)5Fe(C6H4O7)2·2H2O. *J. Am. Chem. Soc.* **120**, 13266-13267 (1998).

26 Lingane, J. J. Polarographic Investigation of Oxalate, Citrate and Tartrate Complexes of Ferric and Ferrous Iron. *J. Am. Chem. Soc.* **68**, 2448-2453 (1946).

27 Meites, L. Polarographic Studies of Metal Complexes. V. The Cadmium(II), Zinc(II) and Iron(III) Citrates. *J. Am. Chem. Soc.* **73**, 3727-3731 (1951).

28 Hamm, R. E., Shull, C. M. & Grant, D. M. Citrate Complexes with Iron(II) and Iron(III)1. *J. Am. Chem. Soc.* **76**, 2111-2114 (1954).

29 Cox, J. & Cummings, T. E. A cyclic voltammetric investigation of the iron(III)/(II) couple in citrate and phosphate media. *J. Electroanal. Chem.* **42**, 153-157 (1973).

30 Battistini, L. & Lopez-Palacios, J. Multistep Mechanism in the Electrochemical Oxidation-Reduction of Fe-Citrate Complexes. *Anal. Chem.* **66**, 2005-2009 (1994).

31 Mahmoudi, L. & Kissner, R. Electrode reactions of iron oxide–hydroxide colloids. *Dalton Trans.* **43**, 15407-15413 (2014).

32 Louie, M. W. & Bell, A. T. An Investigation of Thin-Film Ni-Fe Oxide Catalysts for the Electrochemical Evolution of Oxygen. *J. Am. Chem. Soc.* **135**, 12329-12337 (2013).

33 Yang, L., Xie, L., Ge, R., Kong, R., Liu, Z., Du, G., Asiri, A. M., Yao, Y. & Luo, Y. Core–Shell NiFe-LDH@NiFe-Bi Nanoarray: In Situ Electrochemical Surface Derivation Preparation toward Efficient Water Oxidation Electrocatalysis in near-Neutral Media. *ACS Applied Materials & Interfaces* **9**, 19502-19506 (2017).

34 Görlin, M., Gliech, M., de Araújo, J. F., Dresp, S., Bergmann, A. & Strasser, P. Dynamical changes of a Ni-Fe oxide water splitting catalyst investigated at different pH. *Catal. Today* **262**, 65-73 (2016).

General conclusion and perspectives

The first part of this thesis work has been dedicated to improving and further demonstrating the high stability of our metal-oxide nanocomposite. The material electrodeposited at an electrode surface composed by nanoparticles of metal oxide (NiO_x and CoO_x) entrapped in the positively charged poly(pyrrole-alkylammonium) (denoted as PPN^+) has demonstrated to be highly active towards the electrocatalytic water oxidation in previous works. However, the adherence of the polymeric matrix onto the glassy carbon electrode is lost after a few hours of activity. Although the simple ITO electrode modified with the nanocomposite was not capable to sustain long electrolysis, the introduction of the porosity on its surface enables a long electrolysis that could last over a week. This could be explained by the *zip-like* effect between the crystal defects at the surface and the polymeric material that ensures the stability of the nanocomposite. In addition, as our nanocomposite materials can be highly stable during several days under electrocatalytic conditions, it shows that the polymer film protects the metal oxide particles from degradation processes such as corrosion.

Previous results by TEM studies on the nickel and cobalt oxide nanocomposite displayed a well-dispersed nanostructured material, in which nickel and cobalt oxide nanoparticles were sized as 21 and 31 nm, respectively. The high nanostructuration of the nanocomposite is confirmed by EIS studies performed in the case of cobalt oxide nanocomposite. The great electroactive surface area provided by the nanoparticles embedded into the polymer matrix is at the origin of its great OER electrocatalytic activity under mildly basic electrolyte (pH 9.2) and their high mass activities (1 and 4 A mg^{-1}). In contrast, the nanoparticles of cobalt oxide observed by SEM electrodeposited on the porous ITO electrode (without polymer) revealed agglomerated nanoparticles, which grew outside the crystal defects, while the nickel oxide nanoparticles grew inside the defects and, therefore, are not visible even if the charge used to load the porous ITO electrode was 10 times bigger.

Mechanistic studies by Tafel slope gave close values of 65 and 56 mV dec^{-1} for PPN^+-CoO_x and CoO_x, respectively. This weak discrepancy between these two values seems to indicate that the same OER mechanism is involved for both electrodes and is governed by a chemical step following an electron transfer.

Using an electrochemical strategy was extended to a mixed-metal nanocomposite: PPN^+-$NiFeO_x$. This nanocomposite was synthetized with an intentional addition of iron ammonium citrate, which resulted in a fast method to obtain highly active anodes for OER. For

this synthesis we were inspired by the group of Nocera, as we were able to perform a single-step electrooxidation, with no need of "activation" of the nickel centers.

The perspectives of this thesis work are to develop a new technique to ensure the physisorption of the anode material without compromising the conductivity of the ITO plate, since the nanostructuration in this work was accomplished by creating crystal defects on its surfaces (*via* reduction and acid treatment). A method to reach this objective is to enhance the adhesive properties of the poly(pyrrole-alkyl ammonium) by the insertion of another a bio-inspired adhesive molecule, used by marine mussels to adhere on different surfaces under wet conditions. As has been done very recently, catechol moieties has been already introduced in polymers such as poly(ethylene glycol), polystyrene, polyaniline and polypyrrole to enhance the adherent properties of the material. By adding a catechol moiety to the poly(pyrrole-alkyl ammonium) might be another good approach to improve the stability of our anodes for OER.

Another objective is to follow the synthesis of an iron-doped cobalt oxide nanocomposite by the same oxidative conditions used for iron-doped nickel oxide nanocomposite. As we were able to observe on Chapter IV, intentional addition of iron into the nickel oxide leads to a drastic enhance on the catalytic current towards OER, without any conditioning (anodization) step to active the metal centers. This result is also expected with the cobalt oxide-based anodes.

To simplify the electrochemical process, the next step is to develop the metal oxide-based nanocomposites anodes, in which the synthesis of a negatively charged polymer matrix is desired. By this means, we could avoid the use of negatively charged metal complexes, ($[ML_m]^{n-}$), generated *in situ*, and replace them with simpler metal cations (Ni^{2+}, Co^{2+}…). Likewise, this could be more suitable to the need of an electrolyzer that functions with seawater rather than freshwater since the polymer matrix could be selective towards the OER reactions and anions such as chlorine would be repealed from the matrix.

Finally, as the cobalt oxide catalysts has been used recently for the reduction of carbon dioxide, it would be of special interest to analyze our efficient anodes for OER for its catalytic activity towards this catalytic reduction.

Experimental Section

Index

I. Chemicals and Reagents

The monomer (3-pyrrole-1-yl-propyl)-triethylammonium tetrafluoroborate, denoted PN^+, was prepared as previously reported.[1] Nickel(II) sulfate hexahydrate ($NiSO_4•6H_2O$, 99% Acros), cobalt(II) sulfate hexahydrate ($CoSO_4•6H_2O$, 99% Acros), ammonium iron (III) citrate ($[Fe^{III}_x(C_6H_8O_7)(NH_3)_y]$, reagent grade, Aldrich), sodium oxalate ($Na_2C_2O_4$, 99% Prolabo), boric acid (H_3BO_3, 99.5% Normapur), acetonitrile (Fisher, HPLC grade), sodium sulfate (Na_2SO_4, 99% Laurylab), sodium hydroxide (NaOH, 99% Laurylab), potassium hydroxide (KOH, ≥85% Prolabo) and tetra-*n*-butylammonium perchlorate ($[Bu_4N]ClO_4$, Fluka puriss) were purchased from commercial suppliers. All reagents and solvents were used as received. Distilled water was obtained from an Elga water purification system (milli-Q system, Purelab option, 15.0 MΩ.cm, 24 °C).

II. Electrochemistry

The electrochemical experiments were performed using a conventional three-electrode system. Electropolymerization of poly(pyrrole-alkyl ammonium) film (denoted PPN^+) was performed in acetonitrile in a dry-glove box using an EGG PAR Model 173 potensiostat under argon atmosphere at room temperature. Electrodeposition of Ni^0, Co^0, their electrooxidation into NiO_x and CoO_x, respectively, as well as the electrodecomposition of the $[Ni^{II}(C_2O_4)]^{2+}$ and $[Fe^{III}_x(C_6H_8O_7)(NH_3)_y]$ for the electrodeposition of $NiFeO_x$, and electroanalytical experiments were performed using a CHI 660B Electrochemical analyser (CH Instruments) in aqueous solution. Electrodeposition of Ni^0 and Co^0 were performed in a solution purged with argon while the electrooxidation into NiO_x and CoO_x, and the electrodeposition of $NiFeO_x$, were performed under air atmosphere. Potentials were referred to Ag/AgCl (3 M KCl in water) or $Ag/AgNO_3$ (10 mM $AgNO_3$ in CH_3CN + 0.1 M $[Bu_4N]ClO_4$) references electrodes in aqueous and acetonitrile solutions, respectively. Potentials referred to the Ag/AgCl (3 M KCl) system can be converted to the reversible hydrogen electrode (RHE)[2] according to the Nernst equation S1:

$$E_{RHE} = E_{Ag/AgCl} + 0.059 \times pH + E^{o}_{Ag/AgCl} \qquad (S1)$$

where $E^{o}_{Ag/AgCl}$ = 0.199 V *vs* NHE at 25°C and NHE is the normal hydrogen electrode.

Potentials referred to the $Ag/AgNO_3$ reference electrode can be converted to Ag/AgCl (3 M KCl) by adding 330 mV.

For analytical experiments, the films of PPN^+-Co^0 and the metal mixture PPN^+-$NiFeO_x$ were electrodeposited on glassy carbon working electrodes (denoted C, 3 mm in diameter corresponding to a surface of 0.071 cm^2). These electrodes were polished with 1 µm diamond paste before coating and rinsed with distilled water, ethanol, and acetone. For microscopy characterizations, and for stability measurements which involves a prolonged electrolysis at 1.2 V, the films of PPN^+-NiO_x and PPN^+-CoO_x, and their respective direct deposition versions (NiO_x and CoO_x), were electrodeposited on "porous" indium tin oxide-coated glass electrodes (denoted as ITO_{por}, 0.4 cm^2, 30 Ohms (Solems)). For X-ray photoelectron spectroscopy (XPS) measurements performed on cobalt oxide material, PPN^+ and Co^0 were electrodeposited on carbon pellets (denoted C_{pel}, 6 mm in diameter corresponding to a surface of 0.283 cm^2, (Origalys)). The modified carbon pellets are easily unscrewed from the electrode holder in order to introduce the C_{pel}/PPN^+-CoO_x and C_{pel}/CoO_x samples into the vacuum chamber of the XPS spectrometer. Finally, for electrodeposition carried out onto ITO_{por} of PPN^+ and the metals Ni^0 and Co^0 and their subsequent oxidation of the nickel and cobalt particles into NiO_x and CoO_x, the auxiliary electrode was a platinum plate (≈ 2 cm^{-2}), while in the case of electrodeposition on C and C_{pel} of PPN^+ and Co^0, the auxiliary electrode used was a platinum wire. The overpotential (η) applied to the working electrode for performing water oxidation was calculated from the following equation S2:

$$\eta = E_{RHE} - 1.23\ V \qquad (S2)$$

where 1.23 V is standard potential of water oxidation reaction at pH 0.

Preparation of porous ITO by electrochemistry:

ITO_{por} referred above was prepared following a procedure inspired by the one reported by Zhang et al.[3] In a first step, an ITO plate (0.4 cm^2, 30 Ohms (Solems)) was reduced at -1.15 V *vs* Ag/AgCl (20 mC of charge) in an aqueous phosphate buffer solution (0.1 M KH_2PO_4 and 0.04 M Na_2HPO_4) at pH 7.0, previously degassed under argon during 30 min. The auxiliary electrode used for this reduction was a platinum plate (≈ 2 cm^2). This reduction leads to a partial reduction of the mixture of In_2O_3 and SnO_2 into metallic In^0 and Sn^0, which can be observed as an increase in the opacity on the transparent plate. Then, in a second step, the reduced ITO was soaked in aqua regia (HCl (37%w)/HNO_3 (65%w); 3/1 in volume) for 1 second and immediately transferred into water to stop the action of the acid on the plate and control its porosity. The resulting ITO_{por} electrode is then used for the deposition of PPN^+ and NiO_x or CoO_x as described above.

III. Preparation of the Nanocomposite Film Modified Electrodes

III.1 Electrosynthesis of Poly(pyrrole-alkylammonium) Film (PPN^+) Modified Electrodes

PPN^+ films were deposited either on C, C_{pel}, or ITO_{por} electrodes, by potentiostatic oxidative electropolymerization at E_{app} = +0.95 V *vs* $Ag/AgNO_3$ for C and C_{pel}, and +1.1 V for ITO_{por} from a 4 mM solution of PN^+ in CH_3CN containing $[Bu_4N]ClO_4$ (0.1 M) as supporting electrolyte, without stirring and under inert atmosphere (argon) in a dry glovebox. The polymerization of PN^+ was monitored through the anodic charge recorded during electrolysis. A full description of the procedure was previously reported by our group.[4] The anodic charge used for polymerization of PN^+ is respectively 4, 16, 22.4 mC for C, C_{pel}, ITO_{por} electrodes, which correspond to 56 mC cm^{-2}. The apparent surface coverage in ammonium units Γ_{N^+} (mol cm^{-2}), was determined by integrating the charge of the polypyrrole oxidation wave by cycling between 0.0 to +0.6 V (*vs* $Ag/AgNO_3$) at a low scan rate (10 mV s^{-1}) as previously described,[4] over an average of ten electrodes. Γ_{N^+} values ranging from 1.1 x 10^{-7} to 1.3 x 10^{-7} mol cm^{-2} were obtained for deposition of PPN^+ films onto C electrodes (surface of 0.071 cm^2, denoted C/PPN^+) using a polymerization charge of 4 mC, corresponding to an electropolymerization yield between 44 and 52%. Γ_{N^+} values ranging from 8.2 x 10^{-8} to 10.5 x 10^{-8} mol cm^{-2} were obtained for PPN^+ deposition onto porous ITO electrodes (surface of 0.4 cm^2, denoted ITO_{por}/PPN^+) using a polymerization charge of 22.4 mC, corresponding to an electropolymerization yield in the range of 33 to 42%.

III.2 Electrodeposition of Metallic Nanoparticles (Ni^0 and Co^0) and Electrooxidation into Cobalt Oxide (CoO_x)

Before the electrodeposition of nickel or cobalt, in order to have an optimum incorporation of the anionic oxalate complex ($[M(C_2O_4)_2]^{2-}$, M=Ni, Co) within the PPN^+ film, the C/PPN^+, C_{pel}/PPN^+, and ITO_{por}/PPN^+ working electrodes were soaked under stirring during 1 h in an aqueous borate buffer solution (0.1 M H_3BO_3 + 0.1 M Na_2SO_4) at pH 6 containing 1 mM $NiSO_4$ and 5 mM $Na_2C_2O_4$, in the case of nickel and 4 mM $CoSO_4$ and 20 mM $Na_2C_2O_4$, in the case of cobalt. The deposition solution was previously degassed under argon during 30 min.[5] The electrodeposition of Co^0 within PPN^+ films was then performed by a controlled-potential reduction of the C/PPN^+ modified electrode at E_{app} = -1.3 V *vs* Ag/AgCl (-1.3 V for C_{pel}/PPN^+, -1.5 V for ITO/PPN^+ and ITO_{por}/PPN^+) in this cobalt oxalate solution under an argon atmosphere (Figure 1 in Chapter III). Similarly to the PPN^+ electrodeposition, the charge used for cobalt electrodeposition was 4 mC for C/PPN^+, 16 mC for C_{pel}/PPN^+, 22.4 mC for

ITO_{por}/PPN^+ and 56 mC for ITO/PPN^+, each corresponding to 56 mC cm^{-2}. The nickel electrodeposition within $ITOp_{or}/PPN^+$ was carried out by a controlled-potential reduction at E_{app} = -1.4 V *vs* Ag/AgCl in a nickel oxalate solution under argon by passing 22.4 mC (Figure 2 in Chapter II). For comparative studies, electrodeposition of Co^0 on naked C, ITO and ITO_{por} electrodes, and that of Ni^0 on ITO_{por}, were also performed following the same electrochemical procedure, but without prior soaking the electrode in the cobalt and nickel oxalate solution. Then the Co^0 nanoparticles on electrode are spontaneously oxidized into cobalt oxide (mainly CoO)[6,7] when exposed to oxygen of air before being transferred into an aqueous borate solution (0.1 M H_3BO_3 and 0.05 M NaOH) at pH 9.2. The CoO material was then oxidized in an higher oxidation state than +II (denoted CoO_x) by five repeated cyclic voltammetry scans from 0 to +1.2 V *vs* Ag/AgCl (scan rate 50 mV s^{-1}) in the aforementioned aqueous solution at pH 9.2 (Figures 2 and 9 in Chapter III). The Ni^0 particles are oxidized to NiO_x by 50 repeated cyclic voltammetry scans of ITO_{por}/PPN^+-Ni^0 or ITO_{por}/Ni^0 electrodes from 0 to 1.2 V *vs* Ag/AgCl (scan rate of 50 mV s^{-1}) in borate buffer solution at pH 9.2 (0.1 M H_3BO_3 and 0.05 M NaOH). These steps of metal oxidation do not require argon degassing. The loading of cobalt and nickel deposited on C and ITO_{por} electrodes (denoted Γ_{Co} and Γ_{Ni}) was estimated by ICP-MS (see section 4). The Γ_{Co} values range from 1.82 x 10^{-8} to 2.73 x 10^{-8} mol cm^{-2} for C/PPN^+-CoO_x electrodes and from 4.74 x 10^{-8} to 5.40 x 10^{-8} mol cm^{-2} for C/CoO_x electrodes. In the case of cobalt deposition on porous ITO, Γ_{Co} values range from 2.52 x 10^{-8} to 3.96 x 10^{-8} mol cm^{-2} for ITO_{por}/PPN^+-CoO_x electrodes, and from 1.83 x 10^{-8} to 2.03 x 10^{-8} mol cm^{-2} for ITO_{por}/CoO_x. For the nickel deposition on porous ITO, the Γ_{Ni} values range from 4.28 x 10^{-8} to 7.24 x 10^{-8} mol cm^{-2} for ITO_{por}/PPN^+-NiO_x electrodes, and from 0.68 x 10^{-8} to 1.50 x 10^{-8} mol cm^{-2} for ITO_{por}/NiO_x.

III.3 Electrodeposition by electrooxidation of nickel and iron complexes into mixed metal nickel-iron oxide ($NiFeO_x$)

Before the electrodeposition of nickel and iron, the PPN^+ film is load with nickel and iron precursors by soaking it under stirring during 1 h in an aqueous borate buffer solution (0.1 M H_3BO_3 + 50 mM NaOH) at pH 9.2 containing 1 mM $NiSO_4$ and 5 mM $Na_2C_2O_4$, and 0.4 mM (or 0.8 mM) $[Fe^{III}_x(C_6H_8O_7)(NH_3)_y]$. The electrodeposition of $NiFeO_x$ within PPN^+ films was then performed by a controlled-potential oxidation of the C/PPN^+ modified electrode (S = 0.071 cm^2) at E_{app} = 1.0 V *vs* Ag/AgCl in this nickel oxalate and iron citrate solution. Similarly to the PPN^+ electrodeposition, the charge used for nickel and iron electrodeposition was 4 mC for C/PPN^+ corresponding to 56 mC cm^{-2}. For comparative studies, an electrodeposition of Ni

alone on C/PPN$^+$ was also performed following the same electrochemical procedure, using an electrodecomposition of the complex at an anodic potential of 1.0 V *vs* Ag/AgCl. As there is only one metal involved, the electrodeposition was carried out with 2 mC of charge to obtain the same amounts of nickel oxide in both materials. The C/PPN$^+$-NiO_x (also named C/PPN$^+$-$Ni(Fe)O_x$ due to the involuntary presence of iron inside NiO_x) by electrooxidation had to be "activated" (*i.e.* anodization) by a controlled-potential oxidation at E_{app} = 0.95 V *vs* Ag/AgCl for 45 min (plateaux) in an aqueous borate solution (1.0 M H_3BO_3 and 0.5 M NaOH) at pH 9.2. This process is not necessary in the C/PPN$^+$-$NiFeO_x$ material since as-deposited it reaches the same high levels of current density (j) as the activated C/PPN$^+$-$Ni(Fe)O_x$. The loading of nickel and iron deposited on C/PPN$^+$ electrodes (denoted Γ_{Ni} and Γ_{Fe}) was estimated by ICP-MS (see section 4). The Γ_{Ni} values range from 3.17 x 10^{-8} to 4.93 x 10^{-8} mol cm^{-2} and the Γ_{Fe} values range 3.24 x 10^{-8} to 5.85 x 10^{-8} mol cm^{-2} for C/PPN$^+$-$NiFeO_x$ electrodes, regardless the iron concentration (0.40 or 0.80 mM) in the solution of deposition. In the case of C/PPN$^+$-$Ni(Fe)O_x$ electrodes, the Γ_{Ni} values range from 3.31 x 10^{-8} to 4.76 x 10^{-8} mol cm^{-2} after "anodization" with a Γ_{Fe} values range 0.93 x 10^{-8} to 4.87 x 10^{-8} mol cm^{-2}, due to the iron poisoning during activation process.

IV. Determination of Co, Ni and Fe Contents (q) on Electrode by Inductively Coupled Plasma Mass Spectrometry (ICP-MS)

The amount of nickel, and cobalt were determined by ICP-MS in the PPN$^+$-MO_x (Γ_{N^+} = 9.36 (± 0.46) × 10^{-8} mol cm^{-2} for nickel deposition in Chapter II and Γ_{N^+} = 9.32 (± 0.56) × 10^{-8} mol cm^{-2} for cobalt deposition in Chapter III) on porous ITO electrodes (M=Ni, Co; 0.4 cm^2) prepared with a charge of 22.4 mC for PPN$^+$ and Co^0. These electrodes were first dried in air and then soaked in 5 mL of an acidic aqueous solution containing 0.45 M HNO_3. 30 min of soaking in this acidic solution is needed to entirely dissolve the PPN$^+$-MO_x and MO_x films. The complete films dissolution was then verified by cyclic voltammetry with the fully disappearance of the Ni^{II}/Ni^{III} and Co^{II}/Co^{III} redox process and the associated water oxidation catalytic wave. The nickel and cobalt concentration in the acidic solution was determined using a quadrupole ICP-MS Thermo X serie II (Thermo Electron, Bremen, Germany) equipped with an impact bead spray chamber and a standard nebulizer (0.8 mL min^{-1}). ^{60}Ni and ^{59}Co isotopes were selected for the measurement and ^{103}Rh isotope was used as internal standard. Polyatomic interferences were eliminated using the collision cell mode. The concentrations were obtained using an external calibration curve. In the case of Fe determination, ^{58}Fe and ^{57}Fe isotopes were

used for the measurement of iron content. The dissolution in which the films of PPN^+-$NiFeO_x$ were dissolved was of 1 mL of an acidic aqueous solution containing 0.45 M HNO_3, to ensure a better reproducibility of the amount of iron. Since the iron has no visible redox process, the electrode was left soaking until the associated water oxidation catalytic wave disappeared, along the accompanied Ni^{II}/Ni^{III} redox process. The content of Co, Ni and Fe on C, C/PPN^+, ITO_{por}/PPN^+, ITO_{por} are given in the section 3 above.

V. Electrochemical Impedance Spectroscopy (EIS)

EIS measurements were recorded with an Autolab PGSTAT 100 potentiostat (Eco Chemie, Utrecht, The Netherlands) using the conventional three-electrode system, described above in section 2, in a 0.1 M borate buffer solution at pH 9.2. For EIS measurements, C/PPN^+-CoO_x ($\Gamma_{N^+} = 1.2 \pm 0.1 \times 10^{-7}$ mol cm^{-2}, $\Gamma_{Co} = 2.27 \pm 0.45 \times 10^{-8}$ mol cm^{-2}) and C/CoO_x ($\Gamma_{Co} = 5.07 \pm 0.33 \times 10^{-8}$ mol cm^{-2}) were used and prepared on carbon electrode (3 mm of diameter). The data were recorded and operated using Nova software (version 2.1). A frequency range from 50.000 to 0.1 Hz was scanned using an amplitude of 0.02 Vrms and with a potential range between of +0.2 and +1.0 V *vs* Ag/AgCl. The ZView software was used to fit the experimental impedance data with the appropriate equivalent electrical circuit.

The complex impedance of constant phase elements (CPE) is given by the Equation S3:

$$Z_{CPE} = \frac{1}{Q(j\omega)^n} \qquad \text{(S3)}$$

Where Q is admittance constant of CPE, ω is the frequency expressed in rad/s, and n the exponent. When n=1, this is the same equation as that for the impedance of a capacitor, where Q = C.

VI. Calculation of Mass Activity and Turnover Frequency (TOF)

The TOF value (expressed in s^{-1}) at a given overpotential is usually defined as mole of O_2 produced per second per mole of Co or Ni, O_2 produced being measured by gas chromatography. The TOF values for each Co or Ni based electrode could be also calculated from electrochemical experiments following the equation S4:

$$TOF = \frac{j \times S}{4 \times F \times n} \qquad \text{(S4)}$$

Where *j* is the catalytic current density (A cm^{-2}) at a given overpotential, S is the surface of the electrode (0.071 cm^2 for the carbon electrode), F is the Faraday constant (*vide supra*) and n is the molar number of cobalt or Ni deposited on electrode. This TOF value corresponds to its lower limit (TOF_{min}) since it was considered that all cobalt or Ni sites deposited on the electrode are active for water oxidation. The quantity of Co or Ni deposited was estimated by ICPMS (*vide supra*).

The mass activity (expressed in A mg^{-1}) at a given overpotential is calculated from the equation S5:

$$Mass\ activity = \frac{i}{m} \qquad \text{(S5)}$$

Where *i* is the catalytic current at a given overpotential (A) and m is the mass of cobalt or nickel deposited on electrode (mg).

VII. Tafel Plot

The Tafel curves were plotted as the overpotential (η), corrected by the ohmic potential drop ($\eta - iR$, see below), in function of the current density in logarithm form and should be linear following the equation S6:

$$(\eta - iR) = a + b \log j \qquad \text{(S6)}$$

Where *j* (A cm^{-2}) is the current density at a given corrected overpotential (η (V) $-$ iR) and b is the Tafel slope (V dec^{-1}). The current-overpotential data collected for Tafel plot were obtained by carring out electrolyses with C/PPN^+-CoO_x and C/CoO_x rotating disc electrodes (3 mm of diameter, with a rotation of 1200 rpm) in aqueous borate buffer solution (pH 9.2) at various potentials between +0.90 and +1.2 V *vs* Ag/AgCl, which corresponds to overpotentials η between +0.41 V and +0.71 V (*i.e.* corresponding to corrected overpotentials $\eta - iR$ between +0.41 V and +0.52 V). For each imposed potential, the current data were collected during electrolysis when the latter reaches a steady state after *c.a.* 600 s. The rotation of the electrode for the Tafel plot data collection allows reducing the mass transport effect on the catalytic current. High and low corrected overpotentials (respectively above +0.52 V and below +0.41 V) were ruled out for Tafel analysis in order to avoid respectively a strong oxygen evolution inducing mass transport limitations, and the Co^{II}/Co^{III} redox couple that could lead to erroneous interpretations of the Tafel slope. As mentioned above, the η overpotentials were corrected by

subtracting the ohmic potential drop (iR, where i (A) is current measured at the given overpotential and R (Ω) is the resistance measured between the reference electrode and the working electrode under rotation at 1200 rpm in aqueous borate buffer solution at pH 9.2). The R value was measured for each point of the Tafel plot (*i.e.* for each η value) and ranges between 760 and 813 Ω for C/PPN^+-CoO_x and between 562 and 600 Ω for C/CoO_x. The Tafel analyses were obtained with C/PPN^+-CoO_x (Γ_{N^+} = 1.2 ± 0.1 x 10^{-7} mol cm^{-2}, Γ_{Co} = 2.27 ± 0.45 x 10^{-8} mol cm^{-2}) and C/CoO_x (Γ_{Co} = 5.07 ± 0.33 x 10^{-8} mol cm^{-2}) electrodes that have been prepared with 4 mC of Co and PPN^+ as described above.

VIII. Atomic Force Microscopy (AFM) Observation

For electrodeposition on ITO_{por} electrodes (0.40 cm^2, 30 Ohms, from Solems), the NiO_x and PPN^+-NiO_x nanocomposite samples were prepared by using a charge of 22.4 mC for the deposition of Ni^0 from the nickel oxalate solution (see above the sections 2 and 3). All samples were observed with a Bruker instrument (Dimension Icon with ScanAsyst) equipped with a Bruker Stage controller and a Nanoscope® V Bruker control box. The topography images were recorded by peak force mode with different scanning ranges and a tapping nose was used for imaging. AFM cantilevers with a silicon tip on nitride lever (Bruker scanasyst-air) with a nominal spring constant of 77.6 mN m^{-1} were used. The peak force frequency and amplitude were set to 2 kHz and 150 nm, respectively. All AFM images were displayed and processed using the Gwyddion program.

IX. Scanning Electron Microscopy (SEM) Observation coupled to Energy-dispersive X-Ray Spectroscopy (EDX)

SEM images (top and cross section views) of ITO, ITO_{por}, ITO_{por}/PPN^+, ITO_{por}/PPN^+-NiO_x, ITO_{por}/NiO_x and ITO_{por}/PPN^+-CoO_x were recorded with a FEI Quanta 250 microscope equipped with a field emission gun and operating at 2 kV. SEM images (top view) of ITO, ITO_{por} and ITO_{por}/CoO_x, and EDX spectrum of ITO_{por}, ITO_{por}/NiO_x, ITO_{por}/CoO_x, ITO_{por}/PPN^+, ITO_{por}/PPN^+-NiO_x and ITO_{por}/PPN^+-CoO_x, were recorded with a FEG Zeiss GeminiSEM500 microscope equipped with a SDD detector (EDAX OCTANE ELITE 25 with a ceramic window of Si_3N_4 – 60 mm^2) for EDX. The preparation of ITO_{por}, ITO_{por}/PPN^+, ITO_{por}/MO_x and ITO_{por}/PPN^+-MO_x (M = Ni, Co) is described in the sections 2 and 3.

X. X-ray photoelectron spectroscopy (XPS).

XPS analysis was performed with a Versa Probe II spectrometer (ULVAC-PHI) equipped with a monochromated Al Kα source (hν= 1486.6 eV). Constant pass energy of 23.3 eV was used to record the core level peaks. The fitting of the XPS spectrum was carried out with CasaXPS 2.3.15 software using Shirley background and a combination of Gaussian (70%) and Lorentzian (30%) distributions. Binding energies are referenced with respect to the adventitious carbon (C 1s BE = 284.6 eV). XPS analysis was performed on the electrode surface of C_{pel}/PPN^{+}-CoO_x (see above the section 3 for its preparation).

References

1 Cosnier, S., Deronzier, A., Moutet, J. C. & Roland, J. F. Alkylammonium and pyridinium group-containing polypyrroles, as new class of electronically conducting anion-exchange polymers. *J. Electroanal. Chem.* **271**, 69-81 (1989).

2 Zhong, M., Hisatomi, T., Kuang, Y., Zhao, J., Liu, M., Iwase, A., Jia, Q., Nishiyama, H., Minegishi, T., Nakabayashi, M., Shibata, N., Niishiro, R., Katayama, C., Shibano, H., Katayama, M., Kudo, A., Yamada, T. & Domen, K. Surface Modification of CoOx Loaded BiVO4 Photoanodes with Ultrathin p-Type NiO Layers for Improved Solar Water Oxidation. *J. Am. Chem. Soc.* **137**, 5053-5060 (2015).

3 Zhang, X., Lou, B., Li, D., Hong, W., Yu, Y., Li, J. & Wang, E. A universal method for the preparation of functional ITO electrodes with ultrahigh stability. *Chem. Commun.* **51**, 6788-6791 (2015).

4 Morales, D. V., Astudillo, C. N., Lattach, Y., Urbano, B. F., Pereira, E., Rivas, B. L., Arnaud, J., Putaux, J.-L., Sirach, S., Cobo, S., Moutet, J.-C., Collomb, M.-N. & Fortage, J. Nickel oxide–polypyrrole nanocomposite electrode materials for electrocatalytic water oxidation. *Catal. Sci. Technol.* **8**, 4030-4043 (2018).

5 Zouaoui, A., Stephan, O., Ourari, A. & Moutet, J. C. Electrocatalytic hydrogenation of ketones and enones at nickel microparticles dispersed into poly(pyrrole-alkylammonium) films. *Electrochim. Acta* **46**, 49-58 (2000).

6 Rice, D. W., Phipps, P. B. P. & Tremoureux, R. Atmospheric Corrosion of Cobalt. *J. Electrochem. Soc.* **126**, 1459-1466 (1979).

7 Suryanto, B. H. R., Lu, X., Chan, H. M. & Zhao, C. Controlled electrodeposition of cobalt oxides from protic ionic liquids for electrocatalytic water oxidation. *RSC Advances* **3**, 20936-20942 (2013).

Abstract:

This thesis deals with the development of highly active and stable anodes for electrocatalytic water oxidation under near-neutral pH conditions based on nickel, cobalt or nickel/iron oxide nanoparticles embedded into a poly(pyrrole-alkylammonium) matrix. By this means, early on the thesis we focused on the elaboration and characterization of the nano-structuration performed on the surface of the indium tin oxide (ITO) electrodes in view to enhance the physisorption of our previously reported nanocomposites: poly(pyrrole-alkyl ammonium) with nickel or cobalt oxide nanoparticles (PPN^{+}-MO_x). The procedure successfully prevents the film from desorption under OER electrocatalytic experiments and consequently the catalytic activity of the nanocomposite of both metals is very stable beyond 24 h of electrolysis.

A new mixed-metal Ni-Fe nanocomposite material is developed with a slightly different pathway than the previous nanocomposites, in which the simultaneous electro-decomposition of nickel and iron complexes precursors is concomitant to their electrooxidation. Finally, we confirm what previous studies have observed: the intentional addition of iron and the synergetic association between nickel and iron further enhances the OER performance, rather than simply being present as an impurity.

Titre : Nanoparticules d'oxyde de nickel et de cobalt incorporées dans des films de polypyrrole en tant que matériaux électrocatalytiques efficaces pour l'oxydation de l'eau

Résumé :

Cette thèse porte sur le développement d'anodes très actives et stables pour l'oxydation électrocatalytique de l'eau dans des conditions de pH quasi-neutre, à base de nanoparticules d'oxyde de nickel, de cobalt ou de nickel/fer incorporées dans une matrice de poly(pyrrole-alkylammonium). La première partie de la thèse se concentre sur l'élaboration et la caractérisation de la nano-structuration réalisée à la surface des électrodes d'oxyde d'indium et d'étain (ITO) en vue d'améliorer la physisorption de nos nanocomposites précédemment rapportés : poly(pyrrole-alkylammonium) avec des nanoparticules d'oxyde de nickel ou de cobalt (PPN^{+}-MO_x). La procédure empêche avec succès la désorption du film lors d'expériences électrocatalytiques OER et par conséquent l'activité catalytique du nanocomposite des deux métaux est très stable au-delà de 24 h d'électrolyse.

Un nouveau matériau nanocomposite de métaux mixtes Ni-Fe est développé avec une voie d'électrodéposition légèrement différente de celle des nanocomposites précédents, dans laquelle l'électro-décomposition simultanée des précurseurs de complexes de nickel et de fer est concomitante à leur électrooxydation. Enfin, nous confirmons ce que les études précédentes ont observé : l'ajout intentionnel de fer et l'association synergique entre le nickel et le fer améliore encore les performances OER, plutôt que d'être simplement présent sous forme d'impureté.